Chemical vapor deposition, characterization, and thermodynamic phase diagram calculations of sp^2-boron nitride thin films

Submitted in partial fulfillment of the requirements for

the degree of

Doctor of Philosophy

in

Materials Science and Engineering

Philip M. Jean-Remy

B.S., Materials Science and Engineering, University of Wisconsin-Madison
M. S., Materials Science and Engineering, Carnegie Mellon University

Carnegie Mellon University
Pittsburgh, PA

May, 2022

ACKNOWLEDGEMENTS

I would like to express sincere thanks to my Dissertation Committee Members: Dr. Robert Davis (Committee Chair, Advisor, MSE, ECE), Dr. Lisa Porter (MSE), Dr. Bryan Webler (MSE), and Dr. Andrew Gellman (Chem. E.). I appreciate the time that they all took to not only read my Thesis, but also for serving on my Overview Committee and providing me the critical feedback and encouragement for me to complete my remaining doctoral research.

Dr. Davis, through his mentorship, wisdom, and genuine kindness, has been such a positive and integral force in my development as a PhD student. From the day that I joined his Lab Group in August 2016, he has always treated me as an equal intellectually while still providing me the crucial insights that can only come from years of technical and teaching experience. His collaborative advising style often gave me the confidence and sense of urgency that I needed to take ownership of my research and Thesis. He delighted in my research successes, even at times when I did not recognize the success, and he offered encouragement and suggestions after I faced challenges and setbacks. He treated my deadlines for my various program milestones and article submissions as his own, and has in more ways than one shown how invested he was not just in my successful completion of the PhD program, but also in my life and future career. Dr. Davis, it is with sincere gratitude that I thank you for serving as my Advisor – I could not have come this far without you.

I would like to thank all of the Davis Lab Group of Masters and PhD students that I worked with during my time here: Luis Hernandez Cazares, Robert Simpson, Jingyu Tang, and Kunyao Jiang. I thank each of them for their camaraderie, friendliness, and assistance pertaining to the general upkeep of the Lab. I would especially like to thank Luis; during his time in the Lab Group, he trained me on the safe operation and routine maintenance of the vacuum systems,

roughing and turbomolecular pumps, intricate gas lines, chemical vapor deposition chambers, and highly flammable and toxic precursor gases. Through dealing with these various aspects of the Lab and their issues associated with inevitable malfunction, Luis' expertise and guidance has taught me to develop a calmer mind for troubleshooting problems and a deeper appreciation for the mechanical systems that make our lives easier.

I would like to thank the entire Materials Science and Engineering Staff for providing a wealth of resources and a warm environment for students in the Department. Marygrace Antkowski and Kelly Rockenstein have helped me so much with ordering various equipment and gas bottles for my lab over the years, as well as with sending loads of crucial equipment out for repair. Almost equally appreciated on the days where I could not stay awake in my office were the coffee provisions that Marygrace and Kelly maintained in Roberts and Wean Hall, respectively. I also appreciate Brett Riale's help in always assisting in certain lab malfunctions, especially when heavy objects or electrical hazards were involved. The Materials Characterization Facility Staff have been a phenomenal help to me as well. I thank Dr. Betsy Clark, Tom Nuhfer, Logan Solotky, Dan Flaherty, Dr. Matt Cabral, and Dr. Adam Wise for their superb running of the MCF and always being able to help with the various characterization tools. I seemed to never run out of questions about sample preparation or instrument operation, and I am thankful for them always finding time to help provide answers.

I would like to thank everyone I had the privilege of working with on a technical level for the advancement of my research. Craig McMillan from Allied High Tech Products was instrumental in me developing a semi-automatic polishing process for pyrolytic boron nitride surfaces. Dr. David Cole and Dr. Li Yang from EAG Laboratories were helpful in the acquisition of XPS and SIMS spectra for early boron nitride thin film samples that I synthesized. Dr. Kevin

Abassi from Case Western Reserve University's Swagelok Center for Surface Analysis of Materials was always friendly and helped me on multiple occasions to obtain XPS sputter-depth profiles of various boron nitride thin film samples. Dr. Webler and Dr. Chris Pistorius were instrumental in teaching me how to apply CALPHAD concepts and software to the generation of CVD phase diagrams for the boron nitride polymorphic system. Dr. Cabral, in the relatively short time he has been with MSE, has been friendly and helped me immensely with acquiring and interpreting TEM data of crucial samples for my Thesis.

Funding for the research presented in this Thesis was made possible thanks to the National GEM Consortium Fellowship, the Neil and Jo Bushnell Fellowship in Engineering, and the John and Claire Bertucci Fellowship. I also acknowledge use of the Materials Characterization Facility at Carnegie Mellon University supported by grant MCF-677785.

Last but not least, I would like to thank my parents, step-parents, all of my siblings, and the rest of my extended family for their ongoing love, support, and encouragement throughout my PhD journey. I dedicate my Thesis to you. Throughout challenges, my entire family has remained a source of relief and refuge during phone calls and holiday breaks. I am also very thankful for all of the friends that I have made in graduate school, and especially the ones from the Department as well as the Black Graduate Student Organization. The support of my family and friends has made my PhD process less lonely and much more fulfilling.

ABSTRACT

Jean-Remy, Philip Malik. Chemical Vapor Deposition, Characterization, and Thermodynamic Phase Diagram Calculations of sp^2-Boron Nitride Thin Films. (Under the direction of Dr. Robert F. Davis).

The objectives of the research presented in this Thesis have been to (1) advance the field of homo- and heteroepitaxial growth of sp^2-hybridized boron nitride (sp^2-BN) thin films via chemical vapor deposition (CVD) and (2) evaluate the usefulness of utilizing calculated equilibrium phase diagrams for the prediction of sp^2-BN phases - namely hexagonal BN (h-BN) and rhombohedral BN (r-BN) – prepared by thermal CVD. The deposited sp^2-BN thin films related to objective (1) were characterized to determine the effects of implemented CVD growth parameters on film growth rates, the substrate-film interfacial microstructure, bulk film microstructure and crystallinity, chemical composition and bonding characteristics, and surface morphology and roughness. The calculated equilibrium phase diagrams related to objective (2) were compared with sp^2-BN CVD processes from experimental literature to determine favorable thermodynamic conditions for the deposition of sp^2-BN and to discover discrepancies related to the kinetics of CVD growth and sp^2-BN phase transformations.

The first project related to the achievement of objective (1) of this Thesis was the growth of nanocrystalline sp^2-BN thin films on (0001) 4H-SiC substrates at 1030 ^{o}C via continuous flow and discontinuous flow-modulated CVD techniques using diborane (B_2H_6) and ammonia (NH_3) as the B- and N sources, respectively. The latter technique enabled observations of both the effect of hydrogen purge steps between precursor injections and the length of injection times for B_2H_6 on the stoichiometry and microstructure of the films. Stoichiometric BN was achieved in all films grown continuously within the N/B gas phase ratio range of 20 – 200; this was not

observed for the discontinuously grown films unless both the B_2H_6 flow rate and the injection time were minimized. Cross-section transmission electron microscopy (TEM) of films grown both continuously and discontinuously at N/B = 200 and using short B_2H_6 injection times relative to that of NH_3 for the latter process route revealed the initial growth of ~4 nm thick partially ordered sp^2-BN layers. A transition zone then formed containing randomly oriented polycrystalline grains. Excess B incorporated into the discontinuously grown films during long B_2H_6 injection times resulted in single layer mixtures of amorphous and sp^2-BN without any observed ordering.

In the second project related to objective (1) of this Thesis, nanocrystalline sp^2-BN thin films were grown for 2 and 4.5 hours on mechanically polished polycrystalline pyrolytic boron nitride (PBN) substrates at 1060 ^oC via CVD using B_2H_6 and NH_3 as the B- and N sources, respectively. The use of an N/B gas phase ratio of 200 resulted in sp^2-BN thin films having a stoichiometric surface chemistry, as determined by x-ray photoelectron spectroscopy. Cross-sectional TEM revealed the initial growth of ~4 nm thick partially ordered [0001] sp^2-BN layers regardless of the crystallographic orientation of the sets of layers in the substrate. A transition zone then formed within the deposited films that contained randomly oriented polycrystalline grains and that culminated in the formation of protrusions. Atomic force microscopy verified an increase in roughening of the surfaces of the films with an increase in growth time and the associated thickness.

In the first project related to objective (2) of the Thesis, equilibrium thermodynamic calculations were performed to generate diagrams indicating the phase fields wherein either h- or r-BN can be deposited via chemical vapor deposition as a function of temperature, choice of B source and N/B ratio derived from NH_3 and the B-source. Similar diagrams calculated using

experimental conditions employed by groups who have synthesized r-BN films revealed that both in experiment and equilibrium, the choice of B-source strongly affects the size of the single-phase field for r-BN and, in general, deposition of r-BN can be realized at temperatures more than 100ºC below that predicted by equilibria.

The presence of C in $B(C_2H_5)_3$ makes possible its incorporation into hexagonal boron nitride (h-BN) thin films grown during CVD under select process conditions. In the second project related to objective (2) of the Thesis, a series of CVD phase diagrams that indicate the regions of stability of the phases of h-BN, C and B_4C as a function of temperature and mole ratio of reactants (N/B) under set pressures and H_2 diluent-to-reactant mole ratios (H_2/(B + N)) were calculated and analyzed for the TEB/NH_3/H_2 system. The equilibrium calculations showed that within the total pressure range of 0.01 -100 Torr, increasing the H_2 content in the TEB/NH_3/H_2 gas mixture tends to suppress the stability of C throughout a 400 – 1600˚C temperature range, but it also suppresses the stability of h-BN at higher temperatures. Further, it was determined that increasing the total system pressure suppresses the occurrence of C as a second phase while expanding the stability of h-BN. The thermodynamic equilibrium results were compared to the results of experimental investigations involving the CVD synthesis of sp^2-BN as a means to evaluate their usefulness as a guide for avoiding the co-deposition of C and B_4C with h-BN.

TABLE OF CONTENTS

LIST OF TABLES

LIST OF FIGURES

Section 5

Section 6

1. Thesis Introduction

The most highly studied group III nitrides for semiconductor-based optoelectronic and electronic applications are AlN, GaN, and InN. These nitrides exist in the wurtzite crystal structure at ambient conditions. This structure is three-dimensionally bonded and consists of a hexagonal crystal lattice with two lattice parameters, *a* and *c*. The bandgaps of AlN, GaN and InN are 6.2 eV, 3.4 eV, and 0.7 eV, respectively. Alloy systems of these nitrides allow for tunable bandgaps and the fabrication of optoelectronic devices that either emit or absorb radiation throughout the visible spectrum and into the deep ultraviolet (DUV) region. Device applications include laser diodes, light-emitting diodes, tandem solar cells and UV detectors [1,2]. These group III-nitride materials also have moderate-to-high values for electron mobility, saturated electron drift velocity, breakdown field, and thermal conductivity. As such, select compositions, especially between GaN and $Al_xGa_{1-x}N$, have been fabricated into devices for high-speed and moderate power electronic applications, including high-electron mobility transistors [3], Schottky diodes [4,5] and metal-oxide-field-effect-transistors [6,7]. One major obstacle to using these materials to create DUV emitting devices is the difficulty of p-type doping. For example, the energy of the acceptor level of the Mg p-type dopant has been shown to move substantially deeper into the bandgap as a function of Al content in the $Al_xGa_{1-x}N$ system, from 170 meV at $x = 0$, to 510 meV at $x = 1$ [1,2].

In contrast to the three-dimensional crystal structures of the alloys of AlN and GaN, the hexagonal phase of boron nitride (h-BN) possesses a two-dimensional hexagonal ring structure wherein each layer contains alternating B and N atoms. Thin films of h-BN are chemically inert, thermally stable and conductive, and possess a wide bandgap of about 6 eV, which makes them a strong candidate material for DUV and other optoelectronic applications under harsh

conditions [8]. The basic properties of h-BN are compared with those of AlN, GaN, and InN in Table 1.1.

One advantage of h-BN relative to the aforementioned high AlN-content alloys is that it can be doped both n-type and p-type. Some research in doping h-BN has been conducted, with greater room temperature success observed using p-type dopants, particularly Mg. Dahal et al. [9] observed p-type conductivity as a result of *in situ* Mg doping during synthesis of epitaxial h-BN via metalorganic chemical vapor deposition (MOCVD). Hall measurements at room temperature revealed a hole concentration of ~1.1 x 10^{18} cm^{-3}, a resistivity of 12 Ω-cm, and a mobility of 0.5 cm^2/V-s. Van der Pauw measurements, from which temperature dependent resistivity information was obtained, indicated an acceptor energy level of 31 meV, which is an order of magnitude lower than the Mg acceptor energy level in most $Al_xGa_{1-x}N$ alloys [4]. Another p-type dopant for h-BN is Be [10]. It was determined that rapid thermal annealing at 1000 °C for one minute of Be ion-implanted h-BN thin films resulted in a 10^6 reduction in resistivity, a hole concentration of 3 x 10^{19} cm^{-3}, a mobility of 27 cm^2/V-s, and an estimated acceptor energy level of 210 meV [10]. Zn, introduced by *in situ* radio-frequency bias-sputtering, has also been used to achieve p-type conductivity in h-BN, as reported by Nose et al. [11]. At Zn concentrations of about 20,000 ppm, it was observed that resultant films possessed a room temperature conductivity and an acceptor energy level of 10^{-2} Ω^{-1} cm^{-1} and 110 meV, respectively. However, hole concentration and mobility were not reported. In summary, a review of all the results reported to date for acceptor-type doping of h-BN indicates that Mg is the most promising dopant due its reported low acceptor energy level without the need for post-growth annealing.

In situ n-type doping of h-BN has not yet shown to be as successful or versatile dopant selection as p-type doping. Majety et al. [12] doped MOCVD grown h-BN thin films *in situ* with Si using SiH_4. The doped films exhibited n-type conduction only at temperatures above 800 K with in-plane resistivity, electron mobility, and carrier concentration of 12 Ω-cm, 48 $cm^2/V\text{-}s$, and 10^{16} cm^{-3}, respectively. After annealing the doped films at 1100 ˚C to induce Si substitution into B-sites, the room temperature Si donor level was measured to be ~ 1.2 eV. As a result, the doped films synthesized through that method were insulating at room temperature. He et al. [13] also attempted n-type doping with Si via *ex situ* ion implantation of radio-frequency magnetron sputtered h-BN films. Hall measurements of these implanted films after rapid thermal annealing at 1100 ºC for one minute revealed a resistivity of 0.5 Ω-cm, an electron carrier concentration of 2.0×10^{19} cm^{-3}, and a mobility of 0.6 $cm^2/V\text{-}s$ at room temperature. The donors in the Si ion-implanted doped films exhibited temperature-dependent shallow activation energy levels of 15 meV in the 50 – 300 K range and 60 meV from 300 – 800 K. Although DFT calculations supported the observation of two shallow donor activation levels for Si-doped h-BN, it was acknowledged that Si vacancy complexes created during ion-implantation and rapid thermal annealing may have contributed to the observed electrical properties of the films. The electrical properties of the Si-implanted films were not compared to as-sputtered films without any implantation.

Due to the aforementioned achievement of both p and n-type doping h-BN thin films, there is strong encouragement from the optoelectronics and other engineering communities to pursue research concerning the controlled growth and doping of epitaxial h-BN thin films to produce p-n junction diodes and deep (D) UV emitting devices. At this writing, a p-n junction in only h-BN has not been reported. However, a p-type h-BN/n-type $Al_xGa_{1-x}N$ ($x \sim 0.62$) diode

structure has been reported, which exhibited a current of 7.5 mA at a 20 V bias voltage and a low leakage current of 3 μA at a -10 V reverse bias [14].

To continue to realize h-BN as a viable device material, it is of great importance to achieve large-scale, epitaxial thin film growth of h-BN on appropriate substrates. Chemical vapor deposition (CVD) is the thin film growth method of choice used in this research. This thesis presents the important components of the research that I conducted, namely, the conventional and digital CVD growth of hetero- and homoepitaxial h-BN thin films as well as the optimal equilibrium growth conditions as established by thermodynamic CVD-related phase diagram calculations.

The remaining Sections of the Thesis are organized in the following manner. The Literature Review (Section 2) of sp^2-BN details the synthesis of bulk forms of h-BN, the several relevant aspects of the CVD synthesis of sp^2-BN, the thermodynamic properties of the BN polymorphic system and resulting CVD implications, and the important characterization tools and theories used for the evaluation of sp^2-BN thin films in the subsequently presented Thesis Research Projects. The Experimental Procedures (Section 3) detail the methodology used in CVD experiments and how the characterization tools were utilized. Sections 4, 5, 6, and 7 are Papers 1, 2, 3, and 4, respectively, which detail the four main Research Projects performed for this Thesis.

Paper 1 details the equilibrium thermodynamic calculations that were performed to generate phase diagrams indicating the phase fields wherein either h- or r-BN can be deposited via CVD as a function of temperature, choice of B source and N/B ratio derived from NH_3 and the B-source.

Paper 2 details a series of CVD phase diagrams calculated for the $B(C_2H_5)_3/NH_3/H_2$

system that indicate the regions of stability of the phases of h-BN, C and B_4C as a function of temperature and input mole ratio of reactants (N/B) under set pressures and H_2 diluent-to-reactant mole ratios (H_2/(B + N)).

Paper 3 details the nanocrystalline growth of sp^2-BN thin films on (0001) 4H-SiC substrates at 1030 °C via continuous flow and discontinuous flow-modulated CVD techniques using diborane (B_2H_6) and ammonia (NH_3) as the B- and N sources, respectively.

Paper 4 details the nanocrystalline growth of sp^2-BN thin films on mechanically polished polycrystalline pyrolytic boron nitride substrates at 1060 °C via CVD using B_2H_6 and NH_3 as the B- and N sources, respectively.

To date, Papers 1 and 2 were published in *MRS Communications* and the *Journal of Crystal Growth*, respectively, while Papers 3 and 4 were submitted to the *Journal of Vacuum Science & Technology A*. Paper 3 has been accepted for publication. Paper 4 is currently under Review. My list of papers is as follows:

> **Paper 1**. Jean-Remy, P. M., & Davis, R. F. (2021). On the discrepancies between the experimental realization and the thermodynamic predictions of stability of rhombohedral boron nitride. *MRS Communications*, 11(4), 451-456. DOI: 10.1557/s43579-021-00053-9
>
> **Paper 2**. Jean-Remy, P. M., Webler, B. A., Pistorius, P. C., & Davis, R. F. (2021). Thermodynamic calculations for the chemical vapor deposition of hexagonal boron nitride using triethylboron, ammonia, and hydrogen. *Journal of Crystal Growth*, *572*, 126283. DOI: 10.1016/j.jcrysgro.2021.126283
>
> **Paper 3.** Jean-Remy, P. M., Cabral, M. J., & Davis, R. F. (2022). Flow-modulated deposition of sp^2-boron nitride using diborane and ammonia on chemo-mechanically polished (0001) 4H-SiC substrates. *Journal of Vacuum Science & Technology A*, 40 (2), 023409. DOI: 10.1116/6.0001698
>
> **Paper 4**. Jean-Remy, P. M., Cabral, M. J., & Davis, R. F. Chemical vapor deposition of sp^2-boron nitride on mechanically polished pyrolytic boron nitride substrates. Under Review in the *Journal of Vacuum Science & Technology A*.

Section 8 is the Thesis Summary. Section 9 details the future work and challenges associated with the topics presented in the Research Projects. Section 10 contains an assortment of Appendices that complement much of the experimental and theoretical work performed for this Thesis.

Table 1.1. Basic properties of Group III – Nitrides at 300 K

		AlN	GaN	InN	h-BN
Lattice parameter [A]	a (Å)	3.112	3.189	3.533	2.504
	c (Å)	4.982	5.186	5.693	6.661
Thermal expansion coefficient ($^{\circ}C^{-1}$) [A]	α_a	4.2×10^{-6}	5.59×10^{-6}	3.8×10^{-6}	-2.7×10^{-6}
	α_c	5.3×10^{-6}	3.17×10^{-6}	2.9×10^{-6}	38×10^{-6}
Thermal conductivity (W cm^{-1} $^{\circ}C^{-1}$)		2[A]	1.3[A]	0.8[A]	3.9 ($\perp c$)[B]
					≤ 0.03 ($/\!/ c$)[A]
Band gap (eV)		6.2[C]	3.4[C]	0.7[C]	6.0[D]
Breakdown field (V cm^{-1})		$(1.2 - 1.8) \times 10^{6}$ [A]	5×10^{6} [A]	-	7.0×10^{6} [F]
Electron mobility ($cm^2V^{-1}s^{-1}$) [C]		426	900	3980	-
Saturation electron drift velocity (cm/s)[E]		1.4×10^{7}	2.5×10^{7}	2.5×10^{7}	-

Reference A [15]; Reference B [16]; Reference C [17]; Reference D [8]; Reference E [1]; Reference F [18]

2. Boron Nitride Literature Review

2.1. h-BN powder and bulk single crystal synthesis

Boron nitride does not occur in nature. Its hexagonal modification was first synthesized by Balman in 1842 [19] through the reaction between B_2O_3 and KCN. Today, h-BN is commercially synthesized as powders and micron- to millimeter-sized single crystals. At the industrial scale, 0.1 – 0.5 μm thick and 1 – 10 μm wide crystalline h-BN platelet-shaped particles can be synthesized through, but not limited to, the following reactions [20]:

$$B_2O_3 + 2\,NH_3 \xrightarrow{900\ ^oC} 2\,BN + 3\,H_2O \tag{2.1.1}$$

$$3\,CaB_6 + B_2O_3 + 10\,N_2 \xrightarrow{>1500\ ^oC} 20\,BN + 3\,CaO \tag{2.1.2}$$

The BN product of reaction (2.1.1) must be heated above 1500 ˚C in a N_2 atmosphere for further purification and increased crystallization. Production of h-BN single crystals usually involves the processing of a mixture of BN source material in the form of commercially available h- or amorphous BN powders, rods, or compact discs and a molten solvent under either high temperature or both high pressure and high temperature (HP-HT). There are a variety of different solvents that have been used to aid the precipitation of h-BN crystals. The first report of free standing single crystals of h-BN was made by Ishii and Sato [21], who prepared single crystals of h-BN using a mixture of Si and B powders at 1850 ˚C in a N_2 atmosphere. The Si served as a molten solvent for the reaction to occur. The results of this process were crystals with a lateral size of 2 mm in the dimension of the basal plane, and a thickness of 20 μm, although absorption spectra indicated the product contained N vacancies and C impurities. Later, alkaline earth metal-based solvents such as $Ba_3B_2N_4$ [22], Mg_3BN_3 [23], and $LiCaBN_2$ [23] were used to synthesize h-BN single crystals with low impurity content at high temperatures (1200 – 2000 ˚C) and high pressures (3 – 6 GPa). For example, the $Ba_3B_2N_4$ solvent facilitated the production of

colorless h-BN single crystals that were approximately 400 μm x 200 μm in size, contained less than 10^{18} atoms/cm^3 in O and C impurities, and exhibited DUV band-edge luminescence at 215 nm. However, at such high temperature, alkaline earth metal-based solvents will decompose under atmospheric pressure. In the 1200 – 2000 ˚C temperature range, transition metal solvents have superior chemical stability at atmospheric pressure than alkaline earth metal solvents. Metal alloy solvents such as Ni-Mo [24] and Ni-Cr [25,26] have assisted in the recrystallization of h-BN with comparable structural quality and lower impurity content than that produced using alkaline earth metal-based solvents and are, therefore, attractive solvents for h-BN synthesis at atmospheric pressure. For example, the use of a Ni-Mo solvent resulted in h-BN crystals as large as 300 μm x 200 μm and 10 μm thickness, as well as characteristic band-edge luminescence at 215 nm indicating high purity.

Although the in-plane covalent bonds of h-BN are strong, its out-of-plane bonds are weak Van der Waals bonds, similar to other two-dimensional layered materials. Thus, it has been shown that monolayers of h-BN can be micromechanically cleaved from bulk single crystals via scotch tape exfoliation [27]. It was demonstrated that single monolayers or stacked layers of exfoliated h-BN can be used as the dielectric substrate for graphene field effect transistors (GFETS), which exhibit reduced concentrations of impurities and charge traps compared to graphene/SiO_2 based devices [18,28]. However, micromechanical cleavage of h-BN monolayers from few millimeter-sized bulk single crystals is not conducive for the attainment of wafer-scale processing. Processing of wafer-scale, thickness-controlled h-BN would not only increase the scalability of h-BN/graphene devices but also of h-BN as a main device component for DUV emitting and sensing applications [2,9]. Achieving wafer-scale, semiconducting and crystalline h-BN requires epitaxial growth on suitable substrates through methods that allow for high

reproducibility, precise control of thickness and stoichiometry, and continuous layers over large areas.

2.2. Chemical vapor deposition of sp^2-BN

2.2.1. Epitaxy

Epitaxy is a method of growing thin films with a specific crystallographic orientation governed by the atomic arrangement of the surface of the underlying single-crystal substrate [29]. An epitaxial relationship between a single-crystal substrate and a thin film mandates that the thin film should also be single-crystal, or polycrystalline where the grains possess the same crystallographic orientation as the substrate surface. As a result, epitaxially grown thin films have fewer defects such as grain boundaries, which improve its resistivity and charge mobility properties, and are thus better suited for electronic device applications.

There are two types of epitaxy: homoepitaxy, where the substrate material is the same as the film being grown, and heteroepitaxy, where the substrate and film material are different. As such, in homoepitaxy, the film and substrate are perfectly lattice matched; there is no bond strain at the interface between the substrate and film. In heteroepitaxy, however, strain at the interface can occur which is dependent on the magnitude of the lattice mismatch, coefficient of thermal expansion, and chemistry between the substrate and the film [30]. The extent of the interfacial bond strain in heteroepitaxy results in three epitaxial regimes to consider. The first regime is where the lattice mismatch is small enough that strain at the interface is negligible and the interfacial structure looks similar to that observed in homoepitaxy. When the lattice mismatch between the substrate and film is more significant, however, the resultant film can be either strained or relaxed. In the former case, both the lattices of the film and the top-most layers of the substrate will strain to satisfy each other's crystallographic differences. In the latter case of

relaxed epitaxy, edge type dislocations form at the interface between the substrate and the film, typically during later stages of the film growth, and this mechanism will generally occur regardless of crystallographic differences between the film and substrate [31,32].

2.2.2. Chemical vapor deposition

Chemical vapor deposition (CVD) is a popular method of producing large area (μm^2 – cm^2) epitaxial thin films of Group III nitrides. Thin films are produced by this technique when chemical reactions occur between precursors on a heated substrate surface. Heat provides the necessary thermal energy for precursors to react and for their resultant adatoms to migrate across the substrate surface and nucleate at preferential positions. Precursors are highly reactive chemicals containing the desired atoms that constitute the desired composition of the film. The resulting morphology and crystalline quality of thin films grown via CVD depend on several factors, including: substrate material and surface preparation, growth temperature, total chamber pressure, and precursor and diluent concentrations in the gas phase [33].

The concentration of precursors used in a CVD gas mixture should allow for a sufficient supersaturation that enables thin film growth. Immediately above the substrate surface, there is depletion in the precursor concentration due to its decomposition at an elevated temperature and the adsorption, diffusion and nucleation of the species that lead to film formation. Thus a concentration gradient develops further away from the heat source. The region containing this gradient from the full concentration of precursors in the free stream to the depleted region just above the substrate is known as the boundary layer [34].

In general, there are three main temperature regimes that affect the kinetics of thin film growth. In the low temperature regime, there is not enough thermal energy to decompose precursor species adsorbed on the substrate surface, and the mobility of adatoms is also too low

to allow for sufficient nucleation, cluster formation and film growth. Hence, the low temperature regime is also known as the surface kinetics-limited regime, and the growth rate will increase with increasing temperature. At moderate temperatures, the growth rate is limited by the diffusion rate through the boundary layer, and this regime is referred to as the transport-limited growth regime. In transport-limited growth, growth rates are typically high (relative to that observed in the other temperature regimes) and have a weak, but positive temperature dependence, because the diffusion rate through the boundary layer will increase with temperature. In the transport-limited regime, the growth rate is more strongly controlled by the supply of the precursor reactants to the substrate. At higher temperatures, the equilibrium vapor pressure of the elements of the growing thin film will increase such that the rate of desorption competes with the rate of nucleation. Thus, the growth rate will decrease with increasing temperature in this high temperature, thermodynamically-limited regime [34,35].

The kinetics of CVD growth are in general governed by gas transport processes that occur (1) prior to reactant gas mixing in the deposition chamber, (2) in the gas phase, and (3) at the interface between the vapor and substrate. These processes include: transport of the precursors to the chamber; precursor gas phase reactions; transport of the adduct products of the gas phase reactions to the substrate; adsorption of adatoms on the substrate surface; surface diffusion and substrate reactions; nucleation and incorporation of adatoms into the lattice of the growing film; and desorption of reaction products [31,33].

2.2.3. Precursors

There are several properties that a precursor should have for use in a general CVD process. These include [34,35]:

- Sufficient volatility that allows for satisfactory growth rates, but the temperature required for decomposition should be higher than the storage temperature
- Stability at room temperature for long time periods
- Chemical purity
- By-products should not be incorporated into the growing film
- Ability to be used with other precursors to form compound thin films

For the deposition of h-BN, the Group III source and the nitrogen source may originate from a single precursor, such as borazine ($B_3N_3H_6$). The Group III and nitrogen sources can also come from two separate precursors. The nitrogen source in Group III-nitride thin film growth via CVD is often ammonia (NH_3). A wide variety of classes of boron-source precursors can be used for h-BN growth; these include boron hydrides, boron halides, and organoboranes. Boron hydrides are appealing because they only contain boron and hydrogen in their chemical make-up. This greatly minimizes the chance for contaminants such as carbon to be incorporated into the film during growth. The main drawback of boron hydrides such as diborane (B_2H_6) is that they are both extremely toxic and explosive. Boron halides such as boron chloride (BCl_3) are sometimes used, but the primary drawback of BCl_3 in particular is that the HCl by-product that forms from the reaction between BCl_3 and H_2 can react with NH_3 to form solid ammonium chloride (NH_4Cl), which can damage the vacuum pump(s) on the system. The safest class of precursors regarding human health and vacuum pump longevity are organoboranes, such as triethylboron (TEB, $B(C_2H_5)_3$). The disadvantage of using $B(C_2H_5)_3$ is that it inherently contains carbon in its chemical structure. Thus, precautions must be taken during the establishment of experimental growth parameters to ensure that carbon does not become incorporated into the growing BN film [36]. TEB, $B_3N_3H_6$, and B_2H_6 have all been used as precursors for h-BN CVD

synthesis at some point during the tenure of my research. Table 2.2.3.1 summarizes examples of important published studies where these three precursors were separately used in conjunction with NH_3 to produce h-BN and other BN phases.

Table 2.2.3.1: Summary of diborane, triethyl boron, and borazine usage in CVD of h-BN

Gases used	**Temperature (°C)**	**Reactor Pressure (Torr)**	**Substrate**	**Film quality**	**Ref.**
B_2H_6, NH_3, H_2	800	2	Polished (100) Si	Amorphous and turbostratic BN	[37]
B_2H_6, NH_3, H_2	650 - 1025	0.01	Ni foil, Cu foil, c-plane sapphire	1- 100 layers thick turbostratic and h-BN films	[38]
B_2H_6, NH_3, H_2	600 - 1080	Not listed	Si, Ta, Mo, Ge, fused silica	100-600 nm thick, turbostratic BN	[39]
B_2H_6, NH_3, H_2	1050	0.07	Co,Ni/SiO2/Si	< 25 nm thick h-BN thin films	[40]
TEB, NH_3, H_2 Ar	750 - 1200	Not listed	*c*-plane sapphire and Si	4 – 15 nm thick amorphous and turbostratic BN	[41]
TEB, NH_3, H_2, Ar	850 - 1100	1 - 740	(100) Si	turbostratic and powder BN	[42]
TEB, NH_3, H_2	1050	20 - 500	*c*-plane sapphire	few-layer h-BN films	[43]
TEB, NH_3, H_2	1020	300	(111) Ni	1 μm thick h-BN films	[44]
TEB, NH_3, H_2	1020	300	(0001) 6H-SiC	1 μm thick turbostratic films	[45]
$B_3N_3H_6$	800	7.5×10^{-11} Torr	(111) Ni	Monolayer h-BN	[46]
$B_3N_3H_6$, H_2	1100	0.01 Torr	Pt foil	Monolayer h-BN	[47]
$B_3N_3H_6$, H_2	940	7.5×10^{-4} Torr	Fe/SiO2, Fe/*c*-plane sapphire	Monolayer h-BN, lateral size > 25 um	[48]
$B_3N_3H_6$, H_2	400, then 1000 °C anneal	760 Torr	Ni foil	5 - 50 nm thick, lateral size up to 20 um	[49]

2.2.4. Metalorganic Chemical Vapor Deposition

Metalorganic chemical vapor deposition (MOCVD) is a CVD technique developed specifically for the growth of III-V semiconductor thin films [50]. MOCVD employs the use of a metalorganic precursor, such as TEB, as the source for the Group III element, and a hydride

such as NH_3 for the Group V element. When the MOCVD technique is employed for the purpose of producing epitaxial thin films, specifically, the process is referred to as metalorganic vapor phase epitaxy (MOVPE).

An important property for metalorganic precursors to have is low vapor pressure at room temperature, such that there is no uncontrolled flow of the precursor into the CVD reactor at operating pressures. In recent years, TEB and NH_3 have become popular MOCVD precursors for the growth of h-BN thin films [41–43,51,52]. TEB, like most other metalorganic precursors, exists as a liquid at room temperature. The Clausius-Clapeyron equation can be integrated and manipulated to express the saturated vapor pressure, P_v, of a liquid as

$$P_v = \exp\left(\frac{-\Delta G}{RT}\right) \qquad \text{Eq. (2.2.4.1)}$$

where ΔG represents the Gibbs free energy change upon vaporizing the liquid precursor, R is the ideal gas constant, and T is the temperature of the liquid inside the bubbler, which is a leak-tight vessel in which the precursor is stored. If ΔG is rewritten as the Gibbs free energy equation $\Delta G = \Delta H - T\Delta S$, where ΔH and ΔS are the heat and entropy of vaporization, respectively, the combination of exponential terms yields the standard vapor pressure equation in the form of

$$Log_{10}(P_v) = A - \frac{B}{T} \qquad \text{Eq. (2.2.4.2)}$$

A and B are constants, and equate to $\Delta S/R$ and $\Delta H/R$, respectively. For P_v in units of mmHg and T in K, the A and B constants of vapor pressure of the TEB precursor used in my research (Epichem, Inc.) are 7.812 and 1814, respectively. Because the vapor pressure of TEB and similar metalorganic precursors are lower than that of CVD reactor operating pressures, the bubbler in which it is stored must be used to deliver controlled amounts of it to the reactor. An inlet tube delivers a carrier gas such as H_2, N_2, or Ar below the surface of the liquid inside the bubbler, and an outlet tube that sits in the free volume above the liquid transports away the carrier gas and

vapor mixture. The metalorganic precursor flow rate is precisely controlled by (1) changing the vapor pressure which is controlled using a temperature-regulated bath; (2) the flow rate of the carrier gas which is regulated by a mass flow controller; and (3) the pressure in the free volume in the bubbler above the liquid which is regulated by a pressure controller. NH_3 is a gas at ambient conditions and is thus delivered to the reactor chamber in precise amounts by use of a mass flow controller.

There are certain issues associated with the conventional use of MOCVD to grow h-BN thin films. The conventional use of MOCVD refers to the method of flowing TEB and NH_3 (for example) into the chamber simultaneously. The major drawback of using conventional MOCVD is that premature reactions between the precursors can occur in the gas phase before they arrive on the substrate surface [39]. Such reactions are called parasitic reactions because the premature products or adducts that form in the gas phase tend to consume the precursors before they can reach the surface of the substrate material for crystal growth. This in turn will cause a decrease in the growth rate since the precursors become depleted. The effect is exacerbated at higher chamber pressures; increases in pressure reduces the mean free path of gas particles which results in more collisions and therefore more reactions in the gas phase [41]. Further, the premature adducts that can form are often less reactive than the precursors from which they originate, meaning that once these adducts reach the substrate surface, they may not sufficiently decompose to form the intended crystalline material and, therefore, become incorporated into the film. Thus, the deposited thin film will likely contain unwanted impurities and defects as a result of adduct incorporation [45].

2.2.5. Flow-modulated epitaxy

To reduce the parasitic reactions in the gas phase, a CVD growth technique named flow-modulated epitaxy (FME) (also known as digital epitaxy) has been adopted for the growth of h-BN thin films and other group III-nitrides and their alloys [2,9,44,45]. During FME, the B-source precursor and NH_3 are introduced into the growth chamber in alternating seconds-long pulses usually separated by flushing the chamber with a nonreactive gas. In other words, the precursors are not meant to exist in the chamber at the same time. This technique allows the first precursor to decompose on the substrate to form adsorbed atomic or simple molecular species that are chemically bonded to the surface. The flow of the initial precursor gas is then diverted from the chamber and directly to the pump exhaust, while a nonreactive purge gas is flowed into the chamber to completely flush out this initial precursor gas. The second precursor gas is then flowed into the chamber, after which a final purge step occurs before the advent of the second cycle with the redirection of the first precursor flow back into the chamber. FME also adds another degree of growth optimization by allowing control over the length of each pulse.

FME also helps to address a second problem encountered in conventional MOCVD for h-BN thin film growth: temperatures of at least 1300°C have been both theoretically and experimentally found as a requirement to form highly crystalline, epitaxial h-BN on non-catalytic substrates such as *c*-plane sapphire and (0001) 4H-SiC [41,53,54]. Such high temperatures are needed so that any adducts that form have sufficient kinetic energy to migrate on the substrate surface before decomposing to form h-BN, thereby decreasing the nucleation density and improving the bulk microstructure. However, because FME better restricts precursor reactions closer to the substrate surface, there is improved migration of B atoms there, and the growth temperature can be substantially lowered to 1050 °C [44].

2.2.6. Non-carbon containing precursors

Boron hydride precursors for the CVD synthesis of h-BN such as B_2H_6 have typically been avoided due to their toxicity and flammability. There are only a few studies [37–40,55,56] that cover the CVD growth of h-BN using B_2H_6 and NH_3 while the use of TEB as the B source has increased in recent years. Unlike TEB, however, B_2H_6 does not contain any inherent carbon in its chemical structure, which is useful for the obvious need to prevent the incorporation of carbon into the growing BN film. When using TEB and NH_3 at sufficiently low total reactor chamber pressures, carbon does become incorporated into a growing BN film, even at deposition temperatures as high as 1000 °C [42].

Similar to TEB, however, B_2H_6 is also believed to react parasitically in the gas phase with NH_3 when the two reactants are simultaneously flowed into a CVD reactor chamber [39,45]. Within the temperature range relevant and accessible in this work (600 – 1050 °C) the Gibbs free energy change for the overall reaction between B_2H_6 and NH_3 in producing solid BN is negative [39]:

$$B_2H_6(g) + 2NH_3(g) \rightleftharpoons 2BN\ (s) + 6H_2\ (g) \qquad (2.2.6.1)$$

However, with sufficient NH_3 present, intermediate reactions occur even at room temperature, and involve the formation of solid borohydride ($(NH_3)_2BH_2^+$) [39]:

$$B_2H_6(g) + 2NH_3(g) \rightarrow (NH_3)_2BH_2^+(s) + BH_4^+\ (g) \qquad (2.2.6.2)$$

At temperatures greater than 200 °C, borohydride forms polymeric derivatives of borazine ($B_3N_3H_6$) in the form of $(BNH_2)_n$, where n is an integer specifying the number of monomer units. Subsequent heating (200 – 1200 °C) of this polymeric product is necessary to pyrolyze the residual hydrogen bonds to ultimately form solid BN [37,39,57]. Increasing the temperature beyond 1200 °C to 1450 °C greatly improves the crystallinity of the h-BN product that forms from the pyrolysis

reaction [57]. To suppress the formation of the polymeric, hydrogen-rich product in the gas phase during CVD, the FME process described above should be utilized for the B_2H_6/NH_3 system as well.

2.2.7. Substrates

2.2.7.1. Transition metals

Much of the recent successful growth of h-BN synthesized through CVD has occurred on transition metal (TM) substrates [58–62] such as copper (Cu) [58,59,61,62], nickel (Ni) [46,49,63–66], platinum (Pt) [46,65,67], and palladium (Pd) [46]. These TMs exhibit varying degrees of catalytic activity during h-BN growth on their surfaces due to the mixing of TM *d* orbitals with the h-BN π orbitals at the interface [68,69]. However, this catalytic effect becomes effectively shielded by the formation of just a monolayer of h-BN. Research has revealed that a significantly higher partial pressure of the precursor(s) is needed to continue the growth of h-BN film beyond the first monolayer [70]. As a result, h-BN growth on TM substrates, typically from the utilization of borazine ($B_3N_3H_6$) as the BN precursor, is limited to films that are a monolayer or just a few atomic layers thick.

The degree of difference in the lattice parameters and the crystal structures between h-BN and the substrate of choice can either facilitate commensurate epitaxial growth, corrugated growth, or the growth of an amorphous film if the in-plane stresses are too high to favorably form sequential layers of h-BN. Many of the TMs mentioned above have a sufficiently close *a* lattice parameter to that of the *a* parameter of h-BN to facilitate the growth of the latter material. For example, the lattice spacings of Ni (111) (2.49 Å), Cu (111) (2.56 Å), and Co (0001) (2.51 Å), are mismatched by only -0.4%, 2.4%, and 0.8%, respectively, with the in-plane lattice parameter of h-BN (2.504 Å) [71]. A smaller lattice mismatch decreases the amount of in-plane stress in the developing film [30]. A larger lattice mismatch, such as the 6.7% that occurs when depositing h-BN on Rh

(111) (2.69 Å), results in a tensile stress that is too great for epitaxial h-BN to form commensurately. Instead, the film develops periodic corrugations with respect to the Rh (111) substrate, forming a mesh-like microstructure. In such a microstructure, the h-BN monolayers maintain their intrinsic in-plane lattice parameter of ~ 2.50 Å [72]. Further, each of the TM surfaces described above in their specified single crystal orientations contain six-fold hexagonal symmetry, which increases the favorability for the desired six-fold in-plane structure of h-BN to form on these surfaces. With further deviations from the lattice parameter and hexagonal crystal structure of h-BN, such as with the Si (100) surface, which has four-fold symmetry and a lattice parameter of 5.43 Å, amorphous BN initially forms in order relieve the resulting in-plane compressive stresses [73].

2.2.7.2. 4H-SiC and Sapphire

h-BN films grown on TM foil substrates must be transferred – typically through a wet chemical etching process [74] - to another substrate such as SiO_2/Si if they are to be either fabricated into a device structure or characterized by a technique such as cross-sectional transmission electron microscopy (XTEM), which requires a rigid sandwich structure for sample preparation. For this reason, coupled with the observation described earlier that the thickness of h-BN films on TM substrates is usually limited between a monolayer and a few nanometers, growth on substrates such as the hexagonal polytypes of silicon carbide (4H-SiC and 6H-SiC) or sapphire (α-Al_2O_3) has been investigated.

Similar to the (111) faces of TM substrate surfaces, the (0001) faces of 4H-SiC, 6H-SiC, and *c*-plane sapphire also have a six-fold, hexagonal arrangement, which is thought to facilitate the formation of hexagonal BN during CVD growth. However, because SiC[$11\bar{2}0$] and α-Al_2O_3[$11\bar{2}0$] have lattice-mismatches of 47.4% and 18.5%, respectively, with h-BN[$11\bar{2}0$] and provide no

catalytic effect to assist the decomposition of B and N precursors on their (0001) surfaces, high substrate temperatures in the range of 1300 – 1500 °C on SiC [75,76] and *c*-plane sapphire [9,54,77,78] have been reported to promote epitaxial h-BN growth on these surfaces.

2.2.7.3. Pyrolytic BN

Thus far, all discussions of CVD h-BN growth have concerned heteroepitaxial growth. To the candidate's best knowledge, no attempt has been made to grow h-BN homoepitaxially on highly-oriented pyrolytic boron nitride (HOPBN). The latter material is typically grown using CVD through the pyrolysis reaction between BCl_3 and NH_3 at temperatures ranging from 1800 to 1900 °C and chamber pressures below 1 Torr [79]. Structurally, HOPBN is a textured polycrystalline material composed of close-packed columnar h-BN grains oriented along the *c*-axis or [0001] direction. The basal planes of these grains are also commonly observed to be slightly rotated with respect to each other about the [0001] direction, as a result of the misorientations of the columns [80].

2.3. BN polymorphs and phase stability

2.3.1. BN polymorphic system

The atomic orbitals of BN can stabilize into either the sp^2 or sp^3 hybridizations, allowing the compound to form in various crystalline polytypes which are structurally analogous to the carbon polytypes [71]. Atomic structures of three of these polytypes are shown in Figure 2.3.1.

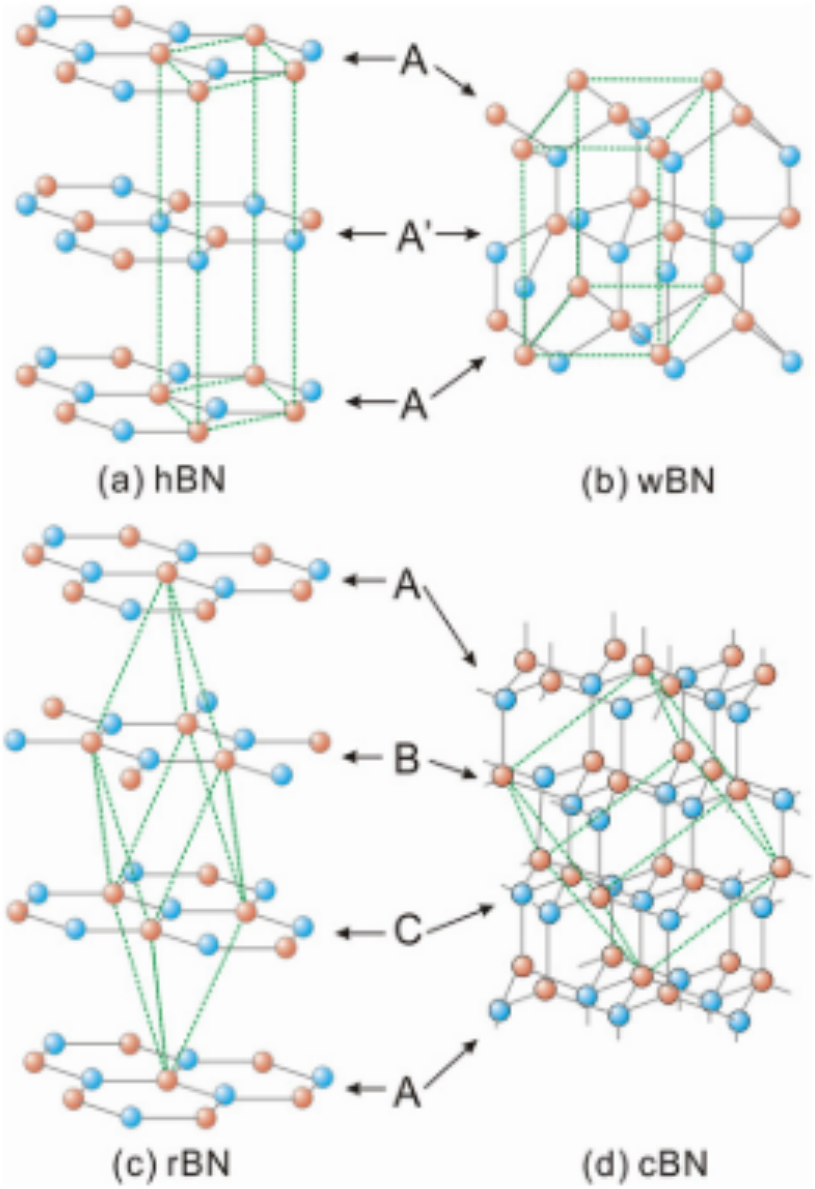

Figure 2.3.1. Crystal structures of (a) h-BN, (b) w-BN, (c) r-BN and (d) c-BN. Ref. [81].

Cubic BN (c-BN) and wurtzite BN (w-BN) possess sp^3 hybridized bonding and are structurally analogous to cubic diamond and hexagonal diamond, respectively. As such, c-BN and w-BN possess the zinc-blende and wurtzite crystal structures, respectively. [82]. The strong sp^3 bonding

in c-BN makes this particular phase extremely hard, second in hardness only to cubic diamond [83]. The sp^3 bonding also occurs in amorphous BN, which forms due to structural disorder during growth.

The sp^2 hybridizations of BN orbitals allow the compound to form in the two-dimensional (2D) geometries of rhombohedral (r) and hexagonal (h) BN. Molecular orbital theory reveals that in sp^2 hybridized BN, both B and N atoms, which alternate in a hexagonal ring, contain three sp^2 hybridized bonds each. This hybridization comes from the combination of a single 2s orbital and the $2p_x$ and $2p_y$ orbitals. Thus, σ bonds form for each B and N atom in the system, giving h-BN and r-BN two dimensional, planar geometries. The individual sp^2- σ bonds are polar because of the electronegativity difference between B and N, but the hexagonal symmetry of the structure causes the net dipole moment in the plane of the sp^2 BN to be zero. Further, there remains on both B and N a non-hybridized p orbital (p_z) normal to the three sp^2 orbitals; the p_z orbital of N is completely filled with two electrons while the p_z orbital of B is empty, and it is speculated that π bonding can occur through the limited transfer of electrons between the two p_z orbitals [84].

As noted above, h-BN forms in a 2D hexagonal crystal structure; it possesses $D_{6h}P6_3/mmc$ symmetry. This hexagonal crystal system has one six-fold axis of rotation, which is the [0001] direction as denoted by the point group D_{6h}. The screw axis 6_3 symbolizes that for every 60^o rotation, a lattice point is displaced by one-half of a translation vector of the unit cell in the direction of the screw axis [0001]. The /mmc notation signifies two mirror operations of the lattice point as well as an axial glide along the c direction [0001], using the basal plane of the unit cell as the mirror plane [85]. The lattice parameters for h-BN are as follows: $a = b = 2.504$ Å, $c = 6.661$ Å, $\alpha = \beta = 90^o$, and $\gamma = 120^o$. Graphite has the same symmetry configuration as h-BN, and its lattice constants are quite similar: $a = b = 2.456$ Å, $c = 6.696$ Å, $\alpha = \beta = 90^o$, and $\gamma = 120^o$. Similar to the bonding in graphite, the covalent intralayer bonding in h-BN is quite strong, while the interlayer bonding along

[0001] is much weaker, as the layers are held together by Van der Waals forces [82]. A sequential layer of h-BN is stacked directly on top of the preceding layer, meaning that the B atom in one layer is directly adjacent to the N atoms above and below it. This type of crystallographic stacking is classified as AA'A stacking [71], and differs from the ABC stacking found in graphite where sequential layers of C atoms are offset from the preceding layer [82].

The AA'A stacking sequence of h-BN also distinguishes this BN polytype from r-BN, which possesses the ABC sequence. In the ABC sequence, the BN layers are staggered and are, therefore, no longer directly stacked above or below each other [86]. The in-plane and out-of-plane lattice parameters are very similar between h-BN and r-BN, making it difficult to distinguish between the two phases using conventional 2θ-θ x-ray diffraction (XRD). However, the two phases can be distinguished by examining asymmetric planes such as the $(10\bar{1}2)$ and $(01\bar{1}2)$ of h-BN and r-BN, respectively, which have discernable interplanar spacings [87].

BN can also form a third, much less ordered sp^2 phase called turbostratic (t) BN. The t-BN phase is semi-crystalline, in that there remains a high degree of in-plane order of BN hexagonal rings, but these layers are not parallel and are randomly rotated and translated with respect to the [0001] axis of the layer. This absence of three-dimensional order along [0001] causes the interplanar spacing for the (0002) planes to vary and possess larger values than that for h-BN and r-BN. As a result the *c* lattice parameter in t-BN can range from 6.7 Å to above 7.1 Å [88,89]. The lack of out-of-plane order and an increase in (0002) interplanar spacing renders t-BN unstable in ambient conditions. Alkoy et al. [89] observed, by x-ray diffraction analysis, a year-long degradation of t-BN powders – synthesized by the nitridation of boric oxide via ammonia for 2 hours at 900 ^{o}C – into an ammonium borate compound ($NH_4 \cdot B_5O_8 \cdot 4H_2O$). It is thus of great importance to know if there are conditions in the CVD process of h-BN synthesis wherein the formation of t-BN can be avoided.

Kobayashi and Akasaka [52] showed that despite a relatively low growth temperature (1080 °C) and a large lattice mismatch between h-BN and *c*-plane α-Al_2O_3 (> 47%), t-BN formation can be suppressed in BN films synthesized from the continuous flow of TEB and NH_3 at 300 Torr when employing a sufficiently high V/III gas phase ratio. The *c* lattice parameter of their BN films decreased from 6.96 Å at a V/III ratio of 210 to the literature value for h-BN of 6.66 Å at V/III ratios of both 1260 and 2100. Growth or epitaxial h-BN films was obtained using these high V/III ratios, as evidenced in micrographs acquired using cross sectional transmission electron microscopy (XTEM). It was postulated that the high V/III ratios were necessary for layer-by-layer growth and the suppression of N vacancies, which in turn help to prevent the formation of t-BN during growth. However, parasitic gas phase reactions between TEB and NH_3 at the high V/III ratios caused slow growth rates. The films deposited using the V/III ratios of 1260 and 2100 had to be grown for 10 hours to yield thick enough films for x-ray diffraction. Also utilizing CVD and TEB and NH_3 as the B and N precursors, respectively, Chubarov [53] showed that at a chamber pressure of 75 Torr and a more moderate V/III ratio of 600 can be used to both produce epitaxial sp2 BN and avoid the formation of t-BN, provided that the growth temperature is high enough (1500 °C) and that the *c*-plane α-Al_2O_3 substrate is nitridated before BN growth. Nitridation of the *c*-plane α-Al_2O_3 surface via NH_3 flow forms a (0001) oriented AlN buffer layer. The in-plane *a* lattice parameter of AlN is 3.112 Å. The lattice mismatch with h-BN is 19.5%, which is smaller than the 47.4 % mismatch between h-BN and *c*-plane α-Al_2O_3. Without the AlN buffer layer, however, a BN film with a measured *c* parameter 6.77 Å was observed, indicative of t-BN formation. Yamada et al. [90] studied the effect of temperature specifically on the resulting structure of CVD BN films grown on *c*-plane α-Al_2O_3 at a chamber pressure of 75 Torr using a flow-modulated growth method with B_2H_6 and NH_3 as precursors. Thus, precursors were alternately supplied to the chamber, so only a nominal V/III ratio

can be described, which was calculated to be 750. At a growth temperature of 1140 °C, no diffraction pattern was obtained, and the resultant film was considered amorphous. Increasing the growth temperature to 1220 °C resulted in the deposition of a film that exhibited an X-ray diffraction peak at 26.2°, indicating a *c* lattice parameter of 6.80 Å and thus t-BN formation. An additional increase in the growth temperature to 1360 °C suppressed t-BN formation and allowed epitaxial h-BN to form on the substrate, as indicated by x-ray diffraction and cross-sectional TEM results.

Though these studies vary in operational parameters, they do provide at least some qualitative insight regarding the avoidance of t-BN formation as a second phase during the epitaxial deposition of h-BN via CVD on large lattice mismatched and non-catalytic substrates such as *c*-plane α-Al_2O_3. A synthesis of these results indicate that (1) when high reactor temperatures $\geq \sim 1300$ °C are experimentally unattainable, very low growth rates and high V/III ratios are necessary to facilitate lateral growth of the two-dimensional layers of h-BN and prevent N vacancy formation; (2) even at high reactor temperatures, the optimal V/III ratio necessary to avoid either amorphous BN or t-BN may depend on the surface chemistry and degree of lattice mismatch between BN and the substrate; and (3) although the flow-modulated growth method decreases the extent of parasitic reactions by restricting deposition chemistry to the substrate surface, too low of a nominal V/III ratio will cause the deposition of t-BN at growth temperatures below 1300 °C.

2.3.2. BN phase stability

Although chemical vapor deposition (CVD) has been a popular deposition method to grow h-BN thin films, aspects of the growth mechanism(s) are not fully understood. The formation and properties of the films are dependent upon several factors including choice of precursor and diluent gases, chamber temperature and pressure, chamber reactor design, and substrate choice and preparation. Since growth was a very important component of my thesis research, considerable time was spent in the determination

of the optimal growth parameters for growing crystalline films of h-BN. The use of many different BN precursors (metalorganics, hydrides, and halides) has been reported throughout the literature for the CVD synthesis of h-BN; however, there is no consensus on which precursor and process route are optimal for the growth of this material. It is thus also a goal of this project to model CVD phase diagrams that indicate the formation of stable phases of BN as a function of temperature and input precursor concentrations at a set chamber pressure and diluent gas concentration.

Prior to the calculation and interpretation of CVD phase diagrams of BN, a discussion of BN phase stability is necessary. As BN has four main polytypes – cubic, hexagonal, wurtzite, and rhombohedral – a discussion regarding the most thermodynamically stable at ambient conditions is imperative and has been greatly contested. Mostly, the debate has been between c-BN and h-BN. h-BN is the phase that is almost universally deposited during the synthesis of undoped BN in the absence of external influences such as plasma decomposition of a precursor gas or ion bombardment of the growing film. Thus, the pressure-temperature (P, T) phase diagram for BN proposed in 1963 by Bundy and Wentorf [23], which indicated that h-BN is more stable than c-BN was readily accepted. However, by analogy with graphitic carbon and diamond, it was thought that this stability should reverse at high pressures. The BN phase diagram proposed by Bundy and Wentorf was obtained by observing the direct transformation of h-BN to its denser cubic and wurtzitic forms at high static pressures and high temperatures. Further, in 1975, Corrigan and Bundy [91] performed shock compression tests as well as static high-pressure and high-temperature experiments that also resulted in direct BN phase transitions. It was thus concluded that w-BN is a metastable phase but that h-BN is the most stable BN phase at ambient conditions. However, in 1995 Solozhenko [92] argued that it is not possible to plot an accurate equilibrium P,T-diagram from data obtained from observational methods of solid-solid phase transformations, because kinetic factors play too great a role.

Solozhenko [92,93] determined via adiabatic calorimetry the relevant thermodynamic properties of the four main BN polytypes, such as the heat of formation and temperature dependent forms of the heat capacity, enthalpy and entropy. It was concluded that c-BN was actually the most thermodynamically stable phase at ambient conditions to a temperature of about 1600 K, the proposed transition temperature for h-BN [92]. Except for a few reports [94,95], most subsequent density functional theory (DFT) studies corroborated the idea that c-BN is the most stable BN phase [96–99]. It was argued in 2011 by Halo [100] that the DFT methods used thus far for the prediction of BN phase stability did not adequately account for long range electron correlation, while Møller-Plesset second order perturbation theory (MP2) does and accurately predicts c-BN as the most stable BN polymorph. As Solozhenko [92] has presented the most reliable thermodynamic data for the BN polymorphs up to date, it is these values that were used in this project to calculate the Gibbs free energy functions needed to generate CVD phase diagrams. The heat capacity of each BN polymorph was measured by Solozhenko [92] and was fitted in this project to a power series form of the heat capacity:

$$C_P(T) = a + bT + cT^{-2} + dT^2 \qquad \text{Eq. (2.3.2.1)}$$

The coefficients of Eq. (2.3.2.1) for each BN phase are presented in Table 2.3.2.1:

Table 2.3.2.1: Coefficients of Eq. (2.3.2.1) for each BN phase

	a	**b**	**c**	**d**
h-BN	3.514×10^{1}	1.223×10^{-2}	-1.771×10^{6}	-2.386×10^{-6}
r-BN	3.393×10^{1}	1.317×10^{-2}	-1.613×10^{6}	-2.502×10^{-6}
c-BN	3.603×10^{1}	9.503×10^{-3}	-2.134×10^{6}	-2.057×10^{-6}
w-BN	3.543×10^{1}	1.016×10^{-2}	-2.066×10^{6}	-2.150×10^{-6}

Further, the standard state thermodynamic properties of each BN phase, according to Solozhenko and Gavrichev [92,93] are presented in Table 2.3.2.2:

Table 2.3.2.2: Thermodynamic properties of each BN phase at standard conditions

	C_p^o(298.15 K) [J/K-mol]	S^o (298.15 K) [J/K-mol]	H^o(298.15 K) – H^o(0 K) [J/mol]	ΔH^o_f(298.15 K) [J/mol]
h-BN	19.85	14.80	2.63×10^3	-2.50×10^5
r-BN	20.63	15.83	2.81×10^3	-2.48×10^5
c-BN	21.58	6.71	1.46×10^3	-2.67×10^5
w-BN	15.95	7.34	1.54×10^3	-2.63×10^5

Because c-BN is the BN polymorph calculated to be the most thermodynamically stable, but is not usually observed at the pressures and temperatures employed in deposition, it is important to discuss the nature of the kinetics of homogeneous (i.e., not occurring on a surface) solid-solid phase transformations in general and in this material. The h-BN polymorph can be thought of as metastable at ambient conditions [92]. External work must be applied to a metastable system to raise its free energy enough to transform it into the most stable system. The required increase in free energy from the external work is called the activation free energy, ΔG^*. The system can remain metastable indefinitely if the external work, usually in the form of thermal energy kT, is small compared to ΔG^* [101]. Assume G_c and G_h are the free energies of c-BN and h-BN, respectively. At the equilibrium transformation temperature T_e, $G_c = G_h$. Therefore, at T_e, the free energy change per unit volume, ΔG_V associated with the c-BN $\leftrightarrow$ h-BN transformation is given by

$$\Delta G_v = G_h - G_c = 0 \qquad \text{Eq. (2.3.2.2)}$$

In general, the Gibbs free energy is defined as

$$\Delta G_v = \Delta H_v - T\Delta S_v \qquad \text{Eq. (2.3.2.3)}$$

where ΔH_v and ΔS_v are the changes in enthalpy and entropy of the transformation per unit volume, respectively. At $\Delta G_V = 0$, it can be seen that $\Delta S_v = \Delta H_v/T_e$. Since neither ΔH_v nor ΔS_v change significantly with temperature, an expression for ΔG_V at temperature deviations away from T_e (i.e., $\Delta T = T_e - T$) is given by

$$\Delta G_V = \frac{\Delta H_V \Delta T}{T_e} \qquad \text{Eq. (2.3.2.4)}$$

ΔG_V is the driving force for the transformation. If the transformation is an exothermic process, ΔH_v will be negative, and at all $T < T_e$, ΔG_V is negative and the transformation should occur spontaneously. However, this does not mean the transformation occurs instantaneously or completely. For the transformation, say from h-BN to c-BN, to happen, atoms in h-BN must rearrange locally to align themselves into the c-BN lattice. However, there is a free energy of activation barrier to this process at all temperatures, even below T_e. Further, atomic rearrangement requires diffusion, a process which itself is time-dependent and thermally initiated. The h-BN $\rightarrow$ c-BN transformation, as an example, requires first the nucleation of c-BN particles in the h-BN matrix followed by the growth of the c-BN nuclei.

The total free energy change associated with creating a spherical nucleus of radius r (ΔG_r) of a new phase within the matrix of a parent phase is given by

$$\Delta G_r = \frac{4}{3}\pi r^3 \Delta G_V + 4\pi r^2 \gamma \qquad \text{Eq. (2.3.2.5)}$$

where the first term is the bulk free energy change associated with nucleus formation while the second term represents the interfacial energy (γ) change. The change in interfacial energy is always a positive term, because it costs energy to create new interfaces, while the bulk free energy change term is negative under certain conditions, such as for exothermic transformations at $T < T_e$. There is a critical nucleus size r^* for which a nucleus must be larger than if the new phase is to continue to

grow with a decrease in ΔG_r. However, if the formed nucleus is smaller than r^*, it will reincorporate itself into to the parent matrix, even when ΔG_V is negative. Hence, there is an energy barrier, ΔG^*, in creating a new, stable nucleus larger than r^*. The number of nuclei at any temperature that can form is proportional to $\exp(-\Delta G^*/kT)$. The total free energy change ΔG_r, has a maximum at r^*. An expression for r^* can be found by setting the derivative of the ΔG_r expression to zero and solving for r^*:

$$r^* = \frac{-2\gamma}{\Delta G_V} \qquad \text{Eq. (2.3.2.6)}$$

This expression for r^* can be used to determine ΔG^* by substituting it for r in Eq. (2.3.2.5):

$$\Delta G^* = \frac{16\pi\gamma^3}{3(\Delta G_v)^2} \qquad \text{Eq. (2.3.2.7)}$$

Also, as noted above, atoms must diffuse and rearrange themselves into the different lattice positions of the new phase in order to form nuclei. The nucleation rate n^* is thus proportional to both the number of stable nuclei and the ability of the atoms to diffuse to these nuclei, such that

$$n^* \propto \exp\left(\frac{-\Delta G^*}{kT}\right) \exp\left(\frac{-Q_d}{kT}\right) \qquad \text{Eq. (2.3.2.8)}$$

where Q_d is the activation energy for diffusion.

Given this discussion, it can be understood why solid-solid transformations such as c-BN $\leftrightarrow$ h-BN, the transformation of interest, are so slow. For one, diffusion rates in solids are small due to large values of Q_d. Further, solid-solid interfacial energies are also large; this in turn increases the activation barrier ΔG^* to forming nuclei, as observed in Eq. (6). The small ΔG_V driving forces for solid-solid transformations also result in an increase in ΔG^*. Finally, for solid-solid transformations, there is a positive strain energy term in the total free energy change, ΔG_r, due to the change in volume between the phases, and this also increases ΔG^*. In the case of the c-BN $\leftrightarrow$ h-BN

transformation, the molar volumes for c-BN and h-BN have been calculated to be 7.118 and 10.892 cm^3/mole, respectively [92]; the difference in molar volumes for the two phases is over 40%. For these reasons, it is difficult for solid-solid transformations such as c-BN $\leftrightarrow$ h-BN to approach equilibrium [101]. Without a significant amount of applied thermal energy, large ΔG^* and Q_d activation barriers result in slow transformation kinetics, and the system will retain its metastable state, h-BN.

2.3.3. Preferrable realization of h-BN in CVD

As noted, the foregoing discussion of ΔG^* pertained to homogeneous nucleation. In a CVD process, reactant gases from an oversaturated vapor condense on a solid substrate surface. Thus, nucleation of a thin film deposited via CVD is inherently a heterogeneous phenomenon. The nucleation of a solid film condensing from the vapor onto a planar substrate surface thus involves three interfacial energies: (1) that between the substrate and the film, γ_{sf}; (2) that between the substrate and the vapor γ_{sv}; and (3) that between the film and the vapor γ_{fv}. Ohring [31] expressed the free energy change to form cap-shaped nuclei of radius r on a substrate as

$$\Delta G_r = a_3 r^3 \Delta G_V + a_1 r^2 \gamma_{vf} + a_2 r^2 (\gamma_{fs} - \gamma_{sv}) \qquad \text{Eq. (2.3.3.1)}$$

where a_1r^2 represents the curved surface area of cap-shaped nuclei, a_2r^2 represents the circular area projected onto the substrate, and a_3r^3 represents the volume of the nucleus. The geometric constants a_1, a_2, and a_3 are equal to $2\pi(1 - \cos\theta)$, $\pi \sin^2\theta$, and $\pi(2 - 3\cos\theta + \cos^3\theta)/3$, respectively. Young's equation [102] describes the mechanical equilibrium among the aforementioned interfacial energies as

$$\gamma_{sv} = \gamma_{fs} + \gamma_{vf} \cos\theta \qquad \text{Eq. (2.3.3.2)}$$

that shows that the wetting contact angle θ of the film nucleus on the substrate is governed by the interfacial properties of the system. It can thus be shown that ΔG^* in heterogeneous nucleation

becomes a function of the contact angle. If the ΔG_r for heterogeneous nucleation (Eq. (2.3.3.1)) is differentiated with respect to r and set to zero, the critical radius r* for heterogeneous nucleation can be determined. Substituting r* for r in Eq (2.3.3.1) as well as the geometric constants for a_1, a_2, and a_3, it can be shown that ΔG^* for heterogeneous nucleation can be expressed as:

$$\Delta G^* = \frac{16\pi\gamma_{vf}{}^3}{3(\Delta G_v)^2}\left(\frac{2-(3\cos\theta)+\cos^3\theta}{4}\right) \qquad \text{Eq. (2.3.3.3)}$$

The first term in Eq (2.3.3.3) represents the activation barrier for homogeneous nucleation while the second term represents the wetting factor that arises when a planar surface is available to facilitate the nucleation of a film from the vapor. At a contact angle of 0^o, the wetting factor equals zero and the film fully wets the substrate, and thus the barrier to nucleation is also zero. At a contact angle of 180^o, the wetting factor is unity, meaning that the film cannot wet the substrate at all and the activation barrier has a maximum value, which is the same as homogeneous nucleation.

To obtain an estimate for ΔG^* associated with the nucleation of h-BN or c-BN during CVD, one would have to know the surface energy of typically encountered growth faces of both polymorphs, i.e., (0001) for h-BN and (111) [73,103–106] for c-BN, as well as the wetting contact angle of h-BN and c-BN nuclei on a particular substrate. Although studies of BN nuclei contact angles on various substrates have not been reported, there have been a few experimental studies where the surface energies of h-BN and c-BN thin films were measured. To estimate the energy of a surface experimentally, typically the wetting contact angles of various test liquids are measured on the surface using a static sessile drop method [107]. The test liquids have a known surface energy and allow determination of the polar and dispersive contributions to the surface energy of the film. Spiesser et al. [108] prepared polycrystalline c-BN thin films on nano-diamond/Si templates by electron cyclotron resonance plasma-enhanced CVD (ECR PECVD) with activated He, Ar, N_2, BF_3, and H_2 species, as well as radio-frequency (RF) magnetron sputtering using pyrolytic h-BN as the

target and Ar and N_2 as the plasma gas mixture. Through contact angle measurements, the c-BN surface energy was determined to be ~ 40 mJ/m^2 on average across both deposition methods. The orientation of the Si template, nano-diamond layer, and resultant c-BN films were not noted in the study. Teii and Matsu [109] reported a similar value of ~ 47 mJ/m^2 for the (111) face of c-BN deposited on WC-Co substrates by inductively coupled plasma-enhanced CVD using He, H_2, N_2, and BF_3 as the plasma gas mixture. In the same study, Teii and Matsu [109] also measured the surface energy of (0002) h-BN on WC-Co (~ 50 mJ/m^2) which formed in the first tens of nanometers of deposition (the phenomenon of h-BN forming before c-BN occurs in virtually all depositions where c-BN is the desired phase [109,110] and will be discussed shortly). Annamalai et al. [111] also measured the surface energy of the (0001) face of few-layer h-BN on Cu foil to be ~ 58 mJ/m^2. Even though these few studies suggest that c-BN thin films have lower surface energy than h-BN thin films, the common deposition of h-BN instead of c-BN during non-plasma-enhanced CVD is not understood.

The CVD synthesis of c-BN always requires some type of plasma enhancement to lower the kinetic activation energy barrier [81,112–116]. By contrast, the CVD synthesis of h-BN thin films are normally achieved without plasma enhancement, although such methods have been used to lower the deposition temperature as well as improve film stoichiometry [117–119]. A qualitative reason why h-BN, instead of c-BN, is preferably encountered during conventional CVD has been offered by Bohr et al. [120], who postulated that the BN CVD system follows the two empirical Ostwald and Ostwald-Volmer rules. The Ostwald rule states that when energy is removed from a system with multiple energy states, the system will traverse all intermediate metastable states instead of directly achieving the equilibrium state. Furthermore, the Ostwald-Volmer rule states that the phase with the lowest density will nucleate first. In a system where the two rules would contradict

each other, the Ostwald-Volmer rule takes precedence. For example, if these rules were applied to the CVD of carbon, the formation of graphite instead of diamond occurs despite diamond being the metastable state because graphite is less dense; thus the Ostwald-Volmer rule overrides the Ostwald rule here. However, when following the new convention that c-BN is the thermodynamically stable phase in the BN system, h-BN is the preferred phase during CVD because it is the metastable state and is less dense than c-BN, thereby obeying both the Ostwald and the Ostwald-Volmer rules.

2.3.4. BN conversion in HP-HT processes

Work has been reported, as summarized in Table 2.3.4.1, regarding the kinetics of the h-BN to higher density (w-BN, c-BN) phase transformation induced by HP-HT processes which included estimations of experimentally determined transformation activation barriers [91,121–125]. Because the h-BN and w-BN crystal structures possess the same AA'A stacking sequence, it has been observed that when applying pressure directly along the c-axis of h-BN to induce a c-BN transformation, metastable w-BN actually forms first [126,127]. The c-BN crystal structure possesses an ABC stacking sequence; for complete transformation, atoms in a crystalline h-BN lattice must undergo diffusion controlled rearrangement via puckering, a folding of the basal (0001) plane which is aided by both high temperature and high pressure [91,126,128]. Turbostratic BN, in addition to rotated and misoriented basal planes along [0001], can contain puckering, which is described as the corrugation or waviness of the h-BN basal planes [126,129]. Thus, the temperature and pressure (and resulting activation energy) can be lowered for the c-BN transformation when the h-BN starting material contains puckering defects [125,127,130]. The most recent research concerned with h-BN defects and their effect on phase transformation into denser *sp3* forms under HP and HT conditions was performed by Schimpf et al. [125,129,131]. The initial study by this group concerned the quantitative characterization of the defects including the extent of turbostratic

disorder, degree of puckering of the basal planes, and the density of stacking faults and dislocations of three types of starting h-BN: hot-pressed h-BN, pyrolytic BN produced by high temperature CVD (T > 1700 °C), and h-BN produced by low temperature CVD (a specific value of temperature was not mentioned). Schimpf et al. [125] subsequently subjected each of the three types of h-BN to HT and HP processes to observe the kinetics of the phase transformation of h-BN to its denser *sp3* forms. Hot-pressed h-BN is defect poor, containing a 10^{11} m^{-2} {001}<112> type edge dislocation density. It transformed into w-BN within the 8-9 GPa pressure range at 1100 °C. The activation energy, calculated using the Avrami equation [132], was ~31 kJ/mol. Pyrolytic BN (p-BN) is polycrystalline h-BN with textured grains of mostly (000*l*) orientation, poor out-of-plane order, and contains a high degree of puckering as its primary defect [129,131]. Because of the inherent puckering, p-BN was transformed, at 11 GPa and 1100 °C, into c-BN while suppressing w-BN formation. The measured activation energy associated with this transformation was ~ 45 kJ/mol [125]. Lastly, low temperature CVD resulted in h-BN that contained less puckering than p-BN but more severe turbostratic disorder, namely, 5 nm crystallites with weak local preferred (00*l*) orientation [129]. As a result, the activation energy to transform the low temperature CVD h-BN to c-BN at 10 – 11 GPa and 1100 °C was measured to be ~ 61 kJ/mol. It was postulated that the turbostratic disorder had to first be annealed out before the transformation to c-BN could begin [125]. Table 2.3.4.1 summarizes the Schimpf et al. [125] results as well as the results of studies concerned with the HP and HT transformation kinetics in BN reported by other research groups. The large variation in reported activation energies is a direct result of different levels of impurities, grain sizes, and defects in the BN starting material; the presence or lack of catalysts in a solvent melt; and different executions of the Avrami model for phase transformation kinetics [132].

Table 2.3.4.1: Reported activation energies for the h-BN → c-BN transformation induced by HP-HT synthesis.

Reference	HP-HT Conditions	Starting material	Transformation observed	Activation energy (kJ/mole)
[91]	Pressure: 4 - 13 GPa; Temperature: 800 - 2400 °C	well crystallized h-BN powder	h-BN → c-BN	630 - 1050
		w-BN powder converted from h-BN by shock-compression	w-BN → c-BN	837
[121]	Pressure: 6.5 GPa; Temperature: 1200 - 1800 °C; AlN solvent	poorly crystalline h-BN powder synthesized from borazine treated at 250 °C and 100 MPa for 1 h + 20 mol% AlN	h-BN → c-BN	46
		turbostratic h-BN powder synthesized from borazine treated at 700 °C and 100 MPa for 1 h + 20 mol% AlN	h-BN → c-BN	84
		h-BN powder + 50 mol% c-BN powder (synthesized from previous mixtures)	h-BN + c-BN→ c-BN	355
[122]	Pressure: 6.6 GPa; Temperature: 1447 - 1547 °C; Li_3N-BN solvent	Commercial h-BN powder (annealed to remove O_2 to less than 0.003 vol.%) + 20 mol.% Li_3N powder	h-BN → c-BN	115 +/- 5
[123]	Pressure: 6.4 GPa; Temperature: 1057 - 1167 °C; NH_4F-BN solvent	Commercial h-BN powder (99.8%) (annealed to remove O_2 and water) + NH_4F powder (99.5 %)	h-BN → c-BN	207 +/- 6
[124]	Pressure: 6.5 GPa; Temperature: 1327 – 1727 °C	pyrolytic h-BN	pyrolytic BN → cBN	300
		h-BN (after annealing turbostratic BN)	h-BN → c-BN	320
[125]	Pressure: 8 - 11 GPa; Temperature: 527 - 1127 °C	high density, defect poor h-BN; 300 nm domains	h-BN → w-BN	30.87 +/- 4.82
		pyrolytic h-BN; 15 nm domains	pyrolytic BN → c-BN	45.34 +/- 6.75
		CVD-BN with turbostratic structure and impurities: 4.9 at.% O and 5.4 at.% H; 5 nm domains	CVD BN → c-BN	60.78 +/- 9.65

2.3.5. CVD phase diagrams

It should be noted that even non-plasma-enhanced CVD, the most common method for synthesizing h-BN thin films, is not a thermodynamic equilibrium process because of the gradients in T, P and the chemical potentials of the reactants and products in the gas phase throughout the deposition chamber and the kinetically controlled processes such as gaseous diffusion through the

boundary layer and decomposition reactions which influence the resulting condensed phase(s) that form. When the kinetic processes occur extremely quickly relative to the amount of time that reactant gases spend in the reaction zone – assumed to be limited to the heated substrate – the resulting condensed film, its deposition rate, and the composition of the gaseous species of the boundary layer above the substrate are limited by thermodynamic variables [133,134]. Calculations of CVD phase diagram are performed under the assumption that the reactor chamber is being employed under equilibrium conditions during the deposition of solid-state films. Though such conditions do not exist during an experimental deposition, these diagrams can serve as an experimental guide, as they indicate the ranges of temperature, pressure, and input gaseous concentrations that lead to the formation of certain condensed phases [133].

The CVD phase diagrams produced in my research were calculated using FactSage, a fully integrated database in chemical thermodynamics and a direct application of the CALPHAD (CALculation of PHAse Diagrams) method [135]. In general, phase diagrams aid the process of materials development because they allow an understanding of phase equilibria and the fundamental thermodynamics of the materials within the predicted phase fields and phase transformations between these fields [136]. Conventionally, materials process development and design is expensive and time consuming. Because CALPHAD can be executed by a host of computational tools and software backed by accurate and reliable thermodynamic databases, this method has been deemed in materials industries as quick and effective for calculations involving multicomponent and multiphase systems [136].

2.4. Characterization techniques used in Thesis

An assortment of materials characterization techniques have been used throughout my research to analyze my sp^2-BN films synthesized via CVD. The following brief discussion about the generation of x-rays is important in understanding the basic concepts of x-ray diffraction, x-ray photon spectroscopy, and energy dispersive x-ray spectroscopy which often accompanies scanning electron microscopy.

2.4.1 X-rays

Many of the characterization techniques used my research rely on x-ray generation and detection. X-rays are electromagnetic waves with wavelengths on the order of angstroms (10^{-10} meters). In general, electromagnetic radiation is generated when charged particles, such as electrons and ions, are accelerated or decelerated. X-rays, in particular, are emitted from high-energy electrons that are brought suddenly to a halt. This can be done when electrons are accelerated between a cathode and anode. The cathode material is heated sufficiently high to cause thermionic emission, and the emitted electrons are accelerated toward the anode (target) by an applied voltage across the gap between these two charged materials. Upon bombardment, the atoms of the anode material will emit x-rays. X-rays are emitted due to the fact that electrons reside in orbitals around an atom's nucleus, and each orbital has a discrete energy level. The lowest energy level that an electron can occupy is its ground state, and whenever an electron is promoted to an energy level beyond that (in this case, by means of high energy electron bombardment), it is in an excited state. An electron in the excited state will return to the ground state after a short time, and when it does, an amount energy that is precisely the difference in energy between the excited and ground states is released in the form of a photon. The atomic number of an element governs the number of electrons and atomic orbitals as well as the discrete energy levels of these orbitals in each atom. Therefore, the energies of

the x-ray photons emitted during core shell transitions are specific to each element and referred to as characteristic x-rays. The core shell transitions are only possible if the energy of the electrons accelerated from the cathode are higher than the ionization energy of the anode [137].

2.4.2. X-ray Diffraction

X-ray diffraction (XRD) is a versatile characterization technique that can be used to identify the crystalline phases present in a material and to analyze the structural properties these phases such as lattice parameter, grain size, extent of strain, and dislocation density. In the field of thin films, XRD is especially important in determining the presence and nature of an epitaxial relationship between the film and the substrate.

Because the distance between atomic planes (a few angstroms) is on the same length scales as x-ray wavelengths, x-rays can be observed after being coherently scattered, or diffracted, by these planes. The XRD system used in this work was a Panalytical X'Pert Pro MRD X-Ray Diffractometer with a monochromatic 1.5406 Å Kα Cu x-ray source. When x-rays are incident upon the crystallographic planes of a sample, diffraction occurs when the scattered x-rays constructively interfere. This condition is known as the Bragg condition, and is described by Bragg's law:

$$n\lambda = 2d_{hkl} \sin \theta_{hkl} \qquad \text{Eq. (2.4.2.1)}$$

where n is an integer, λ is the wavelength of the incident x-ray, d_{hkl} is the distance between a particular family of {*hkl*} crystallographic planes, and θ_{hkl} is the Bragg angle for which coherent scattering occurs for a given (*hkl*) plane in a crystal. In other words, the scattered waves must have a phase difference equal to an integer multiple of the incident x-ray wavelength for diffraction to be observed [138]. However, Bragg's law does not predict expected diffraction intensities from crystallographic planes. What determines the signal intensity of a diffracted beam from a material's specific (*hkl*) plane is the structure factor F_{hkl}, which is the Fourier transform of the atomic positions

of a crystallographic unit cell. The structure factor accounts for the phase difference of diffracted waves from all atoms within an {*hkl*} family of planes. The structure factor is defined as

$$F_{hkl} = \sum_{j=1}^{N} f_j e^{2\pi i} (hx_j + ky_j + lz_j) \qquad \text{Eq. (2.4.2.2)}$$

where N is the number of atoms in a unit cell; f_j is the scattering factor which is the ratio between the amplitude of a wave scattered from a single atom and that of an electron at a given value of sin(θ) and λ; *h*, *k*, and *l* are the Miller indices of the crystallographic planes; and x, y, and z are the positions of each atom in the unit cell. The intensity I of the diffracted beam is determined by squaring the modulus of the structure factor by multiplying the structure factor by its complex conjugate:

$$I = |F_{hkl}|^2 = F_{hkl} F_{hkl}^* \qquad \text{Eq. (2.4.2.3)}$$

The implications of the structure factor are that certain planes in a crystallographic system diffract more strongly than others, and certain planes will not diffract at all if the structure factor results in a summation of zero. In the case of h-BN, its (002) reflection at $2\theta = 26.7^{\circ}$ [139] (using Cu Kα radiation) diffracts much more strongly than (004). Thus, since epitaxial h-BN thin films grow on (001) hexagonal or (111) face-centered cubic surfaces with a preferred (00*l*) orientation, the observation of the (002) reflection is most used for identification and analysis h-BN using XRD.

In the context of the reciprocal lattice, diffraction occurs when the incident x-ray beam vector $\mathbf{k_0}$ and the diffracted beam vector $\mathbf{k_d}$ form the correct angle when interacting with the crystal lattice. At these angles, the scattered vector **S** ($\mathbf{k_d} - \mathbf{k_0}$) is used to investigate the reciprocal lattice. To access certain reciprocal lattice points of a crystal, the length of **S** can be varied by changing the 2θ angle of the incident beam, and θ is the angle where $\mathbf{k_0}$ strikes a crystallographic plane. Further, the angle where $\mathbf{k_0}$ strikes the surface of a sample, ω, can also be changed to vary the direction and

orientation of **S**. For XRD characterization of the h-BN thin films in my research, the diffractometer was configured in the Bragg-Brentano geometry, where ω is set to θ (plus or minus a less than 1° offset due to the instrument and sample mounting) and the **S** vector is perpendicular to the surface of the sample. The result is that only the (00*l*) planes of films, which are parallel to its surface, will be detectable [140].

It is often necessary to investigate planes other than (00*l*) to make inferences regarding in-plane ordering of a film with respect to its substrate. This allows an additional investigation of the epitaxial relationship(s) between the film and its substrate, as well as an estimate of both lattice parameters (*a* and *c*) of an hexagonal crystal structure. On (00*l*) oriented thin films, (*hk*0) planes such as (110) can be investigated by tilting the sample close to 90° so that incident x-rays are not totally externally reflected, but instead graze the sample surface at a low angle. This technique used to observe the asymmetric planes of oriented thin films is known as grazing incidence x-ray diffraction (GIXRD). The formula used to determine the *a* and *c* lattice parameters for hexagonal crystal structures [140], which relates observed d_{hkl} spacings to their corresponding (*hkl*) Miller indices, is given below

$$\frac{1}{d_{hkl}^2} = \frac{4}{3}\frac{h^2+k^2+hk}{a^2} + \frac{l^2}{c^2} \qquad \text{Eq. (2.4.2.4)}$$

Thus, to estimate the lattice constants of a hexagonal crystal structure, both (00*l*) and (hk0) planes should be probed. Figure 2.4.2.1 shows an XRD pattern of pyrolytic boron nitride (PBN) (Morgan Technical Ceramics), which is polycrystalline h-BN whose grains are strongly (00*l*) oriented. The lower 2θ value for the (0002) reflection at ~26.0° instead of 26.7° shows that the d_{002} spacing is larger than the published reference value for ideal h-BN, and this indicates that the BN sample

contains turbostratic disorder. Kurdyumov [141] quantified turbostratic disorder with respect to XRD line broadening:

$$\beta_{hkl}^{turb} = \frac{2l\, d_{hkl}^2}{\pi c^2} \frac{\gamma}{\sqrt{1-\gamma}} \qquad \text{Eq. (2.4.2.5)}$$

β_{hkl}^{turb} is the integral line broadening due to turbostratic disorder and γ is a unitless parameter in the range of [0, 1] representing the extent of turbostratic disorder. If $\gamma = 0$, there is no turbostratic disorder, and at $\gamma = 1$, the structure is fully disordered [129,141]. Schimpf et al. [129] determined from XRD experiments that the magnitude of turbostratic disorder in PBN (also supplied by Morgan Technical Ceramics) is equal to $\gamma = 0.14 \pm 0.01$.

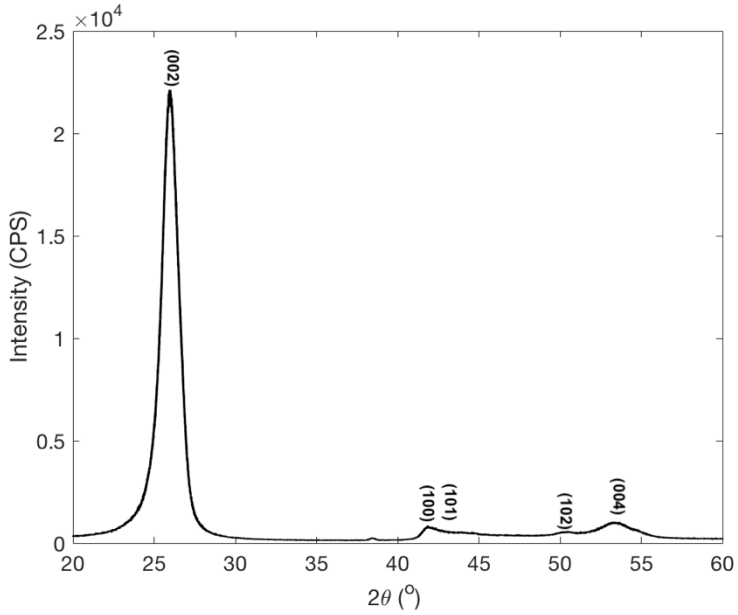

Figure 2.4.2.1: 2θ-ω x-ray diffraction pattern of pyrolytic boron nitride (Morgan Technical Ceramics).

2.4.3. X-ray Photoelectron Spectroscopy

X-ray photoelectron spectroscopy (XPS) is a technique used to study the atomic composition and the nature of chemical bonds at the surface of a sample. In XPS, an x-ray photon with an excitation energy of $h\nu$ bombards a sample target whose atoms become ionized and therefore release a free electron [142]. The kinetic energy (KE) of the released electron is then measured, and if the instrument's work function (Φ) is known, then the binding energy (BE) of the electron can be calculated with the following equation:

$$BE = h\upsilon - KE - \Phi \qquad \text{Eq. (2.4.3.1)}$$

The BE of an electron in a particular atomic orbital is the energy required to remove it from the atom. Because these energies are discrete not only between different types of atoms but also within the different atomic orbitals of the same atom, the calculation of BE determines precisely the type of atom from which the electron was released during the excitation event. I.e., the calculated binding energies in an XPS spectra will reveal the surface composition, typically at a resolution of 0.1 atomic percent, of the measured material. The analysis is limited to the surface of the sample because the escape depth of released electrons after the $h\nu$ excitation is only about 5 nm. In the instrument used in my research the radiation was monochromated Al Kα1 x-rays, which carry a photon energy of $h\nu$ = 1486.7 eV.

Although the BE value for an electron ejected from an atomic orbital can be used to identify the type of atom, BE values are not quite constant due to the presence of other types of atoms that may be in the material and their resulting bond states. In general, for compound materials the BE will increase for an electron of one element if that electron experiences an increased charge from the atomic orbitals of the other element(s). The equation for BE can be modified then to include the chemical shift ΔE which is recorded in the measurement of the kinetic energy:

$$BE = h\upsilon - (KE + \Delta E) - \Phi \qquad \text{Eq. (2.4.3.2)}$$

The observation of ΔE in an XPS spectra allows the determination of other atoms to which an element may be bonded. An increase in the ΔE for an atom to a higher BE typically means that the atom is bonded to another atom which has a larger electronegativty [142].

For sp^2-BN, core-level 1s transitions are expected to occur near the binding energies of ~190 eV for B 1s and ~398 eV for N 1s [143,144]. XPS can also be used to distinguish between sp^2- and sp^3- hybridized BN, which correspond to h-BN and c-(or amorphous) BN, respectively. For both sp^2- and sp^3- hybridized BN, one will observe bulk plasmon loss features at approximately 25 eV and 27 eV above the expected transitions for B 1s and N 1s, respectively. The sp^2-hybridized form of BN can be distinguished from the sp^3-hybridized form, however, because the sp^2-hybridized form alone exhibits π plasmon loss features at an approximately 9 – 10 eV higher binding energy above the expected B 1s and N 1s transitions [145]. Figure 2.4.3.1 shows the B 1s and N 1s XPS spectra of pyrolytic BN (Morgan Technical Ceramics). The π plasmon loss features for both elements can be seen in the figure at ~ 200 eV and ~ 407 eV for B and N, respectively, indicating that the B-N bonds in pyrolytic BN are sp^2-hybridized. The features observed at ~179 eV and ~388 eV for the B 1s and N 1s spectra, respectively, have not been explained in the literature concerning the analysis of BN films, but they are observed in both h-BN and c-BN [143]. These features are most likely Auger peaks, as a reference table [146] displays the Auger electron energies for the B(KLL) and N(KLL) lines as 176 eV and 383 eV, respectively.

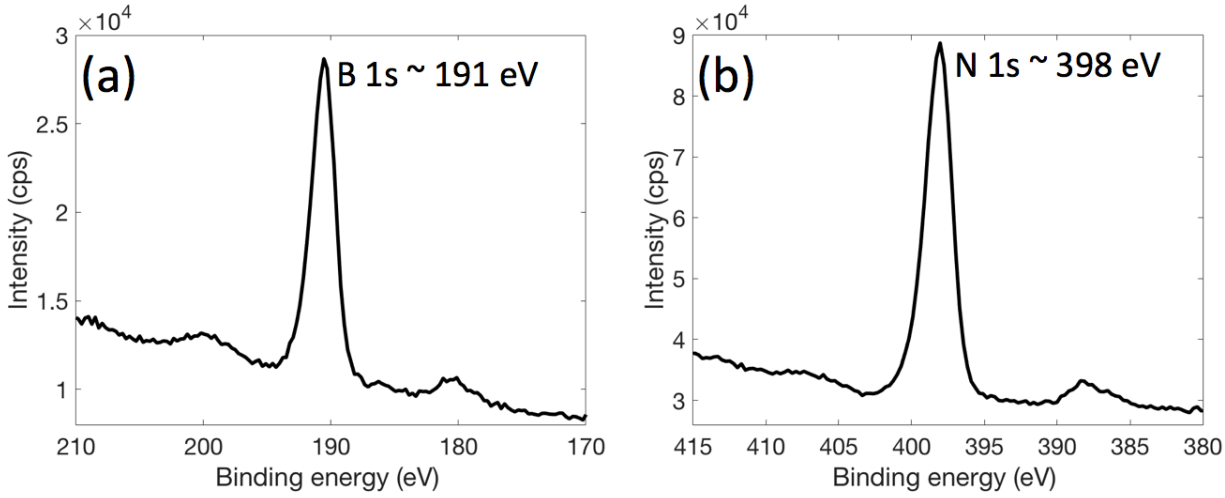

Figure 2.4.3.1: XPS spectra of the (a) B 1s and (b) N 1s of a pyrolytic BN sample (Morgan Technical Ceramics).

2.4.4. Scanning electron microscopy

Scanning electron microscopy (SEM) is an imaging technique used to examine the surface morphology of materials at magnifications as large as 300,000X and resolutions of a few nanometers. Primary electrons originating from either a field emission gun or a charged cathode are accelerated to high voltages (1 – 20kV) in vacuum, focused through a lens system and scanned over a sample surface. At the high energies produced by the acceleration voltage, the De Broglie wavelength of the electrons decreases to just a few nanometers, which provides the high resolution needed to examine nanometer-sized features on a surface. When the scanning beam of electrons penetrates a sample, either electrons or photons can be emitted from the surface. The emitted electrons are either back-scattered electrons or secondary electrons, and the emitted photons are x-rays. The three different types of emission provide different information about the sample [147].

When the incident high-energy electron beam strikes a sample surface, electrons from the atoms within the sample can undergo inelastic scattering. In this phenomenon, the incident electrons impart sufficient energy to the electrons in the atoms such that their new energy surpasses the work

function of the material, and they leave the surface. Electrons emitted in this way are known as secondary electrons (SE) and typically have energies less than 50 eV. Due to this low energy, SE cannot escape from more than a few nm from beneath the surface, and therefore the information gained from SE is limited to topographical surface features. On the other hand, some electrons from the sample are scattered elastically and as a result have energies similar to that of the incident beam. These electrons are called back-scattered electrons (BSE), and their scattering efficiency increases with increasing atomic number (Z). This results in an increased signal from high-Z materials and therefore a brighter image. Because BSE have energies greater than 50 eV, they are able to escape from much deeper beneath the sample surface than the SE. Therefore, the signal from BSE contains information about the bulk of the sample, and its sensitivity to Z provides qualitative information about the sample's elemental composition. Lastly, because the incident beam excites electrons from their ground state, they will emit characteristic x-ray photons upon their return to the ground state in the same manner described as in the discussion of XPS. Therefore, one can use SEM to also perform energy dispersive x-ray spectroscopy (EDS) to quantitatively measure the elemental composition of samples. However, because the incident electron beam energies used in SEM are much higher than that of the incident x-ray photons used in XPS (up to 20 keV in SEM vs < 1.5 keV in XPS), the escape depth of emitted x-ray photons in SEM/EDS are so large that compositional information is reflective of the bulk of the sample and not just its surface [147].

2.4.5. Transmission Electron Microscopy

Transmission electron microscopy (TEM) is a powerful materials characterization tool that utilizes highly energetic (≥ 100 keV) transmitted electron beams to obtain image and diffraction data from a sample with sub-nanometer spatial resolution. In TEM, a high-energy electron beam penetrates an electron-transparent (typically < 200 nm thick) sample, and signals are collected from

both scattered and non-scattered beams that are transmitted through the sample. Electromagnetic lenses that are both in line with and below the sample direct the signal to a fluorescent screen or camera for detection. The high spatial resolution in TEM is attributed to (1) the use of the electron beam as a < 1 μm diameter probe, (2) the extremely small wavelength of the accelerated electrons (at $h\upsilon$ = 100 keV, λ = 0.0037 nm), and (3) the few scattering events of transmitted beams allowed by thinly-prepared specimen [148].

A TEM specimen can be examined via two primary modes, namely, diffraction and imaging. In the diffraction mode, the scattered beam leaving a sample can generate an electron diffraction pattern that can be observed on the fluorescent screen. These electron diffraction patterns are generated by the same mechanism as that of XRD patterns, so the crystallographic information from the former is equivalent to that obtained using the latter. Thus, obtaining electron diffraction patterns of sp^2-BN thin films along a crystallographic zone axis of the substrate allows the evaluation of substrate-film epitaxial relationship if one exists. In the image mode, an image is obtained from the area on the sample illuminated by the electron beam.

There are several types of contrast mechanisms that can contribute to a TEM image, such as mass contrast, thickness contrast, diffraction contrast, and phase contrast. Especially useful in the examination of sp^2-BN thin films is phase contrast that allows the visualization of periodic fringes originating from diffracting planes that satisfy the Bragg condition. The interplanar distance between observed planes is greater than that of the spatial resolution of the TEM unit at the prescribed settings. Phase contrast is made possible through high resolution TEM (HRTEM), a technique enabled by the use of a large objective aperture that allows collection of the transmitted beam and at least one diffracted beam. At high enough magnification, the atomic structure of the sample can be visualized [148]. This technique is important for thin film analysis of sp^2-BN, since it allows one to

determine (a) if epitaxy exists at the substrate-film interface, (b) the stacking order of the atomic layers, and (c) the nature of the microstructure of the bulk film.

2.4.6 Atomic Force Microscopy

Atomic force microscopy (AFM) is a scanning probe microscopy and force measurement technique capable of constructing topographic, three dimensional images of surfaces with ~ 1 nm lateral resolution. AFM units utilize a sharp, square pyramid-shaped tip (~ 55^{o}), typically made of Si_3N_4 is fixed onto a flexible Si cantilever. A piezoelectric transducer enables scanning of the sample surface by the tip. As the tip approaches the surface of a sample, van der Waals forces act repulsively between the tip and the sample. These forces cause the cantilever to deflect, the magnitude of which depends on the distance between the tip and sample. Measurement of these deflections as sample surface is scanned allows the acquisition of three dimensional topographic data of the surface [149]. The AFM technique is important in examining the surface morphology roughness of sp^2-BN films. Depending on CVD growth conditions, AFM has been used to determine if sp^2-BN films grew layer-by-layer with smooth surface features [78,150,151], or layer-plus-island with rougher morphology [51,151].

2.4.7. Raman Spectroscopy

Raman spectroscopy is a nondestructive vibrational spectroscopy light technique used to characterize the molecular structure of materials. The molecules that make up a crystal unit cell vibrate at specific frequencies that are determined by the atomic weight of participating atoms in the system and the bond force constants between the atoms. A crystal unit cell has 3N-3 vibrational modes, where N is the number atoms in the unit cell [152].

In a Raman scattering experiment, monochromatic light (either visible or UV) is incident upon a sample, and the sample scatters that light at a different frequency. Most interactions between

incident photons and the sample are actually elastic, meaning that the energy (and therefore the frequency and wavelength) remains unchanged when scattered. However, a small portion of the interactions between incident photons and the sample are inelastic due to molecules either absorbing energy from or releasing energy to the photons. The scattered photons in this scenario now experience a change in frequency that is a direct measure of the amount of energy involved in the transition between initial and final states of the scattered molecule. The initial state of the molecule is precisely set by its vibrational mode, and therefore the measured change can be used to identify specific types of chemical bonds and how they are structured. The inelastic scattering observed in the Raman effect is due the change in the polarizability of the molecules, which is a measure of how easily the electron clouds of a molecule can become distorted upon interaction with a photon [152].

In the case of h-BN, its identifying Raman shift is observed at a frequency of 1367 cm^{-1} [153]. This frequency corresponds to an in-plane vibrational mode (E_{2g}) between the B and N atoms in their two-dimensional hexagonal lattice. The main peak characteristics of importance are its center, from which deviations often indicate strain as a result of lattice mismatch with the substrate, and the full-width-half-maximum, which, as also observed in XRD, will narrow with increasing crystallinity [154]. In my research, the Raman spectra of h-BN films have been measured (NT-MDT Spectra) using a 532 nm green laser. Figure 2.4.7.1 shows the Raman spectrum for a pyrolytic BN sample (Morgan Technical Ceramics).

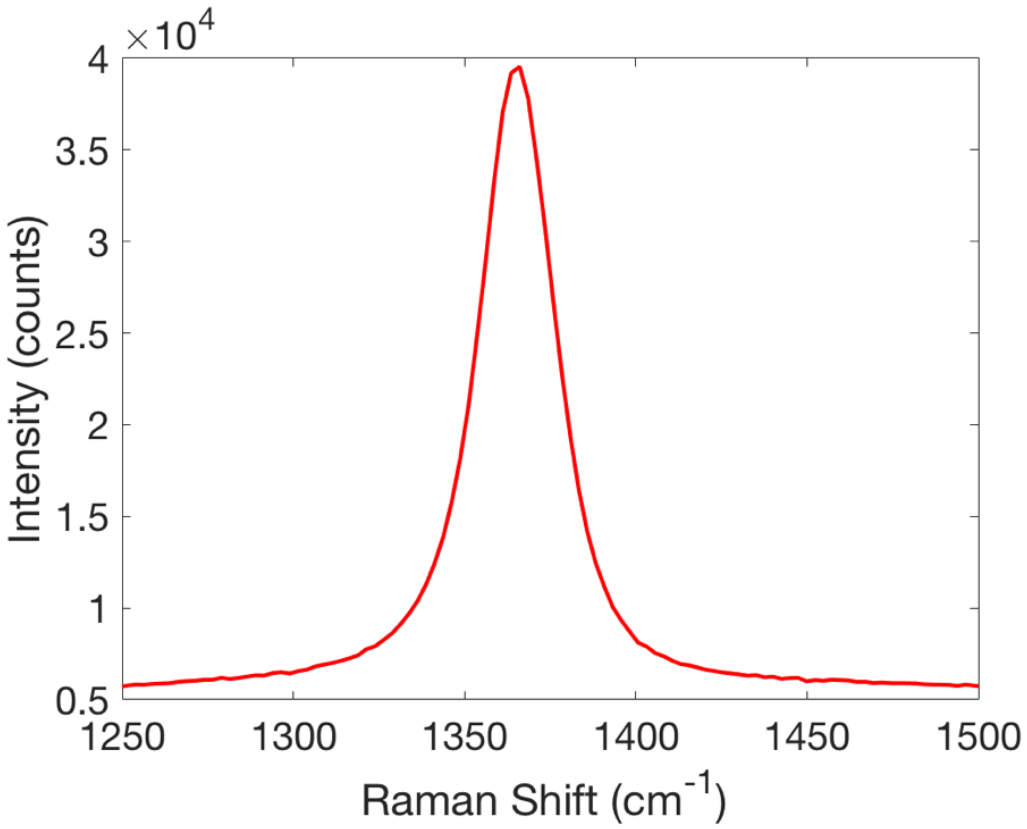

Figure 2.4.7.1: Raman spectra of a pyrolytic BN sample (Morgan Technical Ceramics).

1., 2. References

[1] M. S. Shur, in *High Temp. Electron. Eur.*, edited by V. Dmitriev, T. P. Chow, M. S. Shur, M. G. Spencer, and G. White, 1st ed. (Baltimore, 2000), pp. 61–86.
[2] H. X. Jiang and J. Y. Lin, Semicond. Sci. Technol. **29**, 084003 (2014).
[3] Y. Wu, D. Kapolnek, J. P. Ibbetson, P. Parikh, B. P. Keller, and U. K. Mishra, IEEE **48**, 586 (2001).
[4] R. F. Davis, Proc. IEEE **79**, 702 (1991).
[5] T. Saito, T. Hitora, H. Ishihara, M. Matsuoka, H. Hitora, H. Kawai, I. Saito, and E. Yamaguchi, Metrologia **46**, S272 (2009).
[6] J. A. Del Alamo, Nature **479**, 317 (2011).
[7] K. Zhang, M. Sumiya, M. Liao, Y. Koide, and L. Sang, Sci. Rep. **6**, 23683 (2016).
[8] K. Watanabe, T. Taniguchi, and H. Kanda, Nat. Mater. **3**, 404 (2004).
[9] R. Dahal, J. Li, S. Majety, B. N. Pantha, X. K. Cao, J. Y. Lin, and H. X. Jiang, Appl. Phys. Lett. **98**, 2 (2011).
[10] B. He, W. J. Zhang, Z. Q. Yao, Y. M. Chong, Y. Yang, Q. Ye, X. J. Pan, J. A. Zapien, I. Bello, S. T. Lee, I. Gerhards, H. Zutz, and H. Hofsass, Appl. Phys. Lett. **95**, 2 (2009).
[11] K. Nose, H. Oba, and T. Yoshida, Appl. Phys. Lett. **89**, (2006).
[12] S. Majety, T. C. Doan, J. Li, J. Y. Lin, and H. X. Jiang, AIP Adv. **3**, (2013).
[13] B. He, M. Qiu, M. F. Yuen, and W. J. Zhang, Appl. Phys. Lett. **105**, 012104 (2014).
[14] S. Majety, J. Li, X. K. Cao, R. Dahal, B. N. Pantha, J. Y. Lin, and H. X. Jiang, Appl. Phys. Lett. **100**, (2012).
[15] M. Levinshtein, S. Rumyanstev, M. Shur, A. D. Jackson, S. N. Mohammed, G. L. Harris, and M. G. Spencer, in *Prop. Adv. Semicond. Mater. GaN, AlN, BN, SiC, SiGe*, edited by M. Levinshtein, M. Shur, and S. Rumyanstev (John Wiley & Sons, NewYork, 2001), pp. 66–92.
[16] B. Yates, M. J. Overy, and O. Pirgon, Philos. Mag. **32**, 847 (1975).
[17] A. R. Acharya, Himal. Phys. **4**, 22 (2013).
[18] I. Meric, C. R. Dean, N. Petrone, L. Wang, J. Hone, P. Kim, and K. L. Shepard, Proc. IEEE **101**, 1609 (2013).
[19] W. H. Balman, J. Für Prakt. Chemie **27**, 422 (1842).
[20] A. Lipp, K. A. Schwetz, and K. Hunold, J. Eur. Ceram. Soc. **5**, 3 (1989).
[21] T. Ishii and T. Sato, J. Cryst. Growth **61**, 689 (1983).
[22] T. Taniguchi and K. Watanabe, J. Cryst. Growth **303**, 525 (2007).
[23] O. Fukunaga, Diam. Relat. Mater. **9**, 7 (2000).
[24] Y. Kubota, K. Watanabe, T. Osamu, and T. Taniguchi, Science (80-.). **317**, 932 (2007).
[25] Y. Kubota, K. Watanabe, O. Tsuda, and T. Taniguchi, Chem. Mater. **20**, 1661 (2008).
[26] T. B. Hoffman, B. Clubine, Y. Zhang, K. Snow, and J. H. Edgar, J. Cryst. Growth **393**, 114 (2014).
[27] K. S. Novoselov, D. Jiang, F. Schedin, T. J. Booth, V. V. Khotkevich, S. V. Morozov, and A. K. Geim, Proc. Natl. Acad. Sci. U. S. A. **102**, 10451 (2005).
[28] C. R. Dean, A. F. Young, I. Meric, C. Lee, L. Wang, S. Sorgenfrei, K. Watanabe, T. Taniguchi, P. Kim, K. L. Shepard, and J. Hone, Nat. Nanotechnol. **5**, 722 (2010).
[29] L. Ickert, Krist. Und Tech. **8**, K14 (1973).
[30] M. Ohring, in *Mater. Sci. Thin Film.*, edited by M. Ohring, 1st ed. (Academic Press, San Diego, 1992), pp. 307–354.

[31] M. Ohring, in *Mater. Sci. Thin Film.*, edited by M. Ohring, 1st ed. (Academic Press, San Diego, 1992), pp. 195–248.
[32] J. Ding, A. Gupta, J. Kafka, J. Lee, A. Radomski, E. Saarmaa, E. Snyder, P. Sullivan, R. Swain, E. Taranto, and R. Zadoyan, *MKS Instruments Handbook: Semiconductor Devices and Process Technology* (MKS Instruments, Inc., 2017).
[33] J.-O. Carlsson and P. M. Martin, in *Handb. Depos. Technol. Film. Coatings*, edited by P. M. Martin, 3rd ed. (Willam Andrew, Oxford, 2010), pp. 314–363.
[34] S. O. Kasap and P. Capper, in *Springer Handb. Electron. Photonic Mater.*, edited by S. O. Kasap, P. Capper, and C. Koughia, 1st ed. (Springer Science+Business Media, Inc., New York, 2006), pp. 280–289.
[35] A. C. Jones and M. L. Hitchman, in *R. Soc. Chem.* (2009), pp. 1–36.
[36] M. Imam, C. Höglund, J. Jensen, L. Hultman, J. Birch, H. Pedersen, K. Gaul, A. Stegmüller, and R. Tonner, J. Mater. Chem. C **3**, 10898 (2015).
[37] C. Gomez-Aleixandre, A. Essafti, M. Fernandez, J. L. G. Fierro, and J. M. Albella, J. Phys. Chem. **100**, 2148 (1996).
[38] A. Ismach, ACS Nano **6**, 6378 (2012).
[39] M. J. Rand and J. F. Roberts, J. Electrochem. Soc. **115**, 423 (1968).
[40] S. Sonde, A. Dolocan, N. Lu, C. Corbet, M. J. Kim, E. Tutuc, S. K. Banerjee, and L. Colombo, 2D Mater. **4**, 25052 (2017).
[41] K. Nakamura, J. Electrochem. Soc. **133**, 1120 (1986).
[42] Y. Jin, S. Lee, Y. Nam, J. K. Lee, and D. Park, Korean J. Chem. Eng. **15**, 652 (1998).
[43] Q. S. Paduano, M. Snure, J. Bondy, and T. W. C. Zens, Appl. Phys. Express **7**, 1 (2014).
[44] Y. Kobayashi, T. Nakamura, T. Akasaka, T. Makimoto, and N. Matsumoto, J. Cryst. Growth **298**, 325 (2007).
[45] Y. Kobayashi and T. Makimoto, Japanese J. Appl. Physics, Part 1 Regul. Pap. Short Notes Rev. Pap. **45**, 3519 (2006).
[46] A. Nagashima, N. Tejima, Y. Gamou, T. Kawai, and C. Oshima, Phys. Rev. Lett. **75**, 3918 (1995).
[47] J. H. Park, J. C. Park, S. J. Yun, H. Kim, D. H. Luong, S. M. Kim, S. H. Choi, W. Yang, J. Kong, K. K. Kim, and Y. H. Lee, ACS Nano **8**, 8520 (2014).
[48] S. Caneva, R. S. Weatherup, B. C. Bayer, B. Brennan, S. J. Spencer, K. Mingard, A. Cabrero-Vilatela, C. Baehtz, A. J. Pollard, and S. Hofmann, Nano Lett. **15**, 1867 (2015).
[49] Y. Shi, C. Hamsen, X. Jia, K. K. Kim, A. Reina, M. Hofmann, A. L. Hsu, K. Zhang, H. Li, Z. Y. Juang, M. S. Dresselhaus, L. J. Li, and J. Kong, Nano Lett. **10**, 4134 (2010).
[50] H. M. Manasevit, F. M. Erdmann, and W. I. Simpson, J. Electrochem. Soc. **118**, 1864 (1971).
[51] Q. Paduano, M. Snure, D. Weyburne, A. Kiefer, G. Siegel, and J. Hu, J. Cryst. Growth **449**, 148 (2016).
[52] Y. Kobayashi and T. Akasaka, J. Cryst. Growth **310**, 5044 (2008).
[53] M. Chubarov, H. Pedersen, H. Högberg, V. Darakchieva, J. Jensen, P. O. Å. Persson, and A. Henry, Phys. Status Solidi - Rapid Res. Lett. **5**, 397 (2011).
[54] M. Chubarov, H. Pedersen, H. Högberg, A. Henry, and Z. Czigány, J. Vac. Sci. Technol. A Vacuum, Surfaces, Film. **33**, 061520 (2015).
[55] A. Essafi, C. Gomez-Aleixandre, and J. Albella, Vacuum **45**, 1029 (1994).
[56] S. P. Murarka, J. Electrochem. Soc. **126**, 1951 (1979).
[57] P. J. Fazen, E. E. Remsen, J. S. Beck, P. J. Carroll, A. R. McGhie, and L. G. Sneddon,

Chem. Mater. **7**, 1942 (1995).
[58] P. R. Kidambi, R. Blume, J. Kling, J. B. Wagner, C. Baehtz, R. S. Weatherup, R. Schloegl, B. C. Bayer, and S. Hofmann, Chem. Mater. **26**, 6380 (2014).
[59] K. K. Kim, A. Hsu, X. Jia, S. M. Kim, Y. Shi, M. Hofmann, D. Nezich, J. F. Rodriguez-Nieva, M. Dresselhaus, T. Palacios, and J. Kong, Nano Lett. **12**, 161 (2012).
[60] M. H. Khan, Z. Huang, F. Xiao, G. Casillas, Z. Chen, P. J. Molino, and H. K. Liu, Sci. Rep. **5**, 7743 (2015).
[61] Y. Uchida, T. Iwaizako, S. Mizuno, M. Tsuji, and H. Ago, Phys. Chem. Chem. Phys. **19**, 8230 (2017).
[62] N. Guo, J. Wei, L. Fan, Y. Jia, D. Liang, H. Zhu, K. Wang, and D. Wu, Nanotechnology **23**, 415605 (2012).
[63] W. Auwärter, H. U. Suter, H. Sachdev, and T. Greber, Chem. Mater. **16**, 343 (2004).
[64] W. Auwärter, M. Muntwiler, T. Greber, and J. Osterwalder, Surf. Sci. **511**, 379 (2002).
[65] A. Gibb, N. Alem, and A. Zettl, Phys. Status Solidi **250**, 2727 (2013).
[66] H. Oh, J. Jo, Y. Tchoe, H. Yoon, H. Hwi Lee, S.-S. Kim, M. Kim, B.-H. Sohn, and G.-C. Yi, NPG Asia Mater. **8**, 1 (2016).
[67] Y. Gao, W. Ren, T. Ma, Z. Liu, Y. Zhang, W. Bin Liu, L. P. Ma, X. Ma, and H. M. Cheng, ACS Nano **7**, 5199 (2013).
[68] A. B. Preobrajenski, A. S. Vinogradov, and N. Mårtensson, Surf. Sci. **582**, 21 (2005).
[69] R. Laskowski, P. Blaha, and K. Schwarz, Phys. Rev. B - Condens. Matter Mater. Phys. **78**, 1 (2008).
[70] C. M. Orofeo, S. Suzuki, H. Kageshima, and H. Hibino, Nano Res. **6**, 335 (2013).
[71] M. H. Khan, H. K. Liu, X. Sun, Y. Yamauchi, Y. Bando, D. Golberg, and Z. Huang, Mater. Today **00**, (2017).
[72] M. Corso, Science (80-.). **303**, 217 (2004).
[73] D. J. Kester, K. S. Ailey, and R. F. Davis, Diam. Relat. Mater. **3**, 332 (1994).
[74] C. Wu, A. M. Soomro, F. Sun, H. Wang, C. Liu, X. Yang, J. Kang, and D. Cai, Phys. Status Solidi Basic Res. **253**, 829 (2016).
[75] S. Majety, J. Li, W. P. Zhao, B. Huang, S. H. Wei, J. Y. Lin, and H. X. Jiang, Appl. Phys. Lett. **102**, (2013).
[76] M. Chubarov, H. Pedersen, H. Högberg, Z. Czigany, and A. Henry, CrystEngComm **16**, 5430 (2014).
[77] M. Chubarov, H. Pedersen, H. Högberg, J. Jensen, and A. Henry, Cryst. Growth Des. **12**, 3215 (2012).
[78] A. R. Jang, S. Hong, C. Hyun, S. I. Yoon, G. Kim, H. Y. Jeong, T. J. Shin, S. O. Park, K. Wong, S. K. Kwak, N. Park, K. Yu, E. Choi, A. Mishchenko, F. Withers, K. S. Novoselov, H. Lim, and H. S. Shin, Nano Lett. **16**, 3360 (2016).
[79] A. W. Moore, J. Cryst. Growth **106**, 6 (1990).
[80] D. Belforti, B. Bovarnick, and S. Blum, Nature **190**, 901 (1961).
[81] W. J. Zhang, Y. M. Chong, I. Bello, and S. T. Lee, J. Phys. D. Appl. Phys. **40**, 6159 (2007).
[82] R. T. Paine and C. K. Narula, Chem. Rev. **90**, 73 (1990).
[83] V. L. Solozhenko, V. Z. Turkevich, and W. B. Holzapfel, J. Phys. Chem. B **103**, 2903 (1999).
[84] A. Pakdel, X. Wang, Y. Bando, and D. Golberg, Acta Mater. **61**, 1266 (2013).
[85] M. De Graef and M. E. McHenry, in *Struct. Mater. An Introd. to Crystallogr. Diffraction,*

Symmetry (Cambridge University Press, Cambridge, 2007), pp. 163–197.
[86] L. Bourgeois, Y. Bando, and T. Sato, J. Phys. D. Appl. Phys. **33**, 1902 (2000).
[87] M. Chubarov, H. Pedersen, H. Högberg, V. Darakchieva, J. Jens, P. Persson, and A. Henry, Phys. Status Solidi RRL **5**, 397 (2011).
[88] J. Thomas, Jr., N. E. Weston, and T. E. O'Connor, Phys. Inorg. Chem. **84**, 4619 (1963).
[89] S. Alkoy, C. Toy, T. Gönül, and A. Tekin, J. Eur. Ceram. Soc. **17**, 1415 (1997).
[90] H. Yamada, S. Inotsume, N. Kumagai, T. Yamada, and M. Shimizu, Phys. Status Solidi Basic Res. **257**, 1 (2020).
[91] F. R. Corrigan and F. P. Bundy, J. Chem. Phys. **63**, 3812 (1975).
[92] V. L. Solozhenko, High Press. Res. **13**, 199 (1995).
[93] V. L. Solozhenko and K. S. Gavrichev, in *Wide Band Gap Electron. Mater.*, edited by M. Prelas, P. Gielisse, G. Popovici, B. Spitsyn, and T. Stacy, 1st ed. (Kluwer Academic Publishers, Minsk, Belarus, 1995), pp. 377–392.
[94] R. Ahmed, Fazal-e-Aleem, S. J. Hashemifar, and H. Akbarzadeh, Phys. B Condens. Matter **400**, 297 (2007).
[95] M. Topsakal, E. Aktürk, and S. Ciraci, Phys. Rev. B - Condens. Matter Mater. Phys. **79**, 1 (2009).
[96] T. E. Mosuang and J. E. Lowther, J. Phys. Chem. Solids **63**, 363 (2002).
[97] K. Albe, Phys. Rev. B - Condens. Matter Mater. Phys. **55**, 6203 (1997).
[98] G. Kern, G. Kresse, and J. Hafner, Phys. Rev. B - Condens. Matter Mater. Phys. **59**, 8551 (1999).
[99] W. J. Yu, W. M. Lau, S. P. Chan, Z. F. Liu, and Q. Q. Zheng, Phys. Rev. B - Condens. Matter Mater. Phys. **67**, 1 (2003).
[100] M. Halo, C. Pisani, L. Maschio, S. Casassa, M. Schütz, and D. Usvyat, Phys. Rev. B - Condens. Matter Mater. Phys. **83**, 1 (2011).
[101] C. Barrett, W. Nix, and A. Tetelman, in *Princ. Eng. Mater.*, edited by C. Barrett, W. Nix, and A. Tetelman, 1st ed. (Prentice-Hall, Inc., Englewood Cliffs, New Jersey, 1973), pp. 144–192.
[102] T. Young, Philisophical Trans. R. Soc. London **95**, 65 (1805).
[103] S. Shanfield, J. Vac. Sci. Technol. A Vacuum, Surfaces, Film. **1**, 323 (1983).
[104] R. F. Davis, D. J. Kester, and K. S. Ailey, MRS Proc. **363**, 139 (1994).
[105] M. Keunecke, K. Yamamoto, and K. Bewilogua, Thin Solid Films **398–399**, 142 (2001).
[106] W. Zhang, I. Bello, Y. Lifshitz, K. M. Chan, X. Meng, Y. Wu, C. Y. Chan, and S. T. Lee, Adv. Mater. **16**, 1405 (2004).
[107] F. Hejda, P. Solaˇ, and J. Kousal, WDS'10 Proc. Contrib. Pap. 25 (2010).
[108] A. Spiesser, Y. M. Chong, K. M. Leung, G. Abel, G. G. Ross, M. J. Walzak, R. Jacklin, W. M. Lau, W. J. Zhang, and I. Bello, J. Phys. Chem. C **111**, 12768 (2007).
[109] K. Teii and S. Matsumoto, ACS Appl. Mater. Interfaces **4**, 5249 (2012).
[110] A. Bartl, S. Bohr, R. Haubner, and B. Lux, Int. J. Refract. Met. Hard Mater. **14**, 145 (1996).
[111] M. Annamalai, K. Gopinadhan, S. A. Han, S. Saha, H. J. Park, E. B. Cho, B. Kumar, A. Patra, S. W. Kim, and T. Venkatesan, Nanoscale **8**, 5764 (2016).
[112] W. J. Zhang, S. Matsumoto, Q. Li, I. Bello, and S. T. Lee, Adv. Funct. Mater. **12**, 250 (2002).
[113] S. Matsumoto and W. J. Zhang, Diam. Relat. Mater. **10**, 1868 (2001).
[114] S. Matsumoto and W. Zhang, Japanese J. Appl. Physics, Part 2 Lett. **39**, (2000).

[115] W. J. Zhang, C. Y. Chan, K. M. Chan, I. Bello, Y. Lifshitz, and S. T. Lee, Appl. Phys. A Mater. Sci. Process. **76**, 953 (2003).
[116] W. Dworschak, K. Jung, and H. Ehrhardt, Diam. Relat. Mater. **3**, 337 (1994).
[117] S.-Y. Choi, S. I. Lee, T. K. Kim, S. W. Cho, H. S. Jang, and H. Park, Sci. Rep. **7**, 1 (2017).
[118] T. Sugino, K. Tanioka, S. Kawasaki, and J. Shirafuji, Japanese J. Appl. Physics, Part 2 Lett. **36**, (1997).
[119] J. Kouvetakis, V. V. Patel, C. W. Miller, and D. B. Beach, J. Vac. Sci. Technol. A Vacuum, Surfaces, Film. **8**, 3929 (2002).
[120] S. Bohr, R. Haubner, and B. Lux, Diam. Relat. Mater. **4**, 714 (1995).
[121] S. Hirano, A. Fujii, T. Yogo, and S. Naka, J. Am. Ceram. Soc. **73**, 2238 (1988).
[122] V. L. Solozhenko and V. Z. Turkevich, Diam. Relat. Mater. **7**, 43 (1998).
[123] V. L. Solozhenko, Phys. Chem. Chem. Phys. **4**, 1033 (2002).
[124] O. O. Kurakevych and V. L. Solozhenko, Molecules **21**, 1 (2016).
[125] C. Schimpf, M. R. Schwarz, C. Lathe, E. Kroke, and D. Rafaja, J. Eur. Ceram. Soc. **39**, 944 (2019).
[126] A. V. Kurdyumov, V. F. Britun, and I. A. Petrusha, Diam. Relat. Mater. **5**, 1229 (1996).
[127] J. Y. Huang and Y. T. Zhu, Chem. Mater. **14**, 1873 (2002).
[128] F. P. Bundy and R. H. Wentorf, J. Chem. Phys. **38**, 1144 (1963).
[129] C. Schimpf, M. Motylenko, and D. Rafaja, Mater. Charact. **8**, 190 (2013).
[130] M. Eremets, K. Takemura, H. Yusa, D. Golberg, Y. Bando, and V. Blank, Phys. Rev. B - Condens. Matter Mater. Phys. **57**, 5655 (1998).
[131] C. Schimpf, M. Schwarz, C. Lathe, E. Kroke, and D. Rafaja, Powder Diffr. **30**, S90 (2015).
[132] M. Avrami, J. Chem. Phys. **8**, 212 (1940).
[133] K. E. Spear, Pure Appl. Chem. **54**, (1982).
[134] A. I. Kingon, L. J. Lutz, P. Liaw, and R. F. Davis, J. Am. Ceram. Soc. **66**, 558 (1983).
[135] C. W. Bale, E. Bélisle, P. Chartrand, S. A. Decterov, G. Eriksson, A. E. Gheribi, K. Hack, I. H. Jung, Y. B. Kang, J. Melançon, A. D. Pelton, S. Petersen, C. Robelin, J. Sangster, P. Spencer, and M. A. Van Ende, Calphad Comput. Coupling Phase Diagrams Thermochem. **54**, 35 (2016).
[136] U. R. Kattner, Tecnol. Em Metal. Mater. e Mineração **13**, 3 (2016).
[137] M. De Graef and M. E. McHenry, in *Struct. Mater. An Introd. to Crystallogr. Diffraction, Symmetry*, 1st ed. (Cambridge University Press, Cambridge, 2007), pp. 258–293.
[138] M. F. Toney, in *Encycl. Mater. Charact.*, edited by C. R. Brundle, C. Evans, Jr., and S. Wilson, 1st ed. (Manning Publications Co., Greenwich, Connecticut, 1992), pp. 198–213.
[139] R. S. Pease, Acta Crystallogr. **5**, 356 (1952).
[140] M. A. Moram and M. E. Vickers, Reports Prog. Phys. **72**, 1 (2009).
[141] A. V. Kurdyumov, Sov. Physics, Crystallogr. **20**, (1975).
[142] C. R. Brundle, in *Encycl. Mater. Charact.*, edited by C. R. Brundle, C. Evans, Jr., and S. Wilson, 1st ed. (Manning Publications Co.X-ra, Greenwich, Connecticut, 1992), pp. 282–299.
[143] R. Trehan, Y. Lifshitz, and J. W. Rabalais, J. Vac. Sci. Technol. A Vacuum, Surfaces, Film. **8**, 4026 (1990).
[144] Y. Panayiotatos, S. Logothetidis, M. Handrea, and W. Kautek, Diam. Relat. Mater. **12**, 1151 (2003).

[145] D. H. Berns and M. A. Cappelli, Appl. Phys. Lett. **2711**, 2711 (1995).
[146] R. N. Yasko and R. D. Whitmoyer, J. Vac. Sci. Technol. **8**, 733 (1971).
[147] J. Bindell, in *Encycl. Mater. Charact.*, edited by C. R. Brundle, C. Evans, Jr., and S. Wilson, 1st ed. (Manning Publications Co., Greenwich, Connecticut, 1992), pp. 70–84.
[148] K. E. Sickafus, in *Encycl. Mater. Charact.*, edited by C. R. Brundle, C. A. Evans, Jr, and S. Wilson (Manning Publications Co., Greenwich, Connecticut, 1992), pp. 99–115.
[149] R. S. Howland and M. D. Kirk, in *Encycl. Mater. Charact.*, edited by C. R. Brundle, C. A. Evans, Jr., and S. Wilson (Manning Publications Co., Greenwich, Connecticut, 1992), pp. 85–98.
[150] X. Li, S. Sundaram, Y. El Gmili, T. Ayari, R. Puybaret, G. Patriarche, P. L. Voss, J. P. Salvestrini, and A. Ougazzaden, Cryst. Growth Des. **16**, 3409 (2016).
[151] H. Yamada, S. Inotsume, N. Kumagai, T. Yamada, and M. Shimizu, Phys. Status Solidi Basic Res. **257**, 1 (2020).
[152] Wi. B. White, in *Encycl. Mater. Charact.*, edited by C. R. Brundle, C. Evans, Jr., and S. Wilson, First (Greenwich, Connecticut, 1992), pp. 428–441.
[153] R. Geick, C. Perry, and G. Rupprecht, Phys. Rev. **146**, 543 (1966).
[154] L. Schué, I. Stenger, F. Fossard, A. Loiseau, and J. Barjon, 2D Mater. **4**, 1 (2017).

3. Experimental Procedures

3.1 Substrate preparation

Substrates used for the CVD growth of BN thin films in this research are (0001) 4H-SiC (Cree, Inc.) and highly oriented (0001) pyrolytic boron nitride (PBN) (Morgan Technical Ceramics). The (0001) 4H-SiC substrates were received chemo-mechanically polished on both the (0001)Si and $(000\bar{1})$C faces. BN films were grown on the (0001)Si face. Preparation of the (0001) surface of the 4H-SiC substrates for deposition involved (1) sequential cleaning via sonication in acetone and isopropanol for 10 minutes in each solvent followed by (2) immersion in a 1:10 HF:DI water solution for 10 minutes to remove the native oxide. The as-received PBN substrates have very rough surfaces with an ~ 65 nm RMS roughness over a 2 μm × 2 μm area. Thus, a polishing procedure was developed to prepare surfaces suitable for thin film growth. Precise, semiautomatic polishing of PBN was performed using a Multiprep Polishing System (Allied High Tech Products, Inc.) The sequence of steps typically used to polish the PBN substrates in this research are summarized in Table 3.1.1.

Table 3.1.1. Pyrolytic boron nitride polishing procedure sequence.

Polishing Media/Lubricant	Platen Rotation and Direction	Sample Rotation (RPM)	Target Removal or Duration
6 μm DLF/water	150 RPM, CW	1 RPM, CCW	~ 200 μm
3 μm DLF/water	150 RPM, CW	1 RPM, CCW	~ 100 μm
1 μm DLF/RedLube	150 RPM, CW	1 RPM, CCW	~ 100 μm
Final P Cloth/ 0.04 μm Colloidal Silica	150 RPM, CW	1 RPM, CCW	30 seconds

DLF: diamond lapping film
CW: clockwise
CCW: counter-clockwise
RPM: revolutions per minute

Between each polishing step described in Table 3.1.1, the sample surface and platen were cleaned with micro-organic soap to prevent debris from each previous step from contaminating the sample or subsequent polishing media, thereby reducing the amount of scratches caused by polishing. If contamination-induced scratches developed on the sample surface at any step, then the sample was polished for a few minutes using the diamond lapping film with the grit size of the previous step in order to remove the scratches. The employed polishing procedure produced surface finishes with 2.8 nm RMS roughness over a 2.5 μm × 2.5 μm area. Subjecting the as-polished PBN substrates to a three-hour anneal in 2 slm H_2 atmosphere at ~ 1060 °C and a total chamber pressure of 10 Torr resulted in a further reduction of surface roughness to 1.21 nm over a 2.5 μm × 2.5 μm area. Figure 3.1.1 shows the scanning electron microscopy (SEM) and atomic force microscopy (AFM) images of the as-received PBN surface ((a) and (c)) and the polished surface annealed in H_2 for 3 hours ((b) and (d)).

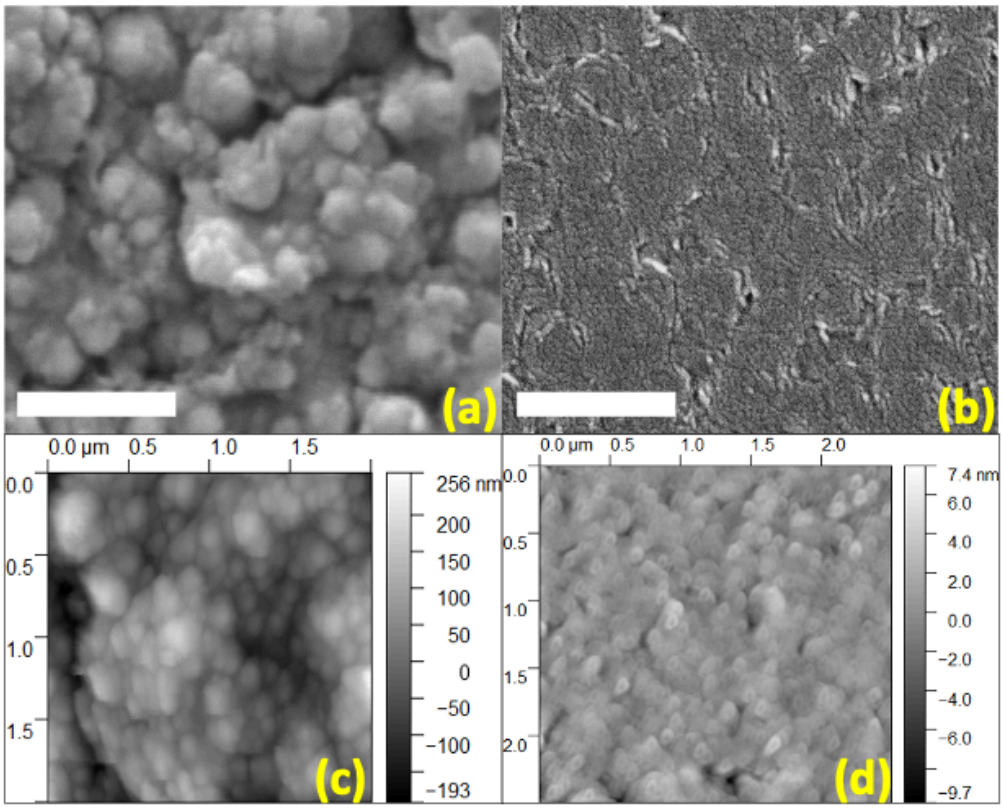

Figure 3.1.1. SEM images of (a) as-received and (b) polished PBN. Scale bars are 500 nm. Panels (c) and (d) show AFM images of the as-received and polished HOPBN scanned over a 2 µm × 2 µm and 2.5 µm × 2.5 µm area, respectively.

3.2. Chemical vapor deposition

BN thin films were grown on chemo-mechanically polished (0001) 4H-SiC substrates and highly oriented (0001) PBN substrates in a cold-wall, vertical shower-head reactor powered by the resistive heating of a graphitic filament. Diborane (5N-semiconductor grade 10% B_2H_6 in H_2) and ammonia (NH_3) were the B- and N-source precursors used in this work, respectively. The substrates were prepared using the procedures described in Section 4.1. Prepared substrates were loaded onto a planar SiC-coated graphite susceptor and placed inside the CVD chamber that was subsequently evacuated to less than 20 mTorr. Because B_2H_6 reacts readily with

moisture in the air to form a boron-containing oxide, it was necessary to rid the chamber walls and substrate surface of any residual moisture prior to growth. Thus, with the substrates loaded, the chamber was heated 15 minutes at 1000 ^{o}C in an atmosphere of 4 slm H_2 at a total pressure of 20 Torr. At the end of this cleaning step, the chamber was evacuated to a base pressure of at least 2.0×10^{-6} Torr using a turbomolecular pump. A growth run was then initiated by closing the valve to the turbomolecular pump and using a rotary vane pump to maintain a total chamber pressure of 10 Torr. In each growth, B_2H_6 was flowed either at 2, 5, or 20 sccm while the flow rate of NH_3 was kept constant at 0.80 slm. H_2 was used as the diluent gas for all growths at a flow rate of 2 slm. During each growth, the substrate temperature was maintained at 1030 ^{o}C, as estimated using an optical pyrometer (Fluke).

3.3 Characterization and analysis methods

3.3.1 Thin film thickness measurements

The thickness of the thin films deposited on the 4H-SiC substrates was estimated using spectral reflectance (Filmetrics F50). The wavelength range of the F50 unit is 380 – 1050 nm. When employing this method for thin film thickness determination, the system was calibrated using a Si wafer as the reflectance standard and a SiO_2/Si wafer of known thickness as the thickness standard. The index of refraction data of h-BN and 4H-SiC used to simulate reflectance as a function of wavelength (and compared against the measured reflectance curves to estimate the thickness of each sample) were taken from [1] and [2], respectively. Because of the lack of change in the index of refraction between BN thin films and the PBN substrate, as well as the opacity of the PBN substrate, it was difficult to estimate the thickness BN/PBN thin films using spectral reflectance. The thickness of these thin films was directly measured from images obtained from cross-sectional transmission electron microscopy.

3.3.2 Raman Spectroscopy

Raman spectra (NT-MDT Spectra) of the BN thin films were measured using a 532 nm green laser and a 600 lines/mm grating. Before each measurement, the instrument was calibrated with a polystyrene standard (1001.4 cm^{-1}) as well as with a PBN standard (E_{2g}: 1366 cm^{-1}).

3.3.3 X-ray photoelectron spectroscopy (XPS)

XPS measurements of grown films were captured using a cylindrical mirror analyzer (DESA 100 Energy Analyzer developed by Staib, Gmb). An Al Kα (1486.6 eV) anode was used as the x-ray emission source. In order to prepare clean thin film surfaces prior to XPS analysis, each sample was (1) sonicated in acetone for 10 minutes, sonicated in isopropanol for 10 minutes, dried with dry N_2 and (2) subjected to a 60 minute anneal in a 10^{-8}-10^{-7} Torr vacuum at ~1100 ^oC via electron beam heating to facilitate thermal desorption of contaminating species. Analyses of the recorded spectra included a charge correction for adventitious sp^2 and sp^3 carbon at the 284.6 eV C 1s peak [3]. Spectra were quantified to obtain the elemental surface composition using CasaXPS software in which a Shirley background was applied to elemental shifts of interest (typically B 1s, N 1s, O 1s, C 1s, Si 2s, and Si 2p). To obtain information about the bonding environment of relevant peaks from spectra, the subcomponents of the B 1s and N 1s spectra were modeled with mixed Gaussian (80%) – Lorentzian (20 %) distributions and a non-linear background using curve-fitting software (Fityk).

3.3.4 Atomic Force Microscopy (AFM)

All AFM (NT-MDT NTegra) micrographs were collected in semi-contact mode with Si cantilevers in the range of 50 – 200 kHz. A scan rate of 1 Hz was typically used, and 256 samples per line were sampled for 256 lines. All post-processing, including plane fit, surface

flattening, and de-streaking were performed using Gwyddion, which was also used to calculate RMS surface roughness of the processed images.

3.3.5 Scanning electron microscopy (SEM)

SEM (FEI XL30 and FEI Quanta 600) images of the BN thin film sample surfaces were recorded between 5 and 30 kV depending on the extent of surface charging. BN thin films grown on 4H-SiC could be imaged without a prior deposition of a metal thin film to make the surface more conductive. BN thin films grown on PBN required a sputter deposition of either 2 nm Pt or Au to mitigate surface charging.

3.3.6 Transmission electron microscopy (TEM)

TEM (FEI Themis 200) images were recorded at 200 kV to characterize the morphology of the layers of the grown BN films and that of the substrate-film interface. Electron-transparent cross-sectional lamellae of the thin films were prepared using both Ga ion (FEI Nova Nanolab 600 Dual Beam) and Xe plasma source (FEI Plasma Dual Beam) focused ion-beam (FIB) milling. For the BN thin films grown on polished PBN, the samples were first coated with ~ 5 nm Au to prevent surface charging during FIB imaging and milling. Both BN/SiC and BN/PBN lamellae were attached (with Pt) to Cu Omniprobe TEM grids, and these grids were then loaded on to double-tilt TEM specimen holders. Before loading TEM specimens into the Themis instrument for analysis, they were first subject to Ar plasma cleaning for five minutes to remove contamination.

During FIB milling of the BN/SiC samples in particular, cross sections were cut along the $[1\bar{1}00]$ direction of the 4H-SiC substrate. Thus, during TEM operation, the α and β angles of the specimen were minimally tilted (typically less than 6^{o} for both) to observe the $[1\bar{1}00]$ zone axis of the 4H-SiC substrate in diffraction mode. The Themis instrument was always operated at 200

kV, and diffraction patterns were acquired at a camera length of 41 cm. High resolution TEM (HRTEM) images were collected along the $[1\bar{1}00]$ zone axis of the 4H-SiC substrate. Because the PBN material is polycrystalline with few nm-sized crystallites, it was not possible to prepare cross-sectional FIB lamellae along any particular zone axis. Regardless of the α and β tilt angles, the diffraction pattern of the BN/PBN samples always consisted of concentric rings, indicative of the polycrystalline substrate.

Acquisition of HRTEM cross-sectional images of both BN/SiC and BN/PBN samples allowed determination of the interplanar spacings of film lattice planes during post analysis. Given the scale bar in each acquired image, the imaging software ImageJ was used to make measurements of the lattice features present in sample images. Using 0.33 nm as the principal monolayer lattice spacing for crystalline sp^2-BN [4], measurements larger than this value for the interplanar spacing indicated the presence of the t-BN phase.

3. References

[1] E. Franke, M. Schubert, J. D. Hecht, H. Neumann, T. E. Tiwald, D. W. Thompson, H. Yao, J. A. Woollam, and J. Hahn, J. Appl. Phys. **84**, 526 (1998). DOI:10.1063/1.368083.
[2] P. T. B. Shaffer and R. G. Naum, J. Opt. Soc. Am. **59**, 1498 (1969). DOI:10.1364/JOSA.59.001498.
[3] C. Guimon, D. Gonbeau, G. Pfister-Guillouzo, O. Dugne, A. Guette, R. Naslain, and M. Lahaye, Surf. Interface Anal. **16**, 440 (1990). DOI:10.1002/sia.740160191.
[4] R. S. Pease. Acta Cryst. **5,** 356 (1952). DOI: 10.1107/S0365110X52001064

4. Paper 1: On the Discrepancies Between the Experimental Realization and the Thermodynamic Predictions of Stability of Rhombohedral Boron Nitride

Authors: Philip M. Jean-Remy[a] and Robert F. Davis[a, b]

[a] Department of Materials Science and Engineering, Carnegie Mellon University, Pittsburgh, PA, 15213, USA

[b] Department of Electrical and Computer Engineering, Carnegie Mellon University, Pittsburgh, PA, 15213, USA

Corresponding author: Philip M. Jean-Remy, 5700 Ellsworth Avenue, Apartment A3, Pittsburgh, PA, 15232, USA Email: pjeanrem@andrew.cmu.edu

4.1 Abstract

Equilibrium thermodynamic calculations were performed to generate diagrams indicating the phase fields wherein either hexagonal or rhombohedral films of boron nitride can be deposited via chemical vapor deposition as a function of temperature, choice of B source and N/B ratio derived from NH_3 and the B-source. Similar diagrams calculated using experimental conditions employed by groups who have synthesized r-BN films revealed that both in experiment and equilibrium, the choice of B-source strongly affects the size of the single-phase field for r-BN and, in general, deposition of r-BN can be realized at temperatures more than 100°C below that predicted by equilibria.

4.2. Introduction

Boron nitride (BN) forms in the sp^2-bonded two-dimensional structures of hexagonal (h)-BN [1–3] and rhombohedral (r)-BN [4–6], as well as the sp^3-bonded three-dimensional structures of cubic (c)-BN [1,7,8] and wurtzitic (w)-BN [9]. BN also commonly occurs within the two-dimensional structures as turbostratic (t)-BN, another layered but much less ordered sp^2-hybridized nonequilibrium phase that retains a high degree of in-plane order of BN hexagonal rings. The layers in t-BN are nonparallel as well as randomly rotated and translated with respect to the c-axis of the primary h-BN layer [10,11].

The debate over the most stable BN polymorph at ambient conditions has long endured. By analogy with the apparent equilibrium stability of graphitic carbon relative to that of diamond [12], h-BN was considered the most stable polymorph of BN, as indicated by the results of the high-pressure and high-temperature induced direct phase transformations reported by Bundy and Wentorf [1]. However, Solozhenko and Gavrichev [8,13] subsequently determined via adiabatic calorimetry the heat of formation and the temperature-dependent equations of heat capacity, enthalpy and entropy of samples of the four main BN polytypes. They concluded that c-BN was the most thermodynamically stable phase at ambient conditions to a temperature of approximately 1600 K, their proposed transition temperature to h-BN [8]. To the present authors' knowledge, however, thin films of c-BN have not been synthesized via methods such as chemical vapor deposition (CVD) without either the introduction of a fluorine-containing compound commonly in tandem with the use of high energy plasmas or direct ion bombardment to significantly increase the residual stress in the growing film, which mimics the effect of an increase in pressure. Moreover, the as-deposited c-BN films are commonly reported to be

nanocrystalline, delaminated and to contain co-deposited sp^2-BN [14–17]. To the authors' knowledge, w-BN thin films have never been synthesized by CVD.

Hexagonal-BN is the most commonly deposited sp^2 BN polymorph via CVD [18–21]. However, Oku et al. [6], Chubarov et al. [22] and Souqui et al. [23] have reported the deposition of r-BN using a variety of substrates, B precursors and deposition temperatures. Further, the results of van der Waals-corrected density functional theory by Pedersen et al. [24] indicate that r-BN is the most stable polymorph at typical CVD conditions for BN deposition within the ranges of ~1100 – 1500 °C and 1 – 10 kPa, which suggests that h-BN is a metastable CVD phase at elevated temperatures. It has also been shown that, due to a large degree of structural similarity (h-BN and r-BN differ only by their ABAB… and ABCABC crystallographic stacking orders, respectively), it is difficult to distinguish the two polymorphs without utilizing advanced x-ray diffraction (XRD) techniques such as grazing-incidence XRD and pole figure measurements, as well as high resolution transmission electron microscopy [25,26].

The purpose of this Letter is to (a) report the results and conclusions of the authors' calculations of equilibrium phase diagrams for r-BN based on experimental thermodynamic data for this phase acquired by Solozhenko [8] and (b) compare these results with experimental results of the synthesis of r-BN via CVD. Further, it will be shown that (c) the choice of the B-source for the CVD of BN has a significant influence on the deposition of single-phase of r-BN, and (d) in general, r-BN is achieved experimentally at temperatures more than 100 °C below those predicted from the phase diagrams.

4.3 Methods

The $C_p(T)$, S^o, and ΔH_f^o values of h-BN and r-BN, referenced from Solozhenko [8], were imported as a customized database into FactSage (Version 8.0, CRCT – Thermfact, Inc. and GTT Technologies) [27], a computational software package that makes thermodynamic equilibrium calculations based on the minimization of Gibbs free energy and mass conservation. Tables showing the standard-state thermodynamic properties of h-BN and r-BN are submitted as Supplementary Materials. The Supplement also contains a description of the method of determining the Gibbs free energy curves for h-BN and r-BN based on this data in the form of Gibbs free energy ($G(T)$) relative to the enthalpy (H) of the standard element reference (SER) (i.e., $G(T)$–HSER). The $G(T)$–HSER curves for h-BN and r-BN derived from the thermodynamic data used in this work are shown in Figure 4.3.1. It should be noted that the values of the free energy curves for h-BN and r-BN are extremely close and that the difference between them decreases substantially with increasing temperature, from roughly 1.2 kJ/mol at 400 °C to less than 0.2 kJ/mol at 1600 °C.

Three separate B-sources (triethylboron ($B(C_2H_5)_3$, TEB), trimethylboron ($B(CH_3)_3$, TMB), and boron trichloride (BCl_3)), mixed with NH_3 and H_2 as the N-source and chamber diluent, respectively, were used in the calculations of the phase diagrams. Except for h-BN and r-BN, the thermodynamic data for all reactants and products of interest and significance were contained within the FactPS database [27], native to the FactSage software package. The gaseous species considered across the three reactant gas-mixture systems were H_2, CH_3, CH_4, C_2H_2, C_2H_4, C_2H_6, HCN, N_2, NH, NH_2, BH_2, BH_3, B_2H_6, B_4H_{10}, HCl, and Cl_2. En route to the evolution of BH_3 from TEB and TMB, experimental and quantum mechanical investigations indicate that the intermediate species of $BH(C_2H_5)_2$ and $BH_2(C_2H_5)$ from TEB [28], and

$BH(CH_3)_2$ and BH_2CH_3 from TMB [29] are active gas phase species that lead to the deposition of B_xC films. The thermodynamic data for these species have not been reported. The condensed species considered were h-BN (s), r-BN (s), C (s) (graphite), B (s) (rhombohedral), and NH_4Cl (s). The introduction of SiH_4 (g) for some $TMB/NH_3/H_2$ calculations allowed for the consideration and prediction of the co-deposition of the solid phases of Si, Si_3N_4 and β-SiC.

The variables of the system included the composition of the input reactant gases in the form of N/B (mol/mol) ratios and temperature as the x- and y-axes of the plots, respectively, the $H_2/(B + N)$ (mol/mol) ratios and the pressure. The last two parameters were fixed for the calculation of each phase diagram. The sum of the amount of B-containing reactant (B*X*), NH_3, and H_2 was set to 1 mole for each calculation. The mole amounts of B*X* and NH_3 decrease and increase, respectively, with an increase in the N/B ratio to maintain both the constant $H_2/(B + N)$ ratio and the $BX + NH_3 + H_2 = 1$ mole conditions.

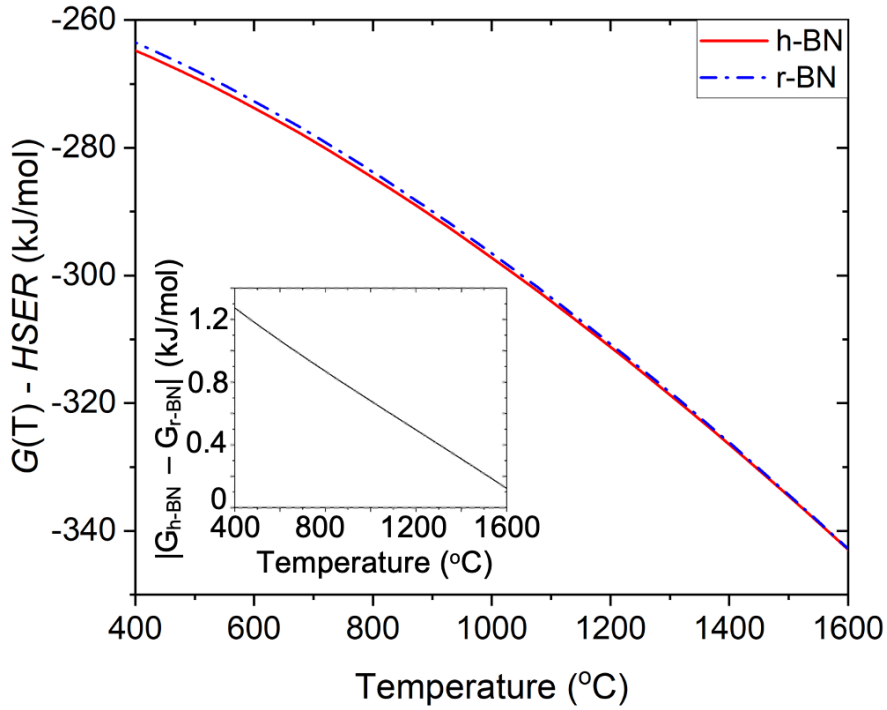

Figure 4.3.1. *G*(T) – HSER curves calculated at atmospheric pressure for h-BN and r-BN in this work. The inset plot shows the absolute difference of the Gibbs free energies of h-BN and r-BN as function of temperature.

4.4 Results and discussion

Figures 4.4.1(a) – (c) show representative phase diagrams calculated for the TEB/NH_3/H_2, TMB/NH_3/H_2, and BCl_3/NH_3/H_2 systems, respectively, at a total pressure of 13.3 kPa (~ 100 Torr) and H_2/(B + N) = 10 within the 1400 – 1800 °C range. A comparison of the diagrams shows that the choice of B precursor is predicted to have a significant effect on the range of N/B ratios that can be used to achieve single-phase r-BN and h-BN. The results shown in Fig. 4.4.1 (a) – (c) indicate that using (1) TEB most limits the window for the deposition of single phase r-BN, (2) TMB allows a slightly broader range of N/B ratios for this purpose and (3) BCl_3 allows the broadest range of N/B ratios which extend to below N/B = 10 for the specific

pressure and $H_2/(B + N)$ conditions. The phase diagrams in Figure 4.4.1 also show that the h-BN ↔ r-BN transition line occurs consistently at ~ 1730 °C regardless of the B precursor.

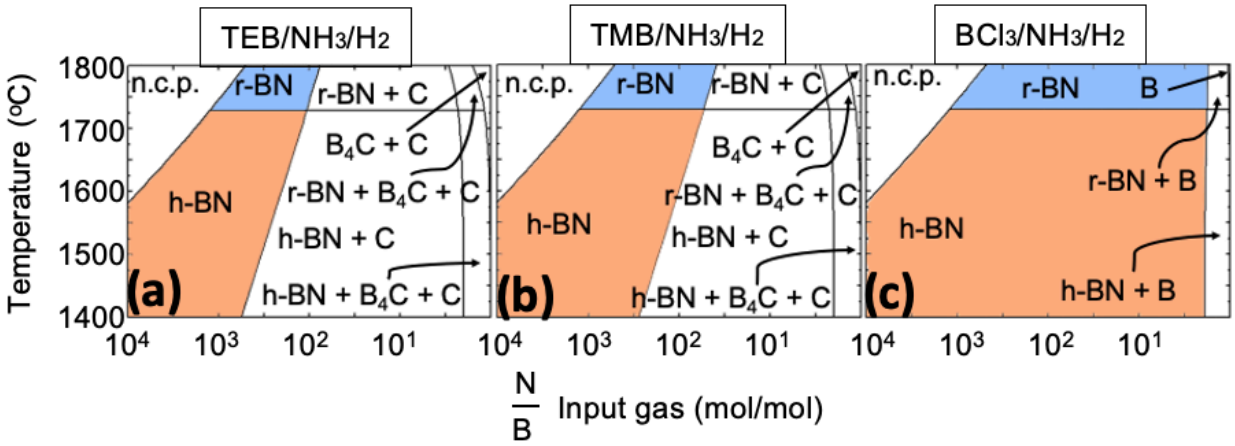

Figure 4.4.1: Phase diagrams of the (a) $TEB/NH_3/H_2$, (b) $TMB/NH_3/H_2$, and (c) $BCl_3/NH_3/H_2$ systems each calculated at a total pressure of 13.3 kPa and a H_2 diluent-reactant ratio of $H_2/(B + N) = 10$. n.c.p. indicates "no condensed phases." The h-BN and r-BN single-phase phase-fields are colored tan and blue, respectively, for visualization.

Figure 4.4.2 shows equilibrium phase diagrams calculated using the growth parameters reported in the papers by Souqui et al. [23] (Fig. 4.4.3(a) and (b)), Chubarov et al. [22] (Figure 4.4.2 (c)), and Oku et al. [6] (Figure 4.4.3(d)). The dots in the diagrams indicate where the (N/B, T) conditions employed by these respective investigators should exist in equilibrium. Again, it is seen that the h-BN ↔ r-BN transition line consistently occurs near ~1730 °C regardless of the boron precursor, $H_2/(B + N)$ ratios and total operating pressure. Experimentally, polytype pure r-BN has been achieved at temperatures well below 1730 °C, as shown in Fig. 4.4.2 (a) – (c). The choice of boron precursor is again shown to have a strong effect on the allowable ranges of N/B ratios for achieving r-BN. As depicted in Fig. 4.4.2 (a) and (b), Souqui et al. [23], using TMB as the B-source precursor, observed epitaxial r-BN on (0001) AlN-coated (0001) α-Al_2O_3 substrates at growth temperatures as low as 1400 °C for a broad range of N/B ratios (~ 300 – 1300) and

different total operating pressures. These investigators also introduced a small amount of silane during CVD-BN growth, which they reported improved the intensity and full-width-half-maximum of the (0003) x-ray diffraction line for r-BN [24]. Although the equilibrium calculations shown in Fig. 4.4.2 (a) and (b) predict the co-deposition of β-SiC with BN, the authors reported that the incorporation of Si into their r-BN films was below the 0.1 atomic percent detection limit of their time-of-flight energy elastic recoil detection instrument. The results shown in Figure 4.4.3(c) reveal that by using TEB as the B-source Chubarov et al. [22] also achieved epitaxial r-BN on (0001) AlN-coated (0001) α-Al_2O_3 substrates at a temperature of 1500 °C but within a much narrower range of N/B ratios (615 – 770) than that employed by Souqui et al. [23]. Detailed experimental and quantum mechanical investigations of the gas phase CVD chemistry of TEB [28] and TMB [29] revealed that the use of these B-containing precursors result in the deposition of B_xC_y:H films at 400 °C and 700 °C, respectively, suggesting that decomposition of TMB occurs more slowly than that of TEB [23]. Thus, since the decomposition kinetics of NH_3 is also slow for the incorporation of free N into growing nitride films [30,31], a broader range of gas phase N/B compositions and lower deposition temperatures were employed by Souqui et al. [23] when using the TMB precursor. Lastly, Oku et al. [6] used graphite substrates, BCl_3 as the B-source and markedly lower N/B ratios (N/B = ~ 0.64) than employed in the two aforementioned studies and achieved t-BN films containing r-BN nano-particles at 1600 °C. Unlike TEB and TMB, the BCl_3 precursor contains no C in its structure, which allows the prediction of much broader single-phase phase-fields for both the sp^2-BN polymorphs, as shown in Figure 4.4.1. However, the use of such low N/B ratios is very uncommon for the growth of III-V nitride thin films.

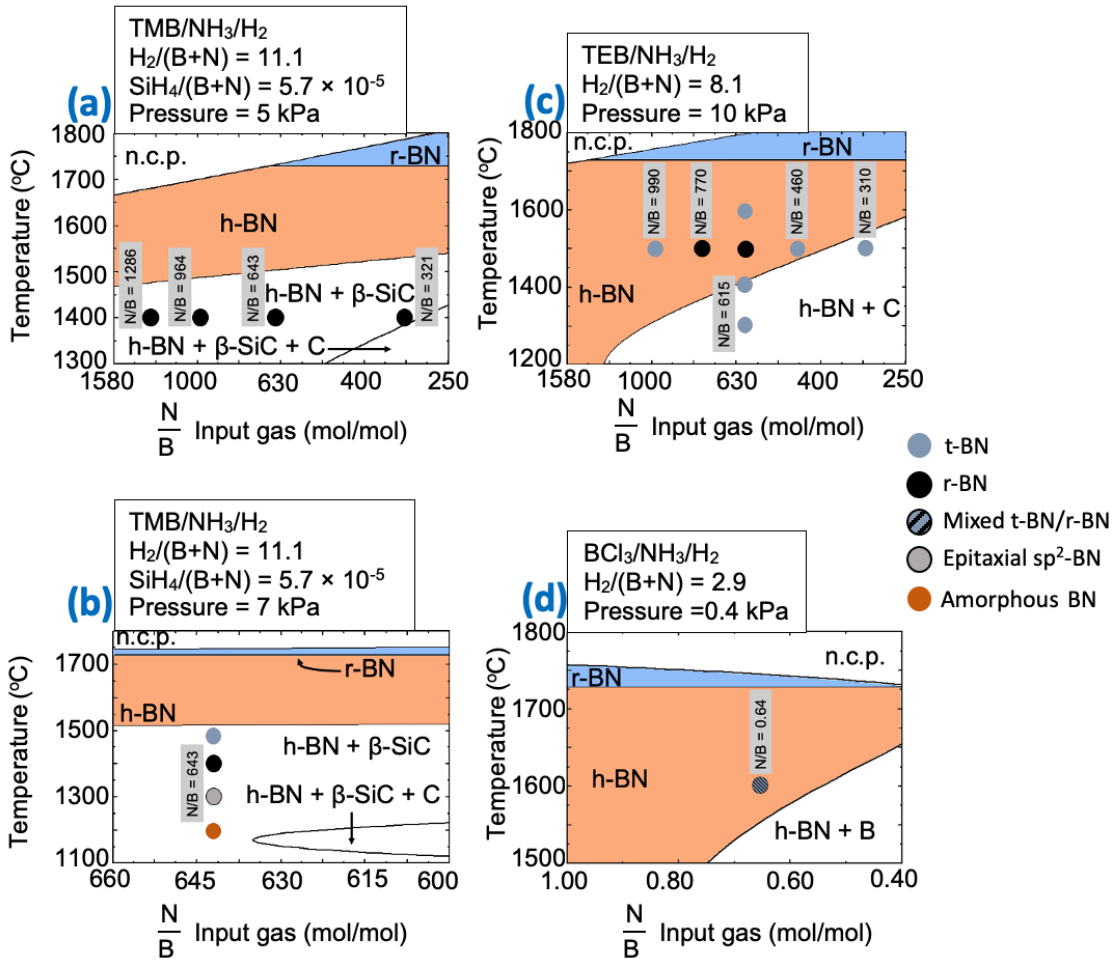

Figure 4.4.2: (a) and (b) $TMB/NH_3/H_2$ phase diagrams with pressure set to 5 kPa and 7 kPa, respectively, and with $H_2/(B+N) = 11.1$ and $SiH_4/(B+N) = 5.7 \times 10^{-5}$ in both cases; (c) $TEB/NH_3/H_2$ phase diagram with pressure set to 10 kPa and $H_2/(B+N) = 8.12$; (d) $BCl_3/NH_3/H_2$ phase diagram with pressure set to 0.4 kPa and $H_2/(B+N) = 2.9$. The dots indicate where the (N/B, T) conditions experimentally employed by Souqui et al. [23] ((a) and (b)), Chubarov et al. [22] (c), and Oku et al. [6] (d) occur in the phase diagram. n.c.p. indicates "no condensed phases." The h-BN and r-BN single-phase phase-fields are colored tan and blue, respectively, for visualization.

Regardless of the deposition conditions and B-containing precursors used by the above mentioned authors, r-BN was realized at temperatures between 100 and 300 °C below that predicted by equilibrium calculations (~ 1730 °C). One reason for this may be the close values of

the thermodynamic properties ($C_p(T)$, S^o, and ΔH_f^o – see Tables S1 and S2 of the Supplementary Materials) of h-BN and r-BN from the referenced data [8] which result in a small difference between their respective Gibbs free energies as depicted in Figure 4.3.1. Despite that, the solid-state transformation of t-BN or h-BN at atmospheric pressure into r-BN has not been achieved without the use of a catalyst or solvent. Ishii et al. [32] observed the growth of r-BN whiskers on the walls of a graphite crucible in N_2 atmosphere at 1500 ^{o} C when h-BN powder inside the crucible was heated between 1700 and 2100 ^{o}C, but no structural transformation was observed of the h-BN itself. Ye et al. [33] synthesized r-BN powder of 94 wt.% phase purity (6 wt.% h-BN) from t-BN powder dissolved in molten $Na_2B_4O_7$ and Mg under N_2 atmosphere at 1000 ^{o}C. Without the use of any BN starting material, Sato [34] found that r-BN powders could be produced from the 24-hours-long reaction between $NaBH_4$ and NH_4Cl at temperatures as low as 900 ^{o}C. It seems as though certain reaction pathways are more conducive toward synthesizing r-BN below the equilibrium temperature, which may be provided by the discussed CVD precursors. Further, a major aspect of CVD growth not accounted for by the equilibrium calculations but which greatly influences the deposition of r-BN is the choice of substrate. In this regard, Chubarov et al. [26], using TEB and NH_3 precursors, showed that at 1500 ^{o}C, 7 kPa, and a N/B ratio of 640, pure r-BN or h-BN could be deposited depending on the crystallographic stacking sequence of the substrate. Deposition on (0001) 6H-SiC resulted in the growth of only the r-BN polytype; growth on (0001) AlN-coated (0001) α-Al_2O_3 occurred as a sequence of ~ 4 nm of h-BN and a transition to r-BN. The observation of the h-BN transition into r-BN was attributed to stress relaxation.

4.5 Summary

Equilibrium thermodynamic data were used to calculate diagrams that indicate the extent of the phase fields wherein films of either h-BN or r-BN can be deposited via CVD as a function of temperature, B-containing precursor and N/B ratio. Both the calculated results and the superposition onto analogous diagrams of reported experimental CVD conditions wherein growth of r-BN films was realized revealed that (1) the choice of B precursor markedly affects the allowable range of the initial gas phase N/B ratio and therefore the extent of the phase fields of both h- and r-BN and (2) the deposition of phase pure r-BN films has been achieved at temperatures well below the predicted h-BN $\longleftrightarrow$ r-BN transition temperature of 1730 ^{o}C. The crystal structure of the substrate surface was also a factor in the growth of either single-phase r-BN or a poly-phase material containing r-BN and t-BN or r-BN and h-BN.

4.6 Acknowledgements

Funding for this work was made possible thanks to the National GEM Consortium Fellowship, the Neil and Jo Bushnell Fellowship in Engineering, and the John and Claire Bertucci Fellowship.

4.7 Keywords

2D materials; chemical vapor deposition; phase equilibria; thermodynamics; thin film

4.8 Data availability statement

All data generated or analyzed during this study are included in this published article and its supplementary information files. The thermodynamic information for all species other than h-BN (s) and r-BN (s) are contained within the FactPS thermodynamic database, native to FactSage computational software [27].

4.9 Conflict of Interest

The authors report no conflict of interest.

4. References

[1] F. P. Bundy and R. H. Wentorf, J. Chem. Phys. **38**, 1144 (1963). Direct transformation of hexagonal boron nitride to denser forms. DOI:10.1063/1.1733815.
[2] T. Ishii and T. Sato, J. Cryst. Growth **61**, 689 (1983). Growth of single crystals of hexagonal boron nitride. DOI:10.1016/0022-0248(83)90199-9.
[3] R. T. Paine and C. K. Narula, Chem. Rev. **90**, 73 (1990). Synthetic routes to boron nitride. DOI:10.1021/cr00099a004.
[4] V. L. Solozhenko, I. A. Petrusha, and A. A. Svirid, High Press. Res. **15**, 95 (1996). Thermal phase stability of rhombohedral boron nitride. DOI:10.1080/08957959608240463.
[5] L. Bourgeois, Y. Bando, and T. Sato, J. Phys. D. Appl. Phys. **33**, 1902 (2000). Tubes of rhombohedral boron nitride. DOI:10.1088/0022-3727/33/15/321.
[6] T. Oku, K. Hiraga, T. Matsuda, T. Hirai, and M. Hirabayashi, Diam. Relat. Mater. **12**, 1138 (2003). Twin structures of rhombohedral and cubic boron nitride prepared by chemical vapor deposition method. DOI:10.1016/S0925-9635(02)00329-1.
[7] R. H. Wentorf, J. Chem. Phys. **26**, 956 (1957). Cubic form of boron nitride. DOI:10.1063/1.1745964.
[8] V. L. Solozhenko, High Press. Res. **13**, 199 (1995). Boron nitride phase diagram. State of the art. DOI:10.1080/08957959508200884.
[9] F. R. Corrigan and F. P. Bundy, J. Chem. Phys. **63**, 3812 (1975). Direct transitions among the allotropic forms of boron nitride at high pressures and temperatures. DOI:10.1063/1.431874.
[10] J. Thomas, Jr., N. E. Weston, and T. E. O'Connor, Phys. Inorg. Chem. **84**, 4619 (1963). Turbostratic boron nitride, thermal transformation to ordered-layer-lattice boron nitride. DOI:10.1021/ja00883a001.
[11] S. Alkoy, C. Toy, T. Gönül, and A. Tekin, J. Eur. Ceram. Soc. **17**, 1415 (1997). Crystallization behavior and characterization of turbostratic boron nitride. DOI:10.1016/S0955-2219(97)00040-X.
[12] F. P. Bundy, J. Chem. Phys. **38**, 631 (1963). Direct conversion of graphite to diamond in static pressure apparatus. DOI:10.1063/1.1733716.
[13] V. L. Solozhenko and K. S. Gavrichev, in *Wide Band Gap Electron. Mater.*, edited by M. Prelas, P. Gielisse, G. Popovici, B. Spitsyn, and T. Stacy, 1st ed. (Kluwer Academic Publishers, Minsk, Belarus, 1995), pp. 377–392. Thermodynamic properties of boron nitride. DOI:10.1007/978-94-011-0173-8.
[14] M. Okamoto, Y. Utsumi, and Y. Osaka, Plasma Sources Sci. Technol. **2**, 1 (1993). Mechanical properties of cubic boron nitride film on Si prepared by ECR plasma. DOI:10.1088/0963-0252/2/1/001.
[15] A. Weber, U. Bringmann, R. Nikulski, and C. P. Klages, Surf. Coatings Technol. **60**, 493 (1993). Electron cyclotron resonance plasma deposition of cubic boron nitride using N-trimethylborazine. DOI:10.1016/0257-8972(93)90139-F.
[16] W. J. Zhang, Y. M. Chong, I. Bello, and S. T. Lee, J. Phys. D. Appl. Phys. **40**, 6159

(2007). Nucleation, growth and characterization of cubic boron nitride films. DOI:10.1088/0022-3727/40/20/S03.

[17] S. Matsumoto and W. J. Zhang, Diam. Relat. Mater. **10**, 1868 (2001). The introducing of flourine into the deposition of BN: a successful method to obtain high-quality, thick cBN films with low residual stress.

[18] Y. Kobayashi and T. Akasaka, J. Cryst. Growth **310**, 5044 (2008). Hexagonal BN epitaxial growth on (0 0 0 1) sapphire substrate by MOVPE. DOI:10.1016/j.jcrysgro.2008.07.010.

[19] Q. S. Paduano, M. Snure, J. Bondy, and T. W. C. Zens, Appl. Phys. Express **7**, 1 (2014). Self-terminating growth in hexagonal boron nitride by metal organic chemical vapor deposition. DOI:10.7567/APEX.7.071004.

[20] Y. Shi, C. Hamsen, X. Jia, K. K. Kim, A. Reina, M. Hofmann, A. L. Hsu, K. Zhang, H. Li, Z. Y. Juang, M. S. Dresselhaus, L. J. Li, and J. Kong, Nano Lett. **10**, 4134 (2010). Synthesis of few-layer hexagonal boron nitride thin film by chemical vapor deposition. DOI:10.1021/nl1023707.

[21] K. K. Kim, A. Hsu, X. Jia, S. M. Kim, Y. Shi, M. Dresselhaus, T. Palacios, and J. Kong, ACS Nano **6**, 8583 (2012). Synthesis and characterization of hexagonal boron nitride film as a dielectric layer for graphene devices. DOI:10.1021/nn301675f.

[22] M. Chubarov, H. Pedersen, H. Högberg, J. Jensen, and A. Henry, Cryst. Growth Des. **12**, 3215 (2012). Growth of high quality epitaxial rhombohedral boron nitride. DOI:10.1021/cg300364y.

[23] L. Souqui, H. Pedersen, and H. Högberg, J. Vac. Sci. Technol. A **37**, 020603 (2019). Thermal chemical vapor deposition of epitaxial rhombohedral boron nitride from trimethylboron and ammonia. DOI:10.1116/1.5085192.

[24] H. Pedersen, B. Alling, H. Högberg, and A. Ektarawong, J. Vac. Sci. Technol. A **37**, 040603 (2019). Thermodynamic stability of hexagonal and rhombohedral boron nitride under chemical vapor deposition conditions from van der Waals corrected first principles calculations. DOI:10.1116/1.5107455.

[25] M. Chubarov, H. Högberg, A. Henry, and H. Pedersen, J. Vac. Sci. Technol. A Vacuum, Surfaces, Film. **36**, 030801 (2018). Review article: Challenge in determining the crystal structure of epitaxial 0001 oriented sp 2 -BN films. DOI:10.1116/1.5024314.

[26] M. Chubarov, H. Pedersen, H. Högberg, Z. Czigány, M. Garbrecht, and A. Henry, Chem. Mater. **27**, 1640 (2015). Polytype pure sp2-BN thin films as dictated by the substrate crystal structure. DOI:10.1021/cm5043815.

[27] C. W. Bale, E. Bélisle, P. Chartrand, S. A. Decterov, G. Eriksson, A. E. Gheribi, K. Hack, I. H. Jung, Y. B. Kang, J. Melançon, A. D. Pelton, S. Petersen, C. Robelin, J. Sangster, P. Spencer, and M. A. Van Ende, Calphad Comput. Coupling Phase Diagrams Thermochem. **54**, 35 (2016). FactSage thermochemical software and databases, 2010-2016. DOI:10.1016/j.calphad.2016.05.002.

[28] M. Imam, C. Höglund, J. Jensen, L. Hultman, J. Birch, H. Pedersen, K. Gaul, A. Stegmüller, and R. Tonner, J. Mater. Chem. C **3**, 10898 (2015). Gas phase chemical vapor deposition chemistry of triethylboron probed by boron-carbon thin film deposition and quantum chemical calculations. DOI:10.1039/C5TC02293B.

[29] M. Imam, L. Souqui, J. Herritsch, A. Stegmüller, C. Höglund, S. Schmidt, R. Hall-Wilton, H. Högberg, J. Birch, R. Tonner, and H. Pedersen, J. Phys. Chem. C **121**, 26465 (2017). Gas phase chemistry of trimethylboron in thermal chemical vapor deposition.

DOI:10.1021/acs.jpcc.7b09538.
[30] R. F. Davis, in *Compr. Semicond. Sci. Technol.*, edited by P. Bhattacharya, R. Fornari, and H. Kamimura (Elsevier B.V., Amsterdam, 2011), pp. 339–367. Organometallic vapor phase epitaxial growth of group III nitrides. DOI:10.1016/j.jallcom.2009.02.108.
[31] T. F. Kuech, in *Handb. Cryst. Growth*, edited by T. F. Kuech, 2nd ed. (Elsevier B.V., Madison, WI, USA, 2015), pp. 869–907. Metal organic vapor phase epitaxy chemical kinetics. DOI:10.1016/B978-0-444-63304-0.00021-4.
[32] T. Ishii, T. Sato, Y. Sekikawa, and M. Iwata, J. Cryst. Growth **52**, 285 (1981). Growth of whiskers of hexagonal boron nitride. DOI:10.1016/0022-0248(81)90206-2.
[33] L. Ye, F. Liang, L. Zhao, X. He, W. Fang, H. Chen, X. Wang, J. Wu, and S. An, Ceram. Int. **42**, 11626 (2016). Catalyzed synthesis of rhombohedral boron nitride in sodium chloride molten salt. DOI:10.1016/j.ceramint.2016.04.062.
[34] T. Sato, Proc. Japan Acad. Ser. B Phys. Biol. Sci. **61**, 459 (1985). Influence of monovalent anions on the formation of rhombohedral boron nitride, rBN. DOI:10.2183/pjab.61.459.

4.10 Supplementary Materials: Thermodynamic Properties of h-BN and r-BN and Determination of Gibbs Free Energy

Equation (1) was developed by Reshetnikov [1] and modified by Solozhenko [2] to fit the experimentally-determined heat capacity data [2,3] for the four primary BN polymorphs in the 4 – 1700 K temperature range.

$$C_p(T) = \delta_0 \left(\frac{T^2}{T^2+\delta_1 T+\delta_2}\right)^2 \qquad \text{Eq. 4.10 S(1)}$$

In this work, each $C_p(T)$ equation in the Reshetnikov form was fitted to the power series form for heat capacity in order to simplify the phase diagram calculations:

$$C_P(T) = a + bT + cT^{-2} + dT^2 \qquad \text{Eq. 4.10 S(2)}$$

The coefficients of Eq. (2) for h-BN and r-BN are presented in Table 4.10.S1. The experimentally determined standard-state thermodynamic properties of h-BN and r-BN are presented in Table 4.10.S2 [2,3].

Table 4.10.S1: Coefficients of Eq. 4.10.S(2) for h-BN and r-BN

	a (J/mol K)	*b* (J/mol K^2)	*c* (J K/mol)	*d* (J/mol K^3)
h-BN	35.14	1.22×10^{-2}	-1.77×10^{6}	-2.39×10^{-6}
r-BN	33.93	1.32×10^{-2}	-1.61×10^{6}	-2.50×10^{-6}

Table 4.10.S2: Standard-state thermodynamic properties of h-BN and r-BN at 298.15 K

	C_p^o (J/mol K)	S^o (J/mol K)	ΔH^o_f (J/mol)	ΔG^o (J/mol)
h-BN	19.85	14.81	-2.51×10^5	-2.54×10^5
r-BN	20.63	15.83	-2.48×10^5	-2.53×10^5

The power series C_p(T) and standard-state thermodynamic properties of h-BN and r-BN were imported as a customized database into FactSage (Version 8.0, CRCT – Thermfact, Inc. and GTT Technologies) [4], a computational software package that makes thermodynamic equilibrium calculations based on the minimization of Gibbs free energy and mass conservation. The customized database contained only the thermodynamic properties of these two BN phases. The database required only the C_p(T) data from Table 4.10.S1 as well as the S^o (298 K) and ΔH^o_f (298 K) values from Table 4.10.S2 to calculate the Gibbs free energy of each BN phase relative to their standard element reference (SER), defined as the enthalpy (H) of the most stable form of the constituting element(s) at 298.15 K and atmospheric pressure [5]. The Gibbs free energy, defined relative to the SER state in this way, is denoted as G–HSER, and can be described in the form of the power series shown in Eq. 4.10.S(3). The coefficients of Eq. (3) for the h-BN and r-BN phases used in this work are given in Table 3.

$$G(T) - HSER = a_0 + \frac{a_1}{T} + a_2 T + a_3 T^2 + a_4 T^3 + a_5 T \ln T \qquad 4.10.S(3)$$

Table 4.10.S3: Coefficients of Eq. 4.10.S(3) for h-BN and r-BN

	a_0 (J/mol)	a_1 (J K/mol)	a_2 (J/ mol K)	a_3 (J/mol K^2)	a_4 (J/mol K^3)	a_5 (J/mol K)
h-BN	-2.67×10^5	8.86×10^5	2.34×10^2	-6.12×10^{-3}	3.98×10^{-7}	-35.14
r-BN	-2.64×10^5	8.07×10^5	2.24×10^2	-6.59×10^{-3}	4.17×10^{-7}	-33.93

4.10. Supplementary References

[1] M. A. Reshetnikov, Zh. Neorg Chim **11**, 1489 (1969).

[2] V. L. Solozhenko, High Press. Res. **13**, 199 (1995). DOI:10.1080/08957959508200884.

[3] V. L. Solozhenko and K. S. Gavrichev, in *Wide Band Gap Electron. Mater.*, edited by M. Prelas, P. Gielisse, G. Popovici, B. Spitsyn, and T. Stacy, 1st ed. (Kluwer Academic Publishers, Minsk, Belarus, 1995), pp. 377–392. DOI:10.1007/978-94-011-0173-8.

[4] C. W. Bale, E. Bélisle, P. Chartrand, S. A. Decterov, G. Eriksson, A. E. Gheribi, K. Hack, I. H. Jung, Y. B. Kang, J. Melançon, A. D. Pelton, S. Petersen, C. Robelin, J. Sangster, P. Spencer, and M. A. Van Ende, Calphad Comput. Coupling Phase Diagrams Thermochem. **54**, 35 (2016). DOI:10.1016/j.calphad.2016.05.002.

[5] A. T. Dinsdale, Calphad **15**, 317 (1991). DOI:10.1016/0364-5916(91)90030-N.

5. Paper 2: Thermodynamic Calculations for the Chemical Vapor Deposition of Hexagonal Boron Nitride Using Triethylboron, Ammonia, and Hydrogen

Authors: Philip M. Jean-Remy[a], Bryan A. Webler[a], Petrus C. Pistorius[a], and Robert F. Davis[a, b]

[a] Department of Materials Science and Engineering, Carnegie Mellon University, Pittsburgh, PA, 15213, USA

[b] Department of Electrical and Computer Engineering, Carnegie Mellon University, Pittsburgh, PA, 15213, USA

Corresponding author: Philip M. Jean-Remy, 5700 Ellsworth Avenue, Apartment A3, Pittsburgh, PA, 15232, USA. Email: pjeanrem@andrew.cmu.edu

5.1 Abstract

The presence of C in $B(C_2H_5)_3$ makes possible its incorporation into hexagonal boron nitride (h-BN) thin films grown during chemical vapor deposition (CVD) under select process conditions. A series of CVD phase diagrams that indicate the regions of stability of the phases of h-BN, C and B_4C as a function of temperature and input mole ratio of reactants (N/B) under set pressures and H_2 diluent-to-reactant mole ratios (H_2/(B + N)) have been calculated and analyzed for the TEB/NH_3/H_2 system. The equilibrium calculations showed that within the total pressure range of 0.01 -100 Torr, increasing the H_2 content in the TEB/NH_3/H_2 gas mixture tends to suppress the stability of C throughout a 400 – 1600˚C temperature range, but it also suppresses the stability of h-BN at higher temperatures. Further, it was determined that increasing the total system pressure suppresses the occurrence of C as a second phase while expanding the stability of h-BN. The thermodynamic equilibrium results were compared to the results of experimental investigations involving the CVD synthesis of sp^2-BN as a means to evaluate their usefulness as a guide for avoiding the co-deposition of C and B_4C with h-BN.

5.2 Keywords: A1. Phase diagrams; A1. Phase equilibria; A3; Metalorganic chemical vapor deposition; B1. Nitrides; B2. Semiconducting III-V materials

5.3 Introduction

Hexagonal boron nitride (h-BN) is a two-dimensional (2D), sp^2-hybridized material that is chemically stable, highly thermally conductive and possesses a bandgap of ~6 eV [1]. Thin films of h-BN are candidate materials for optoelectronic applications operative in the deep ultra-violet under harsh conditions, as well as dielectric layers for graphene-based transistors [2].

Several chemical combinations have been used to synthesize h-BN via chemical vapor deposition (CVD); however, triethylboron ($B(C_2H_5)_3$) (TEB), and ammonia (NH_3) have gradually become precursors of choice and employed for deposition of h-BN at elevated temperatures on non-catalytic substrates including *c*-plane sapphire (1000 – 1350 $^{\circ}$C) [3–5], (100) Si (1000 – 1200 $^{\circ}$C) [3,6], and (0001) 6H-SiC (1050 – 1300 $^{\circ}$C) [7,8]. Imam et al. [9] investigated the CVD gas phase chemistry of TEB decomposition and observed that the reaction rate for β-hydride elimination of the ethyl ligands that produces C_2H_4 that can act as a C source increases dramatically above 1000 ^{o}C. This reaction mechanism suggests a potential problem for C incorporation into h-BN during CVD, as temperatures of at least 1000 ^{o}C have been required to synthesize epitaxial h-BN on the aforementioned substrates [4,5,8,10]. However, the addition of nitrogen to the TEB gas phase chemistry during CVD has been shown to preferentially produce BN in place of either B_xC or $B_xC_yN_z$. For example, Souqui et al. [11] showed that at substrate temperatures of 300 – 400 ^{o}C and chamber pressures of 20 – 60 Torr, the deposition of amorphous $B_xC_yN_z$ thin films on (100) Si wafers using TEB could be achieved in an Ar-N_2 plasma. They observed that the C content in the films remained low (4.8 – 11.6 at. %) and that B and N participated in mainly sp^2 bonding with each other with nearly 1:1 stoichiometry.

Conversely, when Imam et al. [12] studied the room-temperature deposition of hydrogenated B_xC thin films on (100) Si substrates using TEB as a single source in an Ar plasma at a total chamber pressure of ~ 0.23 Torr, significant C was incorporated, in the range of B/C = 1 – 1.7. X-ray photoelectron spectroscopy results showed that B bonded primarily to C (no free B). C existed in the films primarily bonded to B rather than as C-C (free C), and the amount of free C decreased in favor of C-B and C-C-B bonds as the TEB flowrate was increased. For thermal CVD of sp^2-BN, it has been postulated that at high temperatures where TEB is expected to release C_2H_2 as a reactive species [13], the latter is removed by reaction with atomic H released from the decomposition of NH_3 [14]. Thus, except for very few studies [6,14], C-incorporation in BN films grown via thermal CVD where TEB and NH_3 flow simultaneously is not often reported.

In this work, CVD phase diagrams of the TEB/NH_3/H_2 system were calculated and analyzed in order to observe the effects of initial composition (N/B and H_2/(N+B)), temperature, and total pressure on the formation of single-phase h-BN. In CVD, the gradients in temperature, pressure and the chemical potentials of the reactants and products in the gas phase throughout the deposition chamber and the kinetically controlled processes such as gaseous diffusion through the boundary layer and decomposition reactions influence the resulting condensed phase(s) that form. When the kinetic processes occur extremely quickly relative to the amount of time that reactant gases spend in the reaction zone – assumed to be limited to the heated substrate – the resulting condensed film, its deposition rate, and the composition of the gaseous species of the boundary layer above the substrate are limited by thermodynamic variables [15,16]. Calculations of CVD phase diagrams are thus performed under the assumption that the reactor chamber is being operated close to equilibrium conditions during the deposition of solid-state

films. In this work, the usefulness of the CVD phase diagrams will be considered, as the results will be compared to reported studies of CVD BN, where TEB and NH_3 were used as precursors.

5.4 Background

BN has been observed to crystallize in three other primary phases, namely, rhombohedral (r-BN), cubic (c-BN), and wurtzitic (w-BN). The r-BN modification is also a 2D material with sp^2 bonding, while those of c-BN and w-BN possess sp^3 bonding and greater densities. BN can also form as turbostratic (t) BN, a much less ordered sp^2-hybridized nonequilibrium phase. t-BN is semi-crystalline, in that there remains a high degree of in-plane order of BN hexagonal rings; however, these layers are not parallel and are randomly rotated and translated with respect to the *c* axis of the layer. This causes the interplanar spacing for the (0002) planes to vary and possess larger values than that for h-BN and r-BN [17,18].

Solozhenko [19,20] has presented extensive data on experimentally determined heat capacities for each polymorph and predicted c-BN to be the most thermodynamically stable BN phase at ambient conditions. However, experimentally, the thermal CVD synthesis of BN almost always results in the deposition of sp^2-hybridized forms of h-BN, r-BN, or t-BN. To achieve deposition of c-BN films via CVD, a plasma is typically applied during the deposition to induce ion-bombardment of the substrate surface and the growing film [21,22]. These highly energetic (50 – 1000 eV) non-equilibrium processes result in large compressive stresses (5 – 20 GPa) within the growing films which often results in nanocrystallinity, poor film adhesion to the substrate, and a maximum thickness limited to a few hundred nanometers [23,24]. Plasma-enhanced growth of c-BN thin films often involves the co-deposition of sp^2-BN, a situation that is not avoided without the addition of a fluorine-based gas which selectively etches sp^2 bonds and better stabilizes sp^3 bonds [23,24]. Because of these many difficulties surrounding the

stabilization of c-BN during thermal CVD, this polymorph was excluded in the phase diagram calculations of this work. Further, to the best of the authors' knowledge, w-BN has never been synthesized through any type of CVD, and thus consideration of this polymorph was also excluded from the calculations in this work.

It should also be noted that experimental and theoretical studies indicate that r-BN may be the most stable polymorph resulting from thermal CVD, especially at elevated temperatures. Chubarov et al. [25] conducted extensive research concerned with the thermal CVD and characterization of r-BN and provided an in-depth discussion of the challenge of distinguishing the structure of r-BN from that of h-BN. The ABAB… stacking sequence of h-BN is the only structural difference that distinguishes it from the ABCABC… sequence of r-BN [26]. The in-plane and out-of-plane lattice parameters are very similar, which makes it difficult to distinguish between the two phases using conventional 2θ-θ x-ray diffraction (XRD). However, the two phases can be distinguished through other methods such as by examining, via glancing-incidence XRD, asymmetric planes such as the $(10\bar{1}2)$ and $(01\bar{1}2)$ of h-BN and r-BN, respectively, which have discernable interplanar spacings [27], as well as through high resolution transmission electron microscopy (TEM) to observe crystallographic stacking. Thus, there remains the possibility of the existence of r-BN content in reported sp^2-BN films deposited by CVD, if such extensive characterizations efforts are not conducted to verify the h-BN phase with specificity. Further, Pedersen et al. [28] used van der Waals-corrected density functional theory to show that r-BN was the most stable polymorph at typical CVD conditions of ~1100 – 1500 C^o and 7.5 – 75 Torr for epitaxial sp^2-BN, suggesting that h-BN is a metastable CVD phase at high temperatures. Despite these recent findings, the most stable BN polymorph calculated in the present work at all variable conditions using the thermodynamic properties determined by Solozhenko et al. [19]

(excluding c-BN and w-BN) was found to be h-BN. It is important to note, however, that a plot of the Gibbs free energy of the h-BN and r-BN polymorphs based on this data (presented in our previous work [29]) shows that the difference in the free energy of both polymorphs is rather small and decreases substantially with increasing temperature (from roughly 1.2 kJ/mol at 400 °C to less than 0.2 kJ/mol at 1600 °C), as shown in the inset in Figure 5.4.1.

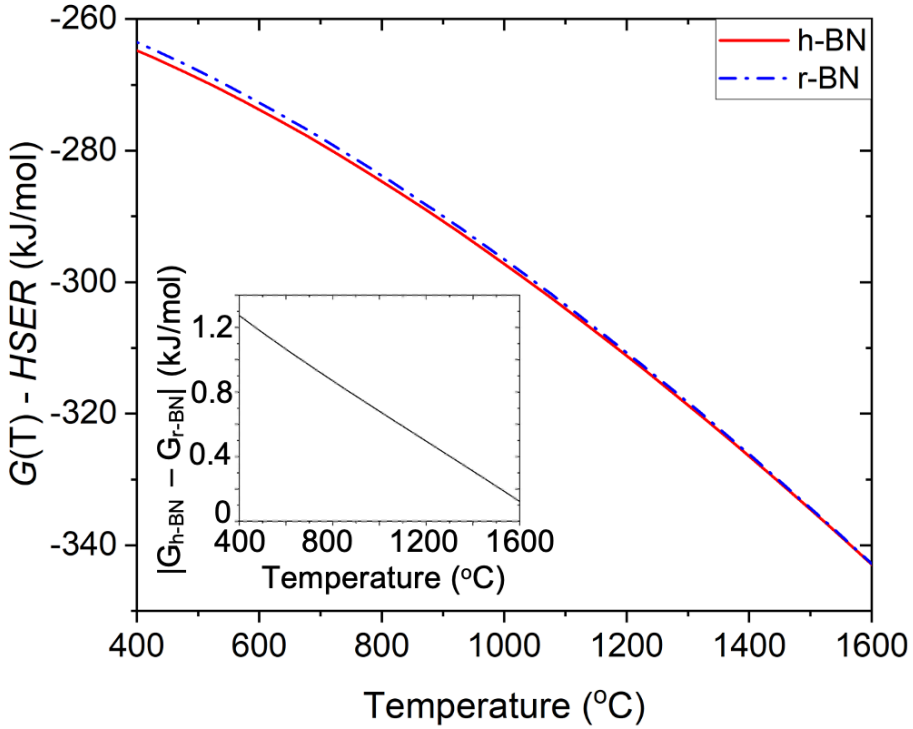

Figure 5.4.1. *G*(T) – HSER calculated at atmospheric pressure for h-BN and r-BN in our previous work [29]. The inset plot shows the absolute difference of the Gibbs free energies of h-BN and r-BN as function of temperature.

5.5 Methods

Solozhenko et al. [19,20] experimentally determined the heat capacity of the four main BN polymorphs within the 16 – 1700 K range, beyond which they used Equation 5.5(1) by Reshetnikov [30] to extrapolate to 3000 K to generate an equilibrium BN (P, T) phase diagram [19].

$$C_p(T) = \delta_0 \left(\frac{T^2}{T^2+\delta_1 T+\delta_2}\right)^2 \qquad 5.5\ (1)$$

In this work, each $C_p(T)$ equation in the Reshetnikov form was fitted to the power series form for heat capacity in order to simplify the phase diagram calculations:

$$C_P(T) = a + bT + cT^{-2} + dT^2 \qquad 5.5\ (2)$$

The coefficients of Eq. 5.5(2) for h-BN and r-BN are presented in Table 5.5.1. The experimentally determined standard-state thermodynamic properties of h-BN and r-BN are presented in Table 5.5.2 [19,20].

Table 5.5.1: Coefficients of Eq. 5.5(2) for h-BN and r-BN

	a (J/mol K)	*b* (J/mol K^2)	*c* (J K/mol)	*d* (J/mol K^3)
h-BN	35.14	1.22×10^{-2}	-1.77×10^{6}	-2.39×10^{-6}
r-BN	33.93	1.32×10^{-2}	-1.61×10^{6}	-2.50×10^{-6}

Table 5.5.2: Standard-state thermodynamic properties of h-BN and r-BN at 298.15 K

	C_p^o (J/mol K)	S^o (J/mol K)	ΔH^o_f (J/mol)	ΔG^o (J/mol)
h-BN	19.85	14.81	-2.51×10^{5}	-2.54×10^{5}
r-BN	20.63	15.83	-2.48×10^{5}	-2.53×10^{5}

The power series C_p(T) and standard-state thermodynamic properties of h-BN and r-BN were imported as a customized database into FactSage (Version 8.0, CRCT – Thermfact, Inc. and GTT Technologies) [31], a computational software package that makes thermodynamic equilibrium calculations based on the minimization of Gibbs free energy and mass conservation. The customized database contained only the thermodynamic properties of these two BN phases. The database required only the C_p(T) data from Table 5.5.1 as well as the S^o (298 K) and ΔH^o_f (298 K) values from Table 5.5.2 to calculate the Gibbs free energy of each BN phase relative to

their standard element reference (SER), defined as the enthalpy (H) of the most stable form of the constituting element(s) at 298.15 K and atmospheric pressure [32]. The Gibbs free energy, defined relative to the SER state in this way, is denoted as G–HSER, and can be described in the form of the power series shown in Eq. 5.5.(3). The coefficients of Eq. 5.5(3) for the h-BN and r-BN phases used in this work are given in Table 5.5.3. A plot of *G*(T)–HSER for h-BN and r-BN at atmospheric pressure in the 400 – 1600 °C temperature range is shown in Figure 5.5.1.

$$G(T) - HSER = a_0 + \frac{a_1}{T} + a_2 T + a_3 T^2 + a_4 T^3 + a_5 T \ln T \qquad 5.5\ (3)$$

Table 5.5.3: Coefficients of Eq. 5.5(3) for h-BN and r-BN

	a_0 (J/mol)	a_1 (J K/mol)	a_2 (J/ mol K)	a_3 (J/mol K^2)	a_4 (J/mol K^3)	a_5 (J/mol K)
h-BN	-2.67×10^5	8.86×10^5	2.34×10^2	-6.12×10^{-3}	3.98×10^{-7}	-35.14
r-BN	-2.64×10^5	8.07×10^5	2.24×10^2	-6.59×10^{-3}	4.17×10^{-7}	-33.93

The thermodynamic properties of all other species besides BN in the B-N-C-H system, gaseous and condensed, were contained within the FactPS database [31] , native to the FactSage software. TEB, NH_3, H_2, and Ar were the input gaseous reactants used in the calculation of the phase diagrams and were set to sum to a total of 1 mole. The S^o, ΔH^o_f and C_p(T) data for each reactant and expected condensed products are listed in Tables 5.9.S1 – 5.9.S9 of the Supplementary Information, where the temperature range of validity for C_p(T) is also specified. For TEB (g) in particular, the C_p(T) data is valid from 298 – 1000 K; thus for temperatures beyond 1000 K, the Gibbs free energy is extrapolated in order perform the phase diagram calculations. The gaseous species considered in this system were: H_2, HCN, CH_4, C_2H_2, C_2H_4, NH_3, CH_3, BH_3, NH_2, C_2H_6, and TEB. The condensed species considered in this system were: h-BN (s), r-BN (s), C (s) (graphite), and B_4C (s). The "n.c.p." label in the forthcoming phase

diagrams stands for “no condensed phases.” The variables of the system include the input gas in the form of N/B (mol/mol) ratio ranging from 1 to 10^7; the mole ratio of $H_2/(B + N)$ set to 0, 10, or 100; total system pressures ranging from 0.01 Torr to 100 Torr; and temperature ranging from 400 to 1600°C. In each phase diagram calculation, $H_2/(B + N)$ is a constant value. With increasing N/B, the mole amount of TEB decreases while that of NH_3 increases in order to maintain both the constant $H_2/(B + N)$ and TEB + NH_3 + H_2 = 1 mole conditions.

5.6 Results and discussion

Figure 5.6.1 shows the calculated phase diagrams for the TEB/NH_3/H_2 system. It is apparent that the aforementioned parameters have a significant impact on the occurrence, range and placement of the single-phase phase field of h-BN. The h-BN phase is predicted for all system pressures investigated (0.01 – 100 Torr) and at each $H_2/(B + N)$ ratio. In general, co-deposition of C and even B_4C with h-BN occurs as the N/B ratio decreases. The addition of H_2 to the gas mixture tends to shrink the h-BN + C phase-fields. Increasing the system pressure at a constant $H_2/(B + N)$ ratio tends to extend the N/B composition over which the single-phase phase field of h-BN occurs. Increasing the $H_2/(B + N)$ ratio at a constant pressure shrinks the compositional range of the h-BN phase field at high temperatures (> 1000 °C) while simultaneously shifting it further along the composition axis. I.e., the ability to obtain single-phase h-BN at lower N/B ratios increases as $H_2/(B + N)$ increases, but the N/B window shrinks at higher temperatures. This effect is most emphasized for the 0.01 and 1 Torr conditions in Figures 5.6.1(a) – (f) as $H_2/(B + N)$ increases.

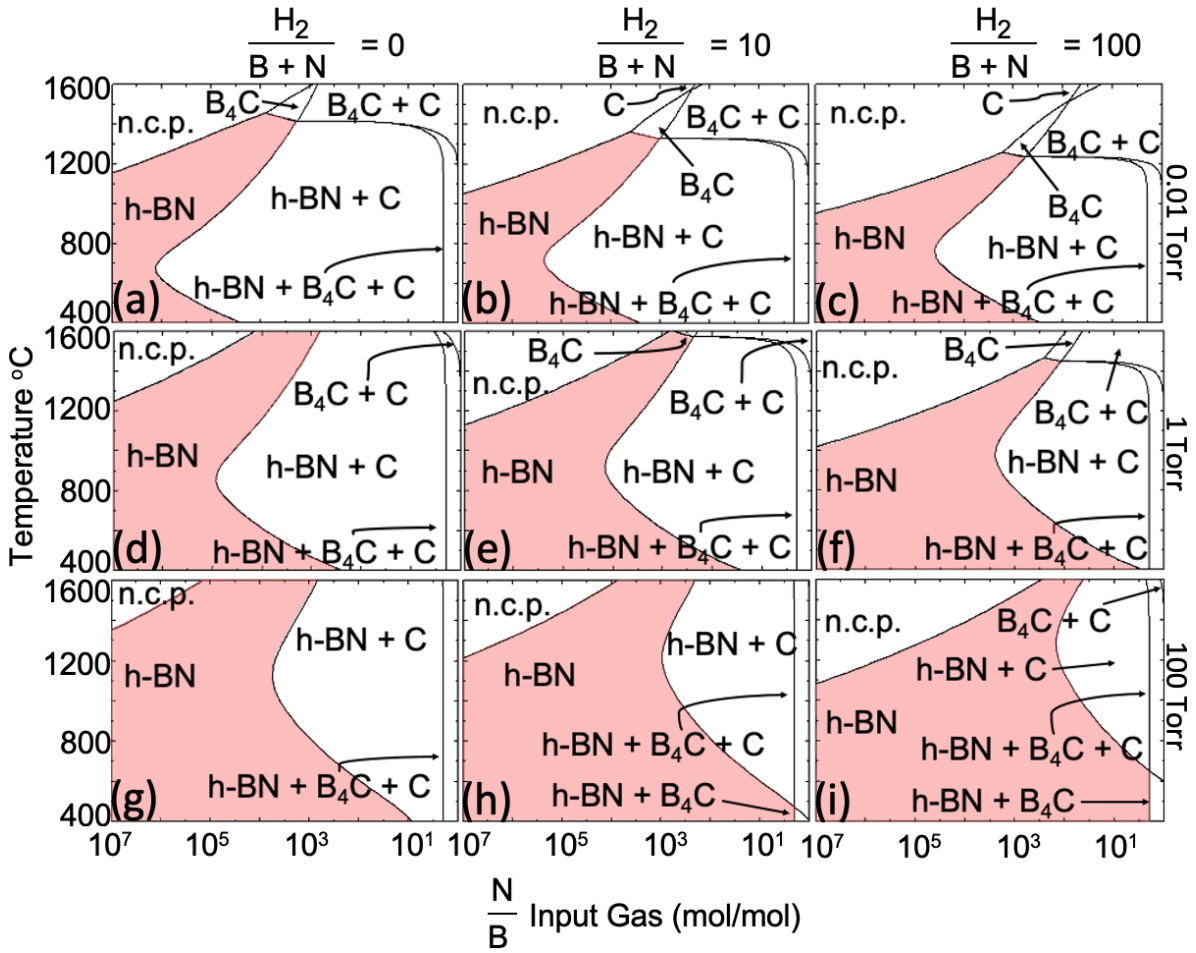

Figure 5.6.1: TEB/NH_3/H_2 phase diagrams calculated as a function of input gas mole ratio (N/B) and temperature. The H_2/(B+N) mole ratio is set to 0, 10, and 100 for each column as indicated. Diagrams (a) – (c), (d) – (f), and (g) – (i) were calculated at total system pressures of 0.01 Torr, 1 Torr, and 100 Torr, respectively. The h-BN phase field in each diagram is shaded red for ease of visualization. Diagrams calculated at 10 Torr are shown in Figure 5.6.2.

Interpretation of the calculated phase diagrams requires knowledge of the competing equilibria that exist in the TEB/NH_3/H_2 system. It must be determined if H_2 participates in the TEB + NH_3 equilibria for all calculations performed with H_2/(B + N) > 0. Calculations were performed at P = 10 Torr using either H_2 (Figures 5.6.2(a) – (c)) or Ar (Figures 5.6.2(d) – (f)) as the diluent gas. Introduction of Ar with Ar/(B + N) = 10 and 100 in Figures 5.6.2(e) and 5.6.2(f), respectively, resulted in a reduction in the magnitude of the single-phase phase field of h-BN,

while the magnitude of the n.c.p. field increased. The total amount of input gas was constrained to 1 mole, meaning that for an increased amount of diluent gas, the amount of reactant gas in the system decreased. Because Ar is inert, it is assumed that it does not participate in the TEB/NH_3 chemistry. Thus, the reduction in the magnitude of the BN single-phase phase fields and the subsequent increased stability for B_4C and C in the Ar diluent system is attributed to a reduction in the amount of reactant gas required to produce BN. In contrast, examination of the 10 Torr TEB/NH_3/H_2 system presented in Figures 5.6.2(a) – (c) reveals that the stability range of the single-phase h-BN field increased with increasing H_2/(B + N) in the manner shown for other pressures in Figure 5.6.1 despite a decreasing amount of TEB and NH_3. Therefore, for H_2/(B + N) mole ratios greater than zero, it is necessary to consider H_2 important in the production of single-phase h-BN and the reduction of C stability.

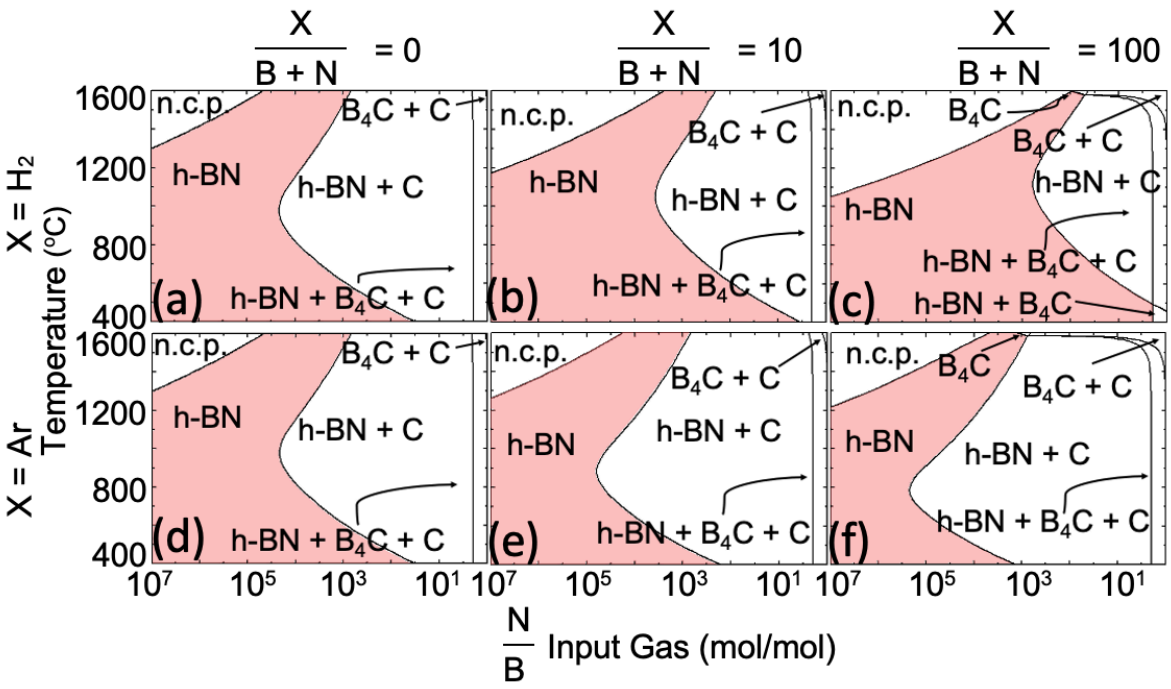

Figure 5.6.2: Phase diagrams calculated using gas mixtures of either TEB/NH_3/H_2 ((a) – (c)) or TEB/NH_3/Ar ((d) – (f)) as a function of the input gas mole ratio, N/B, temperature, and a fixed total system pressure of 10 Torr. Diagrams (a) – (c) were calculated at H_2/(B + N) = 0, 10, and 100, respectively; (d) – (f) were calculated at Ar/(B + N) = 0, 10, and 100, respectively. The h-BN phase field in each diagram is shaded red for ease of visualization.

As noted above, Imam et al. [9] presented evidence that TEB undergoes at least one β-hydride elimination. At a pressure of approximately 38 Torr in the 400 – 1200°C temperature range, kinetic Monte Carlo (KMC) simulations showed that, in decreasing order, the dominant B-containing species in the gas phase product distribution were $B(C_2H_5)_2H$, $B(C_2H_5)H_2$, and BH_3. This study [9] revealed that the Gibbs free energy of the TEB decomposition path to BH_3 is larger (less negative) than that for the decomposition path to the intermediate species of $B(C_2H_5)_2H$ or $B(C_2H_5)H_2$, which explained why BH_3 was the least abundant B-species predicted in the simulation. Further, in a H_2 atmosphere at temperatures below 600° C, it was reported that the decomposition of TEB is aided by the H_2-assisted elimination of C_2H_6 [9]. C_2H_6 can further

decompose into CH_4; however, the latter gas is not expected to act as a source for C incorporation at low temperatures. Above 600 °C, it was reported [9] that the rate of H_2-assisted elimination of C_2H_6 diminishes and only the β-hydride elimination occurs, releasing C_2H_4, which is expected to partially decompose into C_2H_2, and both species are expected to be active sources of C [9,13,14]. Assuming that C_2H_4 and C_2H_6 decompose into C_2H_2 and CH_4, respectively, reactions 5.6(1) and 5.6(2) take into account β-hydride elimination and H_2-assisted ethane elimination, respectively, when NH_3 is added to TEB to eventually produce BN (s).

$$B(C_2H_5)_3(g) + NH_3(g) \rightleftharpoons BN(s) + 3\ C_2H_2(g) + 6\ H_2(g) \qquad 5.6(1)$$

$$B(C_2H_5)_3(g) + NH_3(g) + 3\ H_2(g) \rightleftharpoons BN(s) + 6\ CH_4(g) \qquad 5.6(2)$$

The standard state Gibbs free energy change for reactions 5.6(1) and 5.6(2) is shown in Figure S1 of the Supplementary Information, where it can be seen that the β-hydride elimination reaction becomes more favorable than the H_2-assisted ethane elimination reaction as temperature increases, which agrees with the observations of TEB decomposition [9] described above. Similar reactions considered for the production of C (s) and B_4C (s) and their standard state equilibrium constants are listed in Table 5.9.S10 of the Supplementary Information.

To display the interaction between the β-hydride and H_2-assisted C_2H_6 elimination of TEB decomposition in the presence of NH_3, and its effect on BN equilibrium stability, Figure 5.6.3 was designed which shows the composition of the gas phase (in partial pressure) and the condensed phases (in number of moles) produced in the TEB/NH_3/H_2 system as a function of temperature. In all cases, the input N/B ratio was set to 999 (B/(B+N) = 0.001). The total pressure for Figure 5.6.3 (a)-(c) is 0.01 Torr, and the H_2/(B+N) ratio was set to 0, 10, and 100 in (a), (b), and (c), respectively. The H_2/(B+N) ratio was similarly increased in Figure 5.6.3 (d)-(f) and (g)-(i), at a total pressure of 1 Torr and 100 Torr, respectively.

The BH_3 eventually evolved from TEB decomposition leads to the incorporation of B [33,34]. As described above, the intermediate species, $B(C_2H_5)_2H$ and $B(C_2H_5)H_2$, are likely present in the gas phase, however increasing temperatures lead to the increased elimination of the ethyl groups and subsequent formation of BH_3 [9,34,35]. Thermodynamic data for the intermediate species are unavailable. Thus, BH_3 is the only B-containing vapor species considered in the calculations for Figure 5.6.3. Further, the C species being considered are C_2H_2 and CH_4, because, as shown in Tables 5.9.S12 and 5.9.S13 of the Supplementary Information, they were present in larger partial pressures than C_2H_4 and C_2H_6 from which they, respectively, are expected to be derived. In equilibrium, NH_3 is expected to dissociate almost completely into H_2 and N_2 beyond temperatures of 300 °C, but the kinetics of the thermal decomposition of NH_3 are slow such that the partial pressures of species such as NH_2 and NH radicals are several orders of magnitude lower than residual NH_3 [36–38]. Because NH_2 and NH are considered to be active species for N-incorporation during nitride thin film growth [39], extremely high V/III gas-phase ratios ($10^3 – 10^4$) [36,38] are required to produce sufficient active species for the growth of epitaxial layers. For Figure 5.6.3, only the NH_2 species is highlighted because as shown in Tables 5.9.S12 and 5.9.S13 in the Supplementary Information, its equilibrium partial pressure exceeds that of NH for various temperature, pressure, and H_2/(B+N) conditions. The solid species being considered for Figure 5.6.3 are h-BN, B_4C, and C.

For the 0.01 Torr condition in Figure 5.6.3 (a)-(c), it can be seen that the temperature range for the chemical stability of pure C decreases with increasing H_2/(B+N) ratio. This trend is also observed for the 1 Torr and 100 Torr conditions in Figure 5.6.3 (d)-(f) and (g)-(i), respectively. In all cases, the lower temperature limit for C is associated with a sudden decrease in the partial pressure of CH_4, while at the upper temperature limit the partial pressure of C_2H_2

reaches a maximum, near constant value. For increasing H_2/(B+N) ratios, the onset of the decreasing partial pressure of CH_4 is delayed to higher temperatures; that is, a higher partial pressure of H_2 fosters the stability of CH_4 at higher temperatures. The onset of the maximum and nearly constant partial pressure of C_2H_2 is also delayed to higher temperatures with increasing H_2 content. Further, increasing the pressure also decreases the temperature range of C stability in the system, and it has a similar effect on the partial pressures of CH_4 and C_2H_2 as a function of temperature as does increasing the amount of H_2. An overview of these diagrams indicates that the formation of C can be entirely suppressed over the broad temperature range of 400 – 1600 ^oC at sufficiently high pressures and H_2/(B+N) ratios. For example, Figure 5.6.3 (h) indicates that the operation of a thin film growth system under the conditions of N/B ~ 10^3, a total pressure of 100 Torr, and a H_2/(B+N) = 10 should be sufficient to completely suppress the formation of C during the deposition of h-BN. Figure 5.6.3 also reveals that the pressure and the H_2/(B+N) ratio have an effect on the thermodynamic stability of h-BN. Figures 5.6.3 (a)-(c) show that at both a low pressure of 0.01 Torr and N/B = 999, the high temperature range stability for h-BN decreases with increasing H_2/(B+N). Specifically, h-BN is no longer stable after ~ 1400, 1300 , and 1200 ^oC at H_2/(B+N) = 0, 10, and 100, respectively. In each case, both the partial pressure of BH_3 and NH_2 increase with increasing temperature, but with increasing H_2/(B+N), the partial pressure of BH_3 surpasses that of NH_2 at lower temperatures. This leads to insufficient partial pressures of NH_2 available at higher temperatures to maintain h-BN stability. The same trend as a result of increasing the H_2/(B+N) ratio can be observed for each pressure condition. At a constant H_2/(B+N) ratio, increasing the system pressure causes the partial pressure of BH_3 to surpass that of NH_2 at higher temperatures, thereby increasing the temperature range of stability of the h-BN.

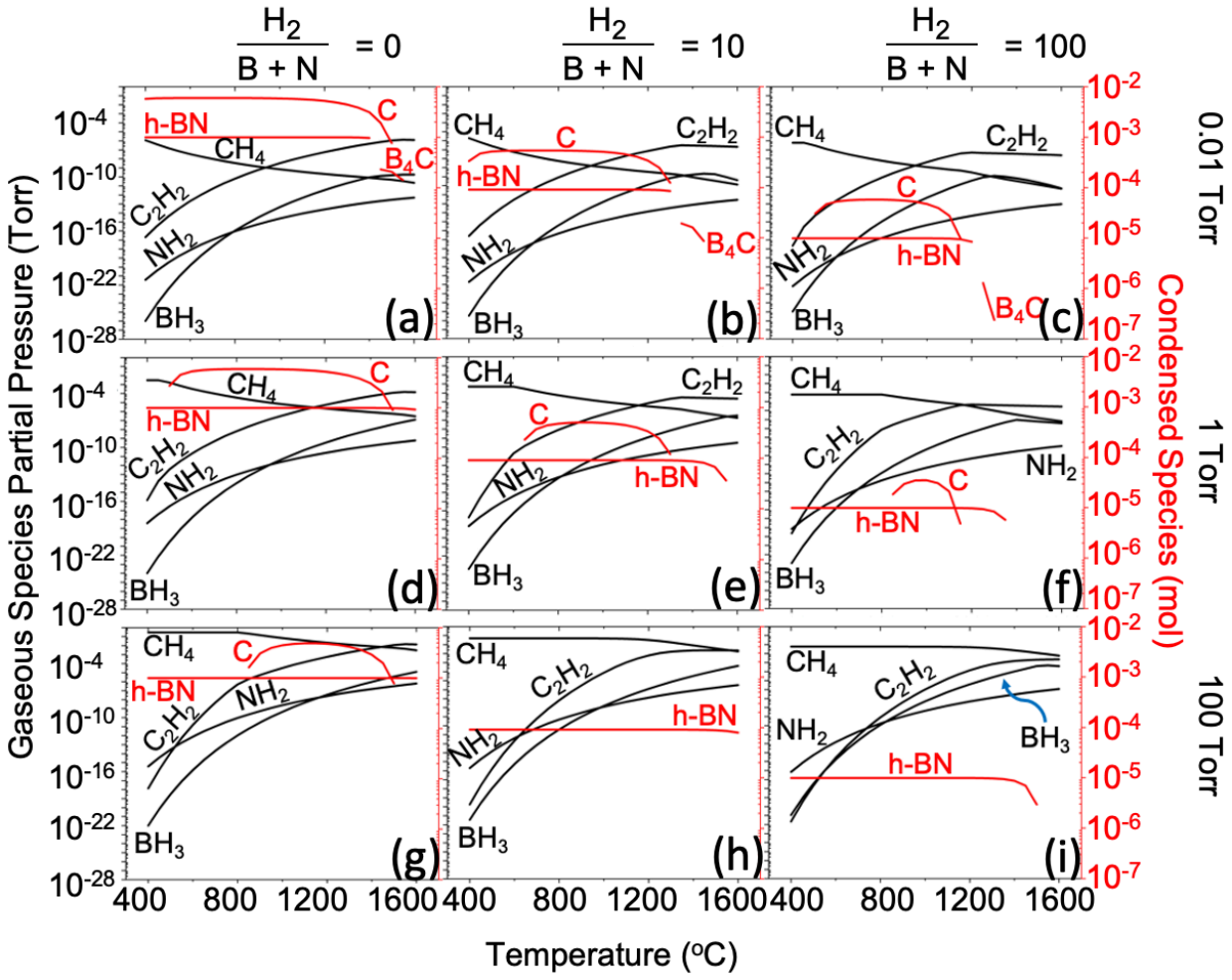

Figure 5.6.3: Composition of gas phase (in partial pressure (Torr)) and the amount of the condensed phases (in number of moles) as a function of temperature for the TEB/NH_3/H_2 system, where N/B = 999. The H_2/(B + N) mole ratio is set to 0, 10, and 100 for each column. Diagrams (a) – (c), (d) – (f), and (g) – (i) were calculated at the total system pressures of 0.01 Torr, 1 Torr, and 100 Torr, respectively.

Jin et al. [6] observed the effect of total chamber pressure on BN thin films deposited on (100) Si single crystal substrates using TEB and NH_3 as precursors and H_2 and Ar as diluent gases. Auger electron spectroscopy depth profiles revealed that maintaining the constant TEB and NH_3 flow rates of 0.5 sccm and 20 sccm (N/B = 40), respectively, a substrate temperature of

1000 °C, and a total chamber pressure of 740 Torr resulted in a BN film without any measurable C incorporation. Reducing the total pressure to 7.4 Torr resulted in detectable C incorporation throughout the film. The Fourier transform infrared spectra of both films revealed in-plane B-N stretching indicative of sp^2 bonding, with the film grown at 7.4 Torr exhibiting a larger full-width-half-maximum, which indicates reduced crystallinity. The H_2 and Ar flow rates used at both pressures were 30 and 40.5 sccm, respectively, which translate roughly to $H_2/(B+N) = 1.46$, and $Ar/(B+N) = 1.98$. These conditions have been simulated to calculate the two phase diagrams shown in Figure 5.6.4. Figure 5.6.4 (a) shows that at 740 Torr, 1000 °C and a composition of N/B = 40, equilibrium calculations predict the co-deposition of C along with h-BN, which contradict the reported absence of detectable C. Figure 5.6.4 (b) shows the 7.4 Torr condition where equilibrium calculations do predict the co-deposition of C with h-BN, which agrees with the experimental observation. For the 7.4 Torr condition, the N/B composition at 1000 °C falls much deeper into the h-BN + C phase-field than for that of the 740 Torr condition. The discrepancy for the 740 Torr condition may be explained by gas phase kinetics. Jin et al. [6] noted that the use of 740 Torr was accompanied by a dramatic decrease in the growth rate in association with homogenous nucleation of fine particles in the reactor chamber during growth. TEB and NH_3 are increasingly likely to react parasitically with one another to form adducts in the gas phase before reaching the substrate as a direct function of increasing total system pressure [4]. At higher pressures, the mean free path of gas particles decrease, and therefore any active C species from TEB in the gas phase is more likely to be fully consumed by NH_3 and H_2.

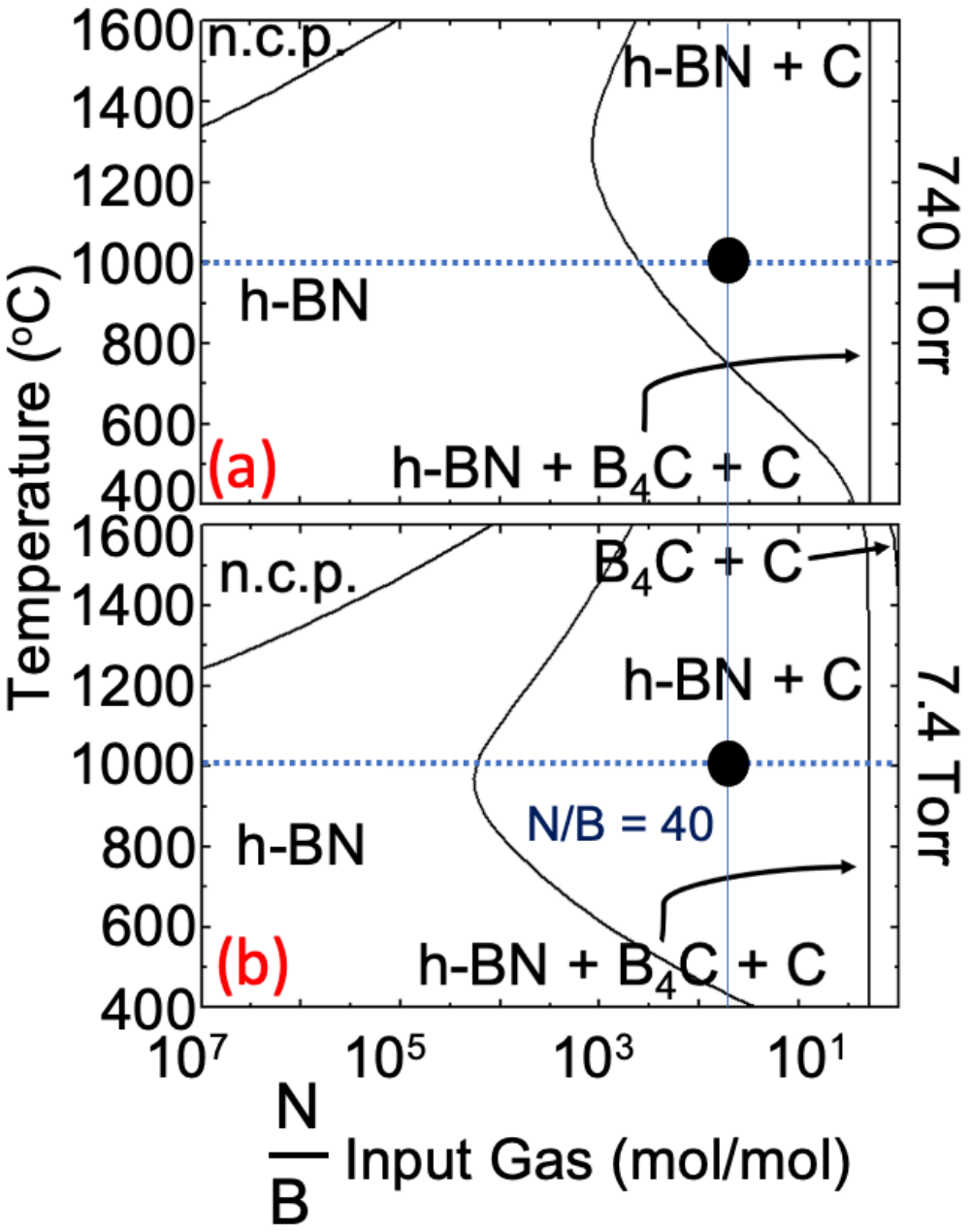

Figure 5.6.4: TEB/NH_3/H_2/Ar phase diagrams with H_2/(B+N) = 1.46 and Ar/(B+N) = 1.98 calculated at (a) 740 Torr and (b) 7.4 Torr. The solid black circles indicate in both cases where the N/B composition experimentally employed by Jin et al. [6] exists in the phase diagrams.

Chubarov et al. [14] extensively studied the effect of CVD growth parameters such as temperature, N/B ratio, and B/H_2 atomic ratio on the structure, composition, and crystalline nature of sp^2 BN films. The authors used *c*-plane sapphire wafers on which was deposited a few nm thick AlN buffer layer as substrates. The TEB flow rate was fixed while the NH_3 flow rate varied in order change the N/B ratio in the range of 300 – 1000. It was determined by X-ray pole figure measurements that using a deposition temperature of 1500 °C, and N/B ratios within the range of 615 – 770 yielded epitaxial r-BN films. Films grown at N/B ratios outside of that range at the same temperature all yielded t-BN. The incorporation of C in the films was not reported for any of the N/B conditions grown at 1500 °C. At a constant N/B ratio of 615, the temperature was varied from 1300 to 1600 °C, and it was determined using time-of-flight elastic recoil detection analysis that C and O impurities in the BN films increased as temperature decreased (0.5 and 0.8 at.% for C and O, respectively at 1500 °C; and 0.7 and 1.3 at.% for C and O, respectively, at 1300 °C). Epitaxial r-BN was only achieved at 1500 °C, while t-BN was realized at all other temperatures. Figure 5.6.5 shows the phase diagram for this experimental system and indicates where equilibrium calculations predict the various (N/B, T) conditions should exist. The total chamber pressure used was 75 Torr, and the B/H_2 atomic ratio was 0.02%, which translates approximately to $H_2/(B + N) = 8.12$. For the constant N/B = 615 condition, the phase diagram shows that a decrease in temperature results in co-deposition of C with h-BN, which partially agrees with the experimental results, although the increase in C content as the temperature was lowered from 1500 to 1300 °C was small (0.2 at.%). Below 1500 °C, t-BN was observed, and its formation was attributed to the increased inclusion of C and O impurities. Further, the experimental observation of r-BN in the h-BN phase-field is of significant interest. As previously mentioned, the difference in the Gibbs free energy of h-BN and r-BN calculated

from the thermodynamic data of these polymorphs used in this work is extremely small, and at 1500 °C (and atmospheric pressure) is expected to be just ~ 0.2 kJ/mol.

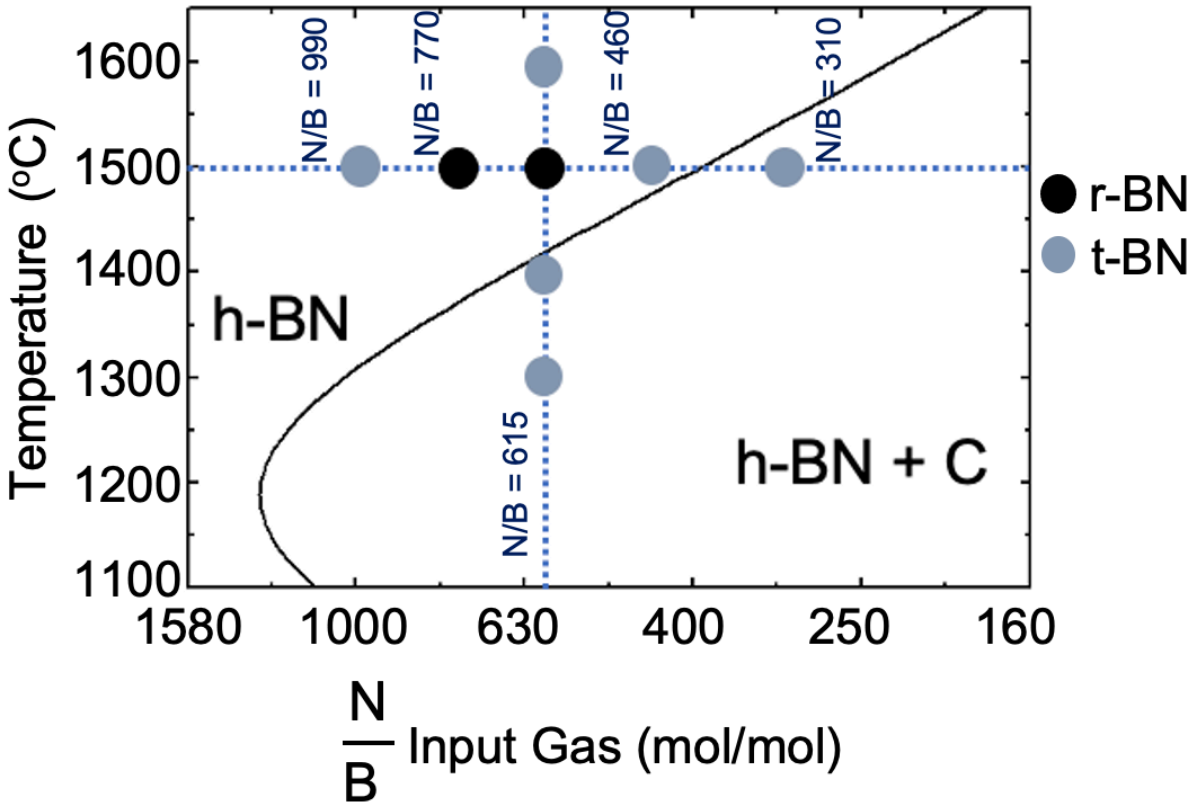

Figure 5.6.5: TEB/NH_3/H_2 phase diagram with pressure set to 75 Torr and H_2/(B+N) = 8.12. The circles indicate where the (N/B, T) conditions experimentally employed by Chubarov et al. [14] exist in the phase diagram.

The information presented in the foregoing calculated equilibrium phase diagrams and the discussion of the experimental results described in the literature indicate that C is more easily incorporated into BN films at lower chamber pressures, and that the presence of H_2 in the total gas mixture as a carrier and diluent tends to suppress C. An example of a set of process conditions for single-phase deposition of h-BN (thus avoiding C co-deposition) via CVD over a

large temperature range have been identified from these equilibrium calculations and include an N/B ratio of ~10^3 , a total pressure of 100 Torr and a H_2/(B + N) ratio of 10. Experimentally, comparable conditions can be met provided that a sufficiently low flow rate of TEB (in the range of tens of μmol/min) is used. Typically, N/B gas phase ratios used in h-BN synthesis from TEB/NH_3 chemistry in a H_2 atmosphere are on the order of 10^2 – 10^3, with chamber pressures in the 10^1 – 10^2 Torr range [4,5,7,14,40]. Thus, most of the recent investigations concerning the CVD synthesis of h-BN have been conducted at conditions that already help suppress the incorporation of C in growing films, which may explain why C incorporation in h-BN films synthesized in this manner largely goes unreported. The main disadvantages in using the phase diagrams presented in this work to predict C in the CVD synthesis of h-BN from the TEB/NH_3/H_2 system is that equilibrium calculations do not account for growth parameter-dependent kinetic processes. For example, the research of Jin et al. [6] showed that higher chamber pressures increase the likelihood of parasitic gas phase reactions which can lead to enhanced removal of C. Thus, using strictly equilibrium calculations can potentially lead to a false prediction of C. Further, the close values for the Gibbs free energy of the h-BN and r-BN used in this work complicates the prediction of one polymorph over the other, especially at temperatures approaching 1500 °C [41].

5.7 Conclusions

The principal objective of this study has been to determine the conditions revealed by calculated CVD phase diagrams for the deposition of h-BN from TEB/NH_3/H_2 mixtures that avoid the co-deposition of C and B_4C. The results indicate that the equilibrium formation of single-phase h-BN is highly dependent on the temperature, total pressure, input reactant composition (N/B) and the H_2 diluent concentration (H_2/B+N) . An example of a set of

equilibrium conditions for producing h-BN, without co-deposition of C were found to be: N/B = ~ 10^3, H_2/(B+N) = 10, and a total pressure of 100 Torr. It was observed that in equilibrium, increasing the pressure extends h-BN stability while decreasing that of C and B_4C. Increasing the H_2/(B+N) ratio suppresses both the formation of C and the decomposition of NH_3 to NH_2 that is imperative for the deposition of h-BN at higher temperatures. Comparison of these results with experimental results reported in literature revealed that the use of H_2 as the carrier and diluent, N/B ratios in the 10^2 – 10^3 range, pressures in the 10^1 – 10^2 Torr range, and temperatures within the range of 1000 °C to 1500 °C are suitable conditions to produce epitaxial sp^2 BN with TEB/NH_3 chemistry. The limitations of using the equilibrium calculations to predict C during CVD h-BN synthesis were also discussed.

5.8 Acknowledgements

Funding for this project was made possible thanks to the National GEM Consortium Fellowship, Neil and Jo Bushnell Fellowship in Engineering, and the John and Claire Bertucci Fellowship.

5. References

[1] K. Watanabe, T. Taniguchi, and H. Kanda, Nat. Mater. **3**, 404 (2004). DOI:10.1038/nmat1134.
[2] C. R. Dean, A. F. Young, I. Meric, C. Lee, L. Wang, S. Sorgenfrei, K. Watanabe, T. Taniguchi, P. Kim, K. L. Shepard, and J. Hone, Nat. Nanotechnol. **5**, 722 (2010). DOI:10.1038/nnano.2010.172.
[3] K. Nakamura, J. Electrochem. Soc. **133**, 1120 (1986). DOI:10.1149/1.2108797.
[4] Y. Kobayashi and T. Akasaka, J. Cryst. Growth **310**, 5044 (2008). DOI:10.1016/j.jcrysgro.2008.07.010.
[5] Q. S. Paduano, M. Snure, J. Bondy, and T. W. C. Zens, Appl. Phys. Express **7**, 1 (2014). DOI:10.7567/APEX.7.071004.
[6] Y. Jin, S. Lee, Y. Nam, J. K. Lee, and D. Park, Korean J. Chem. Eng. **15**, 652 (1998).
[7] Y. Kobayashi and T. Makimoto, Japanese J. Appl. Physics, Part 1 Regul. Pap. Short Notes Rev. Pap. **45**, 3519 (2006). DOI:10.1143/JJAP.45.3519.
[8] S. Majety, J. Li, W. P. Zhao, B. Huang, S. H. Wei, J. Y. Lin, and H. X. Jiang, Appl. Phys. Lett. **102**, (2013). DOI:10.1063/1.4808365.
[9] M. Imam, C. Höglund, J. Jensen, L. Hultman, J. Birch, H. Pedersen, K. Gaul, A.

Stegmüller, and R. Tonner, J. Mater. Chem. C **3**, 10898 (2015). DOI:10.1039/C5TC02293B.
[10] D. Chugh, J. Wong-Leung, L. Li, M. Lysevych, H. H. Tan, and C. Jagadish, 2D Mater. **5**, (2018). DOI:10.1088/2053-1583/aad5aa.
[11] L. Souqui, J. Palisaitis, H. Högberg, and H. Pedersen, J. Mater. Chem. C **8**, 4112 (2020). DOI:10.1039/d0tc00616e.
[12] M. Imam, C. Höglund, S. Schmidt, R. Hall-Wilton, J. Birch, and H. Pedersen, J. Chem. Phys. **148**, (2018). DOI:10.1063/1.5006886.
[13] Ö. Danielsson, A. Henry, and E. Janzén, J. Cryst. Growth **243**, 170 (2002). DOI:10.1016/S0022-0248(02)01486-0.
[14] M. Chubarov, H. Pedersen, H. Högberg, J. Jensen, and A. Henry, Cryst. Growth Des. **12**, 3215 (2012). DOI:10.1021/cg300364y.
[15] K. E. Spear, Pure Appl. Chem. **54**, (1982).
[16] A. I. Kingon, L. J. Lutz, P. Liaw, and R. F. Davis, J. Am. Ceram. Soc. **66**, 558 (1983). DOI:10.1111/j.1151-2916.1983.tb10091.x.
[17] J. Thomas, Jr., N. E. Weston, and T. E. O'Connor, Phys. Inorg. Chem. **84**, 4619 (1963). DOI:10.1021/ja00883a001.
[18] S. Alkoy, C. Toy, T. Gönül, and A. Tekin, J. Eur. Ceram. Soc. **17**, 1415 (1997). DOI:10.1016/S0955-2219(97)00040-X.
[19] V. L. Solozhenko, High Press. Res. **13**, 199 (1995). DOI:10.1080/08957959508200884.
[20] V. L. Solozhenko and K. S. Gavrichev, in *Wide Band Gap Electron. Mater.*, edited by M. Prelas, P. Gielisse, G. Popovici, B. Spitsyn, and T. Stacy, 1st ed. (Kluwer Academic Publishers, Minsk, Belarus, 1995), pp. 377–392. DOI:10.1007/978-94-011-0173-8.
[21] M. Okamoto, Y. Utsumi, and Y. Osaka, Plasma Sources Sci. Technol. **2**, 1 (1993). DOI:10.1088/0963-0252/2/1/001.
[22] A. Weber, U. Bringmann, R. Nikulski, and C. P. Klages, Surf. Coatings Technol. **60**, 493 (1993). DOI:10.1016/0257-8972(93)90139-F.
[23] W. J. Zhang, Y. M. Chong, I. Bello, and S. T. Lee, J. Phys. D. Appl. Phys. **40**, 6159 (2007). DOI:10.1088/0022-3727/40/20/S03.
[24] S. Matsumoto and W. J. Zhang, Diam. Relat. Mater. **10**, 1868 (2001).
[25] M. Chubarov, H. Pedersen, H. Högberg, Z. Czigany, and A. Henry, CrystEngComm **16**, 5430 (2014). DOI:10.1039/c4ce00381k.
[26] L. Bourgeois, Y. Bando, and T. Sato, J. Phys. D. Appl. Phys. **33**, 1902 (2000). DOI:10.1088/0022-3727/33/15/321.
[27] M. Chubarov, H. Pedersen, H. Högberg, V. Darakchieva, J. Jens, P. Persson, and A. Henry, Phys. Status Solidi RRL **5**, 397 (2011). DOI:10.1002/pssr.201105410.
[28] H. Pedersen, B. Alling, H. Högberg, and A. Ektarawong, J. Vac. Sci. Technol. A **37**, 040603 (2019). DOI:10.1116/1.5107455.
[29] P. M. Jean-Remy and R. F. Davis, MRS Commun. **XX**, 1 (2021). DOI:10.1557/s43579-021-00053-9.
[30] M. A. Reshetnikov, Zh. Neorg Chim **11**, 1489 (1969).
[31] C. W. Bale, E. Bélisle, P. Chartrand, S. A. Decterov, G. Eriksson, A. E. Gheribi, K. Hack, I. H. Jung, Y. B. Kang, J. Melançon, A. D. Pelton, S. Petersen, C. Robelin, J. Sangster, P. Spencer, and M. A. Van Ende, Calphad Comput. Coupling Phase Diagrams Thermochem. **54**, 35 (2016). DOI:10.1016/j.calphad.2016.05.002.
[32] A. T. Dinsdale, Calphad **15**, 317 (1991). DOI:10.1016/0364-5916(91)90030-N.

[33] H. O. Pierson and A. W. Mullendore, in *Proc. 7th Int. Conf. Chem. Vap. Depos.*, edited by T. O. Segwick and H. Lydtin (The Electrochemical Society, Princeton, 1979), p. 360.
[34] J. S. Lewis, S. Vaidyaraman, W. J. Lackey, K. Agrawal, G. B. Freeman, and E. K. Barefield ', Mater. Lett. **27**, 327 (1996). DOI:10.1016/0167-577X(96)00014-6.
[35] H. Pedersen, C. Höglund, J. Birch, J. Jensen, and A. Henry, Chem. Vap. Depos. **18**, 221 (2012). DOI:10.1002/cvde.201206980.
[36] B. Beaumont, P. Gibart, and J. P. Faurie, J. Cryst. Growth **156**, 140 (1995). DOI:10.1016/0022-0248(95)00296-0.
[37] A. Koukitu, N. Takahashi, and H. Seki, Japanese J. Appl. Physics, Part 2 Lett. **36**, (1997). DOI:10.1143/jjap.36.l1136.
[38] R. F. Davis, in *Compr. Semicond. Sci. Technol.*, edited by P. Bhattacharya, R. Fornari, and H. Kamimura (Elsevier B.V., Amsterdam, 2011), pp. 339–367. DOI:10.1016/j.jallcom.2009.02.108.
[39] T. F. Kuech, in *Handb. Cryst. Growth*, edited by T. F. Kuech, 2nd ed. (Elsevier B.V., Madison, WI, USA, 2015), pp. 869–907. DOI:10.1016/B978-0-444-63304-0.00021-4.
[40] Y. Kobayashi, T. Nakamura, T. Akasaka, T. Makimoto, and N. Matsumoto, J. Cryst. Growth **298**, 325 (2007). DOI:10.1016/j.jcrysgro.2006.10.034.
[41] M. Chubarov, H. Pedersen, H. Högberg, Z. Czigány, M. Garbrecht, and A. Henry, Chem. Mater. **27**, 1640 (2015). DOI:10.1021/cm5043815.

5.9 Supplementary Information for: Thermodynamic Calculations for the Chemical Vapor Deposition of Hexagonal Boron Nitride Using Triethylboron, Ammonia, and Hydrogen

Standard state thermodynamic properties of phase diagram input reactants ($B(C_2H_5)_3$ (g) (triethylboron, TEB), NH_3 (g), H_2 (g), and Ar (g)) and expected condensed species (C (graphite) (s), B_4C (s), h-BN (s), and r-BN (s)) from the TEB/NH_3/H_2(and/or)Ar system:

The standard state thermodynamic properties of the aforementioned gaseous and condensed species relevant for the calculation of phase diagrams in this work are referenced from the FactPS database [1], native to the full version of the FactSage computational software package (Version 8.0, CRCT – Thermfact, Inc. and GTT Technologies). Except for h-BN (s) and r-BN (s), whose properties are referenced [2,3] and discussed in the paper, the thermodynamic properties of all other calculated equilibrium species are referenced from [1].

Table 5.9.S1: Standard state properties of relevant reactants and condensed products.

	S^o (298 K) (J/mol K)	ΔH^o_f (298 K) (J/mol)
TEB (g)	4.38×10^2	-1.58×10^5
NH_3 (g)	1.93×10^2	-4.59×10^4
H_2 (g)	1.30×10^2	-
Ar (g)	1.55×10^2	-
C (graphite) (s)	5.74	-
B_4C (s)	27.18	-6.27×10^4
h-BN (s)	14.81	-2.51×10^5
r-BN (s)	15.83	-2.48×10^5

The heat capacity $C_p(T)$ of the aforementioned relevant species can be expressed in the form

$$C_p = \sum_i^n C_{(i)} T^{P(i)} \qquad 5.9S(1)$$

The $C_{(i)}$ and P(i) for each increment of *i* as well as the temperature range validity is specified for each of the aforementioned species in the following tables. As the temperature range used in the work was 400 – 1600 °C, the $C_p(T)$ of TEB had to be extrapolated in order for calculations beyond 1000 K to be performed.

Table 5.9.S2: **TEB (g)**

Valid for 1 atm, 298 - 1000 K		
i	**$C_{(i)}$**	**P(i)**
1	5.31E+00	0
2	5.96E-01	1
3	-2.33E-04	2

Table 5.9.S3: **NH_3 (g)**

Valid for 1 atm, 298 - 1800 K		
i	**$C_{(i)}$**	**P(i)**
1	2.87E+01	0
2	5.38E+05	-2
3	-2.88E+03	-1
4	3.77E-02	1
5	-7.53E-06	2
Valid for 1 atm, 1800 - 5100 K		
i	**$C_{(i)}$**	**P(i)**
1	1.74E+02	0
2	-2.73E+07	-2
3	-5.89E+03	-0.5
4	8.08E+01	0
5	-5.58E-03	1
6	9.79E+04	-1

Table 5.9S4: **H_2 (g)**

Valid for 1 atm, 298 - 1200 K		
i	**$C_{(i)}$**	**P(i)**
1	1.98E+01	0
2	-2.95E+05	-2
3	1.95E+02	-0.5
4	3.08E-03	1
5	1.43E-06	2
Valid for 1 atm, 1200 - 4100 K		
i	**$C_{(i)}$**	**P(i)**
1	1.44E+01	0
2	2.08E+07	-2
3	2.13E+03	-0.5
4	2.06E-03	1
5	-7.44E+04	-1

Table 5.9.S5: **Ar (g)**

Valid for 1 atm, 298 - 6000 K		
i	**$C_{(i)}$**	**P(i)**
1	20.79	0

Table 5.9.S6: **C (graphite) (s)**		
Valid for 1 atm, 298 - 1000 K		
i	**$C_{(i)}$**	**P(i)**
1	6.12E+01	0
2	8.26E+05	-2
3	-6.60E+06	-3
4	-8.02E-03	1
5	-1.02E+03	0.5
Valid for 1 atm, 1000 - 6000 K		
i	**$C_{(i)}$**	**P(i)**
1	2.48E+01	0
2	-2.88E+06	-2
3	9.59E-04	1
4	-3.97E+01	-0.5

Table 5.9.S8: **h-BN (s)**		
Valid for 1 atm, 298 - 3000 K		
i	**$C_{(i)}$**	**P(i)**
1	3.51E+01	0
2	1.22E-02	1
3	-1.77E+06	-2
4	-2.39E-06	2

Table 5.9.S7: **B_4C (s)**		
Valid for 1 atm, 298 - 600 K		
i	**$C_{(i)}$**	**P(i)**
1	2.41E+01	0
2	-2.47E+06	-2
3	2.94E-03	1
Valid for 1 atm, 600 - 3200 K		
i	**$C_{(i)}$**	**P(i)**
1	6.59E+02	0
2	-2.41E+07	-2
3	-7.89E+00	0.5
4	6.48E-02	1
5	2.52E+05	-1
6	-1.86E+04	-0.5

Table 5.9.S9: **r-BN (s)**		
Valid for 1 atm, 298 - 3000 K		
i	**$C_{(i)}$**	**P(i)**
1	3.39E+01	0
2	1.32E-02	1
3	-1.61E+06	-2
4	-2.50E-06	2

Table 5.9.S10: Chemical reactions (and their associated equilibrium constants) considered for the production of BN (s), B_4C (s), and C (s) using TEB (g) and NH_3 (g) as starting reagents which take into account the β-hydride elimination of TEB and its H_2-assisted elimination of ethane in the presence of H_2

	β-hydride elimination	
BN	$B(C_2H_5)_3(g) + NH_3(g) \rightleftharpoons BN(s) + 3\ C_2H_2(g) + 6\ H_2(g)$ $\ln(K_{eq}) = -8.14 \times 10^4 / T + 103.42$	5.9.S (2)
B_4C	$8\ B(C_2H_5)_3(g) \rightleftharpoons 2\ B_4C(s) + 23\ C_2H_2(g) + 37\ H_2(g)$ $\ln(K_{eq}) = -7.96 \times 10^5 / T + 790.88$	5.9.S(3)
C	$B(C_2H_5)_3(g) \rightleftharpoons 2\ C(s) + BH_3\ (g)\ 2\ C_2H_2(g) + 4\ H_2(g)$ $\ln(K_{eq}) = -8.92 \times 10^4 / T + 88.90$	5.9.S(4)
	H_2-assisted ethane elimination	
BN	$B(C_2H_5)_3(g) + NH_3(g) + 3\ H_2(g) \rightleftharpoons BN(s) + 6\ CH_4\ (g)$ $\ln(K_{eq}) = 6.41 \times 10^4 / T + 4.90$	5.9.S(5)
B_4C	$4\ B(C_2H_5)_3(g) + 16\ H_2\ (g) \rightleftharpoons B_4C(s) + 23\ CH_4\ (g)$ $\ln(K_{eq}) = 1.60 \times 10^5 / T + 17.77$	5.9.S(6)
C	$B(C_2H_5)_3(g) + 4\ H_2\ (g) \rightleftharpoons C(s) + BH_3\ (g) + 5\ CH_4\ (g)$ $\ln(K_{eq}) = 1.86 \times 10^4 / T + 10.01$	5.9.S(7)

The standard state Gibbs free energy change as a function of temperature of reactions 5.9S(2) – (7) as well as their corresponding equilibrium constants in the form of $\ln(K_{eq})$ vs 1/T are plotted in Figure 5.9.S1.

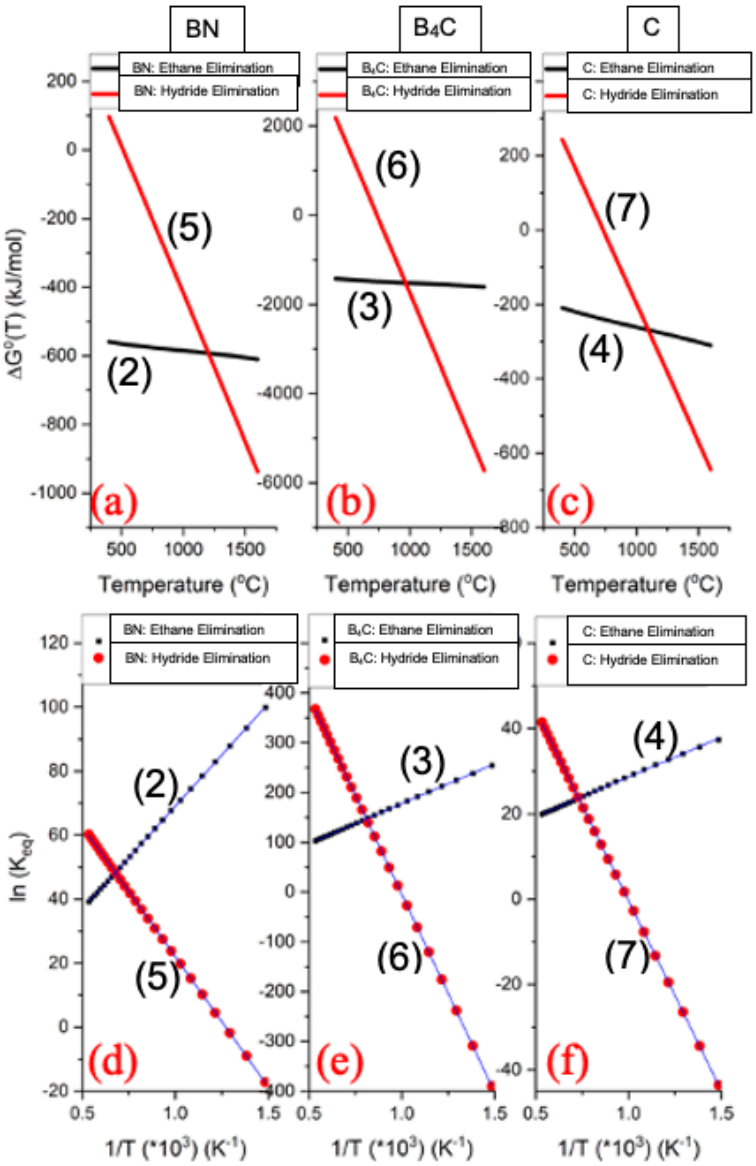

Figure 5.9.S1: $\Delta G^{o}(T)$ of reactions (2) and (5), (3) and (6), and (4) and (7) in (a), (b), and (c), respectively; and their corresponding $\ln(K_{eq})$ vs 1/T plots in (d), (e), and (f), respectively.

Calculation of equilibrium gaseous and solid species given the starting conditions of $B/(B + N) = 0.001$ ($N/B = 999$), $H_2/(B + N) = 0 – 100$, temperature in the range of 400 – 1600 ^oC, and pressure in the range of 0.01 – 100 Torr:

Regarding the calculation of equilibrium gaseous (in partial pressure (Torr)) and solid species (in moles) as illustrated in Figure 5.6.3 of the paper, the specific reactant amounts in moles that satisfy the $B/(B + N) = 0.001$ condition (and the TEB + NH_3 + H_2 = 1 mole condition) for $H_2/(B + N) = 0$, 10, and 100 are summarized in Table 5.9.S11.

Table 5.9.S11: Initial input reactant conditions used for the calculations in Figure 5.6.3.

Amount of reactant in moles			
H_2/(B+N)	**TEB**	**NH_3**	**H_2**
0	0.001	0.999	0
10	0.000090909	0.090818	0.90909
100	0.000009901	0.009891	0.9901

Supplementary Tables 5.9.S12 and 5.9.S13 show equilibrium partial pressures of several gaseous species not shown in Figure 4 of the paper. Table 5.9.S12 shows the equilibrium gas phase composition at T = 1000 and 1500 ^oC and total pressures of 0.01 and 100 Torr, while $H_2/(B + N) = 0$. Table 5.9.S13 shows the equilibrium gas phase composition at the same conditions except for $H_2/(B + N) = 10$.

Table 5.9.S12: **TEB/NH_3/H_2 System: Equilibrium Gas Phase Composition at 1000 and 1500 °C (B/(B+N) = 0.001; H_2/(B + N) = 0**

	Species partial pressure (Torr)			
Species	P = 0.01 Torr T = 1000 °C	P = 100 Torr T = 1000 °C	P = 0.01 Torr T = 1500 °C	P = 100 Torr T = 1500 °C
H_2	7.51E-03	7.50E+01	6.93E-03	7.49E+01
BH_3	4.49E-14	4.48E-10	1.50E-10	3.71E-06
N_2	2.49E-03	2.49E+01	2.40E-03	2.48E+01
NH	1.71E-17	1.71E-13	3.65E-13	3.86E-09
NH_2	2.39E-15	2.39E-09	2.93E-13	3.22E-07
NH_3	6.03E-12	6.03E-04	1.18E-12	1.35E-04
HCN	6.84E-07	6.84E-03	2.18E-05	2.30E-01
CH_3	3.63E-12	3.62E-06	1.16E-10	1.31E-04
CH_4	6.91E-10	6.90E-02	5.01E-11	5.86E-03
C_2H_2	3.29E-09	3.29E-05	1.11E-06	1.20E-02
C_2H_4	1.18E-13	1.17E-05	2.58E-13	3.02E-05
C_2H_6	3.29E-09	8.77E-08	1.11E-06	4.12E-09

Table 5.9.S13: **TEB/NH_3/H_2 System: Equilibrium Gas Phase Composition at 1000 and 1500 °C (B/(B+N) = 0.001; H_2/(B + N) = 10**

	Species partial pressure (Torr)			
Species	P = 0.01 Torr T = 1000 °C	P = 100 Torr T = 1000 °C	P = 0.01 Torr T = 1500 °C	P = 100 Torr T = 1500 °C
H_2	9.58E-03	9.58E+01	8.86E-03	9.57E+01
BH_3	1.58E-13	1.58E-09	1.89E-10	1.31E-05
N_2	4.15E-04	4.16E+00	3.99E-04	4.13E+00
NH	7.89E-18	7.89E-14	1.68E-13	1.78E-09
NH_2	1.25E-15	1.25E-09	1.53E-13	1.68E-07
NH_3	3.55E-12	3.55E-04	6.99E-13	7.99E-05
HCN	3.16E-07	1.36E-03	4.25E-06	4.15E-02
CH_3	5.23E-12	2.26E-06	7.13E-11	7.37E-05
CH_4	1.13E-09	4.86E-02	3.47E-11	3.74E-03
C_2H_2	4.20E-09	7.84E-06	2.55E-07	2.33E-03
C_2H_4	1.92E-13	3.57E-06	7.58E-14	7.50E-06
C_2H_6	1.83E-19	3.41E-08	1.22E-21	1.31E-09

5.9. Supplementary References

[1] C. W. Bale, E. Bélisle, P. Chartrand, S. A. Decterov, G. Eriksson, A. E. Gheribi, K. Hack, I. H. Jung, Y. B. Kang, J. Melançon, A. D. Pelton, S. Petersen, C. Robelin, J. Sangster, P. Spencer, and M. A. Van Ende, Calphad Comput. Coupling Phase Diagrams Thermochem. **54**, 35 (2016). DOI:10.1016/j.calphad.2016.05.002.

[2] V. L. Solozhenko, High Press. Res. **13**, 199 (1995). DOI:10.1080/08957959508200884.

[3] V. L. Solozhenko and K. S. Gavrichev, in *Wide Band Gap Electron. Mater.*, edited by M. Prelas, P. Gielisse, G. Popovici, B. Spitsyn, and T. Stacy, 1st ed. (Kluwer Academic Publishers, Minsk, Belarus, 1995), pp. 377–392. DOI:10.1007/978-94-011-0173-8.

6. Paper 3: Flow-modulated Deposition of sp^2-Boron Nitride Using Diborane and Ammonia on Chemo-mechanically Polished (0001) 4H-SiC Substrates

Philip M. Jean-Remy[1, a)], Matthew J. Cabral[1], and Robert F. Davis[1, 2]

[1] Department of Materials Science and Engineering, Carnegie Mellon University, Pittsburgh, PA, 15213, USA

[2] Department of Electrical and Computer Engineering, Carnegie Mellon University, Pittsburgh, PA, 15213, USA

[a)] Electronic mail: pjeanrem@andrew.cmu.edu

6.1 Abstract

Nanocrystalline sp^2-BN thin films have been grown on (0001) 4H-SiC substrates at 1030 °C via continuous flow and discontinuous flow-modulated chemical vapor deposition (CVD) techniques using diborane (B_2H_6) and ammonia (NH_3) as the B- and N sources, respectively. The latter technique enabled observations of both the effect of hydrogen purge steps between precursor injections and the length of injection times for B_2H_6 on the stoichiometry and microstructure of the films. Stoichiometric BN was achieved in all films grown continuously within the N/B gas phase ratio range of 20 – 200; this was not observed for the discontinuously grown films unless both the B_2H_6 flow rate and the injection time were minimized. Cross-section transmission electron microscopy of films grown both continuously and discontinuously at N/B = 200 and using short B_2H_6 injection times relative to that of NH_3 for the latter process route revealed the initial growth of ~4 nm thick partially ordered sp^2-BN layers. A transition zone then formed containing randomly oriented polycrystalline grains. Excess B incorporated into the discontinuously grown films during long B_2H_6 injection times resulted in single layer mixtures of amorphous and sp^2-BN without any observed ordering.

6.2 Introduction

The hexagonal phase of boron nitride (h-BN) possesses a two-dimensional (2D) hexagonal ring structure containing alternating B and N atoms. Thin films of h-BN are chemically inert, thermally stable, possess a large in-plane thermal conductivity [1,2], as well as a wide bandgap of about 6 eV and can be doped with sufficiently shallow acceptor atoms to produce p-type conductivity [3,4]. It has been shown that h-BN/SiO_2/Si based photodetectors can be fabricated with an on/off ratio > 10^3 operating under 212 nm DUV light [5]. Heterostructures of p-h-BN/n-$Al_xGa_{1-x}N$ that exhibit rectifying behavior have been fabricated; however, DUV emission has not yet been realized [6,7]. As h-BN is chemically inert and possesses a 1.7% lattice mismatch with graphene, it also has been used as dielectric layers for graphene-based transistors [8,9]. Hexagonal BN and the companion 2D polytype of rhombohedral (r) BN are bonded via sp^2-hybridization. The ABAB… stacking sequence of h-BN is the only structural difference that distinguishes it from the ABCABC… sequence of r-BN [10]. The in-plane and out-of-plane lattice parameters of these two polytypes are very similar; thus, advanced characterization techniques such as grazing incidence x-ray diffraction (XRD) and cross-sectional transmission electron microscopy (TEM) are required to distinguish the crystal structure of one polytype from the other [11,12]. BN also forms a less ordered sp^2-BN phase called turbostratic (t) BN which retains a high degree of in-plane order of BN hexagonal rings; however, its layers are roughly parallel, as well as randomly rotated and translated with respect to the *c* axis of the structure [13]. In addition to turbostratic disorder, sp^2-BN can also contain puckering, a type of defect described as the waviness of the basal planes [14,15] causing variations in the (000*l*) interplanar spacing beyond the 0.33 nm reported for the (0002) and (0003) planes of h-BN and r-BN, respectively [13,16,17].

Chemical vapor deposition (CVD) is the most common method utilized for the growth of sp^2-BN films. Triethylboron (TEB, $B(C_2H_5)_3$) and ammonia (NH_3) have become the B- and N-containing precursors of choice for deposition over a wide range of temperatures from 1000 to 1500 °C on substrates such as *c*-plane α-Al_2O_3 [18–21] and (0001) (4H, 6H)-SiC [22–24]. It has been predicted [25] and shown experimentally [26,27] that high substrate temperatures of ~ 1500 °C are useful in the epitaxial growth of these films using TEB and NH_3. The use of growth temperatures at the higher end of this range can be bypassed in favor of temperatures closer to 1000 °C when TEB and NH_3 and N/B gas phase ratios > 1000 are employed; however, film growths often self-terminates after a few nm [18,19]. The high N/B ratios lead to self-termination because of parasitic reactions between TEB and NH_3 in the gas phase prior to reaching the substrate surface [22]. To avoid this problem, these precursors can be injected into the deposition chamber separately and sequentially, thereby limiting film-forming reactions to the substrate surface using the CVD method called flow-modulated (or digital) epitaxy (FME) [22,28–30]. However, because TEB contains C in its molecular structure, it has been determined that this element can become incorporated during growth of a FME-based sp^2-BN film if the nominal V/III ratio and choice of diluent gas are not optimized [30–33]. During conventional CVD where these precursors are simultaneously and continuously flowed into the chamber at high temperatures, C incorporation is rare, because the addition of N via NH_3 to TEB tends to starve the system of C in favor of sp^2-BN formation [34].

Diborane (B_2H_6) is an appealing B-source for the deposition of BN because it lacks any inherent C that could become incorporated into a growing film. However, it also reacts parasitically with NH_3 in the gas phase to produce hydrogen rich polymeric adducts beginning at 200 °C [35]. Yamada et al. [36,37] employed the FME process using B_2H_6 and NH_3 to deposit

epitaxial sp^2-BN on *c*-plane α-Al_2O_3 at a temperature of 1360 °C and N/B ratios in the 750 – 1500 range. However, experimentation with the length of either B_2H_6 or NH_3 injection pulses was not explored, and interrupting purge steps were not introduced between precursor pulses. Chubarov et al. were unable to achieve the deposition of epitaxial sp^2-BN on (0001) 6H-SiC substrates below 1500 °C using TEB and NH_3 at N/B ratios of 643 – 750 [38,39]. By contrast, deposition on (0001) AlN/α-Al_2O_3 substrates was achieved by these researchers at temperatures as low as 1200 °C. It was postulated that the mobility of the precursor-derived adatoms is lower on (0001) SiC surfaces than on (0001) AlN/α-Al_2O_3 surfaces which would limit the formation of epitaxial sp^2-BN layers on the former at lower temperatures [38]. Thus, the introduction of purge steps within the FME process could be important in both (1) the mitigation of parasitic gas phase reactions by insuring that that the chamber is free of one precursor before the introduction of the other, and (2) the promotion of epitaxial sp^2-BN at lower temperatures (~ 1000 °C) by allowing additional time for the adatoms to find equilibrium positions on a (0001) SiC surface.

The research reported herein investigated the comparison between sp^2-BN films on (0001) 4H-SiC grown at relatively low temperature (1030 °C) from continuous and FME-based CVD using B_2H_6 and NH_3 as the B- and N-source precursors, respectively. B_2H_6 was chosen to eliminate the risk of C incorporation into the growing films. Purge steps were included within the FME cycles between B_2H_6 and NH_3 injections. It was determined that regardless of the N/B ratio between 20 and 200, stoichiometric BN could be produced via continuous CVD, while the same was not true for FME-CVD unless a large nominal N/B ratio of 200 and short B_2H_6 injection times were used relative to that of NH_3. In general, the microstructure of the grown films ranged from amorphous to nanocrystalline. For select conditions of both continuous and FME depositions, a transition from the growth of a few-nm thick, continuous and partially-ordered

layers of sp^2-BN to the deposition of discontinuous and randomly orientated sp^2-BN layers was observed.

6.3 Experimental

BN thin films were grown on chemo-mechanically polished and resistively heated (0001) 4H-SiC (Cree, Inc.) substrates in a cold-wall, vertical shower-head configured reactor. B_2H_6 (5N-semiconductor grade 10% B_2H_6 in H_2) and NH_3 (99.9992% research grade) were the respective B and N precursors. The substrates were cleaned using a sequence of 10 minute sonications in both acetone and isopropanol to remove contamination and a 1:10 HF:DI water solution to remove surface oxide. After rinsing with DI water and drying with UHP N_2, they were loaded onto a planar SiC-coated graphite susceptor and placed inside the CVD chamber that was subsequently evacuated to less than 20 mTorr. As B_2H_6 reacts readily with water vapor to form an oxide in a BN film growth atmosphere, the chamber was heated for 15 minutes at 1000 ^{o}C in a dynamic atmosphere of 4 slm H_2 at a total pressure of 20 Torr to remove residual moisture from the chamber walls and the substrate surface prior to deposition. The chamber was then evacuated to a base pressure of $\leq 2.0 \times 10^{-6}$ Torr using a turbomolecular pump. This pump was subsequently isolated, the flow rates of the gases established using a vent line procedure, the substrate heated to 1030 °C and the process gases admitted into the chamber. A rotary vane process pump fitted with a back-streaming filter maintained a total chamber pressure of 10 Torr during each deposition. For each separate growth run, B_2H_6 was flowed at either 2 or 5 or 20 sccm, while the flow rate of NH_3 was kept constant at 0.80 slm to produce N/B ratios of either 200 or 80 or 20, respectively. H_2 flowing at a rate of 2 slm was used as the diluent gas for all growths.

Two series of FME growths were compared with conventional 1-hour CVD growths of the BN films. The samples in the FME and the conventional series are referred to as

"Discontinuous" and "Continuous," respectively. A full and repetitive FME cycle consisted of B_2H_6 injection, H_2 purge, NH_3 injection and a final H_2 purge. H_2 was constantly flowed during each deposition. During the purge steps, B_2H_6 and NH_3 were both re-routed to the roughing pump, such that only H_2 flowed through the chamber. The first series of FME growths, labeled as Discontinuous I (DI), utilized a sequence of 4 s B_2H_6 – 2 s H_2 – 4 s NH_3 – 2 s H_2. The goal of the DI series was to deliver the same amount of each reactant gas to the chamber as used in a companion continuous series. To achieve this, the duration of the B_2H_6 and the NH_3 pulses had to be equivalent. The number of cycles and the duration of the pulses were chosen such that multiplying the length of the injection pulse by the number of cycles provided the same amount of time for which B_2H_6 and NH_3 were supplied to the chamber in the continuous series. Thus, 900 cycles provided the equivalent of 3600 s (1 hour) of flow of both precursors. Adding in two H_2 2 s purge steps to the cycle sets a total cycle duration of 12 s; thus, 900 cycles resulted in a 3-hour total growth time, with B_2H_6 and NH_3 being supplied to the chamber for a total of 1 hour each. The second FME series, labeled Discontinuous II (DII) utilized a sequence of 1 s B_2H_6 – 2 s H_2 – 4 s NH_3 – 2 s H_2. The goal of series DII was to reduce the total amount of B_2H_6 flowing into the chamber by decreasing the B_2H_6 injection time and leaving all other parameters the same. Thus, 900 cycles of a DII series growth resulted in a total deposition time of 2.25 hours. The flow modulated cycle parameters for the DI and DII growth series are listed in Table 2. The 2 sccm B_2H_6 deposition conditions within the Continuous and DII series were repeated for 3.5 hours and 4.5 hours, respectively, in order to achieve thicker films for analysis by x-ray photoelectron spectroscopy (XPS) and TEM.

Thickness values for films with thickness greater than ~ 30 nm and less than ~ 30 nm were estimated using a Filmetrics spectral reflectance unit and a Panalytical X'Pert x-ray

reflectivity system, respectively. Atomic force microscopy (AFM) images were collected using an NT-MDT NTegra unit operated in the semi-contact mode with Cr/Pt-coated Si cantilevers possessing a resonant frequency of 190 kHz. A scan rate of 0.5 Hz was typically used, and 512 samples per line were sampled for 512 lines. All post-processing, including plane fit surface flattening (fifth order polynomial), and de-streaking as well as the calculation of the RMS surface roughness of the processed images were performed using Gwyddion software [40]. Raman spectroscopy of select samples was performed using an NT-MDT Spectra unit equipped with a 532 nm laser and a 600 lines/mm grating. The atomic composition and chemical bonding states at the surface of each film were determined from XPS spectra acquired using an Al Kα (1486.6 eV) anode x-ray emission source and a Staib cylindrical mirror analyzer. To prepare clean sample surfaces prior to XPS analyses, each film was subjected to (1) a sequence of 10 minute sonications in both acetone and isopropanol and dried with dry UHP N_2 and (2) electron beam heating for 30 minutes at ~1000 ^{o}C and 10^{-7} Torr to facilitate thermal desorption of contaminants. The XPS spectra were charge calibrated to the C 1s binding energy of 284.6 eV for adventitious carbon [41]. The subcomponents of the B 1s and N 1s spectra were modeled with mixed Gaussian (80%) – Lorentzian (20 %) distributions [42] and a non-linear background using curve-fitting software. Quantification of the XPS spectra for surface composition analysis was performed using CasaXPS (Casa Software Ltd); an escape depth correction was applied to each spectra using the electron attenuated length approximation [43]. Electron-transparent cross-sectional lamellae of the thin films were prepared for high resolution TEM (HRTEM) studies using an FEI Helios Plasma Dual Ion Beam milling system containing a Xe plasma source. Pt was deposited as a protection layer on top of the area of interest in the films prior to the milling steps. Cross-sectional TEM investigations with a FEI Themis 200 microscope

operated at 200 kV were conducted to determine the microstructure and BN phases within the films and at the substrate-film interfaces. Scanning TEM (STEM) in tandem with energy dispersive spectroscopy (EDS) were used to probe compositional changes across the BN/SiC interface of select samples. See supplementary material in Section 6.9 for the results of this latter study. Both 2θ-ω and grazing incidence x-ray diffraction (XRD) were employed to probe the crystallinity of the grown films; however no reflections for sp^2-BN were observed using either technique. The microstructural and electron diffraction data from TEM investigations presented below revealed that the sp^2-BN crystallites were a few nm in size and thus were too small and randomly oriented to produce observable reflections during XRD measurements.

6.4 Results and discussion

Table 6.4.1 shows the measured thickness of each film. Figure 6.4.1 shows the growth rates of the BN films as a function of B_2H_6 flow rate (q_B). As expected, the growth rate of the films increased as q_B increased for all three growth processes. At each given q_B, the DI series condition resulted in the fastest growth rates out of the three growth series. This can be attributed to the fact that with the DI series, the longest exposure times (4 s) of B_2H_6 were used, and the deposition of B from B_2H_6 was expected to occur readily at the growth temperature (1030 °C) used in this study [44,45]. Except for the high q_B of 20 sccm, the slowest growth rates were observed in the DII series, because of the shorter B_2H_6 exposure times (1 s) and thus the least amount of B_2H_6 supplied to the chamber for each growth.

Table 6.4.1. Thickness (in nm) of BN films.

B_2H_6 flow rate	N/B	Continuous	Discontinuous I	Discontinuous II
2 sccm	200	3.2 ± 0.3	107 ± 2.7	5.4 ± 0.5
5 sccm	80	30 ± 1.6	652 ± 17.2	39 ± 0.7
20 sccm	20	216 ± 3.9	4,457 ±187.8	1,006 ± 7.9

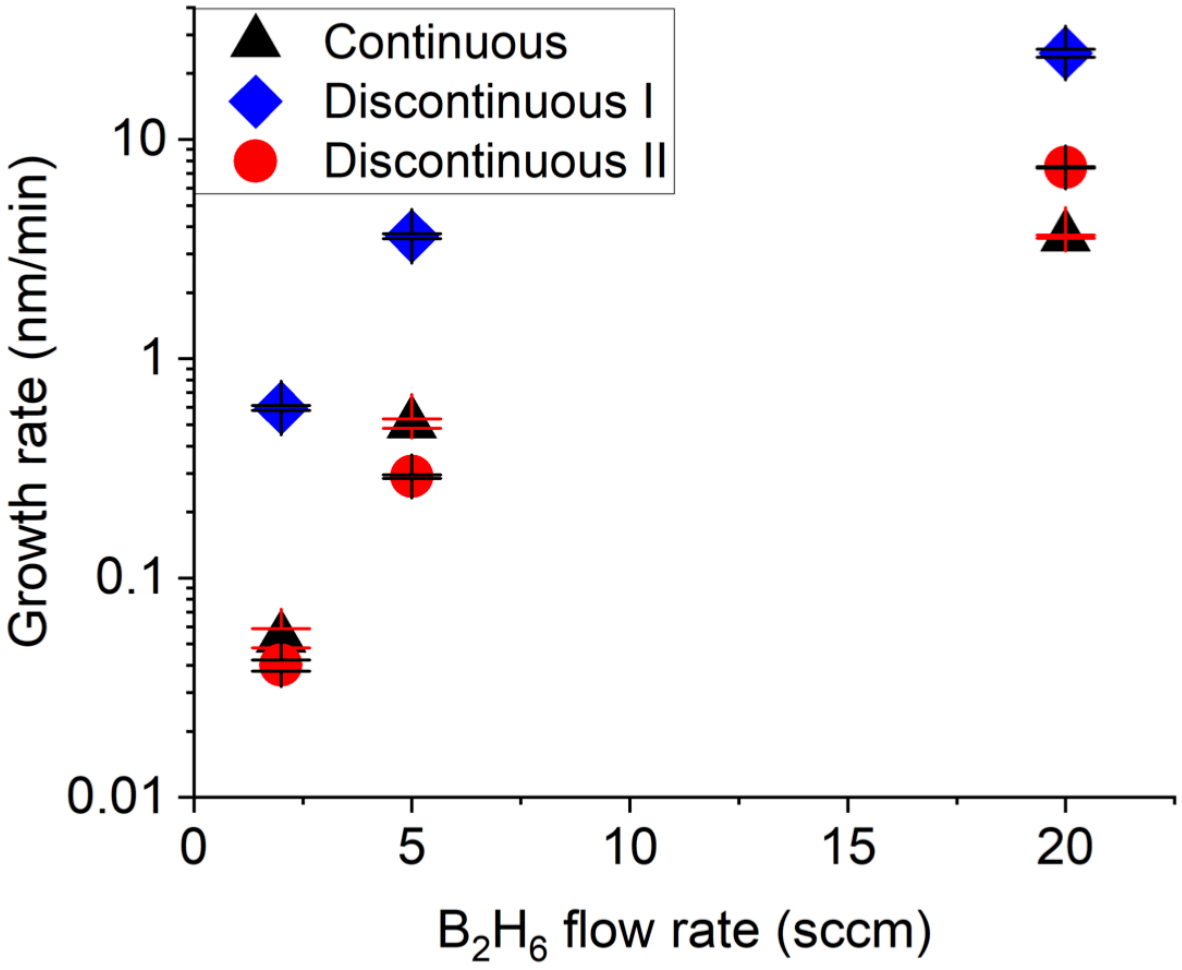

Figure 6.4.1. Growth rate of BN films on (0001) 4H-SiC substrates as a function of B_2H_6 flow rate for each method of CVD employed in this study.

Figure 6.4.2 shows the Raman spectra of the continuous, DI, and DII BN films grown using q_B = 20 sccm. The films grown at q_B = 2 and 5 sccm were unable to produce any measurable spectra unless longer growth times were employed. The peak in each spectrum is for

the E_{2g} vibrational mode which represents in-plane B-N stretching and is expected to occur near 1366 cm^{-1} for bulk sp^2-BN [46]. This figure shows that changing the growth method from continuous to discontinuous and varying the length of B_2H_6 injection pulses in the latter method from 4 s (DI) to 1 s (DII) had a strong effect on the intensity, full-width at half-maximum (FWHM) and position of the E_{2g} shift of the characteristic sp^2-BN peaks. Larger FWHM values for the peaks indicate smaller crystallite sizes [47] as well as the presence of t-BN inclusions [26], while shifts above the ideal value for bulk sp^2-BN indicate compressive film strain [48], likely induced by the sp^2-BN/4H-SiC in-plane lattice parameter mismatch. Of the three growth methods, it can be seen in Figure 2 that the continuously grown film exhibits both the most intense and narrowest (34.9 cm^{-1}) E_{2g} peak at 1374.0 cm^{-1}. The DI film exhibits the least intense and broadest (66 cm^{-1}) peak near 1364.7 cm^{-1}. The very fast growth rate of ~25.5 nm/min for the DI film resulted in the growth of relatively smaller crystallites, which increased the E_{2g} FWHM. The E_{2g} shift closer to the ideal value for bulk sp^2-BN is likely an effect of film relaxation as the film grew in thickness [49], while the low intensity is due to inclusions of excess free B, which XPS results revealed, as discussed below. The spectrum for the DII film grown using the shorter 1 s injection pulse time for B_2H_6 exhibits a narrower FWHM (47.8 cm^{-1}) for its E_{2g} peak with respect to the DI film but broader than that of the continuous film, and the peak is centered near 1372.8 cm^{-1}. As noted above the growth rate of the DII film was intermediate (~7.4 nm/min) between that of the continuous (~3.6 nm/min) and the DI films (25.5 nm/min). Likewise its E_{2g} peak properties were also intermediate. XPS results showed that the DII film also contained excess free B which contributed to the lower intensity of E_{2g} peak relative to that of the stoichiometric continuously grown film, but the effect was not as strong as it was for the DII film. The FWHM ($\Gamma_{1/2}$) of the E_{2g} peak for sp^2-BN was used to estimate the

planar crystallite size L_a of the films with L_a (nm) = $(1417 \times 10^{-8}) / \Gamma_{1/2} - 8.7$ [47]. The calculated crystallite sizes within the films grown using the Continuous, DI, and DII processes at q_B = 20 sccm were 5.4, 2.5, and 3.6 nm, respectively. The shoulder in the ~ 1300 – 1330 cm^{-1} range of each spectrum originated from the underlying 4H-SiC substrate.

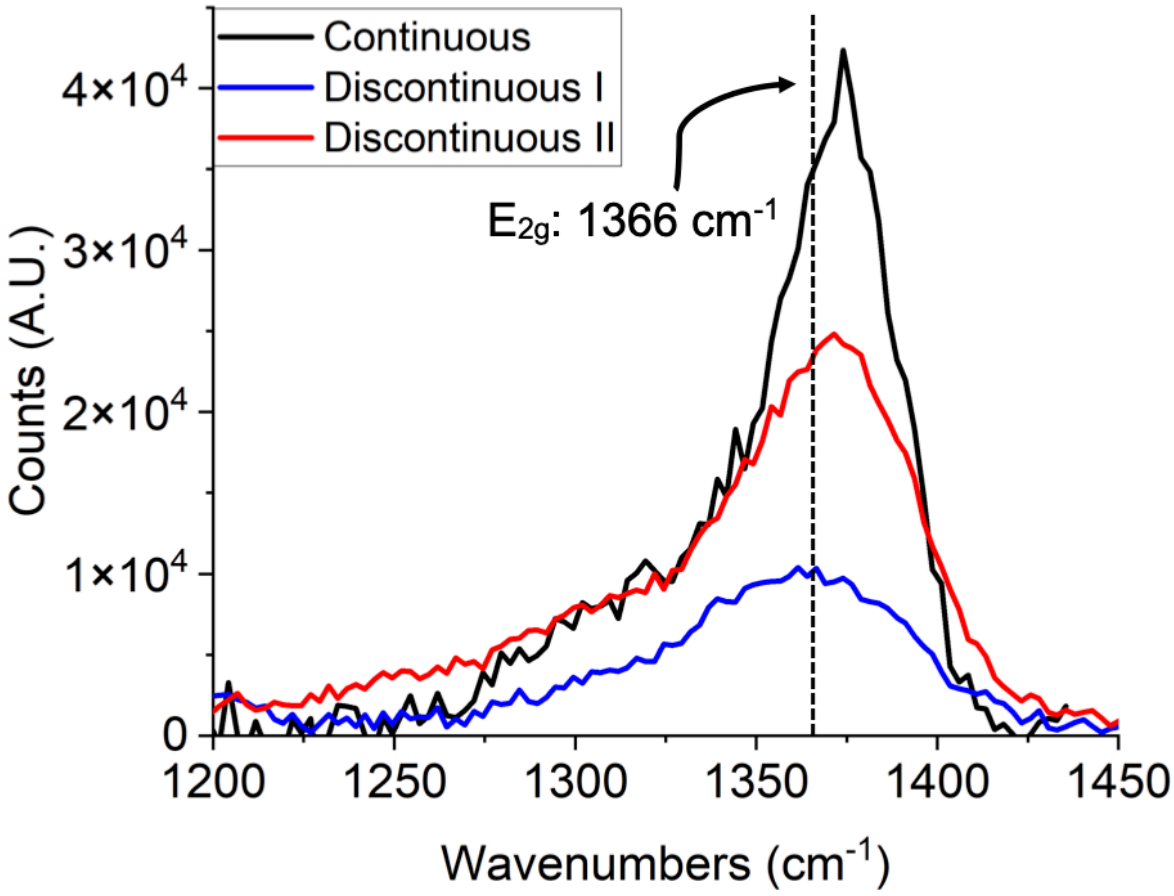

Figure 6.4.2. Raman spectra for the BN films grown using a B_2H_6 flow-rate of 20 sccm for the Continuous, Discontinuous I, and Discontinuous II methods of deposition. The peak in each spectrum represents the E_{2g} vibrational mode exhibited by sp^2-BN.

Figure 6.4.3(a) shows the B:N atomic ratio at the surface region of each sample as acquired by XPS measurements. The data in 6.4.3(b) and (c) were acquired from a 3.5 hour BN

film continuously grown using q_B = 2 sccm. The deconvoluted B 1s spectra of each sample are presented in Figures (d) – (l). It can be seen from Fig. 6.4.3(a) that each continuously grown sample possessed a near 1:1 B:N atomic ratio at its surface. For films grown using the DI method, increasing q_B caused excess B to form as detected at the surface. The same trend is observed for films grown with the DII method, although the effect of q_B is less strong because a 1 s pulse of B_2H_6 was used here instead of 4 s; in fact, the data point in Figure 6.4.3(a) for the DII film grown with q_B = 2 sccm indicates that any free B was below the detection limit of the instrument, just as observed for the continuously grown films. This is further evidenced by the spectra of B 1s bonded chemical species in Figs. 6.4.3(d) – (l). Regardless of the value of q_B, the continuously grown films exhibited a main bonding component of B-N_3 in the 190.5 – 190.7 eV range, which indicates that B is bonded solely to N, and the range represents typical binding energies observed for sp^2-BN [41,42]. The low intensity spectra in the 191.6 – 192.5 eV range are indicative of B-O_x-N_{3-x} bonding [42] which is attributed to surface contamination. All of the DI series films exhibited a B-B_x component in the 187.0 – 188.0 eV range which is indicative of excess free B [50,51]. The percent area of the B-B_x component in the B 1s spectra for the DI series decreases with decreasing q_B. The same effect is observed for the DII series which employs a 1 s pulse of B_2H_6 instead of a 4 s pulse, but at the q_B = 2 sccm condition, the B-B_x component is nonexistent and the spectrum looks similar to that of the continuously grown film grown with q_B = 2 sccm.

The broader ranges of the B 1s and N 1s spectra are shown in Figs. 6.4.3(b) and (c), respectively, of a 3.5 hour continuously grown film using q_B = 2 sccm. The N 1s shift occurs near 398.5 eV, which is close to values observed in the literature for N bonded to B [42,52–54]. Both spectra show the existence of a π-plasmon peak ~ 9 eV above the main 1s core shell peaks

which is indicative of sp^2-BN bonding; the absence of this π-plasmon peak would indicate the formation of sp^3-bonded B-N networks as observed in cubic or amorphous BN [55]. Most of the films grown in this research, except for the DI and DII series films grown using q_B = 20 sccm, exhibited a prominent π-plasmon peak for both B 1s and N 1s core shell spectra. Further, all films regardless of growth conditions exhibited a N 1s spectrum with main components in the range of 398.4 – 398.7 eV, as well as a lesser component in the range of 399.7 – 401.1 eV, which also indicates the presence of $B\text{-}O_x\text{-}N_{3-x}$, from surface contamination. Collectively, the XPS results imply that for the growth temperature used in this study a flow-modulated deposition method for sp^2-BN synthesis using B_2H_6 and NH_3 is not beneficial unless the flow rate and length of the initial B_2H_6 pulse is small enough relative to that of NH_3. Otherwise, subsequent NH_3 pulses will not fully convert a preceding B-layer into BN.

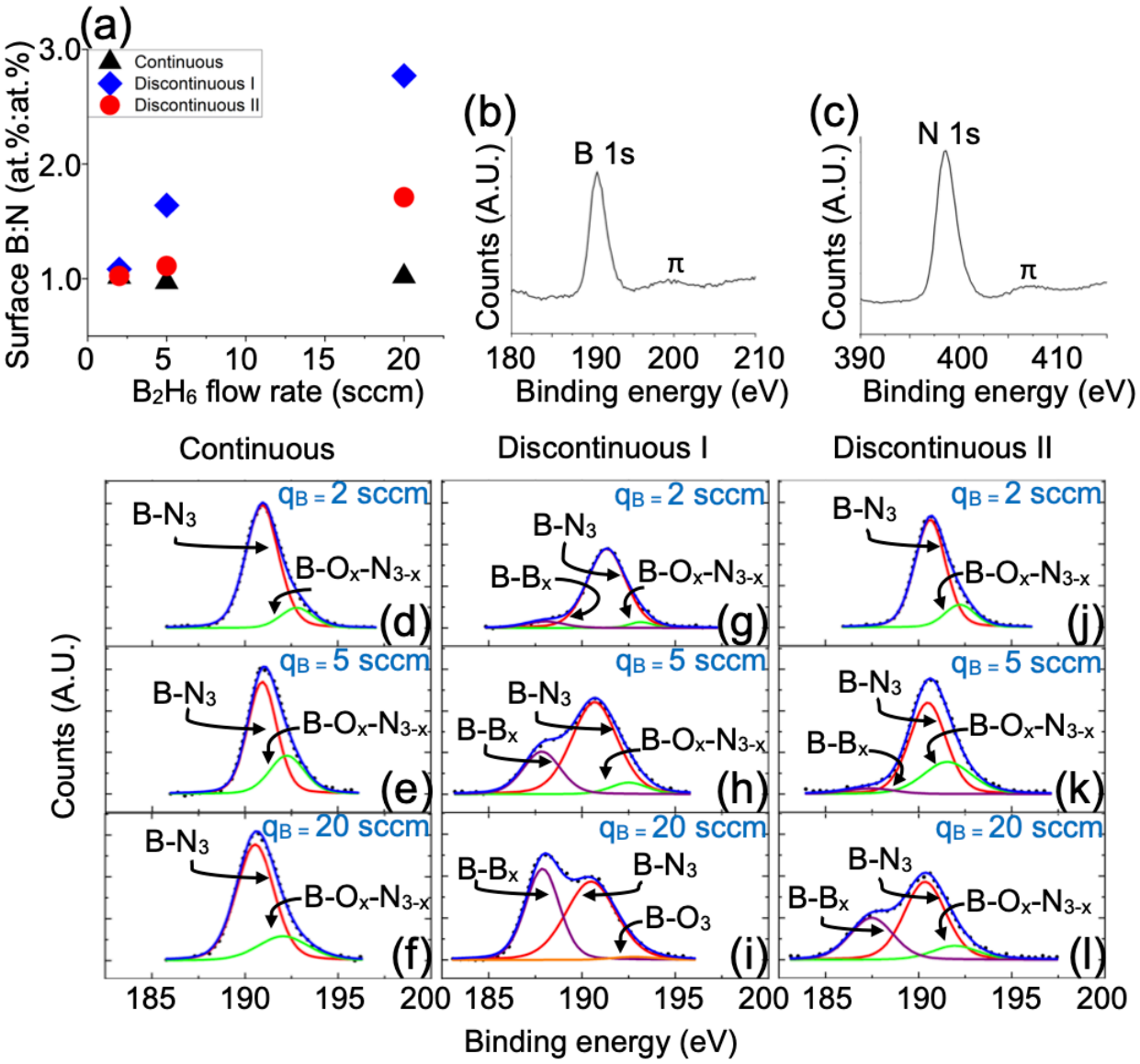

Figure 6.4.3. (a) XPS results of the surface B:N atomic ratios of the BN thin films as a function of B_2H_6 flow rate and deposition method; (b) and (c) B 1s and N 1s spectra, respectively, of a 3.5 hour, continuously grown BN film deposited using q_B = 2 sccm; (d) – (f), (g) – (i), and (j) – (l) deconvoluted B 1s spectra of each BN film deposited within the Continuous, Discontinuous I, and Discontinuous II series, respectively, at the various B_2H_6 flow rates indicated. The chemical species indicated by each spectrum are labeled within each Figure. The black dots are the experimental data points. The blue curves are the model sums of the underlying curves.

Figure 6.4.4 shows the TEM micrographs of the cross-sections of BN films deposited on (0001) 4H-SiC at q_B = 2 sccm using the three different growth methods. All images were acquired along the [$1\bar{1}00$] zone axis of the 4H-SiC substrate. Fig. 6.4.4(a) shows a HRTEM image of the (3.5 hour) continuously grown BN film. It can be seen that the first few layers of sp^2-BN are partially ordered. The BN/SiC interface is indicated with a yellow dotted line. The initial sp^2-BN layers do not grow in perfect registry with the substrate, as evidenced by the waviness and the numerous discontinuities of the sp^2-BN lattice planes. The lattice spacing of the (000*l*) sp^2-BN layers in this film are estimated to be ~ 0.35 nm, which is close to the ideal spacing of 0.33 nm for the (0002) planes of h-BN or the (0003) planes of r-BN. Within the selected region of Fig. 6.4.4 (a), it can also be observed that the stacking order of the sp^2-BN layers is aperiodic; i.e., there is no long range order in atomic stacking, either in the ABAB… sequence of h-BN or the ABCABC… sequence of r-BN, thus prohibiting a strict identification of either sp^2-BN phase. After 3 – 4 nm of deposition, the sp^2-BN lattice planes grow in several different directions that are non-parallel and, in some areas, perpendicular to the substrate. A few of these random directions have been indicated by yellow arrows for reference. Fig. 6.4.4 (b) shows the FFT of the region enclosed by the yellow dotted rectangle in Fig. 6.4.4 (a). The pronounced spots in the center of Fig. 6.4.4 (b) represent the ordered (000*l*) planes. The streaks on either side of these spots indicate twisting of the ($\bar{1}\bar{1}2l$) and ($11\bar{2}l$) planes, characteristic of t-BN [20]. Fig. 6.4.4 (c) shows the selected area electron-diffraction (SAED) pattern of the BN/SiC interface of the sample discussed in Fig. 6.4.4 (a). The SAED pattern reveals the expected spots for the [$1\bar{1}00$] zone axis reflections of 4H-SiC as well as the rings from the polycrystalline sp^2-BN film. The latter are caused by the randomly oriented growth of sp^2-BN beyond the first few deposited layers.

Figures 6.4.4 (d) and (e) show the BN/SiC interfaces and cross-sectional film microstructures for the films grown using the DI and the 4.5 hour DII processes, respectively. The long times of the B_2H_6 pulses used in the DI method caused too rapid a growth rate to allow ordering of the initial BN layers on the 4H-SiC. Polycrystalline sp^2-BN instead of partially ordered layers immediately developed on the substrate. The polycrystalline nature of the film is evidenced by the rings observed within the inset FFT pattern, which are partially obscured by halos that indicate the presence of amorphous BN. Indeed, although inclusions of (000*l*) sp^2-BN lattice planes can be observed in the DI film structure, these planes do not extend as far as they do for the continuously grown film and are interrupted by regions of amorphous BN. Rectangle #1 in Figure 6.4.4 (e) reveals that the DII film initially grew similarly to that of the continuously grown film, that is, in partially ordered layers that are almost parallel to the substrate for a thickness of ~ 4 nm. The sp^2-BN planes then began to grow in random directions, as shown in Rectangle #2. The images in the insets in this micrograph, labeled 1 and 2, show the FFT patterns of the similarly numbered rectangular regions. The FFT corresponding to Rectangle #2 also contains halos indicative of some amorphous BN but the polycrystalline rings are more well defined here than that of the DI film. Collectively, the images shown in Fig. 6.4.4 (e) reveal that using 1 s pulses of B_2H_6 resulted in a slow enough growth rate of ~ 0.04 nm/min to allow for partial ordering of the initial sp^2-BN layers at the interface, but this rate was not sufficiently slower than that of the continuously grown film (~ 0.05 nm/min) to prevent the nucleation of randomly orientated grains after the growth of approximately 10 monolayers.

It should also be noted that for both the DI and DII films, an amorphous layer of approximately 1.5 nm and 0.7 nm, respectively, formed on the substrate surface prior to the nucleation of BN. The results of EDS mapping of both interfaces shown in Supplementary

Figure 6.9.S1 reveal that this layer contains oxygen. Figure 6.9.S2 shows the accompanying XPS spectra of the Si 2p, B 1s, and N 1s binding energy shifts acquired of a ~5 nm thick DII film. These graphs indicate that the oxide layer consists of Si primarily bonded to N and O as well as BN_xO_{1-x}. The Si-O bonds were likely formed from the reaction of the (0001) 4H-SiC surface with residual water vapor in the growth chamber when the substrate was initially heated. It is surmised that during the first pulse of B_2H_6 this gas also reacted with any remaining water vapor in the atmosphere and on the substrate surface and with the SiO_X. The subsequent 4 s pulse of NH_3 allowed N to be incorporated into the B-containing oxide layer. This explains why the amorphous layer for of the DI film (1.5 nm) is thicker than that of the DII film (0.7 nm), since the length of the initial B_2H_6 pulse was shorter for the latter film. In the particular case of the DII film in Fig. 6.4.4 (e), the observation of the growth of a few-layer crystalline sp^2-BN on amorphous material is surprising, as a crystallographic relationship between the crystalline film and the crystalline substrate is lost. However, Tay et al. [56] observed the direct growth of up to 50 layers of nanocrystalline sp^2-BN parallel to and on a 285 nm thick amorphous SiO_2 layer grown on a Si substrate. The BN was deposited at 1000 ^oC using ammonia borane (NH_3-BH_3) as a single-source precursor for both B and N.

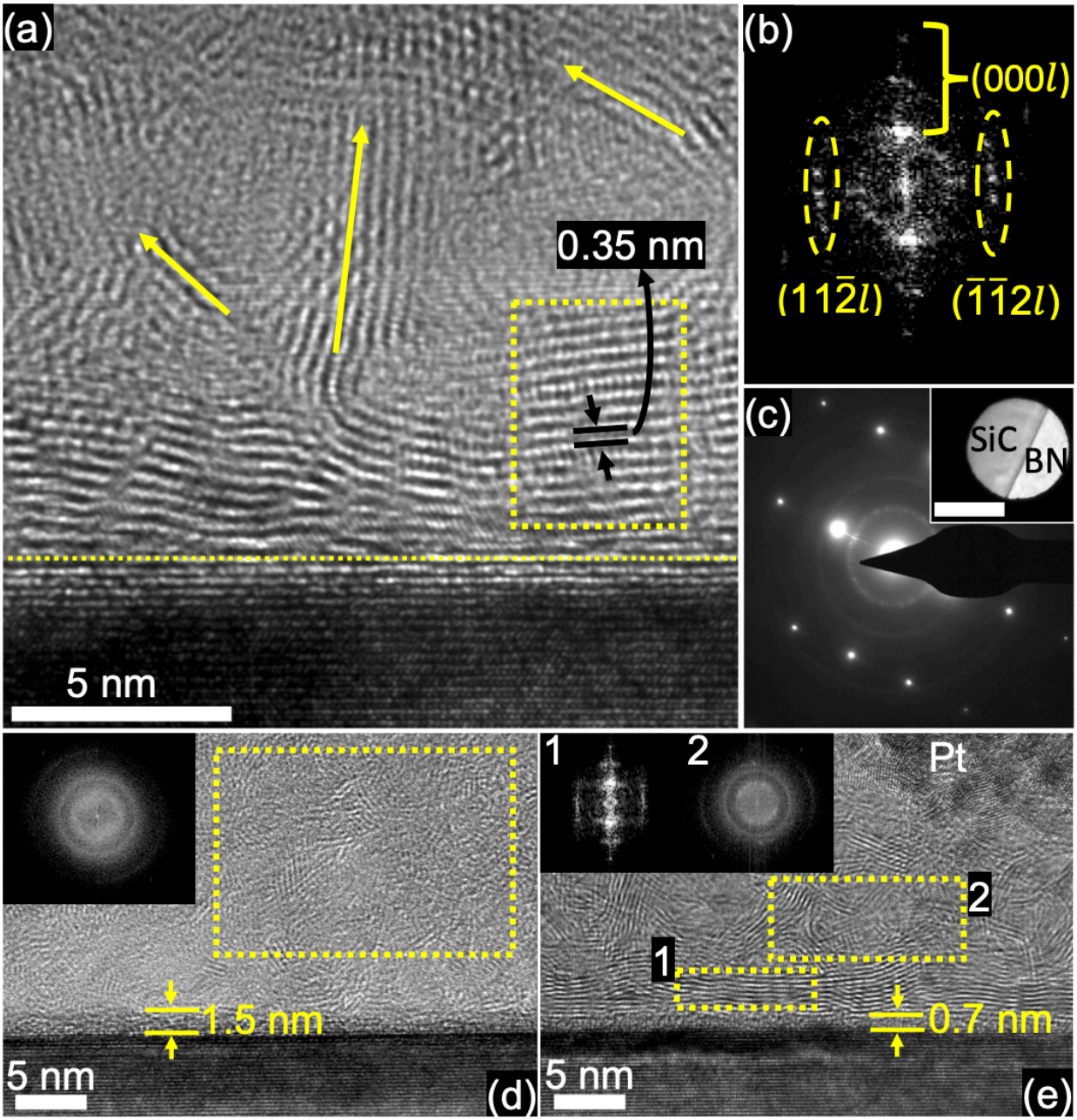

Figure 6.4.4. (a) HRTEM image of a 3.5 hour continuously grown BN film on (0001) 4H-SiC using $q_B = 2$ sccm (N/B = 200). The sample is imaged along the [1$\bar{1}$00] zone axis of 4H-SiC. The yellow dotted line demarcates the BN/SiC interface. (b) FFT of the sp^2-BN film region enclosed by the yellow dotted rectangle in (a). (c) SAED pattern of the interface of the same sample shown in (a); the inset shows the area selected with the aperture, and the scale bar is 100 nm. (d) and (e) BN/SiC interfacial images of BN films grown using the DI and DII (4.5 hour) growth schemes, respectively, with $q_B = 2$ sccm. The yellow-dotted squares show where inset FFTs were acquired.

The randomly oriented nanocrystalline growth of the sp^2-BN films also influenced the microstructure of the surface of these films. As a representative example, Figure 6.4.5 (a), (b), (c) and (d) shows the AFM, Raman spectrum, low magnification cross-sectional TEM, and high resolution TEM images, respectively, of a BN film continuously grown for 3.5 hours using q_B = 2 sccm. The AFM image in Fig. 6.4.5 (a) reveals that the microstructure of the surface of the film (RMS roughness (R_q) ~ 2.5 nm) consists of either spherical or hemispherical particulate features, which are roughly 30 $\pm$ 9.5 nm in nominal diameter. One of these features is circled in Fig. 6.4.5 (a) for reference. These are not single grains of sp^2-BN. Analysis of the Raman spectrum in Figure 6.4.5 (b) suggests that the crystallite size is approximately 8 nm, i.e., much smaller than the size of the features shown in Fig. 6.4.5 (a). The low-magnification cross-sectional TEM image in Fig. 6.4.5 (c) shows where the surface of the BN film meets the Pt protective coating. It can be seen that surface features are actually hemispherical or dome-shaped. As shown in Fig. 6.4.5 (c), the size of a typical dome at the surface range from approximately 30 - 40 nm, which corroborates with the size of the features observed in AFM. The high resolution cross-sectional TEM image Fig. 6.4.5 (d) reveals more of the lattice structure of the bulk film region. A representative area within the film where the sp^2-BN planes are continuous is indicated by the black square and displayed in the more highly magnified image in the inset. Crystallites having approximate lengths and widths of 2.5 nm $\times$ 6.5 nm, respectively, can be observed in the latter image before their lattices are interrupted by crystallites growing in different directions. The length of the basal planes along $[11\bar{2}0]$ and out-of-plane layers along [0001] in this film were measured to be 6.4 $\pm$ 1.5 nm and 2.6 $\pm$ 0.6 nm, respectively. The dimension along $[1\bar{1}00]$ is similarly expected to be no more than a few nm. The size of these crystallites were corroborated with the estimation of ~8 nm from Raman spectroscopy, and thus are too small to individually

comprise the entirety of the dome-shaped features on the surface. Most likely, the latter features are combinations of multiple nanocrystalline sp^2-BN grains that are oriented in random directions, and the termination of these randomly oriented sp^2-BN planes results in round or dome-like shapes at the surface.

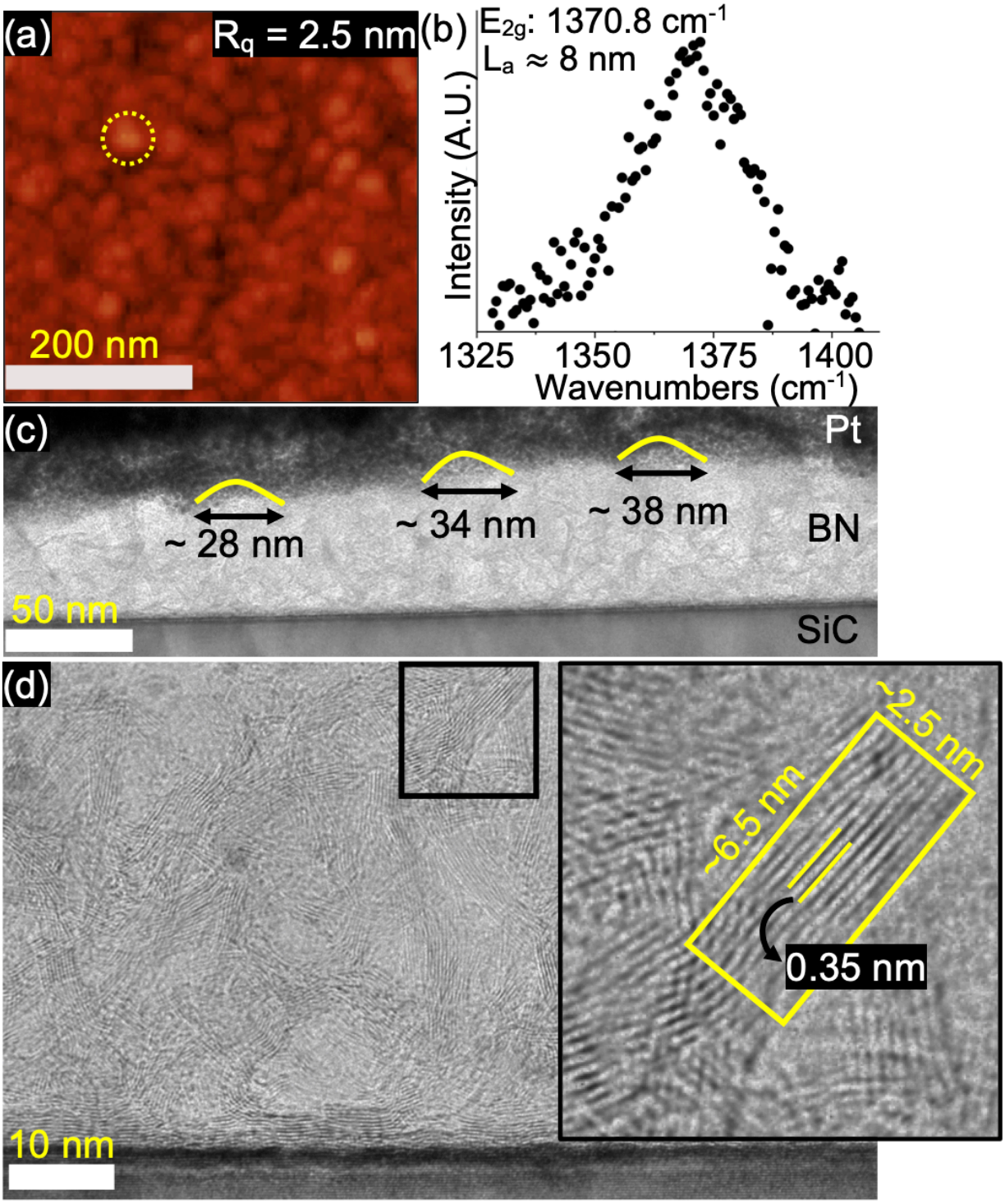

Figure 6.4.5. (a) AFM image, (b) Raman spectrum, (c) low magnification and (d) high resolution cross sectional TEM images, of a 3.5 hour continuously grown BN film on (0001) 4H-SiC using q_B = 2 sccm. The inset in (d) is a magnification of the region enclosed by the black square.

Figure 6.4.6 shows the AFM images (2.5 μm × 2.5 μm) for the continuous, DI, and DII methods of BN deposition on 4H-SiC and their corresponding RMS roughness values. For a given deposition method, increasing q_B increased the size of the dome-shaped features of the BN films as well as the surface roughness. For each q_B condition, the use of the DI deposition method resulted in films with the fastest growth rates and the roughest surface microstructures due to the ability for more free B to reach the surface during each 4 s pulse of B_2H_6. By contrast, the use of the DII deposition resulted in films with the slowest growth rates and the lowest values of R_q at each q_B condition, because the least amount of B was supplied to the chamber in each growth sequence.

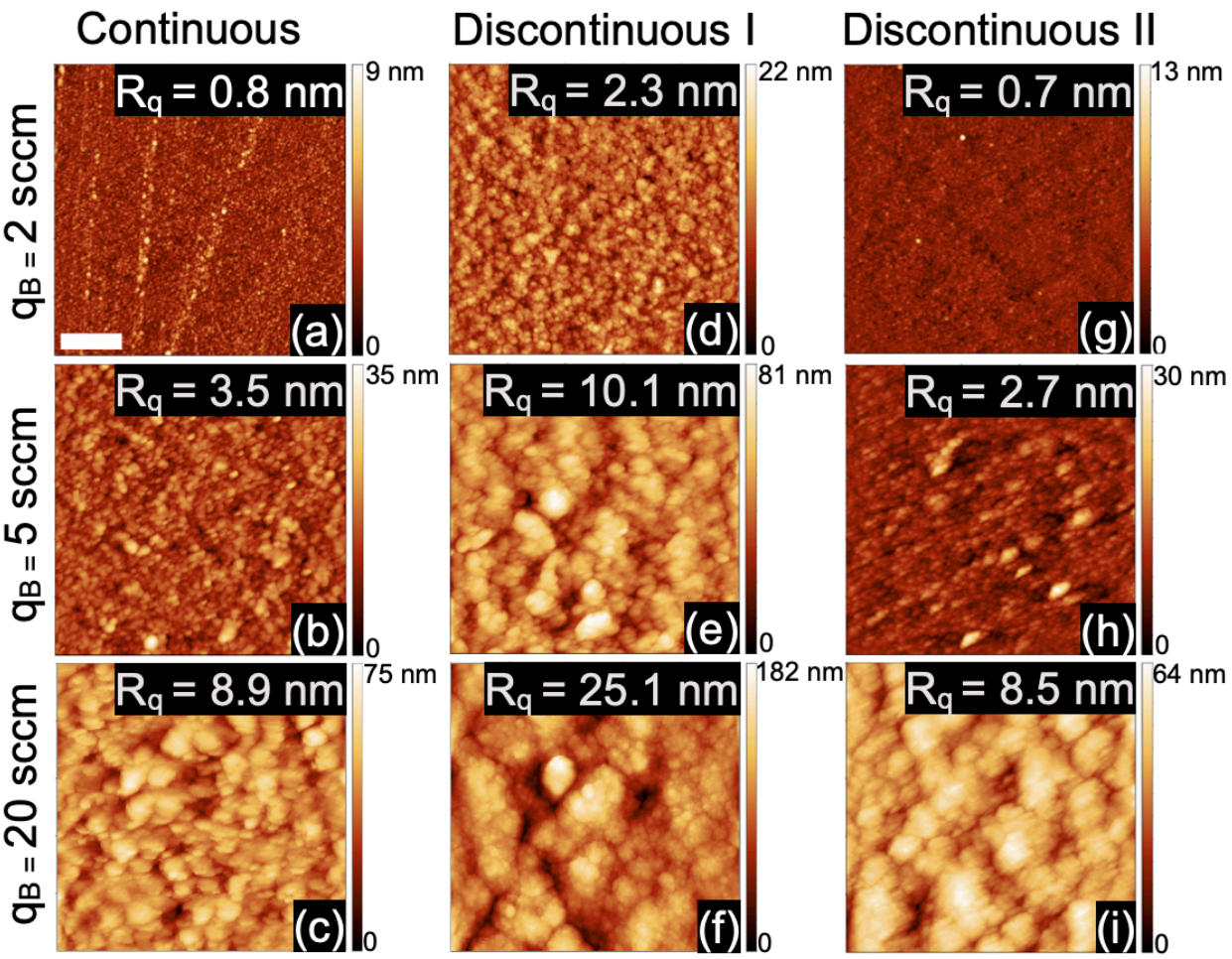

Figure 6.4.6. AFM images (2.5 μm × 2.5 μm) of BN films grown on (0001) 4H-SiC for increasing flow rates, q_B, of B_2H_6 using the Continuous ((a) – (c)), Discontinuous I ((d) – (f)) and Discontinuous II ((g) – (i)) deposition methods. The scale bar in (a) is 500 nm and is the representative length scale for all images in this Figure. The roughness value of the surface of each film is given as R_q.

Based on the foregoing microstructural, optical and chemical data, a mechanism for continuous and discontinuous BN growth on (0001) 4H-SiC at the prescribed growth conditions can be proposed. In studies investigating both the temperature and N/B gas phase ratio dependence of CVD reactions between B_2H_6 and NH_3 to synthesize BN thin films, it was shown that temperatures ≥ 775 °C [57] and N/B ≥ 8 [58] lead to the formation of borazine ($B_3N_3H_6$) as the dominant gas phase species en route to the eventual deposition of stoichiometric BN. Thus, all of the continuously grown films deposited in this research exhibited a compositional B:N

surface ratio near unity, since the growth temperature was above 1000 °C and the N/B gas phase ratios employed were in the range of 20 – 200.

The situation was different for the discontinuously grown films, since B_2H_6 and NH_3 have significantly different decomposition kinetics and were separately introduced into the reactor. The decomposition of B_2H_6 occurs quite readily under CVD conditions. Pure B layers can be deposited on Si surfaces at temperatures as low as 400 °C at atmospheric pressure in a H_2 diluent atmosphere. The activation energy for this process decreases with increasing temperature [45]. By comparison, the decomposition kinetics of NH_3 are slow, which is why V/III ratios in the 10^2 - 10^3 range are needed to produce sufficient partial pressures of active NH and NH_2 species for the growth and compositional stability of III-nitride thin films [59–62]. Thus, for the case of the discontinuously grown films, some of the N/B gas phase ratios used in this study were too low to convert the preceding B-layer(s) into stoichiometric BN. The major exception was the use of an N/B ratio of 200, 1 s pulses of B_2H_6 and 4 s pulses of NH_3. At the N/B ratio of 200, both continuous and DII films grew partially layer-by-layer parallel to the substrate, to a thickness of ~ 4 nm. The subsequently deposited sp^2-BN layers grew in random directions.

The transition from layer-by-layer growth of the sp^2-BN into a more random structure can be attributed to multiple phenomena. The theoretical critical thickness of sp^2-BN on (0001) 6H-SiC was calculated by Chubarov et al. [11] to be ~ 4.5 nm. However, at the 1500 °C growth temperature and N/B ratio of 640 employed in their study, the films were determined to be phase pure r-BN with no transition into a disordered structure or other BN phases beyond the critical thickness. Thus, the transition into a random structure observed in the films grown on 4H-SiC in this research likely relieved the increasing stress in the underlying layers. However, the temperature was not sufficiently high to retain the partially-ordered structure beyond the critical

thickness. Ismach et al. [63] also observed a similar divided microstructure of sp^2-BN deposited on *c*-plane α-Al_2O_3 at 1025 ^oC and 135 mTorr chamber pressure using B_2H_6 and NH_3 and the N/B ratio of 9. Similar results have also been reported by Paduano et al. [19] who deposited 14.5 nm thick BN films on *c*-plane α-Al_2O_3 at 1000^oC using TEB and NH_3 in the N/B ratio of 450. The use of N/B ratios ≥ 2700 also resulted in the growth of initial, well-ordered h-BN epilayers; however, the growth self-terminated at a thickness of 1.7 nm, and no transition into polycrystalline growth was observed.

6.5 Summary and conclusions

Microstructural, optical and chemical characterization of nanocrystalline sp^2-BN thin films grown on (0001) 4H-SiC wafers via continuous CVD and two variations of the FME process using B_2H_6 and NH_3 have been conducted. In the latter method, H_2 purge steps were included in each cycle, and the injection times for B_2H_6 were varied. The use of continuous CVD within the 20 – 200 N/B gas phase ratio range produced stoichiometric sp^2-BN. Films grown continuously only at N/B = 200 resulted in the initial growth of ~ 4 nm thick and partially ordered sp^2-BN layers. To essentially reproduce the results of initial layer formation using a discontinuous FME process it was necessary to also use an N/B ratio of = 200 as well as a flow rate and injection time for B_2H_6 of 2 sccm and 1 s, respectively, and an injection time for the NH_3 of ≥ 4s. Each initial region of these films also (1) contained increasing concentrations of polycrystalline BN and (2) served as a transition zone to a region of randomly oriented polycrystalline material. Using longer B_2H_6 injection times in the FME grown films resulted in the incorporation of excess B and a single mixed amorphous and crystalline sp^2-BN layer without ordering of the initial layers at the substrate.

6.6 Acknowledgements

Funding for this project was made possible thanks to the National GEM Consortium Fellowship, the Neil and Jo Bushnell Fellowship in Engineering, and the John and Claire Bertucci Fellowship. The authors also acknowledge use of the Materials Characterization Facility at Carnegie Mellon University supported by grant MCF-677785.

6.7 Data availability

The data that supports the findings of this study are available within the article and its supplementary material.

6.8 Author declarations

Conflict of interest: The authors have no conflicts to disclose.

6. References

[1] A. W. Moore, J. Cryst. Growth **106**, 6 (1990). DOI:10.1016/0022-0248(90)90281-O.

[2] L. Duclaux, B. Nysten, J. Issi, and A. W. Moore, Phys. Rev. B **46**, 3362 (1992). DOI:10.1103/PhysRevB.46.3362.

[3] R. Dahal, J. Li, S. Majety, B. N. Pantha, X. K. Cao, J. Y. Lin, and H. X. Jiang, Appl. Phys. Lett. **98**, 2 (2011). DOI:10.1063/1.3593958.

[4] H. X. Jiang and J. Y. Lin, Semicond. Sci. Technol. **29**, 084003 (2014). DOI:10.1088/0268-1242/29/8/084003.

[5] H. Liu, J. Meng, X. Zhang, Y. Chen, Z. Yin, D. Wang, Y. Wang, J. You, M. Gao, and P. Jin, Nanoscale **10**, 5559 (2018). DOI:10.1039/c7nr09438h.

[6] S. Majety, J. Li, X. K. Cao, R. Dahal, B. N. Pantha, J. Y. Lin, and H. X. Jiang, Appl. Phys. Lett. **100**, (2012). DOI:10.1063/1.3682523.

[7] A. Mballo, A. Srivastava, S. Sundaram, P. Vuong, S. Karrakchou, Y. Halfaya, S. Gautier, P. L. Voss, A. Ahaitouf, J. P. Salvestrini, and A. Ougazzaden, Nanomaterials **11**, 1 (2021). DOI:10.3390/nano11010211.

[8] I. Meric, C. R. Dean, N. Petrone, L. Wang, J. Hone, P. Kim, and K. L. Shepard, Proc. IEEE **101**, 1609 (2013). DOI:10.1109/JPROC.2013.2257634.

[9] S. M. Kim, A. Hsu, M. H. Park, S. H. Chae, S. J. Yun, J. S. Lee, D.-H. Cho, W. Fang, C. Lee, T. Palacios, M. Dresselhaus, K. K. Kim, Y. H. Lee, and J. Kong, Nat. Commun. **6**, 8662 (2015). DOI:10.1038/ncomms9662.

[10] L. Bourgeois, Y. Bando, and T. Sato, J. Phys. D. Appl. Phys. **33**, 1902 (2000). DOI:10.1088/0022-3727/33/15/321.

[11] M. Chubarov, H. Pedersen, H. Högberg, Z. Czigány, M. Garbrecht, and A. Henry, Chem. Mater. **27**, 1640 (2015). DOI:10.1021/cm5043815.

[12] M. Chubarov, H. Högberg, A. Henry, and H. Pedersen, J. Vac. Sci. Technol. A Vacuum, Surfaces, Film. **36**, 030801 (2018). DOI:10.1116/1.5024314.

[13] J. Thomas, Jr., N. E. Weston, and T. E. O'Connor, Phys. Inorg. Chem. **84**, 4619 (1963). DOI:10.1021/ja00883a001.

[14] A. V. Kurdyumov, V. F. Britun, and I. A. Petrusha, Diam. Relat. Mater. **5**, 1229 (1996). DOI:10.1016/0925-9635(96)00515-8.

[15] C. Schimpf, M. Motylenko, and D. Rafaja, Mater. Charact. **8**, 190 (2013).

[16] S. Alkoy, C. Toy, T. Gönül, and A. Tekin, J. Eur. Ceram. Soc. **17**, 1415 (1997). DOI:10.1016/S0955-2219(97)00040-X.

[17] P. M. Jean-Remy, B. A. Webler, P. C. Pistorius, and R. F. Davis, J. Cryst. Growth **572**, 1 (2021). DOI:10.1016/j.jcrysgro.2021.126283.

[18] Y. Kobayashi and T. Akasaka, J. Cryst. Growth **310**, 5044 (2008). DOI:10.1016/j.jcrysgro.2008.07.010.

[19] Q. Paduano, M. Snure, D. Weyburne, A. Kiefer, G. Siegel, and J. Hu, J. Cryst. Growth **449**, 148 (2016). DOI:10.1016/j.jcrysgro.2016.06.012.

[20] X. Li, S. Sundaram, Y. El Gmili, T. Ayari, R. Puybaret, G. Patriarche, P. L. Voss, J. P. Salvestrini, and A. Ougazzaden, Cryst. Growth Des. **16**, 3409 (2016). DOI:10.1021/acs.cgd.6b00398.

[21] M. Chubarov, H. Pedersen, H. Högberg, and A. Henry, CrystEngComm **15**, 455 (2013). DOI:10.1039/c2ce26423d.

[22] Y. Kobayashi and T. Makimoto, Japanese J. Appl. Physics, Part 1 Regul. Pap. Short Notes

Rev. Pap. **45**, 3519 (2006). DOI:10.1143/JJAP.45.3519.
[23] S. Majety, J. Li, W. P. Zhao, B. Huang, S. H. Wei, J. Y. Lin, and H. X. Jiang, Appl. Phys. Lett. **102**, (2013). DOI:10.1063/1.4808365.
[24] M. Chubarov, H. Pedersen, H. Högberg, Z. Czigany, and A. Henry, CrystEngComm **16**, 5430 (2014). DOI:10.1039/c4ce00381k.
[25] K. Nakamura, J. Electrochem. Soc. **133**, 1120 (1986). DOI:10.1149/1.2108797.
[26] M. Chubarov, H. Pedersen, H. Högberg, V. Darakchieva, J. Jensen, P. O. Å. Persson, and A. Henry, Phys. Status Solidi - Rapid Res. Lett. **5**, 397 (2011). DOI:10.1002/pssr.201105410.
[27] M. Chubarov, H. Pedersen, H. Högberg, J. Jensen, and A. Henry, Cryst. Growth Des. **12**, 3215 (2012). DOI:10.1021/cg300364y.
[28] Y. Kobayashi, T. Nakamura, T. Akasaka, T. Makimoto, and N. Matsumoto, J. Cryst. Growth **298**, 325 (2007). DOI:10.1016/j.jcrysgro.2006.10.034.
[29] X. Yang, S. Nitta, K. Nagamatsu, S. Y. Bae, H. J. Lee, Y. Liu, M. Pristovsek, Y. Honda, and H. Amano, J. Cryst. Growth **482**, 1 (2018). DOI:10.1016/j.jcrysgro.2017.10.036.
[30] D. Chugh, J. Wong-Leung, L. Li, M. Lysevych, H. H. Tan, and C. Jagadish, 2D Mater. **5**, (2018). DOI:10.1088/2053-1583/aad5aa.
[31] P. A. Caban, D. Teklinska, P. P. Michalowski, J. Gaca, M. Wojcik, J. Grzonka, P. Ciepielewski, M. Mozdzonek, and J. M. Baranowski, J. Cryst. Growth **498**, 71 (2018). DOI:10.1016/j.jcrysgro.2018.06.001.
[32] P. A. Caban, P. P. Michalowski, I. Wlasny, J. Gaca, M. Wojcik, P. Ciepielewski, D. Teklinska, and J. M. Baranowski, J. Alloys Compd. **815**, 152364 (2020). DOI:10.1016/j.jallcom.2019.152364.
[33] M. Snure, Q. Paduano, M. Hamilton, J. Shoaf, and J. Matthew Mann, Thin Solid Films **571**, 51 (2014). DOI:10.1016/j.tsf.2014.09.065.
[34] L. Souqui, J. Palisaitis, H. Högberg, and H. Pedersen, J. Mater. Chem. C **8**, 4112 (2020). DOI:10.1039/d0tc00616e.
[35] M. J. Rand and J. F. Roberts, J. Electrochem. Soc. **115**, 423 (1968). DOI:10.1149/1.2411238.
[36] H. Yamada, S. Inotsume, N. Kumagai, T. Yamada, and M. Shimizu, Phys. Status Solidi Basic Res. **257**, 1 (2020). DOI:10.1002/pssb.201900318.
[37] H. Yamada, S. Inotsume, N. Kumagai, T. Yamada, and M. Shimizu, Phys. Status Solidi Basic Res. **257**, 1 (2020). DOI:10.1002/pssb.201900521.
[38] M. Chubarov, H. Pedersen, H. Högberg, A. Henry, and Z. Czigány, J. Vac. Sci. Technol. A Vacuum, Surfaces, Film. **33**, 061520 (2015). DOI:10.1116/1.4935155.
[39] M. Chubarov, H. Pedersen, H. Högberg, Z. Czigany, and A. Henry, CrystEngComm **16**, 5430 (2014). DOI:10.1039/c4ce00381k.
[40] D. Nečas and P. Klapetek, Cent. Eur. J. Phys. **10**, 181 (2012). DOI:10.2478/s11534-011-0096-2.
[41] R. Trehan, Y. Lifshitz, and J. W. Rabalais, J. Vac. Sci. Technol. A Vacuum, Surfaces, Film. **8**, 4026 (1990). DOI:10.1116/1.576471.
[42] C. Guimon, D. Gonbeau, G. Pfister-Guillouzo, O. Dugne, A. Guette, R. Naslain, and M. Lahaye, Surf. Interface Anal. **16**, 440 (1990). DOI:10.1002/sia.740160191.
[43] A. Jablonski and C. J. Powell, Surf. Sci. Rep. **47**, 33 (2002). DOI:10.1016/s0167-5729(02)00031-6.
[44] D. R. Lamborn, D. W. Snyder, X. X. Xi, and J. M. Redwing, J. Cryst. Growth **299**, 358

(2007). DOI:10.1016/j.jcrysgro.2006.11.253.
[45] V. Mohammadi, W. B. De Boer, and L. K. Nanver, Appl. Phys. Lett. **101**, 1 (2012). DOI:10.1063/1.4752109.
[46] R. Geick, C. Perry, and G. Rupprecht, Phys. Rev. **146**, 543 (1966). DOI:10.1103/PhysRev.146.543.
[47] R. J. Nemanich, S. A. Solin, and R. M. Martin, Phys. Rev. B **23**, 6348 (1981).
[48] R. V. Gorbachev, I. Riaz, R. R. Nair, R. Jalil, L. Britnell, B. D. Belle, E. W. Hill, K. S. Novoselov, K. Watanabe, T. Taniguchi, A. K. Geim, and P. Blake, Small (2011). DOI:10.1002/smll.201001628.
[49] M. A. Moram and M. E. Vickers, Reports Prog. Phys. **72**, 1 (2009). DOI:10.1088/0034-4885/72/3/036502.
[50] S. Jacques, A. Guette, X. Bourrat, F. Langlais, C. Guimon, and C. Labrugere, Carbon N. Y. **34**, 1135 (1996). DOI:10.1016/0008-6223(96)00075-9.
[51] T. P. Fehlner and S. A. Fridmann, Inorg. Chem. **9**, 2288 (1970). DOI:10.1021/ic50092a016.
[52] P. R. Kidambi, R. Blume, J. Kling, J. B. Wagner, C. Baehtz, R. S. Weatherup, R. Schloegl, B. C. Bayer, and S. Hofmann, Chem. Mater. **26**, 6380 (2014). DOI:10.1021/cm502603n.
[53] N. Guo, J. Wei, L. Fan, Y. Jia, D. Liang, H. Zhu, K. Wang, and D. Wu, Nanotechnology **23**, 415605 (2012). DOI:10.1088/0957-4484/23/41/415605.
[54] A. B. Preobrajenski, A. S. Vinogradov, and N. Mårtensson, Surf. Sci. **582**, 21 (2005). DOI:10.1016/j.susc.2005.02.047.
[55] D. H. Berns and M. A. Cappelli, Appl. Phys. Lett. **2711**, 2711 (1995). DOI:10.1063/1.115573.
[56] R. Y. Tay, S. H. Tsang, M. Loeblein, W. L. Chow, G. C. Loh, J. W. Toh, S. L. Ang, and E. H. T. Teo, Appl. Phys. Lett. **106**, 3 (2015). DOI:10.1063/1.4914474.
[57] C. Gómez-Aleixandre, D. Díaz, F. Orgaz, and J. M. Albella, J. Phys. Chem. **97**, 11043 (1993). DOI:10.1021/j100144a023.
[58] C. Gomez-Aleixandre, A. Essafti, M. Fernandez, J. L. G. Fierro, and J. M. Albella, J. Phys. Chem. **100**, 2148 (1996). DOI:10.1021/jp951200d.
[59] B. Beaumont, P. Gibart, and J. P. Faurie, J. Cryst. Growth **156**, 140 (1995). DOI:10.1016/0022-0248(95)00296-0.
[60] A. Koukitu, N. Takahashi, and H. Seki, Japanese J. Appl. Physics, Part 2 Lett. **36**, (1997). DOI:10.1143/jjap.36.l1136.
[61] R. F. Davis, in *Compr. Semicond. Sci. Technol.*, edited by P. Bhattacharya, R. Fornari, and H. Kamimura (Elsevier B.V., Amsterdam, 2011), pp. 339–367. DOI:10.1016/j.jallcom.2009.02.108.
[62] K. Rönnby, H. Pedersen, and L. Ojamäe, J. Vac. Sci. Technol. A **38**, 050402 (2020). DOI:10.1116/6.0000369.
[63] A. Ismach, H. Chou, D. A. Ferrer, Y. Wu, S. Mcdonnell, H. C. Floresca, A. Covacevich, C. Pope, R. Piner, M. J. Kim, R. M. Wallace, L. Colombo, and R. S. Ruoff, 6378 (2012).

6.9 Supplementary Information for: Flow-modulated Deposition of sp^2 - Boron Nitride Using Diborane and Ammonia on Chemo-mechanically Polished (0001) 4H-SiC Substrates

Authors: Philip M. Jean-Remy[a], Matthew J. Cabral[a], and Robert F. Davis[a, b]

[a] Department of Materials Science and Engineering, Carnegie Mellon University, Pittsburgh, PA, 15213, USA

[b] Department of Electrical and Computer Engineering, Carnegie Mellon University, Pittsburgh, PA, 15213, USA

Corresponding author: Philip M. Jean-Remy, Carnegie Mellon University, Pittsburgh, PA, 15213, USA. Email: pjeanrem@andrew.cmu.edu

Figure 6.9.S1 shows scanning transmission electron microscopy (STEM) images of (a) DI and (b) DII films grown using q_B = 2 sccm, along with composition profiles ((c) and (d)) across the BN/SiC interface acquired using energy dispersive spectroscopy (EDS). The prominence of an oxide layer can be clearly observed in the composition profiles.

Because EDS does not adequately quantify lighter elements such as B and N, more sensitive techniques were needed to understand the nature of the oxide layer that first forms on the (0001) 4H-SiC substrate for films grown discontinuously. Figure 6.9.S2 shows the (a) Si 2p, (b) B 1s, and (c) N 1s x-ray photoelectron spectroscopy (XPS) spectra of a DII film (q_B = 2 sccm) grown for shorter times (900 cycles) such that the final thickness was ~ 5 nm. Thus, the film was sufficiently thin to allow analysis of the Si 2p bonding state. It can be seen in Fig. S2(a) that there are three main components of the Si 2p shift: SiC at 100.7 eV [1] for tetrahedrally coordinated Si by C as expected in 4H-SiC, while the two components of higher binding energy near 101.9 eV and 103.4 eV are close to reported binding energy values of Si-O_x-N_{1-x} [1–4] and Si_xO_{1-x} [1,5]. The B 1s and N 1s spectra indicate that both B and N are bonded primarily to each other (B-N_3 and N-B_3) and to a lesser extent there is partial BN bonding with O. In the N 1s spectra, there is a small subcomponent near 396.7 eV which has been attributed to N_x-Si_{1-x} as it is

close to value for N bonded to Si in Si_3N_4 [2]. Thus, the oxide layer seems to consist primarily of Si bonded to N and O as well as BN_xO_{1-x}.

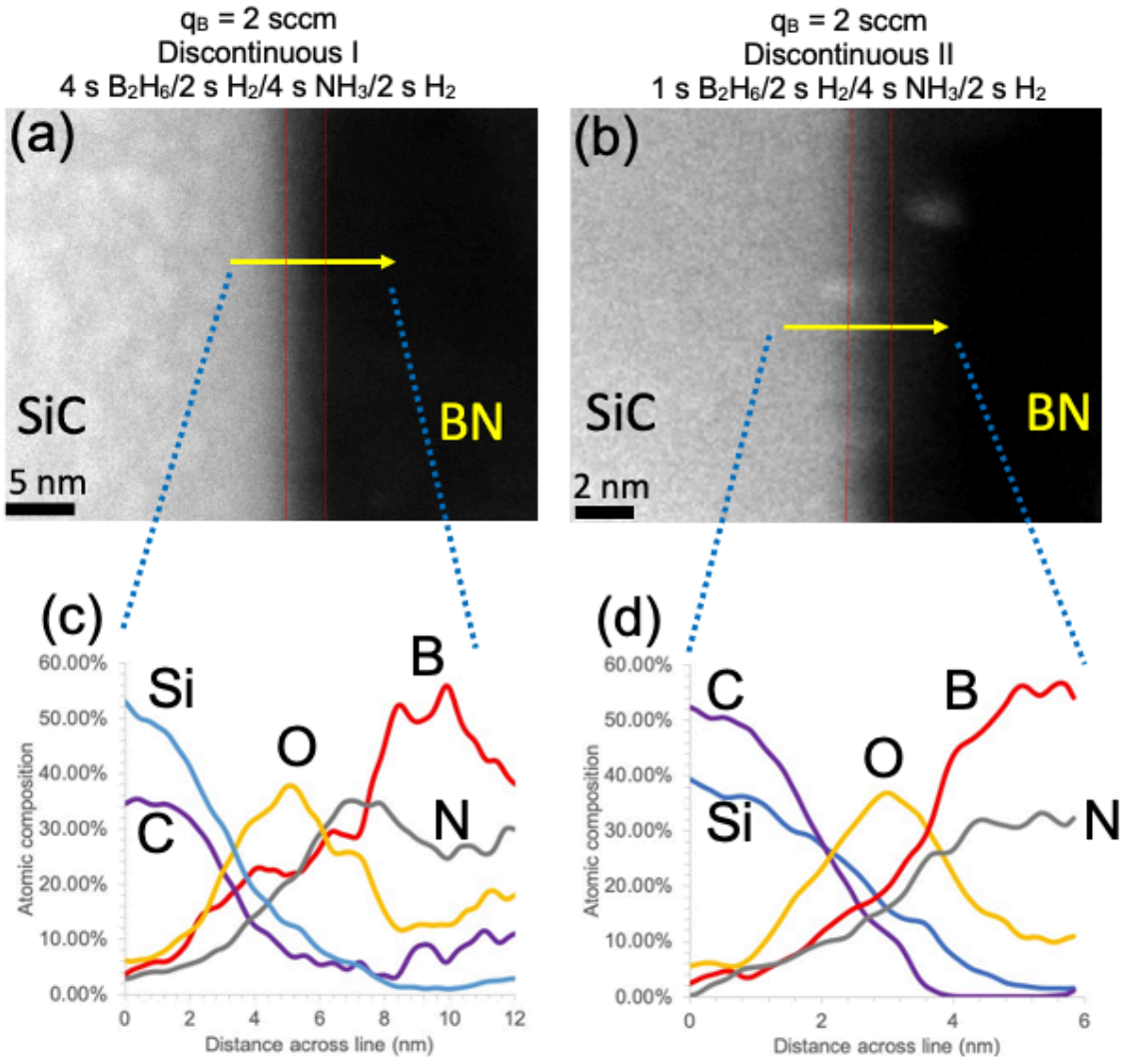

Figure 6.9.S1: STEM images of the cross-sections of BN thin films grown on (0001) 4H-SiC using a B_2H_6 flow rate of 2 sccm and the Discontinuous I (a) and II (b) deposition styles, respectively. The atomic composition across the interface as indicated in both images by the arrow was measured with EDS and is shown in plots (c) and (d).

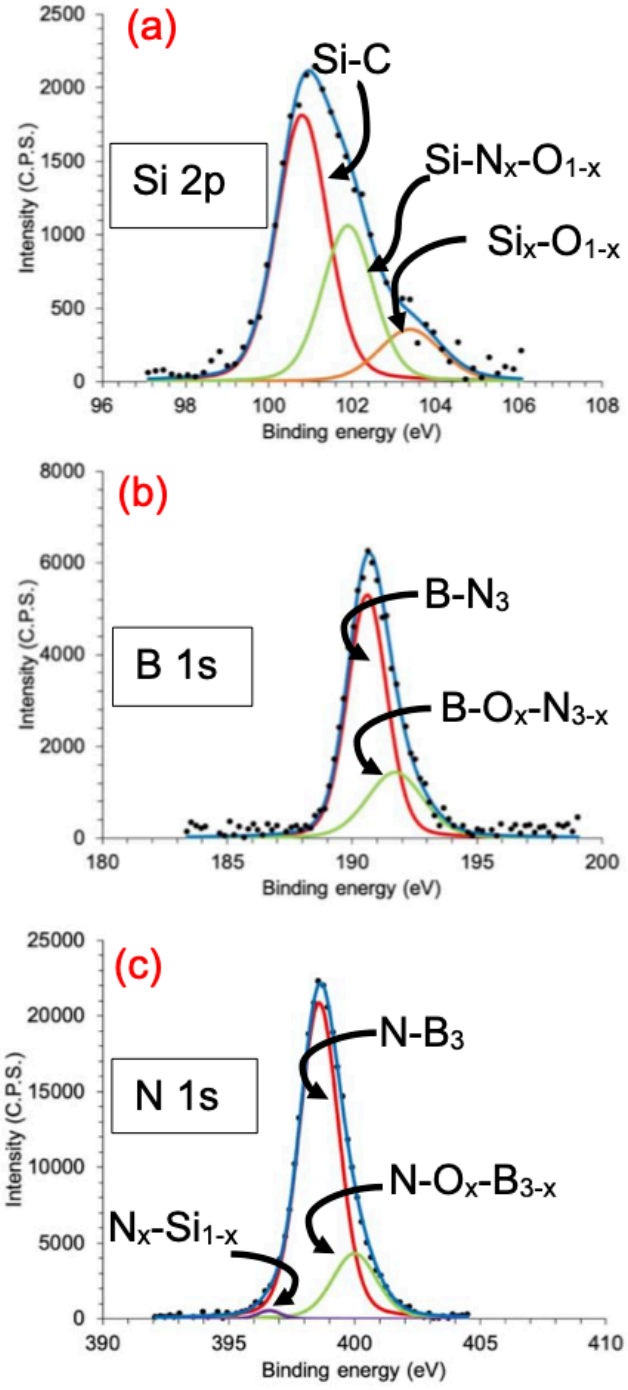

Figure 6.9.S2. (a) Si 2p, (b) B 1s, and (c) N 1s XPS spectra of a discontinuously grown ~ 5 nm thick BN film on (0001) 4H-SiC where q_B = 2 sccm. The DII growth process route consisted of 900 cycles of 1 s B_2H_6/2 s H_2/4 s NH_3/2 s H_2. The subcomponents of each spectrum are indicated. The black dots and blue curves are the experimental data and the model sum of the underlying spectra, respectively.

6.9 Supplementary References

[1] C. Guimon, D. Gonbeau, G. Pfister-Guillouzo, O. Dugne, A. Guette, R. Naslain, and M. Lahaye, Surf. Interface Anal. **16**, 440 (1990). DOI:10.1002/sia.740160191.
[2] J. A. Taylor, G. M. Lancaster, and J. W. Rabalais, J. Electron Spectros. Relat. Phenomena **13**, 435 (1978). DOI:10.1016/0368-2048(78)85047-6.
[3] R. van Weeren, E. A. Leone, S. Curran, L. C. Klein, and S. C. Danforth, J. Am. Ceram. Soc. **77**, 2699 (1994). DOI:10.1111/j.1151-2916.1994.tb04664.x.
[4] E. Pitthan, A. L. Gobbi, H. I. Boudinov, and F. C. Stedile, J. Electron. Mater. **44**, 2823 (2015). DOI:10.1007/s11664-015-3757-x.
[5] H. Watanabe and T. Hosoi, in *Phys. Technol. Silicon Carbide Devices*, edited by Y. Hijikata (IntechOpen, Tokyo, 2012), pp. 235–250. DOI:10.5772/51514.

7. Paper 4: Chemical Vapor Deposition of sp^2-Boron Nitride on Mechanically Polished Pyrolytic Boron Nitride Substrates

Authors: Philip M. Jean-Remy[a], Matthew J. Cabral[a], and Robert F. Davis[a, b]

[a] Department of Materials Science and Engineering, Carnegie Mellon University, Pittsburgh, PA, 15213, USA

[b] Department of Electrical and Computer Engineering, Carnegie Mellon University, Pittsburgh, PA, 15213, USA

Corresponding author: Philip M. Jean-Remy, Carnegie Mellon University, Pittsburgh, PA, 15213, USA. Email: pjeanrem@andrew.cmu.edu

7.1 Abstract

Nanocrystalline sp^2-BN thin films have been grown for 2 and 4.5 hours on mechanically polished polycrystalline pyrolytic boron nitride (PBN) substrates at 1060 °C via chemical vapor deposition (CVD) using diborane (B_2H_6) and ammonia (NH_3) as the B- and N sources, respectively. The use of an N/B gas phase ratio of 200 resulted in sp^2-BN thin films having a stoichiometric surface chemistry, as determined by x-ray photoelectron spectroscopy. Cross-sectional transmission electron microscopy revealed the initial growth of ~4 nm thick partially ordered [0001] sp^2-BN layers regardless of the crystallographic orientation of the sets of layers in the substrate. A transition zone then formed within the deposited films that contained randomly oriented polycrystalline grains and that culminated in the formation of protrusions. Atomic force microscopy verified an increase in roughening of the surfaces of the films with an increase in growth time and the associated thickness.

7.2 Introduction

The sp^2-hybridized form of boron nitride (sp^2-BN) possesses a two-dimensional (2D) hexagonal ring structure containing alternating B and N atoms. Thin films of h-BN are chemically inert, thermally stable, possess a large in-plane thermal conductivity [1,2], as well as a wide bandgap of about 6 eV and can be doped with sufficiently shallow acceptor atoms to produce p-type conductivity [3,4]. It has been shown that h-BN/SiO_2/Si based photodetectors can be fabricated with an on/off ratio > 10^3 operating under 212 nm DUV light [5]. Heterostructures of p-h-BN/n-$Al_xGa_{1-x}N$ that exhibit rectifying behavior have been fabricated; however, DUV emission has not yet been realized [6,7]. As h-BN is chemically inert and possesses a 1.7% lattice mismatch with graphene, it also has been used as dielectric layers for graphene-based transistors [8,9].

Hexagonal BN and the companion 2D polytype of rhombohedral (r) BN are bonded via sp^2-hybridization. The ABAB… stacking sequence of h-BN is the only structural difference that distinguishes it from the ABCABC… sequence of r-BN [10]. The in-plane and out-of-plane lattice parameters of these two polytypes are very similar; thus, advanced characterization techniques such as grazing incidence x-ray diffraction (XRD) and cross-sectional transmission electron microscopy (TEM) are required to distinguish the crystal structure of one polytype from the other [11,12]. BN also forms a less ordered sp^2-BN phase called turbostratic (t) BN which retains a high degree of in-plane order of BN hexagonal rings; however, its layers are roughly parallel, as well as randomly rotated and translated with respect to the *c* axis of the structure [13]. The t-BN phase is often indicated by the observation of variations in the (000*l*) interplanar spacing beyond the 3.33 Å reported for the (0002) and (0003) planes of h-BN and r-BN, respectively [13–15].

Much of the recent successful growth of sp^2-BN synthesized via CVD has occurred on transition metal (TM) substrates [16–20] such as copper (Cu) [16,17,19,20], nickel (Ni) [21–26], platinum (Pt) [24,25,27], and palladium (Pd) [24]. These TMs exhibit varying degrees of catalytic activity during h-BN growth on their surfaces due to the mixing of TM *d* orbitals with the h-BN π orbitals at the interface [28,29]. Another attractive feature of these TMs is a close value of the *a* lattice parameter to that of the *a* parameter of sp^2-BN that facilitates the growth of the latter material. For example, the values of the lattice spacings of Ni (111) (2.49 Å), Cu (111) (2.56 Å), and Co (0001) (2.51 Å), are mismatched by only -0.4%, 2.4%, and 0.8%, respectively, with the in-plane lattice parameter of h-BN (2.504 Å) [30]. However, this catalytic effect becomes effectively shielded by the formation of just a monolayer of sp^2-BN. Research has revealed that a significantly higher partial pressure of the precursor(s) is needed to continue the growth of sp^2-BN film beyond the first monolayer [31]. As a result, sp^2-BN growth on TM substrates is limited to films that are either a monolayer or just a few atomic layers thick. Further, sp^2-BN films grown on TM foil substrates must be transferred – typically through a wet chemical etching process [32] - to another substrate such as SiO_2/Si if they are to be fabricated into a device structure.

It has been predicted [33] and shown experimentally [34,35] that relatively high growth temperatures (~ 1500 ^oC) are typically needed to produce epitaxial sp^2-BN films on non-catalytic substrates. The high temperature requirement for epitaxial sp^2-BN can be bypassed in favor of temperatures closer to 1000 ^oC if N/B gas phase ratios > 1000 are used [36,37]. At lower N/B ratios at these low temperatures, BN film growth is susceptible to the inclusion of t-BN and nanocrystalline grains. Thus, at high N/B ratios, the growth of epitaxial sp^2-BN over wide temperature ranges has been reported on substrates such as *c*-plane sapphire (1000 – 1350

°C) [33,37,38], (100) Si (1000 – 1200 °C) [33,39], and (0001) 6H-SiC (1050 – 1500 °C) [40–42]. The use of such high N/B ratios, however, results in the self-termination of film growth after a few nm due to parasitic reactions between B- and N-source precursors in the gas phase [37,38]. Lastly, due to the negative in-plane coefficient of thermal expansion of sp^2-BN [43], BN films deposited on both non-catalytic and catalytic substrates often exhibit wrinkle features developed during post-growth cooling [44–46].

To the authors' best knowledge there have been no reports of homoepitaxial CVD synthesis of sp^2-BN films on bulk single crystals of this phase, as the reported lateral size of the latter ranges only from nm [47] to a few mm [48] and is dependent on the molten solvent and the temperature/pressure conditions used. Polycrystalline pyrolytic boron nitride (PBN), however, can be commercially grown by CVD up to several cm^2 in cross-section. The grains within PBN are primarily oriented along (000*l*). The degree of out-of-plane order along the *c*-axis depends on process conditions; Moore [1], using a BCl_3/NH_3 gas mixture, showed that using a deposition temperature of 1680 °C, low density (1.94 g/cm^3) PBN formed having mainly the t-BN phase with a d_{0002} spacing of 3.42 Å. By contrast, deposition at 2000 °C resulted in the formation of higher density (2.22 g/cm^3) PBN with d_{0002} spacing of 3.34 Å, which is close to the bulk crystalline value of 3.33 Å for sp^2-BN [43].

Schimpf et al. [49] have described and quantified the types of defects in their PBN samples. They determined that the prominent defect was puckering [50], described as waviness within the sp^2-BN basal planes which caused deviations of d_{0002} spacing away from the ideal value. In the same study, Schimpf et al. also determined that the crystallite sizes ranged from a few nm to tens of nm which agrees with the reports from other studies [2,51]. Although the lateral size of sp^2-BN crystallites grown on PBN would be limited to that of the dimensions of

the PBN substrate, defects arising from mismatches in the lattice parameters and the coefficients of thermal expansion should be reduced in a CVD-BN/PBN system, and thus may allow for more flexible growth conditions such as lower temperatures and N/B ratios.

The research reported herein investigated the CVD growth of sp^2-BN thin films on mechanically polished PBN substrates. The initial layers of sp^2-BN were roughly [0001] oriented regardless of the underlying substrate orientation. A transition zone then formed containing randomly oriented polycrystalline grains. Surface stoichiometric, nanocrystalline sp^2-BN was obtained on PBN under the growth conditions employed. The roughness of the surfaces of the films increased with thickness.

7.3 Experimental

The as-received PBN substrates (Morgan Technical Ceramics) possessed very rough surfaces - ~ 65 nm RMS roughness over a 2 μm × 2 μm area. Thus, a polishing procedure was developed to prepare surfaces suitable for thin film growth. Precise, semiautomatic polishing of PBN was performed using a Multiprep Polishing System (Allied High Tech Products, Inc.). Table 7.3.1 summarizes the steps typically used to polish PBN substrates in this research.

Table 7.3.1. Pyrolytic boron nitride polishing procedure.

*Polishing media/Lubricant	Platen rotation and direction	Sample rotation (RPM)	Target thickness removal/Duration
6 μm DLF/water	150 RPM, CW	8 RPM, CCW	~ 200 μm
3 μm DLF/water	150 RPM, CW	8 RPM, CCW	~ 100 μm
1 μm DLF/RedLube	150 RPM, CW	8 RPM, CCW	~ 100 μm
Final P Cloth/ 0.04 μm Colloidal Silica	150 RPM, CW	8 RPM, CCW	30 seconds

DLF: diamond lapping film
CW: clockwise
CCW: counter-clockwise
RPM: revolutions per minute
* All DLFs, polishing cloths, and lubricant materials were acquired from Allied High Tech Products, Inc.

A 600 g load was applied to each sample during each polishing step. The sample surface and platen were cleaned with micro-organic soap between each polishing step to prevent debris from the previous step from contaminating the sample or subsequent polishing media. This procedure markedly reduced the density of scratches caused by polishing. If any contamination-induced scratches developed on the sample surface at any step, the sample was repolished for a few minutes using the diamond lapping film with the grit size of the previous step to remove the scratches. The final thickness of the PBN substrates ranged from 200 – 300 μm. Surface finishes with 2.8 nm RMS roughness over a 2.5 μm × 2.5 μm area were achieved. Annealing the as-polished PBN substrates for three-hours in a 2 slm H_2 atmosphere at ~ 1060 °C and a total chamber pressure of 10 Torr further reduced the surface roughness to 1.2 nm over the same area. Figure 7.3.1 shows the atomic force microscopy (AFM) (NT-MDT NTegra) images of the as-received PBN surface (a), the as-polished surface (b), and the polished surface annealed in H_2 for 3 hours (c).

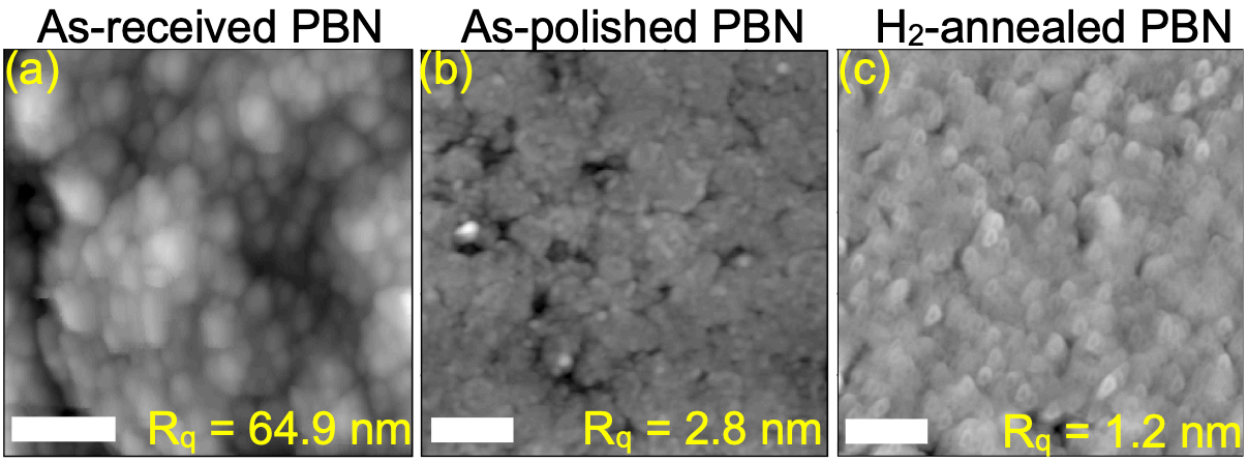

Figure 7.3.1. AFM images of (a) as-received, (b) as-polished PBN, (c) and polished and H_2-annealed surfaces of PBN. Scale bars are 500 nm. Rq is the value of RMS surface roughness.

Prior to the growth of each thin film, an as-polished PBN substrate was cleaned sequentially using a ten-minute sonication in acetone, a ten-minute sonication in isopropanol, a final rinse in DI water and then dried with UHP N_2. A single substrate was then loaded onto a planar SiC-coated graphite susceptor, placed inside a cold-wall, vertical showerhead reactor and heated resistively via graphite filament. After the 3 hour anneal described above, the chamber was evacuated to a base pressure of at least 2.0×10^{-6} Torr using a turbomolecular pump. Each growth run was initiated by closing the valve to the turbomolecular pump and using a rotary vane pump to maintain a total chamber pressure of 10 Torr during growth. B_2H_6 (5N-semiconductor grade 10% B_2H_6 in H_2) and NH_3 (99.9992% research grade) were the B- and N-source precursors, respectively. The diluent gas was H_2, flowed at 2 slm. The V/III ratio of N/B = 200 was established and maintained using a B_2H_6 flow rate of 2 sccm and an NH_3 flow rate of 0.80 slm. The growth temperature, measured using a pyrometer (Fluke Process Instruments), was set to ~ 1060 °C. The growth times were 2 hours and 4.5 hours.

AFM micrographs were collected in semi-contact mode with Cr/Pt-coated Si cantilevers possessing a resonant frequency of 190 kHz. A scan rate of 1 Hz was typically used, and 256

samples per line were sampled for 256 lines. All post-processing including plane fit, surface flattening, and de-streaking were performed using Gwyddion [52]; this software was also used to calculate RMS surface roughness of the processed images. Raman spectroscopy (NT-MDT Spectra) of select samples was performed using a 532 nm laser and a 600 lines/mm grating. The atomic composition and chemical bonding states at the surface of select samples were analyzed using x-ray photoelectron spectroscopy (XPS). The spectra of the grown films were captured using a cylindrical mirror analyzer (Staib Instruments, Inc.). An Al Kα (1486.6 eV) anode was used as the x-ray emission source. To prepare clean surfaces immediately prior to XPS analysis, all samples were sonicated in both acetone and isopropanol for 10 minutes each, dried with UHP N_2 and heated at ~1000 ^{o}C via an electron beam for 30 minutes at 10^{-7} Torr to facilitate thermal desorption of contaminant species. The XPS spectra were charge calibrated to the C 1s binding energy of 284.6 eV for adventitious carbon [53]. The subcomponents of the B 1s and N 1s spectra were modeled with mixed Gaussian (80%) – Lorentzian (20 %) distributions [54] and a non-linear background using curve-fitting software. Quantification of XPS spectra for surface composition analysis was performed using CasaXPS (Casa Software Ltd), where an escape depth correction was applied to each spectra using the electron attenuated length approximation [55]. Cross-sectional high resolution TEM (HRTEM) (FEI Themis) operated at 200 kV was used to characterize the microstructure of the layers of the grown BN films and that of the substrate-film interface. Electron-transparent cross-sectional lamellae were prepared using focused-ion beam (FIB) milling (FEI Xe Plasma Dual Beam). Prior to loading samples into the FIB chamber, their surfaces were made more conductive by the deposition of an ~ 10 nm Au film via dc sputtering at room temperature. A 2 μm × 15 μm rectangular section of Pt was subsequently deposited via electron-beam evaporation as a protective layer for the cross-sectional regions of interest.

7.4 Results and discussion

Representative structural, chemical and microstructural properties of the PBN substrates used as BN growth templates in this study are summarized in Figure 7.4.1. Figure 7.4.1 (a) shows the 2θ-ω XRD pattern of the PBN material. It is apparent from the multiple indexed peaks that the PBN material consists of polycrystalline grains of various crystallographic orientations. The principal (0002) reflection used to identify sp^2-BN occurs at a 2θ angle of ~ 26.0° instead of 26.7° as reported for crystalline sp^2-BN in the literature [43]. The measured 26.0° 2θ angle for the (0002) reflection results in a d_{0002} spacing of ~ 0.34 nm, which is larger than the reported 0.33 nm and thus suggestive of t-BN. Further, the $(10\bar{1}0)$ and $(10\bar{1}1)$ planes, which reflect at 2θ angles of 41.6° and 43.9°, respectively, in crystalline sp^2-BN are indistinguishable for the PBN material which suggests poor in-plane order. These reflections have been labeled $(10\bar{1}l)$ in Figure 7.4.1 (a). The Raman spectrum of PBN is shown in Fig. 7.4.1 (b). The peak in this spectrum is for the E_{2g} vibrational mode, which represents in-plane B-N stretching and occurs at 1369 cm^{-1}; this value is close to that of 1366 cm^{-1} for bulk sp^2-BN [56]. Figs. 7.4.1 (c) and (d) show the B 1s and N 1s XPS spectra, respectively, of a polished and cleaned PBN surface. The B 1s and N 1s binding energy shifts occur at 190.7 eV and 398.8 eV, respectively, which are both close to the reported binding energies of B 1s [53,54] and N 1s [16,20,28,54] in sp^2-BN. The B:N surface atomic ratio was measured to be 1:0.98. Both B 1s and N 1s spectra show the existence of a π-plasmon peak at ~ 9 eV above the main 1s core shell peaks, which is indicative of sp^2-BN bonding; the absence of this π-plasmon peak would indicate the formation of sp^3-bonded B-N networks as observed in cubic or amorphous BN [57]. The TEM image in Fig. 7.4.1 (e) shows the representative cross-sectional microstructure of the PBN material. From the image, it can be observed that the (0002) lattice planes are not of a single orientation. The rings

observed in the selected area electron diffraction (SAED) pattern shown in the inset of Fig. 7.4.1 (e) indicate that the PBN is polycrystalline. The region enclosed by the yellow rectangle in Fig. 7.4.1 (e) is magnified in the adjacent inset image. The d_{0002} spacing in this image is ~ 0.34 nm. This value is corroborated by the XRD analysis as discussed above and again indicates the presence of t-BN.

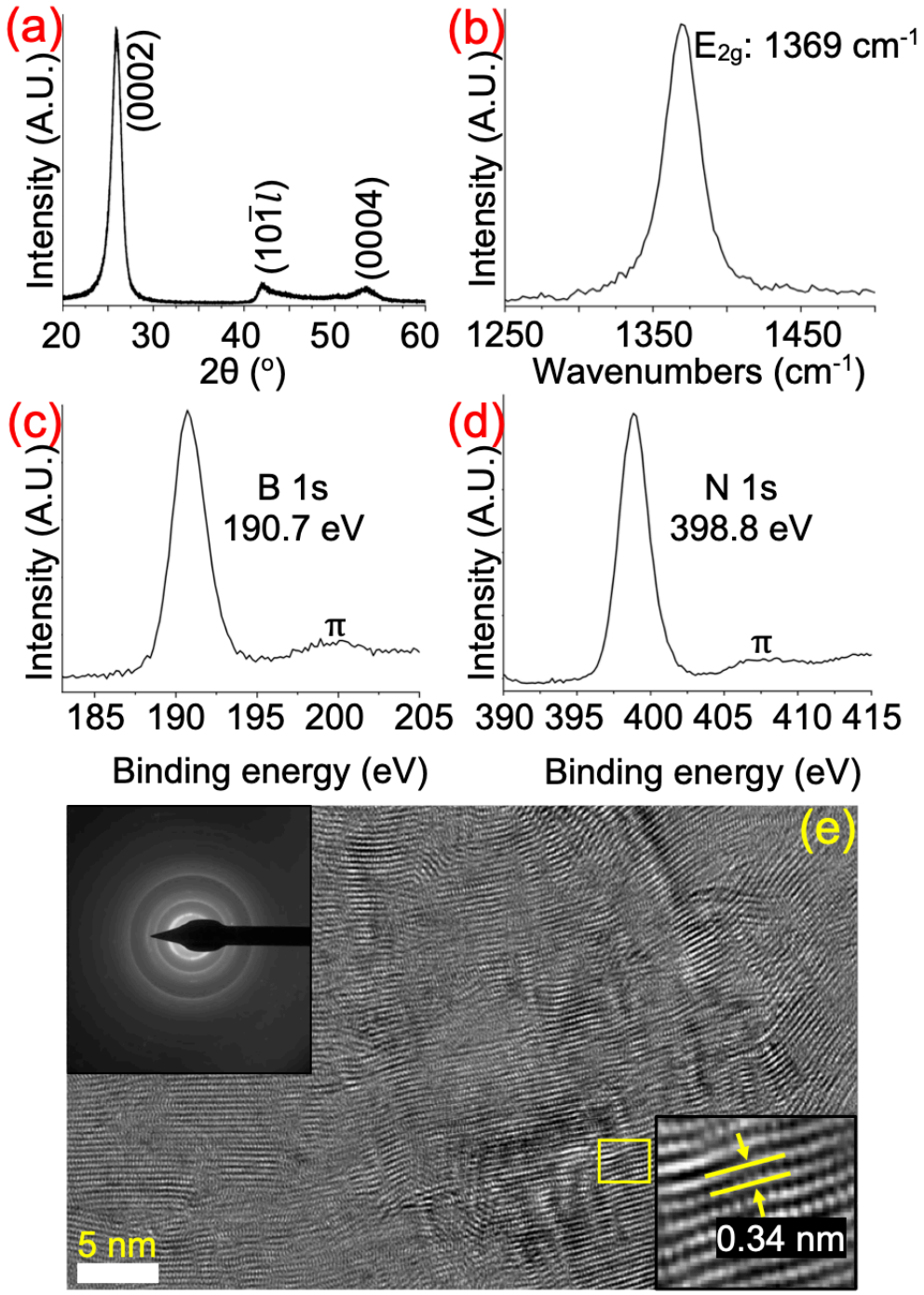

Figure 7.4.1. (a) 2θ-ω XRD scan, (b) Raman spectrum, (c) B 1s XPS spectrum, (d) N 1s XPS spectrum, (e) HRTEM and (f) SAED pattern of the PBN substrates used as BN growth templates in this study. The inset in (e) is a magnified image of the region enclosed by the yellow box.

Figure 7.4.2 shows the AFM and cross-sectional HRTEM images of an sp^2-BN thin film grown on a mechanically polished PBN substrate for 2 hours at 1060 ^oC. The AFM image in Fig. 7.4.2 (a) reveals protruding features that extend from the growth surface, which was determined to have an RMS roughness of R_q = 3.7 nm. For reference, one of these features is enclosed by a yellow circle. The average cross-sectional length of the protruding features ascertained from the measurement of 50 of these features is 34 $\pm$ 9 nm. A representative TEM micrograph of the microstructure of the cross section of a CVD-BN/PBN film is shown in Fig. 7.4.2 (b). The average thickness of these films was 26.4 $\pm$ 4.4 nm, as measured at 25 locations across 5 cross-sectional images of the same specimen. The interface between the PBN substrate and CVD-BN film is demarcated by a yellow dotted line. The interface is discernible because of an abrupt orientation change in the microstructure of the CVD-BN relative to the PBN. In this particular region it can be seen that the (0002) plane orientation in the PBN substrate is such that the [0001] direction is nearly perpendicular to the horizontal. However, the initial layers of CVD-BN do not grow in the same direction as the underlying orientation of the substrate. Rather, they grow only partially ordered with [0001] orientation, and they are interrupted frequently by discontinuities. The partially ordered layers grow for 3 – 4 nm before transitioning into random orientations, which extend as a few-layers of sp^2-BN that wind throughout the film. The film eventually meets the Au coating where the surface protrusions observed via AFM (see Fig. 7.4.2 (a)) meet at sharp angles. The widths at the bottoms of the two protrusions shown in Fig. 7.4.2 (b) are approximately 22 and 28 nm, which is in agreement with the feature size measured from the AFM image. I. e., each of the very small features shown in 7.4.2 (a) (of which one is indicated by a yellow circle) is the same feature shown in the magnified image of the protrusion enclosed by the dotted yellow rectangle in Fig. 7.4.2 (b). Fig. 7.4.2 (c) reveals that the surface of the

protrusion consists of approximately 10 sp^2-BN monolayers (having a total thickness of ~3.6 nm) that had continuously wound and bent out of plane within the bulk of the film and then emerged from this underlying volume. The inset shows a magnified image of the region enclosed by the white rectangle; the monolayer spacing was measured to be ~ 0.35 nm. The increased spacing, coupled with the chaotic growth of few-layer sp^2-BN, indicates that the film possesses more turbostratic disorder than the PBN substrate under the prescribed growth conditions.

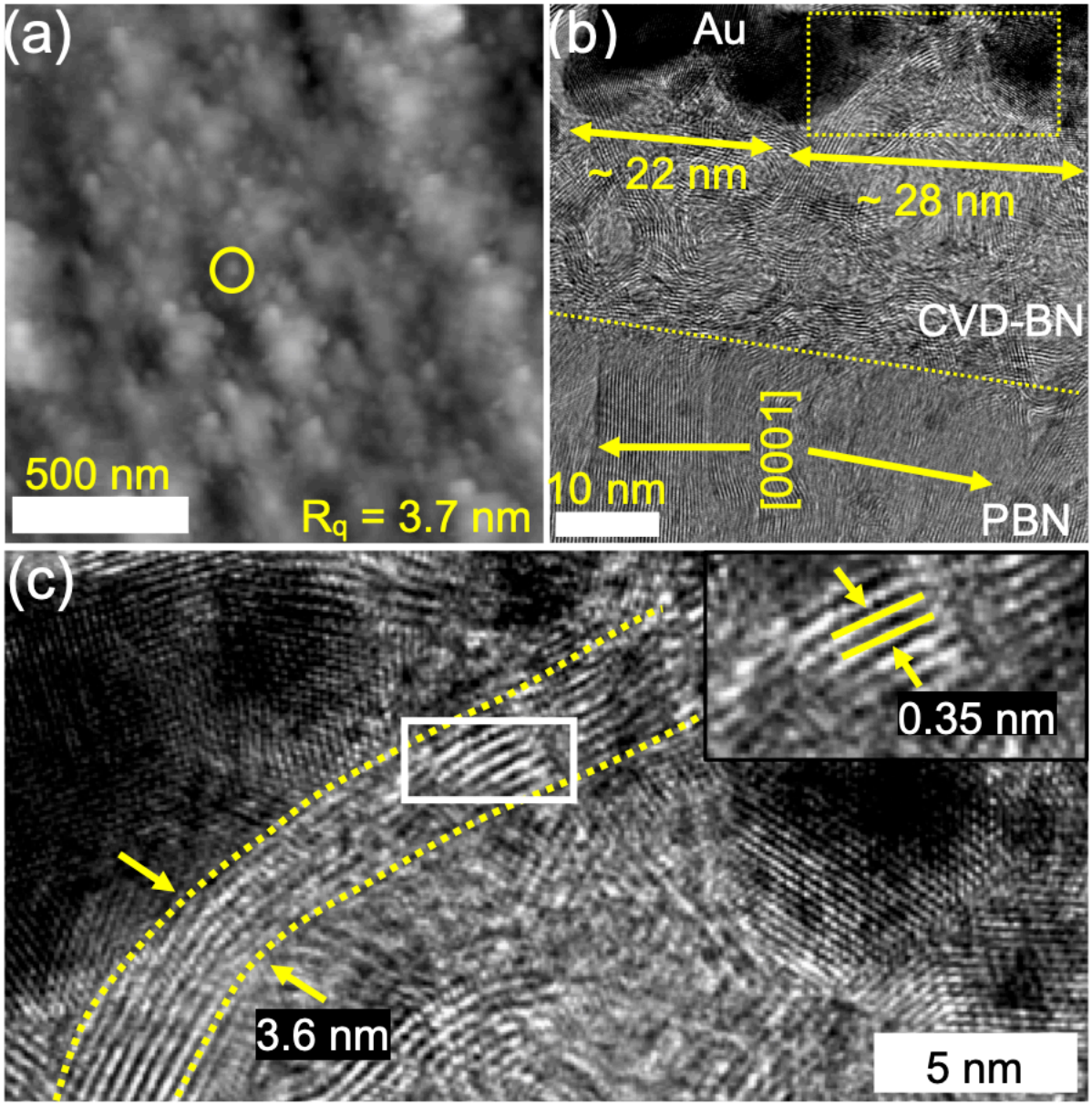

Figure 7.4.2. (a) AFM and (b) cross-sectional HRTEM images of a CVD-BN thin film grown for 2 hours on polished PBN. (c) Magnification of region of a protrusion enclosed by the dotted yellow rectangle in (b); the inset in (c) is a magnification of the region enclosed by the white rectangle.

Figures 7.4.3 (a), (b) and (c) show the AFM, low-magnification cross-sectional TEM, and HRTEM images, respectively, of a CVD-BN thin film grown for 4.5 hours on polished PBN. The resulting film was on average 108.8 $\pm$ 10.8 nm thick as measured from 25 locations across 5 cross-sectional images of the same specimen. The AFM results in Fig. 7.4.3 (a) reveal that a longer deposition time resulted in a much rougher surface (R_q = 35.5 nm) with more pronounced out-of-plane protruding features than that of the film grown for 2 hours. An example of a protruding feature is enclosed by the yellow oval in the image; the average size of these features is 155 $\pm$ 40 nm. Verification of the larger sizes of these protrusions was obtained using low magnification TEM as shown in Fig. 7.4.3 (b), where width at the bottom of the protrusion shown was measured to be ~175 nm.

In Fig. 7.4.3 (c), the yellow dotted line marks the CVD-BN/PBN interface. Just as in Fig. 7.4.3 (b), Fig. 7.4.3 (c) shows that regardless of the underlying crystallographic orientations that are present at the surface of the substrate, the initial layers of CVD-BN are partially ordered in the [0001] direction. The initial layer region enclosed by the yellow rectangle #1 corresponds to the inset FFT #1. The $(000l)$ reflection spots can be observed, as well as the $(10\bar{1}0)$ and $(10\bar{1}1)$ rings and streaking for the $(10\bar{1}2)$ reflection. As implied by the X-ray diffraction results shown in Fig. 7.4.3 (a) and the associated text, the $(10\bar{1}0)$ and $(10\bar{1}1)$ interplanar spacings are very close (~ 2.17 Å and 2.06 Å, respectively) and are thus difficult to distinguish in the FFTs. As such, they are labeled $(10\bar{1}l)$. FFT #1 indicates that while the initial layers have a preferred [0001] orientation, the in-plane order is poor. Beyond roughly 3 – 4 nm of initial growth, it is again observed that the sp^2-BN layers grow in random orientations. Sets of 3 – 4 nm thick, roughly oriented [0001] planes of sp^2-BN can be observed winding throughout all of the bulk of the film. For reference, examples of these winding sets of planes are indicated by asterisks located

between the three sets of parallel lines in Fig. 7.4.3 (c). The random growth directions of the planes results in polycrystalline sp^2-BN, as suggested by the patterns within inset FFT #2 of the region enclosed by Rectangle #2. From FFT #2, it is apparent that the out-of-plane order of the CVD-BN becomes poor as evidenced by the inner full ring for $(000l)$ and the much more pronounced rings representing the $(10\bar{1}l)$ and $(10\bar{1}2)$ reflections. Beyond the initial 3 – 4 nm partially ordered layers of growth, it is again likely that the intersection of the winding sets of sp^2-BN planes which travel to the surface result in the protrusions observed in Figs. 7.4.3 (a) and 4(b).

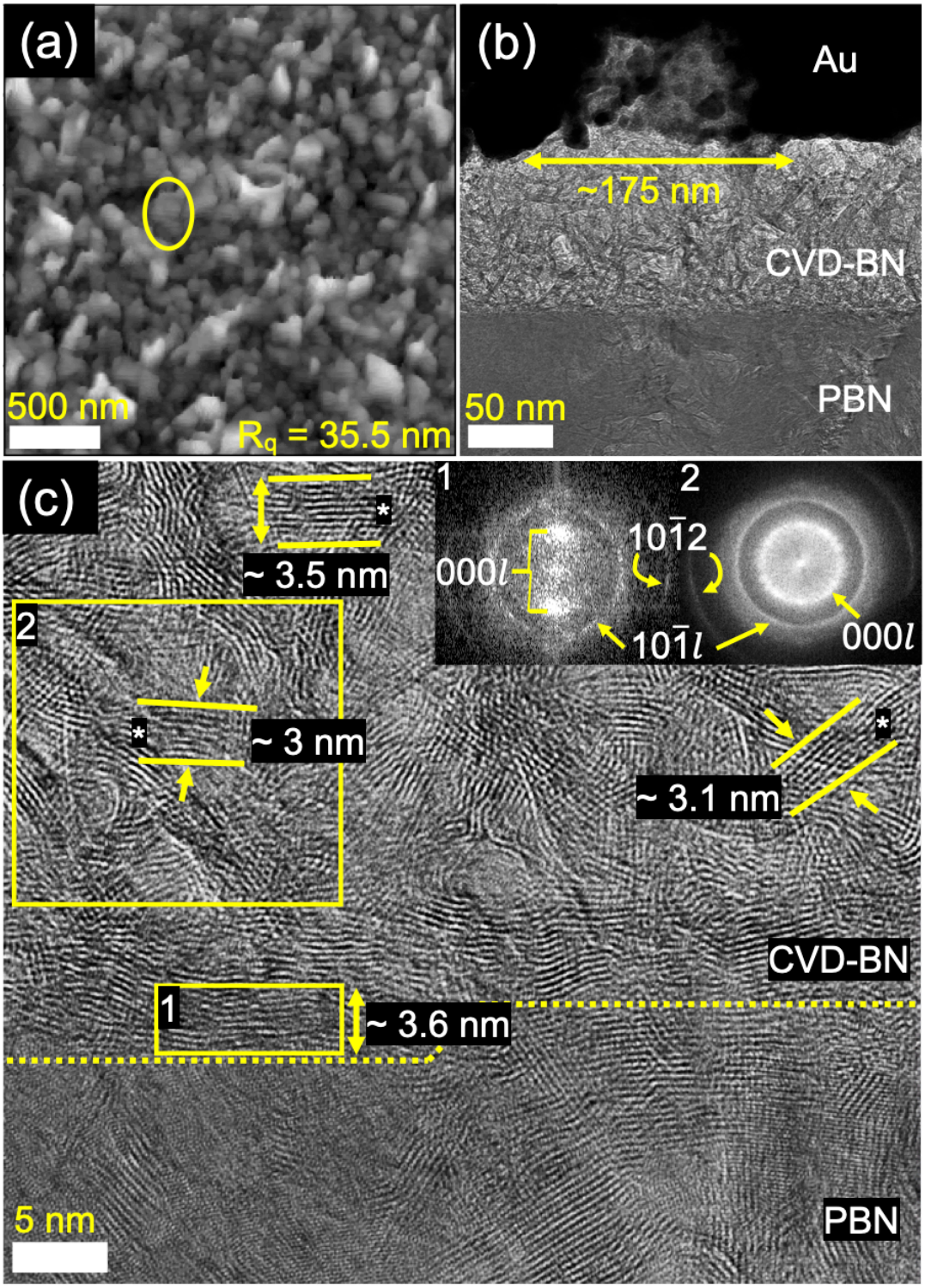

Figure 7.4.3. (a) AFM, (b) low-magnification cross-sectional TEM, and (c) HRTEM images of a CVD-BN thin film grown for 4.5 hours on a polished PBN substrate. The insets in (c) are FFTs of the regions of CVD-BN film enclosed by the correspondingly numbered yellow rectangles.

Figure 7.4.4 shows a dark-field TEM image of a CVD-BN thin film grown for 4.5 hours on polished PBN. The selected area (SA) aperture is centered on the (0002), $(10\bar{1}0)$, $(10\bar{1}1)$, and $(10\bar{1}2)$ PBN reflections and the resulting pattern is shown in the inset. Again, the $(10\bar{1}0)$ and $(10\bar{1}1)$ ring reflections are labeled $(10\bar{1}l)$. While the (0002) reflection is the most intense in this pattern, we cannot distinguish (0002) oriented crystallites from ones contributing to the other rings. What can be observed is an accumulation of CVD-BN crystallites with orientations at the film-substrate interface, which do not match that of the underlying substrate. I.e., there is not a true homoepitaxial relationship between the CVD-BN film and the polycrystalline PBN substrate even though they are the same material. Beyond the interface, it can be seen that the diffracting crystallites wind throughout the bulk of the film in various directions, which is consistent with the observations from Figures 7.4.2 (b) and 7.4.3 (c).

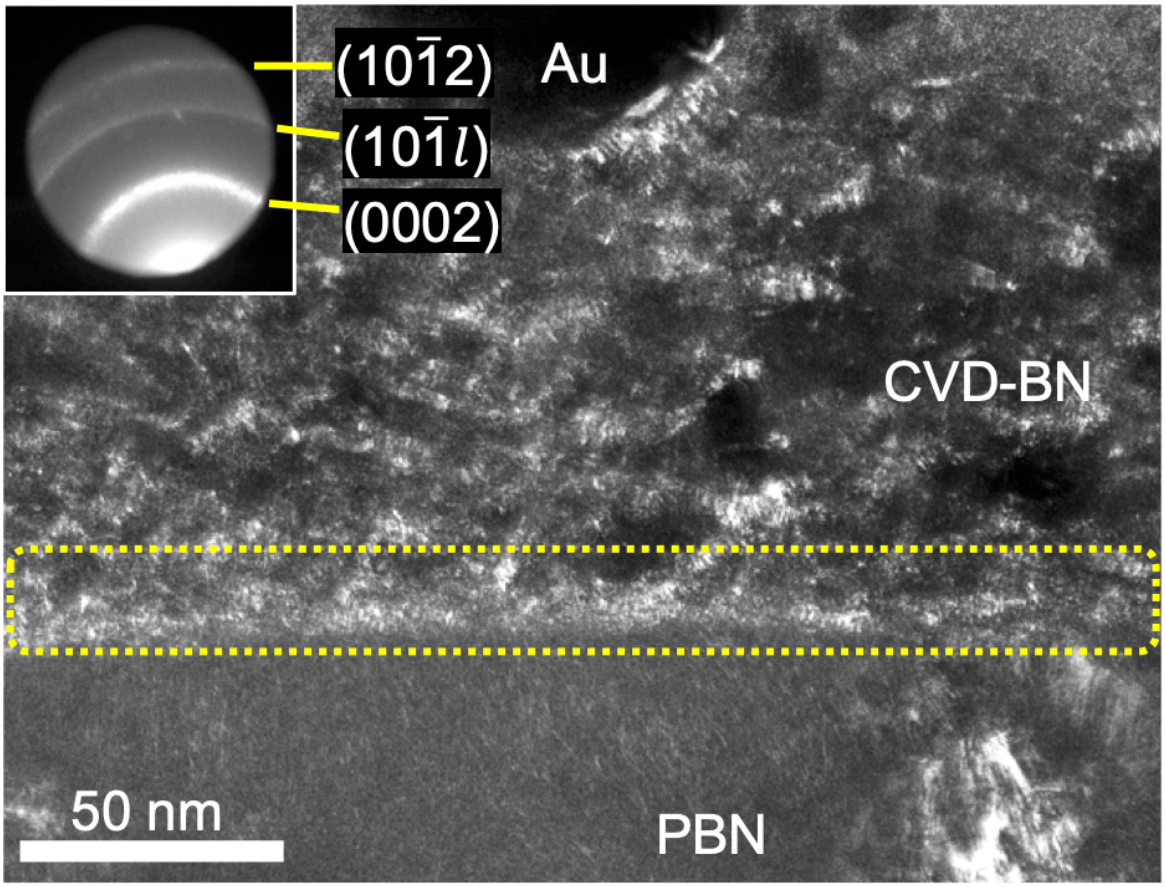

Figure 7.4.4. Dark field TEM image of a CVD-BN thin film grown for 4.5 hours on polished PBN. The SA aperture captures the (0002), (10$\bar{1}l$) , and (10$\bar{1}$2) PBN reflections.

Figures 7.4.5 (a) and (b) show the respective B 1s and N 1s XPS spectra of the ~ 100 nm thick, CVD-BN film deposited for 4.5 hours on polished PBN. The subcomponents of B 1s and N 1s can be observed in both spectra. Fig. 7.4.5 (a) shows the main bonding component of B-N_3 at 190.5 eV, which is within the 190.1 – 191 eV range of binding energies that indicates that B is bonded solely to three N atoms in an sp^2 network [53,54,58,59]. The low intensity spectra at 192.5 eV is indicative of B-O_x-N_{3-x} bonding [54] which is attributed to surface contamination. Similarly, the N 1s spectra in Fig. 7.4.5 (b) shows the main sp^2-BN bonding component for N at 398.4 eV and the smaller component attributed to O contamination at 400.5 eV [16,20,28,54]. The B:N surface atomic ratio was measured to be 1:0.97. In studies investigating both the

temperature and N/B gas phase ratio dependence of CVD reactions between B_2H_6 and NH_3 to synthesize BN thin films, it was shown [60] that at using temperatures ≥ 775 °C [61] and N/B ratios ≥ 8 result in the formation of borazine ($B_3N_3H_6$) as the dominant gas phase species en route to the eventual deposition to stoichiometric BN. Thus, all the films deposited in this research exhibited a compositional B:N surface ratio near unity, since the growth temperature was above 1000 °C and the N/B gas phase ratio was 200.

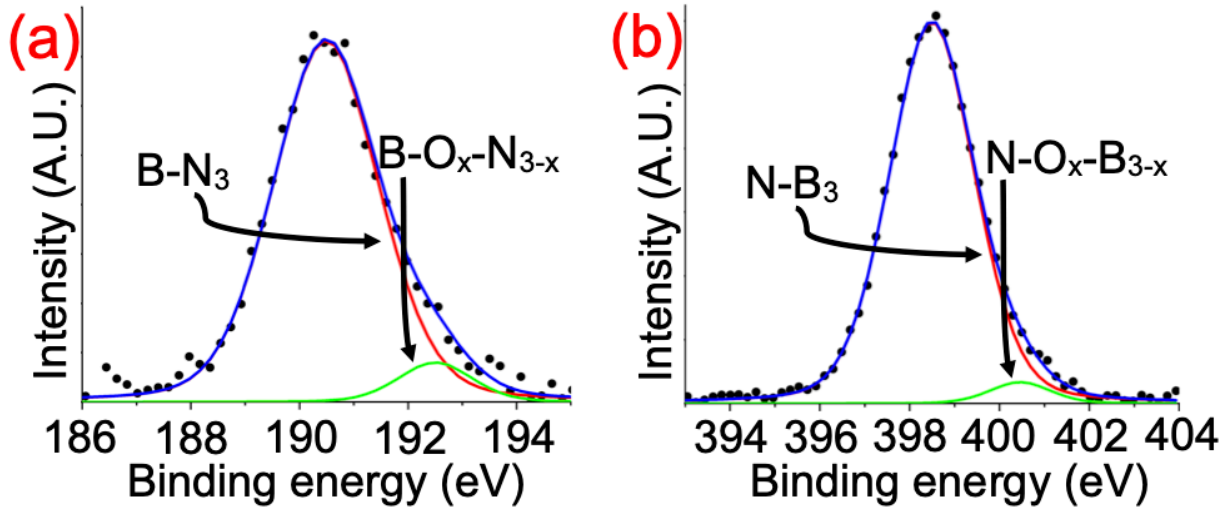

Figure 7.4.5. Deconvoluted (a) B 1s and (b) N 1s XPS spectra of a CVD-BN thin film grown for 4.5 hours on polished PBN. The black dots are the experimental data points. The blue curves are the model sums of the underlying curves.

As discussed above with regards to Figures 7.4.2 (b) and 7.4.3 (c), the initially deposited sp^2-BN layers are discontinuous, wavy, and tend to follow the contour of the substrate surface, which consists of the intersection of sets of layers with different orientations. It seems that [0001] is the preferred orientation for sp^2-BN during thermal CVD deposition at moderate temperatures even when there is no epitaxial relationship with the substrate. In a related study, Tay et al. [62] obtained the direct growth of up to 50 layers of nanocrystalline [0001] oriented sp^2-BN parallel to and on a 285 nm thick amorphous SiO_2 layer grown on a Si substrate. The BN was deposited at 1000 °C using ammonia borane (NH_3-BH_3) as a single-source precursor for both

B and N. Because of the absence of epitaxy of the deposited sp^2-BN films with the PBN substrates in the present study there were many local areas of lattice-mismatch between the [0001] oriented film layers and the underlying PBN orientations.

The transition within the films from an initial few nm of partially ordered sp^2-BN layers to randomly oriented growth is believed to be caused by the release in stresses generated within the film at and just above the substrate/film interface by the differences in lattice parameters of the PBN planes that commonly possess a nearly perpendicular intersection with this interface and the ordered sp^2-BN layers that are parallel to this interface. We can consider a hypothetical case where the [0001] direction of the crystallites in the substrate and film are exactly perpendicular to each other. Assuming that that both substrate and film are phase pure h-BN, the *a* constant of the film along the $[1\bar{1}00]$ direction is 2.504 Å and that of the $\frac{1}{2}c$ constant of the substrate (corresponding to one monolayer) along [0001] is 3.331 Å nm. The resulting lattice mismatch is ~ -24.8 %. Deposition studies at higher temperatures with the same precursors would be informative for determining if either (1) the initial layered and partially ordered structure in the CVD-BN on PBN is retained past a few nm or (2) the microstructure at the surface of the PBN is reproduced in the CVD-BN and thus homoepitaxy is obtained or (3) there is no change in the microstructure within the films from that observed in this research.

7.5. Summary and conclusions

Microstructural and chemical characterizations of stoichiometric nanocrystalline sp^2-BN thin films separately grown for 2 hrs. and 4.5 hrs. on mechanically polished, polycrystalline PBN via CVD at 1060 °C using B_2H_6 and NH_3 and an N/B ratio of 200 have been conducted. Film roughness increased with thickness. The initial 3 – 4 nm of the CVD-BN films consisted of partially oriented [0001] sp^2-BN layers that were microstructurally independent of the several

crystallographic orientations observed for sets of layers in the substrate. Growth within the films subsequently and sequentially transitioned into (a) randomly oriented and similarly thick sets of sp^2-BN planes and (b) the formation of protrusions at the top of each film for which much of the volume appeared to originate from continued growth of sets of layers from beneath the substrate surface. The absence of a homoepitaxial relationship is postulated to have induced stresses within the films at areas of lattice mismatch and subsequently triggered the transition to randomly oriented growth after the initial layers.

7.6 Acknowledgements

Funding for this project was made possible thanks to the National GEM Consortium Fellowship, the Neil and Jo Bushnell Fellowship in Engineering, and the John and Claire Bertucci Fellowship. The authors also acknowledge use of the Materials Characterization Facility at Carnegie Mellon University supported by grant MCF-677785.

7.7 Data availability

The data that supports the findings of this study are available within the article and its supplementary material.

7.8 Author declarations

Conflict of interest: The authors have no conflicts to disclose.

7. References

[1] A. W. Moore, J. Cryst. Growth **106**, 6 (1990). Characterization of pyrolytic boron nitride for semiconductor materials processing. DOI:10.1016/0022-0248(90)90281-O.

[2] L. Duclaux, B. Nysten, J. Issi, and A. W. Moore, Phys. Rev. B **46**, 3362 (1992). Structure and low temperature thermal conductivity of pyrolytic boron nitride. DOI:10.1103/PhysRevB.46.3362.

[3] R. Dahal, J. Li, S. Majety, B. N. Pantha, X. K. Cao, J. Y. Lin, and H. X. Jiang, Appl. Phys. Lett. **98**, 2 (2011). Epitaxially grown semiconducting hexagonal boron nitride as a deep ultraviolet photonic material. DOI:10.1063/1.3593958.

[4] H. X. Jiang and J. Y. Lin, Semicond. Sci. Technol. **29**, 084003 (2014). Hexagonal boron nitride for deep ultraviolet photonic devices. DOI:10.1088/0268-1242/29/8/084003.

[5] H. Liu, J. Meng, X. Zhang, Y. Chen, Z. Yin, D. Wang, Y. Wang, J. You, M. Gao, and P. Jin, Nanoscale **10**, 5559 (2018). High-performance deep ultraviolet photodetectors based on few-layer hexagonal boron nitride. DOI:10.1039/c7nr09438h.

[6] S. Majety, J. Li, X. K. Cao, R. Dahal, B. N. Pantha, J. Y. Lin, and H. X. Jiang, Appl. Phys. Lett. **100**, (2012). Epitaxial growth and demonstration of hexagonal BN/AlGaN p-n junctions for deep ultraviolet photonics. DOI:10.1063/1.3682523.

[7] A. Mballo, A. Srivastava, S. Sundaram, P. Vuong, S. Karrakchou, Y. Halfaya, S. Gautier, P. L. Voss, A. Ahaitouf, J. P. Salvestrini, and A. Ougazzaden, Nanomaterials **11**, 1 (2021). Towards p-type conduction in hexagonal boron nitride: Doping study and electrical measurements analysis of HBN/algan heterojunctions. DOI:10.3390/nano11010211.

[8] I. Meric, C. R. Dean, N. Petrone, L. Wang, J. Hone, P. Kim, and K. L. Shepard, Proc. IEEE **101**, 1609 (2013). Graphene field-effect transistors based on boron-nitride dielectrics. DOI:10.1109/JPROC.2013.2257634.

[9] S. M. Kim, A. Hsu, M. H. Park, S. H. Chae, S. J. Yun, J. S. Lee, D.-H. Cho, W. Fang, C. Lee, T. Palacios, M. Dresselhaus, K. K. Kim, Y. H. Lee, and J. Kong, Nat. Commun. **6**, 8662 (2015). Synthesis of large-area multilayer hexagonal boron nitride for high material performance. DOI:10.1038/ncomms9662.

[10] L. Bourgeois, Y. Bando, and T. Sato, J. Phys. D. Appl. Phys. **33**, 1902 (2000). Tubes of rhombohedral boron nitride. DOI:10.1088/0022-3727/33/15/321.

[11] M. Chubarov, H. Pedersen, H. Högberg, Z. Czigány, M. Garbrecht, and A. Henry, Chem. Mater. **27**, 1640 (2015). Polytype pure sp2-BN thin films as dictated by the substrate crystal structure. DOI:10.1021/cm5043815.

[12] M. Chubarov, H. Högberg, A. Henry, and H. Pedersen, J. Vac. Sci. Technol. A Vacuum, Surfaces, Film. **36**, 030801 (2018). Review article: Challenge in determining the crystal structure of epitaxial 0001 oriented sp 2 -BN films. DOI:10.1116/1.5024314.

[13] J. Thomas, Jr., N. E. Weston, and T. E. O'Connor, Phys. Inorg. Chem. **84**, 4619 (1963). Turbostratic boron nitride, thermal transformation to ordered-layer-lattice boron nitride. DOI:10.1021/ja00883a001.

[14] S. Alkoy, C. Toy, T. Gönül, and A. Tekin, J. Eur. Ceram. Soc. **17**, 1415 (1997). Crystallization behavior and characterization of turbostratic boron nitride. DOI:10.1016/S0955-2219(97)00040-X.

[15] P. M. Jean-Remy, B. A. Webler, P. C. Pistorius, and R. F. Davis, J. Cryst. Growth **572**, 1 (2021). Thermodynamic calculations for the chemical vapor deposition of hexagonal boron nitride using triethylboron, ammonia, and hydrogen.

DOI:10.1016/j.jcrysgro.2021.126283.
[16] P. R. Kidambi, R. Blume, J. Kling, J. B. Wagner, C. Baehtz, R. S. Weatherup, R. Schloegl, B. C. Bayer, and S. Hofmann, Chem. Mater. **26**, 6380 (2014). In situ observations during chemical vapor deposition of hexagonal boron nitride on polycrystalline copper. DOI:10.1021/cm502603n.
[17] K. K. Kim, A. Hsu, X. Jia, S. M. Kim, Y. Shi, M. Hofmann, D. Nezich, J. F. Rodriguez-Nieva, M. Dresselhaus, T. Palacios, and J. Kong, Nano Lett. **12**, 161 (2012). Synthesis of monolayer boron nitride on Cu foil using chemical vapor deposition. DOI:10.1021/nl203249a.
[18] M. H. Khan, Z. Huang, F. Xiao, G. Casillas, Z. Chen, P. J. Molino, and H. K. Liu, Sci. Rep. **5**, 7743 (2015). Synthesis of large and few atomic layers of hexagonal boron nitride on melted copper. DOI:10.1038/srep07743.
[19] Y. Uchida, T. Iwaizako, S. Mizuno, M. Tsuji, and H. Ago, Phys. Chem. Chem. Phys. **19**, 8230 (2017). Epitaxial chemical vapour deposition growth of monolayer hexagonal boron nitride on Cu(111)/sapphire substrate. DOI:10.1039/C6CP08903H.
[20] N. Guo, J. Wei, L. Fan, Y. Jia, D. Liang, H. Zhu, K. Wang, and D. Wu, Nanotechnology **23**, 415605 (2012). Controllable growth of triangular hexagonal boron nitride domains on copper foils by an improved low-pressure chemical vapor deposition method. DOI:10.1088/0957-4484/23/41/415605.
[21] W. Auwärter, H. U. Suter, H. Sachdev, and T. Greber, Chem. Mater. **16**, 343 (2004). Synthesis of one monolayer of hexagonal boron nitride on Ni(111) from B-trichloroborazine (ClBNH)3. DOI:10.1021/cm034805s.
[22] W. Auwärter, M. Muntwiler, T. Greber, and J. Osterwalder, Surf. Sci. **511**, 379 (2002). Co on h-BN/Ni(1 1 1): From island to island-chain formation and Co intercalation. DOI:10.1016/S0039-6028(02)01545-5.
[23] Y. Shi, C. Hamsen, X. Jia, K. K. Kim, A. Reina, M. Hofmann, A. L. Hsu, K. Zhang, H. Li, Z. Y. Juang, M. S. Dresselhaus, L. J. Li, and J. Kong, Nano Lett. **10**, 4134 (2010). Synthesis of few-layer hexagonal boron nitride thin film by chemical vapor deposition. DOI:10.1021/nl1023707.
[24] A. Nagashima, N. Tejima, Y. Gamou, T. Kawai, and C. Oshima, Phys. Rev. Lett. **75**, 3918 (1995). Electronic structure of monolayer hexagonal boron nitride physisorbed on metal surfaces. DOI:10.1103/PhysRevLett.75.3918.
[25] A. Gibb, N. Alem, and A. Zettl, Phys. Status Solidi **250**, 2727 (2013). Low pressure chemical vapor deposition synthesis of hexagonal boron nitride on polycrystalline metal foils. DOI:10.1002/pssb.201300088.
[26] H. Oh, J. Jo, Y. Tchoe, H. Yoon, H. Hwi Lee, S.-S. Kim, M. Kim, B.-H. Sohn, and G.-C. Yi, NPG Asia Mater. **8**, 1 (2016). Centimeter-sized epitaxial h-BN films. DOI:10.1038/am.2016.178.
[27] Y. Gao, W. Ren, T. Ma, Z. Liu, Y. Zhang, W. Bin Liu, L. P. Ma, X. Ma, and H. M. Cheng, ACS Nano **7**, 5199 (2013). Repeated and controlled growth of monolayer, bilayer and few-layer hexagonal boron nitride on Pt foils. DOI:10.1021/nn4009356.
[28] A. B. Preobrajenski, A. S. Vinogradov, and N. Mårtensson, Surf. Sci. **582**, 21 (2005). Monolayer of h-BN chemisorbed on Cu(1 1 1) and Ni(1 1 1): The role of the transition metal 3d states. DOI:10.1016/j.susc.2005.02.047.
[29] R. Laskowski, P. Blaha, and K. Schwarz, Phys. Rev. B - Condens. Matter Mater. Phys. **78**, 1 (2008). Bonding of hexagonal BN to transition metal surfaces: An ab initio density-

functional theory study. DOI:10.1103/PhysRevB.78.045409.
[30] M. H. Khan, H. K. Liu, X. Sun, Y. Yamauchi, Y. Bando, D. Golberg, and Z. Huang, Mater. Today **20**, 611 (2017). Few-atomic-layered hexagonal boron nitride: CVD growth, characterization, and applications. DOI:10.1016/j.mattod.2017.04.027.
[31] C. M. Orofeo, S. Suzuki, H. Kageshima, and H. Hibino, Nano Res. **6**, 335 (2013). Growth and low-energy electron microscopy characterization of monolayer hexagonal boron nitride on epitaxial cobalt. DOI:10.1007/s12274-013-0310-1.
[32] C. Wu, A. M. Soomro, F. Sun, H. Wang, C. Liu, X. Yang, J. Kang, and D. Cai, Phys. Status Solidi Basic Res. **253**, 829 (2016). Seven-inch large-size synthesis of monolayer hexagonal BN film by low-pressure CVD. DOI:10.1002/pssb.201552619.
[33] K. Nakamura, J. Electrochem. Soc. **133**, 1120 (1986). Preparation and Properties of Boron Nitride Films by Metal Organic Chemical Vapor Deposition. DOI:10.1149/1.2108797.
[34] M. Chubarov, H. Pedersen, H. Högberg, V. Darakchieva, J. Jensen, P. O. Å. Persson, and A. Henry, Phys. Status Solidi - Rapid Res. Lett. **5**, 397 (2011). Epitaxial CVD growth of sp2-hybridized boron nitride using aluminum nitride as buffer layer. DOI:10.1002/pssr.201105410.
[35] M. Chubarov, H. Pedersen, H. Högberg, J. Jensen, and A. Henry, Cryst. Growth Des. **12**, 3215 (2012). Growth of high quality epitaxial rhombohedral boron nitride. DOI:10.1021/cg300364y.
[36] Q. Paduano, M. Snure, D. Weyburne, A. Kiefer, G. Siegel, and J. Hu, J. Cryst. Growth **449**, 148 (2016). Metalorganic chemical vapor deposition of few-layer sp2 bonded boron nitride films. DOI:10.1016/j.jcrysgro.2016.06.012.
[37] Y. Kobayashi and T. Akasaka, J. Cryst. Growth **310**, 5044 (2008). Hexagonal BN epitaxial growth on (0 0 0 1) sapphire substrate by MOVPE. DOI:10.1016/j.jcrysgro.2008.07.010.
[38] Q. S. Paduano, M. Snure, J. Bondy, and T. W. C. Zens, Appl. Phys. Express **7**, 1 (2014). Self-terminating growth in hexagonal boron nitride by metal organic chemical vapor deposition. DOI:10.7567/APEX.7.071004.
[39] Y. Jin, S. Lee, Y. Nam, J. K. Lee, and D. Park, Korean J. Chem. Eng. **15**, 652 (1998). A Study of Deposition Rate and Characterization of BN Thin Films Prepared By CVD.
[40] Y. Kobayashi and T. Makimoto, Japanese J. Appl. Physics, Part 1 Regul. Pap. Short Notes Rev. Pap. **45**, 3519 (2006). Growth of boron nitride on 6H-SiC substrate by flow-rate modulation epitaxy. DOI:10.1143/JJAP.45.3519.
[41] S. Majety, J. Li, W. P. Zhao, B. Huang, S. H. Wei, J. Y. Lin, and H. X. Jiang, Appl. Phys. Lett. **102**, (2013). Hexagonal boron nitride and 6H-SiC heterostructures. DOI:10.1063/1.4808365.
[42] M. Chubarov, H. Pedersen, H. Högberg, Z. Czigany, and A. Henry, CrystEngComm **16**, 5430 (2014). Chemical vapour deposition of epitaxial rhombohedral BN thin films on SiC substrates. DOI:10.1039/c4ce00381k.
[43] R. S. Pease, Acta Crystallogr. **5**, 356 (1952). An x-ray study of boron nitride. DOI:10.1107/S0365110X52001064.
[44] J. C. Koepke, J. D. Wood, Y. Chen, S. W. Schmucker, X. Liu, N. N. Chang, L. Nienhaus, J. W. Do, E. A. Carrion, J. Hewaparakrama, A. Rangarajan, I. Datye, R. Mehta, R. T. Haasch, M. Gruebele, G. S. Girolami, E. Pop, and J. W. Lyding, Chem. Mater. **28**, 4169 (2016). Role of pressure in the growth of hexagonal boron nitride thin films from ammonia-borane. DOI:10.1021/acs.chemmater.6b00396.

[45] X. Li, S. Sundaram, Y. El Gmili, T. Ayari, R. Puybaret, G. Patriarche, P. L. Voss, J. P. Salvestrini, and A. Ougazzaden, Cryst. Growth Des. **16**, 3409 (2016). Large-area two-dimensional layered hexagonal boron nitride grown on sapphire by metalorganic vapor phase epitaxy. DOI:10.1021/acs.cgd.6b00398.

[46] D. Chugh, J. Wong-Leung, L. Li, M. Lysevych, H. H. Tan, and C. Jagadish, 2D Mater. **5**, (2018). Flow modulation epitaxy of hexagonal boron nitride. DOI:10.1088/2053-1583/aad5aa.

[47] Y. Gu, M. Zheng, Y. Liu, and Z. Xu, J. Am. Ceram. Soc. **90**, 1589 (2007). Low-temperature synthesis and growth of hexagonal boron-nitride in a lithium bromide melt. DOI:10.1111/j.1551-2916.2007.01551.x.

[48] T. B. Hoffman, B. Clubine, Y. Zhang, K. Snow, and J. H. Edgar, J. Cryst. Growth **393**, 114 (2014). Optimization of Ni-Cr flux growth for hexagonal boron nitride single crystals. DOI:10.1016/j.jcrysgro.2013.09.030.

[49] C. Schimpf, M. Motylenko, and D. Rafaja, Mater. Charact. **86**, 190 (2013). Quantitative description of microstructure defects in hexagona boron nitrides usng x-ray diffraction analysis.

[50] A. V. Kurdyumov, Sov. Physics, Crystallogr. **20**, (1975). Stacking faults in graphitic boron nitride.

[51] T. Matsuda, N. Uno, H. Nakae, and T. Hirai, J. Mater. Sci. **21**, 649 (1986). Synthesis and structure of chemically vapour-deposited boron nitride. DOI:10.1007/BF01145537.

[52] D. Nečas and P. Klapetek, Cent. Eur. J. Phys. **10**, 181 (2012). Gwyddion: an open-source software for SPM data analysis. DOI:10.2478/s11534-011-0096-2.

[53] R. Trehan, Y. Lifshitz, and J. W. Rabalais, J. Vac. Sci. Technol. A Vacuum, Surfaces, Film. **8**, 4026 (1990). Auger and x-ray electron spectroscopy studies of hBN, cBN, and N2+ ion irradiation of boron and boron nitride. DOI:10.1116/1.576471.

[54] C. Guimon, D. Gonbeau, G. Pfister-Guillouzo, O. Dugne, A. Guette, R. Naslain, and M. Lahaye, Surf. Interface Anal. **16**, 440 (1990). XPS study of BN thin films deposited by CVD on SiC plane substrates. DOI:10.1002/sia.740160191.

[55] A. Jablonski and C. J. Powell, Surf. Sci. Rep. **47**, 33 (2002). The electron attenuation length revisited. DOI:10.1016/s0167-5729(02)00031-6.

[56] R. Geick, C. Perry, and G. Rupprecht, Phys. Rev. **146**, 543 (1966). Normal Modes in Hexagonal Boron Nitride. DOI:10.1103/PhysRev.146.543.

[57] D. H. Berns and M. A. Cappelli, Appl. Phys. Lett. **2711**, 2711 (1995). Cubic boron nitride synthesis in low-density supersonic plasma flows. DOI:10.1063/1.115573.

[58] K. S. Park, D. Y. Lee, K. J. Kim, and D. W. Moon, Appl. Phys. Lett. **70**, 315 (1997). Observation of a hexagonal BN surface layer on the cubic BN film grown by dual ion beam sputter deposition. DOI:10.1063/1.118402.

[59] A. Pilli, J. Jones, V. Lee, N. Chugh, J. Kelber, F. Pasquale, and A. LaVoie, J. Vac. Sci. Technol. A **36**, 061503 (2018). In situ XPS study of low temperature atomic layer deposition of B2O3 films on Si using BCl3 and H2O precursors. DOI:10.1116/1.5044396.

[60] C. Gómez-Aleixandre, A. Essafti, M. Fernandez, J. L. G. Fierro, and J. M. Albella, J. Phys. Chem. **100**, 2148 (1996). Influence of diborane flow rate on the structure and stability of CVD boron nitride films. DOI:10.1021/jp951200d.

[61] C. Gómez-Aleixandre, D. Díaz, F. Orgaz, and J. M. Albella, J. Phys. Chem. **97**, 11043 (1993). Reaction of diborane and ammonia gas mixtures in a chemical vapor deposition hot-wall reactor. DOI:10.1021/j100144a023.

[62] R. Y. Tay, S. H. Tsang, M. Loeblein, W. L. Chow, G. C. Loh, J. W. Toh, S. L. Ang, and E. H. T. Teo, Appl. Phys. Lett. **106**, 3 (2015). Direct growth of nanocrystalline hexagonal boron nitride films on dielectric substrates. DOI:10.1063/1.4914474.

8. Thesis Summary

Papers 1 and 2 were published in *MRS Communications* and the *Journal of Crystal Growth*, respectively. They both detail the methodology and analysis of equilibrium phase diagram calculations as they relate to the CVD synthesis of thin films of sp^2-BN phases.
In Paper 1, equilibrium thermodynamic data were used to calculate diagrams that indicate the extent of the phase fields wherein films of either h-BN or r-BN can be deposited via CVD as a function of temperature, B-containing precursor, and N/B ratio. Both the calculated results and the superposition onto analogous diagrams of reported experimental CVD conditions wherein growth of r-BN films was realized revealed that (1) the choice of B precursor markedly affects the allowable range of the initial gas phase N/B ratio and therefore the extent of the phase fields of both h- and r-BN and (2) the deposition of phase pure r-BN films has been achieved at temperatures well below the predicted h-BN ↔ r-BN transition temperature of 1730°C. The crystal structure of the substrate surface was also a factor in the growth of either single-phase r-BN or a poly-phase material containing r-BN and t-BN or r-BN and h-BN.

The principal objective of Paper 2 was to determine the conditions revealed by calculated CVD phase diagrams for the deposition of h-BN from TEB/NH_3/H_2 mixtures that avoid the co-deposition of C and B_4C. The results indicated that the equilibrium formation of single-phase h-BN is highly dependent on the temperature, total pressure, input reactant composition (N/B) and the H_2 diluent concentration (H_2/B + N). An example of a set of equilibrium conditions for producing h-BN, without co-deposition of C were found to be: N/B = ~ 10^3, H_2/(B + N) = 10, and a total pressure of 100 Torr. It was observed that in equilibrium, increasing the pressure extends h-BN stability while decreasing that of C and B_4C. Increasing the H_2/(B + N) ratio suppresses both the formation of C and the decomposition of NH_3 to NH_2 that is imperative for

the deposition of h-BN at higher temperatures. Comparison of these results with experimental results reported in literature revealed that the use of H_2 as the carrier and diluent, N/B ratios in the 10^2–10^3 range, pressures in the 10^1–10^2 Torr range, and temperatures within the range of 1000 ◦C to 1500 ◦C are suitable conditions to produce epitaxial sp^2-BN with TEB/NH_3 chemistry. The limitations of using the equilibrium calculations to predict C during CVD h-BN synthesis were also discussed in Paper 2.

Papers 3 and 4 were both submitted to the *Journal of Vacuum Science & Technology A*; Paper 3 was accepted for publication while Paper 4 is currently under Review. These papers detail the CVD synthesis and characterizations of sp^2-BN thin films deposited on (0001) 4H-SiC and pyrolytic boron nitride (PBN), respectively. Paper 3 details the microstructural, optical and chemical characterizations of nanocrystalline sp^2-BN thin films grown on (0001) 4H-SiC wafers via continuous CVD and two variations of the FME process using B_2H_6 and NH_3 that have been conducted for this Thesis. In the latter method, H_2 purge steps were included in each cycle, and the injection times for B_2H_6 were varied. The use of continuous CVD within the 20 – 200 N/B gas phase ratio range produced stoichiometric sp^2-BN. Films grown continuously only at N/B = 200 resulted in the initial growth of ~ 4 nm thick and partially ordered sp^2-BN layers. To essentially reproduce the results of initial layer formation using a discontinuous FME process it was necessary to also use an N/B ratio of = 200 as well as a flow rate and injection time for B_2H_6 of 2 sccm and 1 s, respectively, and an injection time for the NH_3 of ≥ 4s. Each initial region of these films also (1) contained increasing concentrations of polycrystalline BN and (2) served as a transition zone to a region of randomly oriented polycrystalline material. Using longer B_2H_6 injection times in the FME grown films resulted in the incorporation of excess B and a single

mixed amorphous and crystalline sp^2-BN layer without ordering of the initial layers at the substrate.

The homoepitaxial CVD growth of sp^2-BN on bulk sp^2-BN substrates has never been reported. The work presented in Paper 4 where sp^2-BN was deposited via CVD onto polished PBN provides initial progress in this endeavor. Microstructural and chemical characterization of stoichiometric nanocrystalline sp^2-BN thin films were separately grown for 2 hrs and 4.5 hrs on mechanically polished, polycrystalline PBN via CVD at 1060 °C using B_2H_6 and NH_3 and an N/B ratio of 200. A polishing procedure for PBN surfaces was developed and its steps were summarized. Film roughness of the grown films increased with thickness. The initial 3 – 4 nm of the CVD-BN films consisted of partially-oriented [0001] sp^2-BN layers that were microstructurally independent of the several crystallographic orientations observed for sets of layers in the substrate. Growth within the films subsequently and sequentially transitioned into (a) randomly oriented and similarly thick sets of sp^2-BN planes and (b) the formation of protrusions for which much of the volume appeared to originate from growth from sets of layers intersecting the substrate surface. The absence of a homoepitaxial relationship likely induced stresses from areas of lattice mismatch, thus triggering a transition into randomly oriented growth after the initial layers.

9. Future work and challenges

The research described and analyzed in this Thesis opens the door to interesting and necessary work that could further advance the field of sp^2-BN CVD synthesis and understanding of sp^2-BN phase equilibria. The thermodynamic functions of the BN polymorphs, especially h-BN and r-BN, should be updated. These functions and their relevance in the creation of thermal CVD phase diagrams are discussed at length in the Literature Review in Section 2.3 and Papers 1 and 2. Although the reference thermodynamic data for the BN polymorphs is comprehensive, they were all determined by the same group of researchers more than twenty years ago. The results of density functional theory calculations of BN phase stability often depend on the method of calculation. Also, most CVD sp^2-BN investigators do not employ the more stringent characterization techniques to determine with specificity the realization of either h-BN or r-BN. Thus, it is important for advancement in this field that the heat capacity curves (and subsequent entropy and Gibbs free energy calculations) be experimentally determined again. The original heat capacity and Gibbs free energy curves of h-BN and r-BN are extremely close in value, and it would be of interest for a future group to determine if similar numbers can be repeated.

As discussed in both the Literature Review in Section 2.2 and the Introduction sections of Papers 3 and 4 of this Thesis, epitaxial growth of sp^2-BN films on non-catalytic substrates such as sapphire, aluminum nitride and silicon carbide requires either (1) high temperatures (1300 – 1500 ^{o}C) at moderate V/III ratios (500 - 800) or (2) low growth temperatures and high V/III ratios (1000 – 2000). Because the high temperature CVD growth chambers needed in situation (1) may not be readily available in most research laboratories and situation (2) leads to very slow growth rates (e.g., several hours to grow a few nm thick film), a remaining challenge in the field of CVD of sp^2-BN is epitaxial growth at lower temperatures and moderate growth rates. One

technique that has potential to meet this challenge is the incorporation of a "surface-active," or surfactant species during thin film growth [1]. This method lowers the surface energy of the substrate and growing film and suppresses island formation. When films grow beneath a surfactant adlayer, film adatom lateral diffusion is enhanced on the substrate surface and thus can potentially lower the growth temperature for high melting temperature materials such as the Group III-nitrides [2]. This method has been explored for the growth of AlN, GaN, InN and their alloys by using Ga [2–4] or In [2, 5–7] as the surfactant species. Thus, it is of interest to explore surfactant-assisted CVD growth of sp^2-BN. The two-dimensional nature of its structure makes lateral adatom diffusion imperative to achieve one-dimensional or atomic layer-by-atomic layer growth, especially on technologically important non-catalytic substrates such as 4H- and 6H-SiC. In this context, it has been observed that adatom mobility of B and N species on (0001) 4H-SiC is poorer than on (0001)AlN/α-Al_2O_3 at the same growth temperature [8].

Paper 4 was the first research of its kind where sp^2-BN thin films were grown via CVD on pyrolytic boron nitride (PBN) substrates in the attempt to achieve homoepitaxial growth. The main challenge encountered during this project was the lack of a single orientation within the PBN substrates. This led to local areas of lattice mismatch with CVD sp^2-BN, which often did not grow with the same orientation as the substrate. A two-pronged approach could lead to the growth of higher quality sp^2-BN on PBN: (1) acquire commercial PBN that possesses near single [0001] orientation and/or (2) grow CVD sp^2-BN at higher temperatures (1300 – 1500 ^{o}C) to improve crystallinity of the grown layers and possibly reproduce the same microstructure of the PBN substrate.

Beyond the achievement of thick, large-area CVD-grown sp^2-BN thin films, more work in the field still must be explored to realize sp^2-BN as a functional device material, especially for

DUV device applications. As discussed in the Introduction (Section 1), shallow p-type doping of sp^2-BN has been achieved with Mg, but viable n-type dopants for sp^2-BN with shallow room-temperature activation energies need to be discovered and employed.

9. References

[1] M. Copel, M. C. Reuter, E. Kaxiras, and R. M. Tromp, Phys. Rev. Lett. **63**, 632 (1989). Surfactants in Epitaxial Growth.

[2] J. Neugebauer, T. K. Zywietz, M. Scheffler, J. E. Northrup, H. Chen, and R. M. Feenstra, Phys. Rev. Lett. **90**, 4 (2003). Adatom Kinetics On and Below the Surface: The Existence of a New Diffusion Channel. DOI:10.1103/PhysRevLett.90.056101.

[3] T. M. Al Tahtamouni, J. Li, J. Y. Lin, and H. X. Jiang, J. Phys. D. Appl. Phys. **45**, (2012). Surfactant effects of gallium on quality of AlN epilayers grown via metal-organic chemical-vapour deposition on SiC substrates. DOI:10.1088/0022-3727/45/28/285103.

[4] B. Daudin, G. Mula, C. Adelmann, J. Oullier, and S. Moehl, Phys. Rev. B - Condens. Matter Mater. Phys. **64**, 1 (2001). Surfactant effect of gallium during molecular-beam epitaxy of GaN on AlN (0001). DOI:10.1103/PhysRevB.64.195406.

[5] S. Nicolay, E. Feltin, J. F. Carlin, M. Mosca, L. Nevou, M. Tchernycheva, F. H. Julien, M. Ilegems, and N. Grandjean, Appl. Phys. Lett. **88**, 1 (2006). Indium surfactant effect on AlN/GaN heterostructures grown by metal-organic vapor-phase epitaxy: Applications to intersubband transitions. DOI:10.1063/1.2186971.

[6] S. Keller, S. Heikman, I. Ben-Yaacov, L. Shen, S. P. DenBaars, and U. K. Mishra, Appl. Phys. Lett. **79**, 3449 (2001). Indium-surfactant-assisted growth of high-mobility AlN/GaN multilayer structures by metalorganic chemical vapor deposition. DOI:10.1063/1.1420573.

[7] Y. Chen, H. Wu, E. Han, G. Yue, Z. Chen, Z. Wu, G. Wang, and H. Jiang, Appl. Phys. Lett. **106**, (2015). High hole concentration in p-type AlGaN by indium-surfactant-assisted Mg-delta doping. DOI:10.1063/1.4919005.

[8] M. Chubarov, H. Pedersen, H. Högberg, A. Henry, and Z. Czigány, J. Vac. Sci. Technol. A Vacuum, Surfaces, Film. **33**, 061520 (2015). Initial stages of growth and the influence of temperature during chemical vapor deposition of sp 2 -BN films . DOI:10.1116/1.4935155.

10. Appendices

10.1. Appendix A: Initial research concerning MOCVD growth of AlN(0001) films on 4H-SiC(0001) substrates

My initial investigations involved a collaborative effort with another student (Luis Hernandez) in the Davis Group concerned with the growth of AlN(0001) films on chemomechanically polished (CMP) 4H-SiC(0001) substrates and the characterization of the former. This research allowed me to develop an understanding of (1) the science and technology of metalorganic chemical vapor deposition (MOCVD), (2) the technology and operation of the multitude of electrical and mechanical components of a vertical, water-cooled system, (3) the safe and computer-controlled operation of the deposition systems in the Davis laboratories, (4) the safe handling and use of pyrophoric gases for deposition and (5) the function and successful use of the several analytical tools for the characterization of the AlN films. One component of this research involved the determination of the effects of the group V (nitrogen) to group III (aluminum) molar ratio (V/III) in the gas phase on the growth rate and microstructure of the AlN(0001) films.

Trimethylaluminum (TMA) and ammonia (NH_3) were used as the group III and group V sources, respectively. The V/III ratio was changed from 12,000 (12K) to 130,0000 (130K). Most samples were grown at 1100°C for 2 hours; the sample having the V/III ratio = 24,000 was grown for 2.5 hours. Although better surface adduct migration and film coalescence may be achievable at higher growth temperatures, 1100˚C is the highest operating temperature of the Davis Group MOCVD system. Thus, it was necessary to increase the V/III ratio by decreasing the molar flow rate of the TMA (q_{TMA}), which decreased the growth rate and thus enhanced the surface adduct mobility.

The thickness of each sample was measured using an F50 Filmetrics system. The samples grown with a V/III ratio of 12K, 24K, and 32K, had thickness values of 915 nm, 511 nm, and 292 nm, respectively. The samples grown with V/III = 65K and 130K did not yield repeatable values of thickness measurements; it is suspected that these films were less than 30 nm thick, as this is the lower measurement limit for the F50 system. The growth rates of the films were determined from this data and are displayed in Figure 10.1.1. The growth rate of each film is primarily controlled by the concentration of the Al-containing species that reacts with the more abundant ammonia either very near or on the substrate surface. As q_{TMA} is larger at lower V/III ratios, it was expected that (a) the sample grown at V/III = 12K would have the fastest growth rate (~ 7.6 nm/min) and therefore be the thickest film and (b) the growth rate and film thickness would decrease with increasing V/III ratio. The data presented in Figure 1 support these prior assumptions.

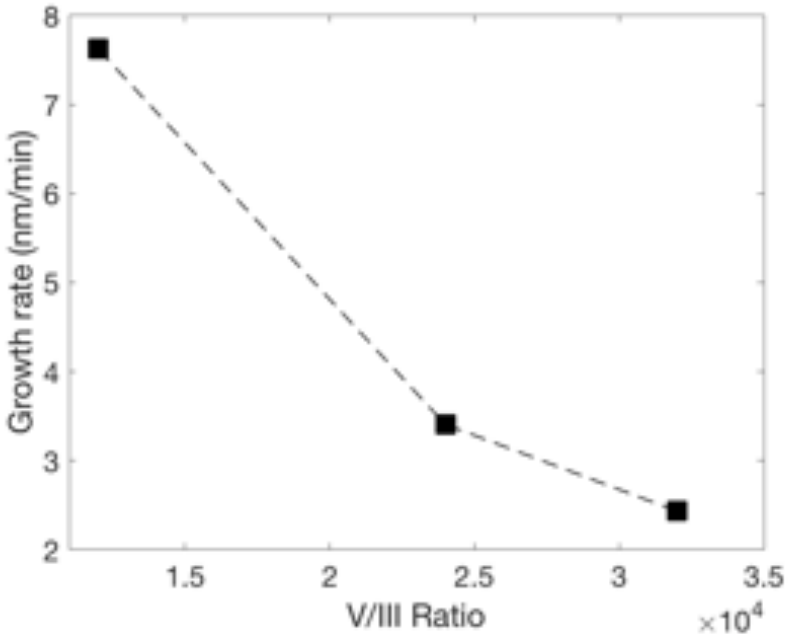

Figure 10.1.1. Plot of AlN growth rate on CMP SiC-4H as a function of V/III ratio for V/III = 12K, 24K, and 32K.

Images of the microstructures of the as-grown surface of each of the films were acquired using scanning electron microscopy (SEM). These are shown in Figure 10.1.2. These micrographs reveal that with increasing V/III ratios, the AlN films become less porous and more coalesced.

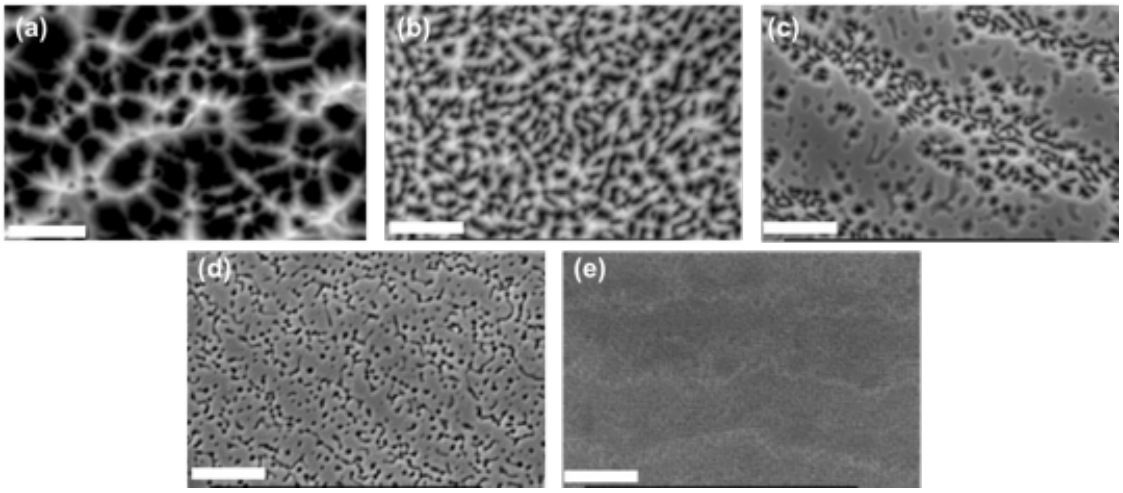

Figure 10.1.2: SEM images of AlN (0001) thin films grown on CMP 4H-SiC(0001) substrates via MOCVD at V/III ratios of (a) 12K (b) 24K (c) 32K (d) 65K, and (e) 130K. Scale bars are 500 nm.

The structure and strain within each of the AlN films were probed using x-ray diffraction (XRD). The diffractometer was carefully aligned for the (0004) peak of the 4H-SiC(0001) substrate at $2\theta \approx 35.59^{o}$. A 2θ-ω scan was performed about the expected (0002) reflection for the wurtzite phase of AlN at the standard value of $2\theta \approx 36.04^{o}$ for bulk, unstrained AlN [1]. The 2θ-ω scans for each sample grown at the various V/III ratios are plotted in Figure 10.1.3a. For each sample, an obvious shift either above or below the standard 2θ value for (0002) is observed, with varying degrees of peak broadening and intensity.

The shifts in each of the (0002) reflections are due to the net strain in the respective thin films caused primarily by the differences with that of the substrate in the *a* lattice parameters at the 1100°C growth temperature and the coefficients of thermal expansion on cooling. In

addition, the density of defects, particularly threading dislocations, formed within the films during growth and relaxation during cooling [2,3] are affected by the V/III ratio in that it affects the growth rate of each film and thus the degree of stress and associated strain in each film. The *a* lattice parameter of 4H-SiC is 3.073 Å, while that of AlN is 3.112 Å [4]. This difference creates ~ -1.24% lattice mismatch at room temperature with respect to the AlN film. The average coefficient of thermal expansion in the (0001) basal plane, α_a, for 4H-SiC is 4.5×10^{-6} °C^{-1} [5], and that for AlN is slightly smaller with $\alpha_a = 4.2 \times 10^{-6}$ °C^{-1} [4]. Table 10.1.1 summarizes these important parameters for AlN and 4H-SiC. Because the value of α_a of 4H-SiC is larger than that of AlN, the basal plane of the former should contract more than the basal plane for AlN during cooling, resulting in compression in the latter. Due to conservation in volume compression of *a* (AlN) should result in an elongation of *c*. The *c* lattice parameters for each AlN/4H-SiC sample can be estimated directly using the respective (0002) peak positions plotted in Figure 3a. In order to estimate the *a* constant of each film, a high index plane, $(10\bar{1}5)$, was probed, and the resulting XRD scans are plotted in Figure 10.1.3b. Acquiring both *c* and *d* data for the {105} family allowed *a* for each sample to be estimated using the relationship between the interplanar spacing *d* and the *h, k,* and *l* values for hexagonal crystals given in Eq. 10.1.1 [6]:

$$\frac{1}{d_{hkl}^2} = \frac{4}{3}\left[\frac{h^2+k^2+hk}{a^2}\right] + \frac{l^2}{c^2} \qquad \text{Eq. 10.1.1}$$

Both lattice constants for each film are plotted as *c* as a function of *a* in Figure 10.1.4a. The general trend is that for a compression in *a*, there is an elongation in *c*, as one would expect for the sake of unit cell volume conservation. However, it is seen that the values estimated for *a* are far smaller than the bulk, relaxed value of 3.112 Å. Because of this, the strain in the basal plane for each sample is negative relative to the relaxed value, and the out-of-plane strain is plotted as

a function of in-plane strain in Figure 10.1.4b. It is neither known all the reasons why the in-plane strain varies so strongly across each V/III ratio while a much smaller change in the out-of-plane strain is observed nor the extent to which the very high concentration of threading dislocations affect the stress and relaxation within the films [7].

Table 10.1.1. Lattice parameter and coefficient of thermal expansion for AlN and 4H-SiC

		AlN	4H-SiC
Lattice parameter	a (Å)	3.112	3.073
Thermal expansion coefficient ($^oC^{-1}$)	α_a	4.2×10^{-6}	4.5×10^{-6}

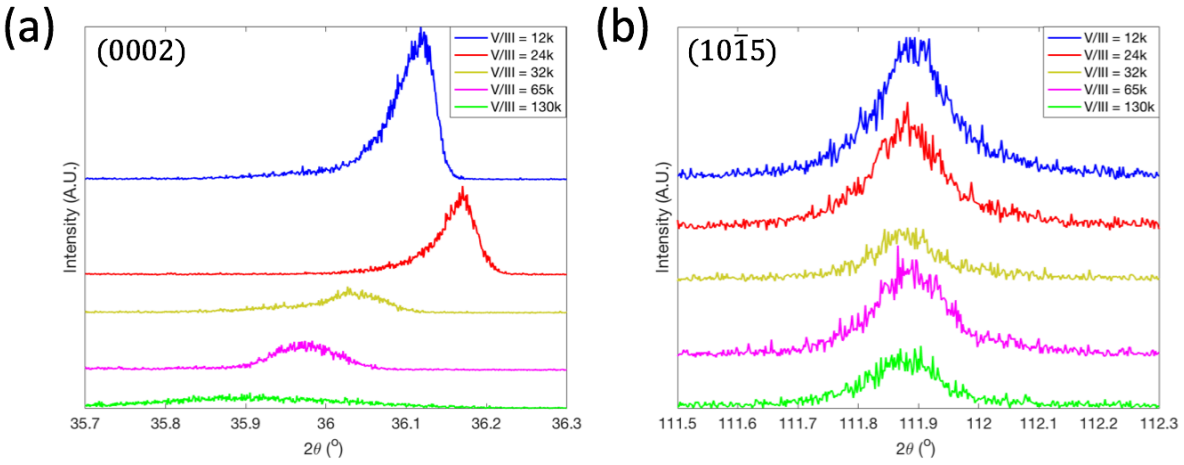

Figure 10.1.3. 2θ-ω scans about the (a) (0002) and (b) (10$\bar{1}$5) reflections for AlN at various V/III ratios.

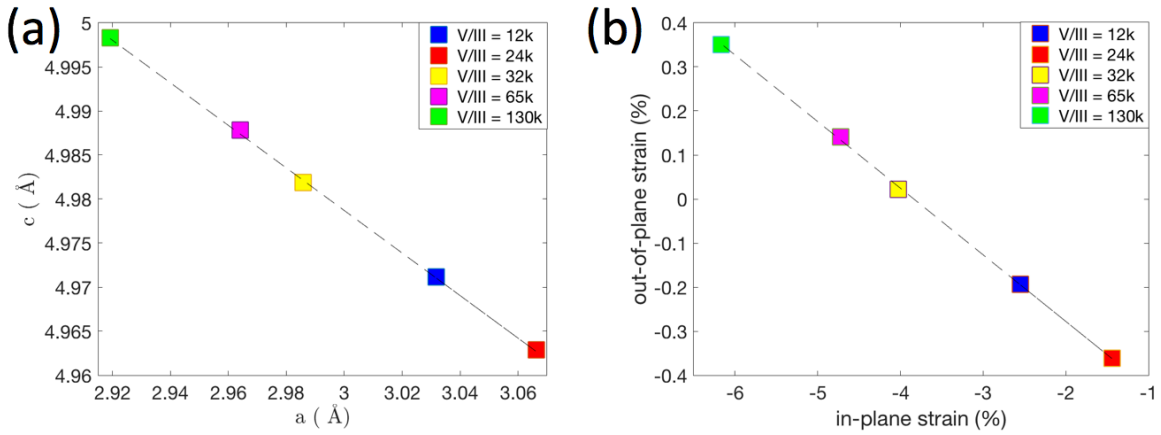

Figure 10.1.4. A plot of (a) AlN *c* lattice parameter as a function of the *a* lattice parameter at each V/III ratio, and (b) the out-of-plane strain plotted against the in-plane strain, calculated relative to the bulk, relaxed *a* and *c* parameters of AlN.

Appendix A References

[1] N. Matsunami, H. Kakiuchida, M. Sataka, and S. Okayasu, Adv. Mater. Phys. Chem. **03**, 101 (2013). XRD Characterization of AlN Thin Films Prepared by Reactive RF-Sputter Deposition. DOI:10.4236/ampc.2013.31A012.

[2] J. Narayan, Acta Mater. **61**, 2703 (2013). Recent progress in thin film epitaxy across the misfit scale (2011 Acta Gold Medal Paper). DOI:10.1016/j.actamat.2012.09.070.

[3] D. Nilsson, E. Janzén, and A. Kakanakova-Georgieva, J. Phys. D. Appl. Phys. **49**, 175108 (2016). Lattice parameters of AlN bulk, homoepitaxial and heteroepitaxial material. DOI:10.1088/0022-3727/49/17/175108.

[4] M. Levinshtein, S. Rumyanstev, M. Shur, A. D. Jackson, S. N. Mohammed, G. L. Harris, and M. G. Spencer, in *Prop. Adv. Semicond. Mater. GaN, AlN, BN, SiC, SiGe*, edited by M. Levinshtein, M. Shur, and S. Rumyanstev (John Wiley & Sons, NewYork, 2001), pp. 66–92. Boron Nitride.

[5] Z. Li and R. C. Bradt, J. Appl. Phys. **60**, 612 (1986). Thermal expansion of the hexagonal (4H) polytype of SiC. DOI:10.1063/1.337456.

[6] M. A. Moram and M. E. Vickers, Reports Prog. Phys. **72**, 1 (2009). X-ray diffraction of III-nitrides. DOI:10.1088/0034-4885/72/3/036502.

[7] Z. J. Reitmeier, S. Einfeldt, R. F. Davis, X. Zhang, X. Fang, and S. Mahajan, Acta Mater. **57**, 4001 (2009). Sequential growths of AlN and GaN layers on as-polished 6H-SiC(0001) substrates. DOI:10.1016/j.actamat.2009.04.026.

10.2. Appendix B: Flow modulated epitaxial growth of h-BN on Ni foil

I have performed a flow-modulated thin film deposition of *h*-BN on 25 μm thick polycrystalline Ni foil (Alfa Aesar) at 1050 °C. An XRD pattern of the Ni foil revealed the presence of the (111) and (200) grains. The Ni foil was cleaned using a 10 minute sonication in acetone followed by a 10 minute sonication in isopropanol. The foil was then annealed within an atmosphere of NH_3, H_2, and N_2 at the growth temperature of 1050 °C for 30 minutes to further remove surface contaminants as well as enlarge the Ni grains prior to growth. The foil was then exposed to a 1 second pulse of TEB at a flowrate of 80 sccm followed by a 1 second pulse of NH_3 at a flowrate of 3 slm, and this cycle was repeated for one hour without any purge steps. Figure 10.2.1 shows the scanning electron microscopy images of a bare Ni surface and BN film in (a) and (b), respectively. Figure 10.2.2 shows the x-ray diffraction (XRD) pattern of the *h*-BN film on the Ni foil. The (0002) peak for the *h*-BN film appeared at $2\theta = 26.745^{o}$, resulting in an interplanar spacing d_{0002} measurement of ~3.26 Å. The literature values for the 2θ and interplanar spacing for the (0002) peak for *h*-BN are 26.7° and 3.33 Å, respectively [1]. The appearance of *h*-BN is attributed to the Ni foil being a near ideal substrate in terms of small lattice mismatch and catalytic activity as previously discussed. It is important to note that during this growth run, a (0001) oriented AlN/Al_2O_3 (sapphire) (Kyma Technologies, Inc.) substrate was also used. The AlN layer, pre-grown by the manufacturer, was roughly 25 nm. However, even when using the flow-modulated process, no *h*-BN pattern could be acquired using XRD.

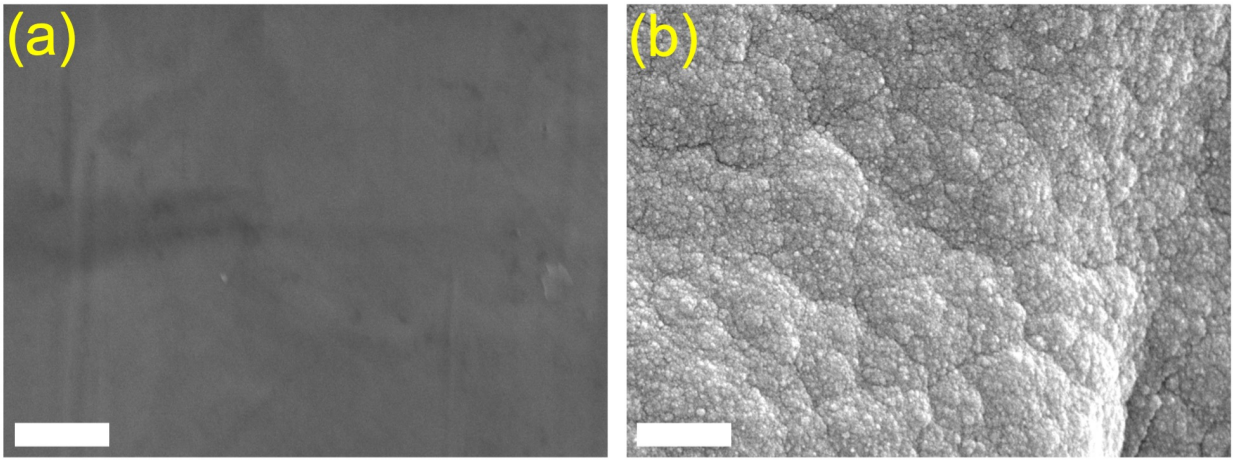

Figure 10.2.1. Scanning electron microscopy images of a bare Ni surface and BN film in (a) and (b), respectively. The scale bars are 1 μm.

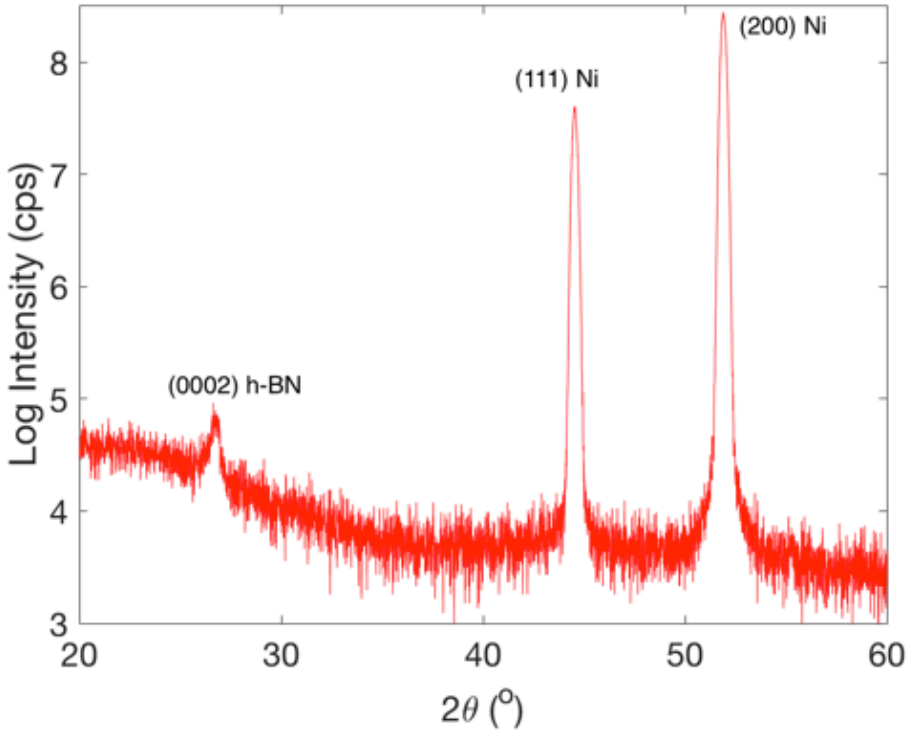

Figure 10.2.2. XRD pattern for *h*-BN on Ni foil grown through flow modulated epitaxy.

Appendix B References

[1] R. S. Pease, Acta Crystallogr. **5**, 356 (1952). An X-ray study of boron nitride. DOI:10.1107/S0365110X52001064.

10.3. Appendix C: Initial CVD synthesis of BN thin films on *c*-plane sapphire using triethylboron and ammonia

Boron nitride (BN) films were grown on sapphire (Kyma) substrates inside a vertical, water-cooled "showerhead" reactor. The precursor reactant gases were triethylboron ($B(C_2H_5)_3$) (TEB) and ammonia (NH_3), for boron and nitrogen, respectively. Temperature and the H_2 diluent flow rate were the only growth parameters that were varied in this study. The growth temperature was held either at 1050 °C or 750 °C. The H_2 diluent flow rate was set to either 8 standard liters per minute (slm) or 1 slm. All other growth parameters including a total chamber pressure of 40 Torr, a TEB molar flow rate of 272 μmol/min, an NH_3 flow rate of 3 slm, and the deposition time of 1 hour were held constant. The x-ray photoelectron spectroscopy (XPS) and secondary ion-mass spectroscopy (SIMS) data were acquired by EAG Laboratories in November of 2017.

Figure 10.3.1 shows the scanning electron microscopy (SEM) images of four BN/sapphire samples. Samples 1 and 2 were deposited at T = 750 °C with Q_{H2} set to either 1 slm (a) or 8 slm (b), respectively. Samples 3 and 4 were deposited at T = 1050 °C with Q_{H2} set to either 1 slm (c) or 8 slm (d), respectively. Table 10.3.1 shows the atomic compositions at the surface of the four samples, as measured by x-ray photoelectron spectroscopy (XPS). Samples grown at 1050 °C contained much lower atomic percentages of carbon at the surface than those grown at 750 °C. The sample grown in a H_2 diluent atmosphere of 8 slm at 1050 °C contained the least carbon of 14 at.%. The B/N atomic ratios were also closer to unity in the two samples grown at 1050 °C. The H_2 diluent flow rate had a more pronounced effect on film morphology and composition at the lower temperature (750 °C) condition.

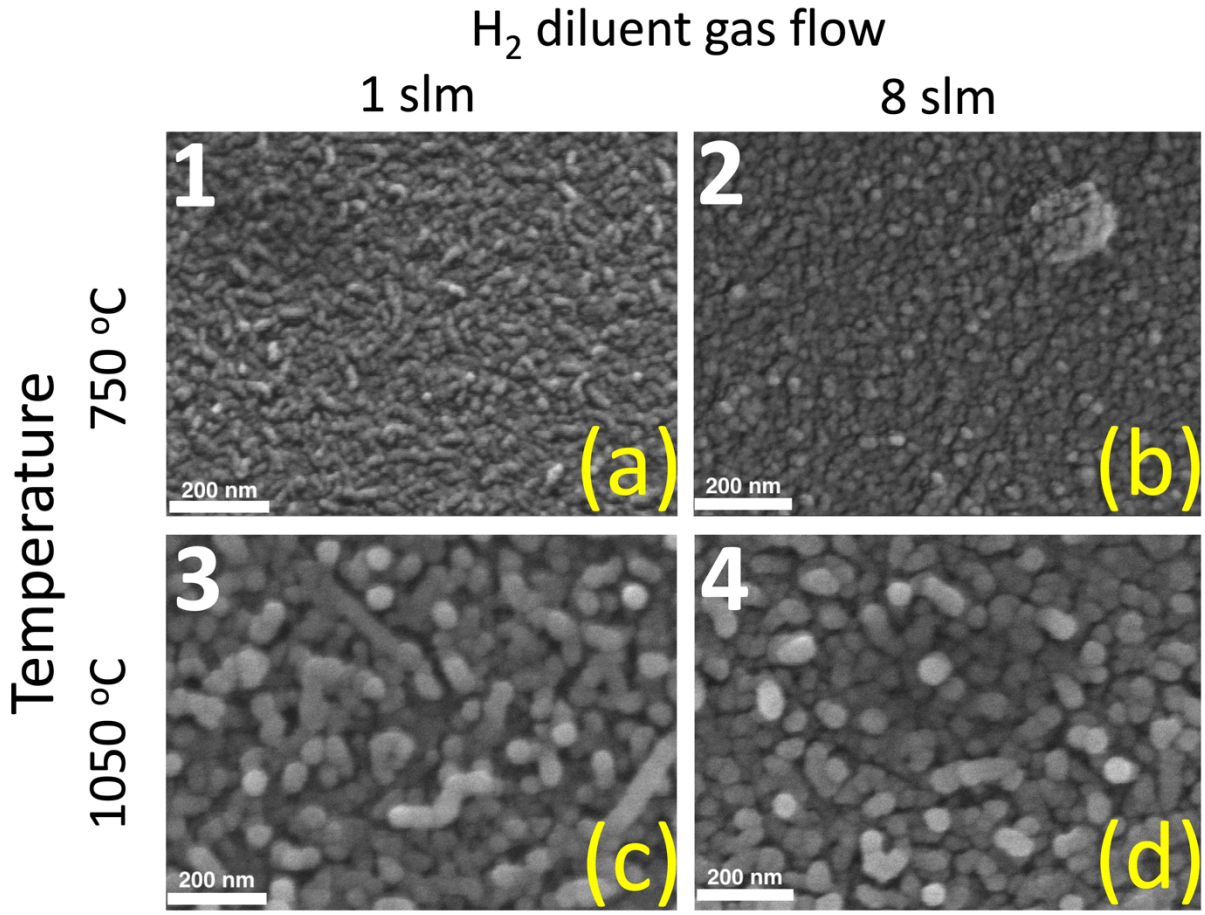

Figure 10.3.1. SEM images of four BN/sapphire samples. Samples 1 and 2 were deposited at T = 750 °C with Q_{H2} set to either 1 slm (a) or 8 slm (b), respectively. Samples 3 and 4 were deposited at T = 1050 °C with Q_{H2} set to either 1 slm (c) or 8 slm (d), respectively.

Table 10.3.1. Atomic surface compositions of Samples 1 – 4

Growth conditions			Surface atomic composition (at. %)				
Sample No.	Temperature (°C)	Q_{H2} (slm)	B 1s	N 1s	C 1s	O 1s	B/N
1	750	1	34.2	28.7	32.0	5.2	1.19
2	750	8	28.5	23.7	39.8	7.9	1.20
3	1050	1	40.8	36.7	17.9	4.6	1.11
4	1050	8	43.2	38.3	14.0	4.4	1.13

Figure 10.3.2 shows the deconvoluted B 1s (a), N 1s (b), and C 1s (c) XPS spectra of Sample 4. The spectrums in Fig. 2(a) and 2(b) suggest that B and N are primarily bonded to each other; however, the spectrum in Fig. 10.3.2(c) reveals that C is bonded mostly to B in a boron carbide network. The small (~ 4.8% area) component for B 1s in Fig. 2(a) further supports this evidence that some B is also bonded to C.

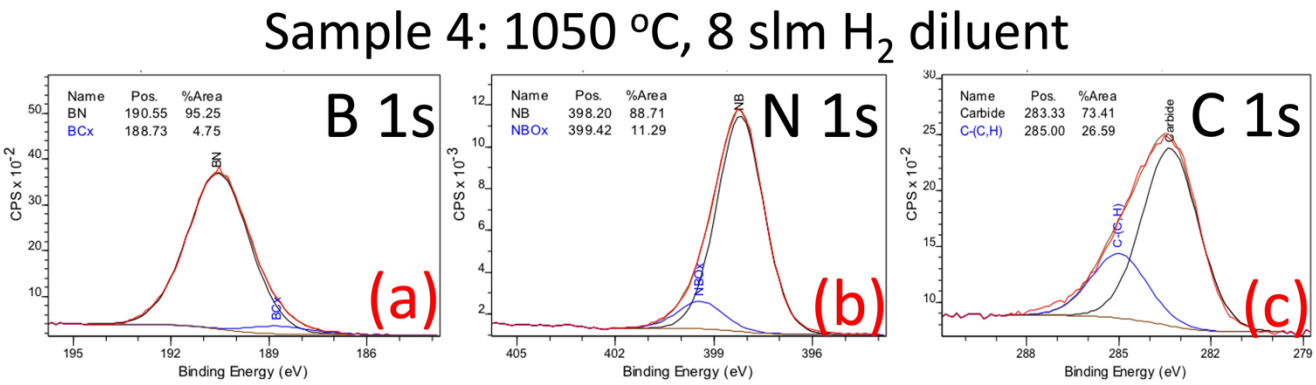

Figure 10.3.2. Deconvoluted B 1s (a), N 1s (b), and C 1s (c) XPS spectra acquired from the surface of Sample 4, which was grown using T = 1050 °C and Q_{H2} = 8 slm.

Figures 10.3.3 -10.3.5 show the SIMS profiles of Samples 1, 3, and 4, respectively. Sample 2 was excluded from analysis. The SIMS profiles show the atomic concentration of C and the raw ion counts of B and Al. The observation of C profiles in the grown samples eventually prompted the use of B-source precursors that did not inherently contain C in their molecular structure.

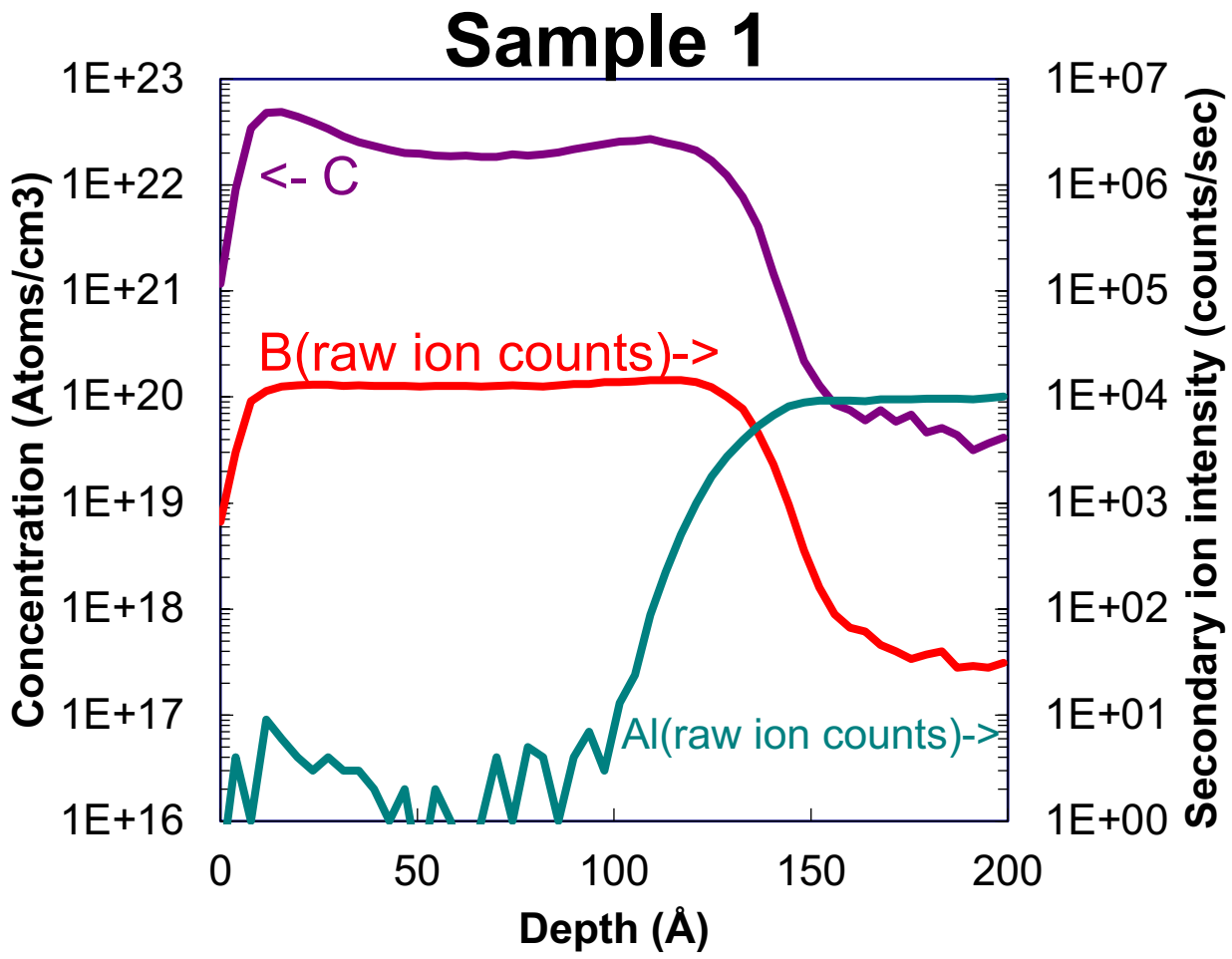

Figure 10.3.3. SIMS profile of Sample 1, showing the atomic concentration of C and the raw ion counts of B and Al. Sample 1 was grown under the conditions of T = 750 °C, Q_{H2} = 1 slm.

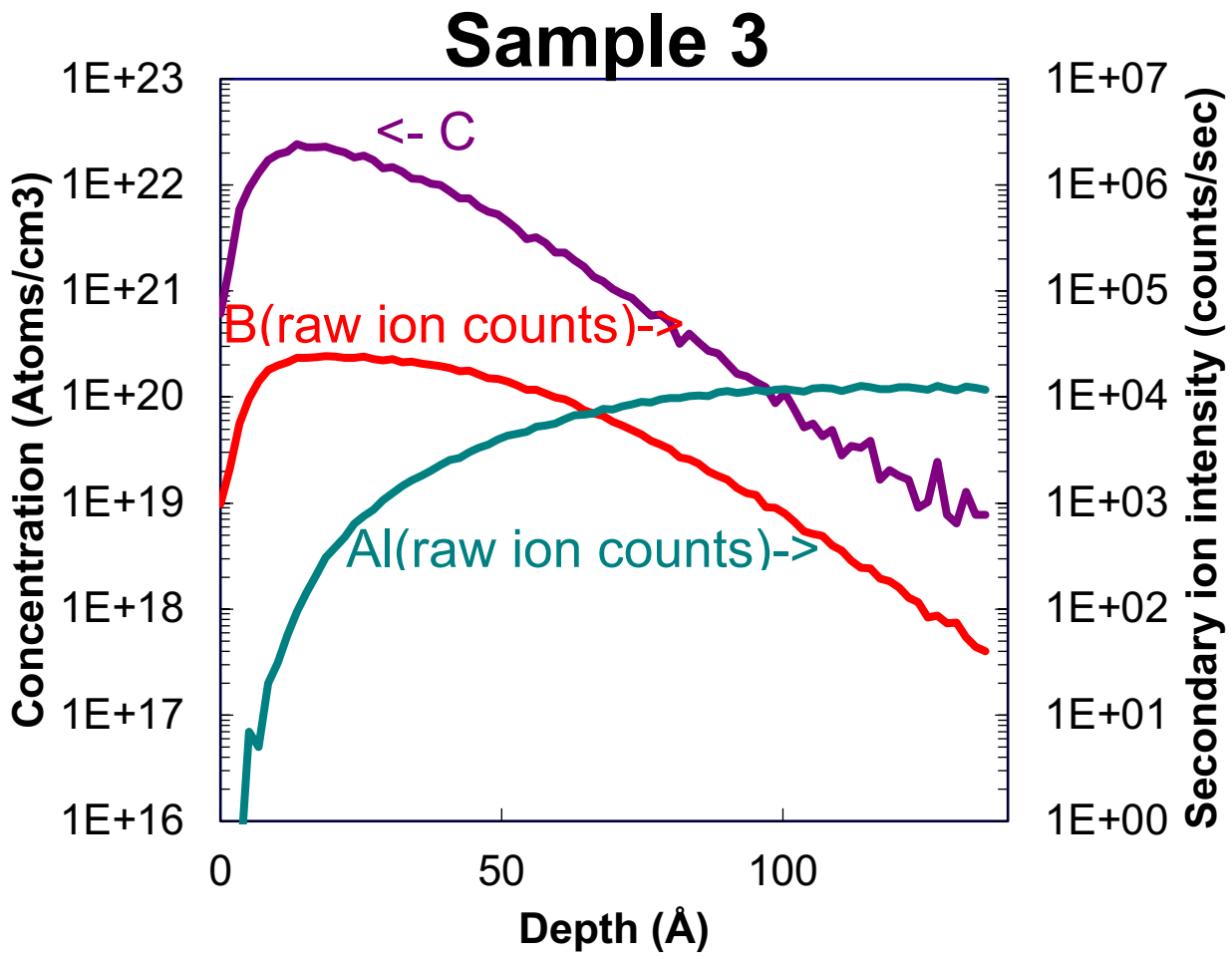

Figure 10.3.4. SIMS profile of Sample 3, showing the atomic concentration of C and the raw ion counts of B and Al. Sample 3 was grown under the conditions of T = 1050 °C, Q_{H2} = 1 slm.

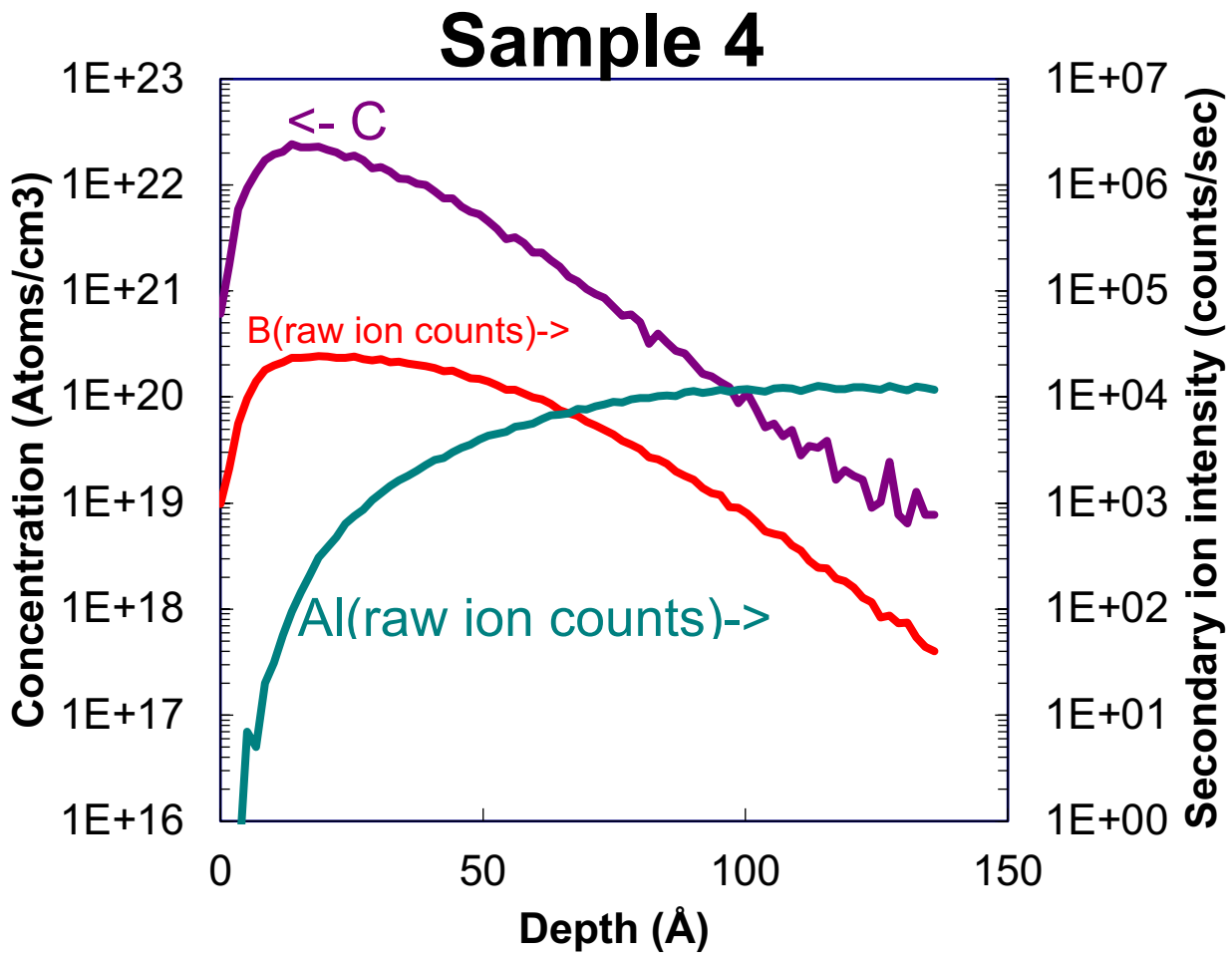

Figure 10.3.5. SIMS profile of Sample 4, showing the atomic concentration of C and the raw ion counts of B and Al. Sample 4 was grown under the conditions of T = 1050 °C, Q_{H2} = 8 slm.

10.4. Appendix D: Polishing pyrolytic boron nitride surfaces in preparation for chemical vapor deposited sp^2-BN thin films

As explained in the Experimental Procedures section of this Thesis, the as-received pyrolytic boron nitride (PBN) substrates acquired from Morgan Technical Ceramics have very rough surfaces (~ 65 nm RMS roughness over a 2 μm × 2 μm area). This roughness is also revealed in the SEM image shown in Fig. 10.4.1 (a). Thus, a polishing procedure was eventually developed to produce surface finishes with ~ 1.5 – 4 nm RMS roughness.

The early stages of preparing deposition-ready PBN surfaces involved polishing by hand using diamond-lapped films (DLFs) as the polishing cloth and a hand-held stainless-steel jig to hold the PBN samples still during polishing. In succession, grit sizes of 30, 9, 3, and 1 μm DLFs were used. The DLFs had adhesive backing and were adhered to a stationary glass surface. Water was used as the polishing media for all DLFs except for the 1 μm DLF where 0.02 μm colloidal silica was used. Polishing was achieved at each step by pressing the sample surface firmly against the DLF and moving the jig clock-wise for roughly sixty seconds. The sample surface was sprayed with isopropyl alcohol and compressed air to remove debris and contaminants between each DLF step. An image acquired using scanning electron microscopy (SEM) of the microstructure of a diamond lapped PBN surface at the completion of the total polishing process is shown in Fig. 10.4.1 (b). This method of hand-held polishing proved not to be useful in reproducing deposition-ready surfaces due to unavoidable human error during such a process.

PBN polishing was subsequently attempted using Ar ion milling (Fischione). The general settings for milling the as-received samples were a continuous stage rotation at 4 RPM, a 2^{o} beam angle for both Ar^{+} sources, an accelerating beam voltage of 6 kV, and a milling time of 1

hour. SEM images of the resulting surfaces showed that the samples were milled in preferential directions and that features were non-uniform over the entire surface. A representative image of effect of this preferential polishing on the surface microstructure is revealed in Fig. 10.4.1 (c). Some samples that were originally diamond-lapped were also subject to the described ion-milling process; an image of the resulting surface microstructure is shown in Fig. 10.4.1 (d).

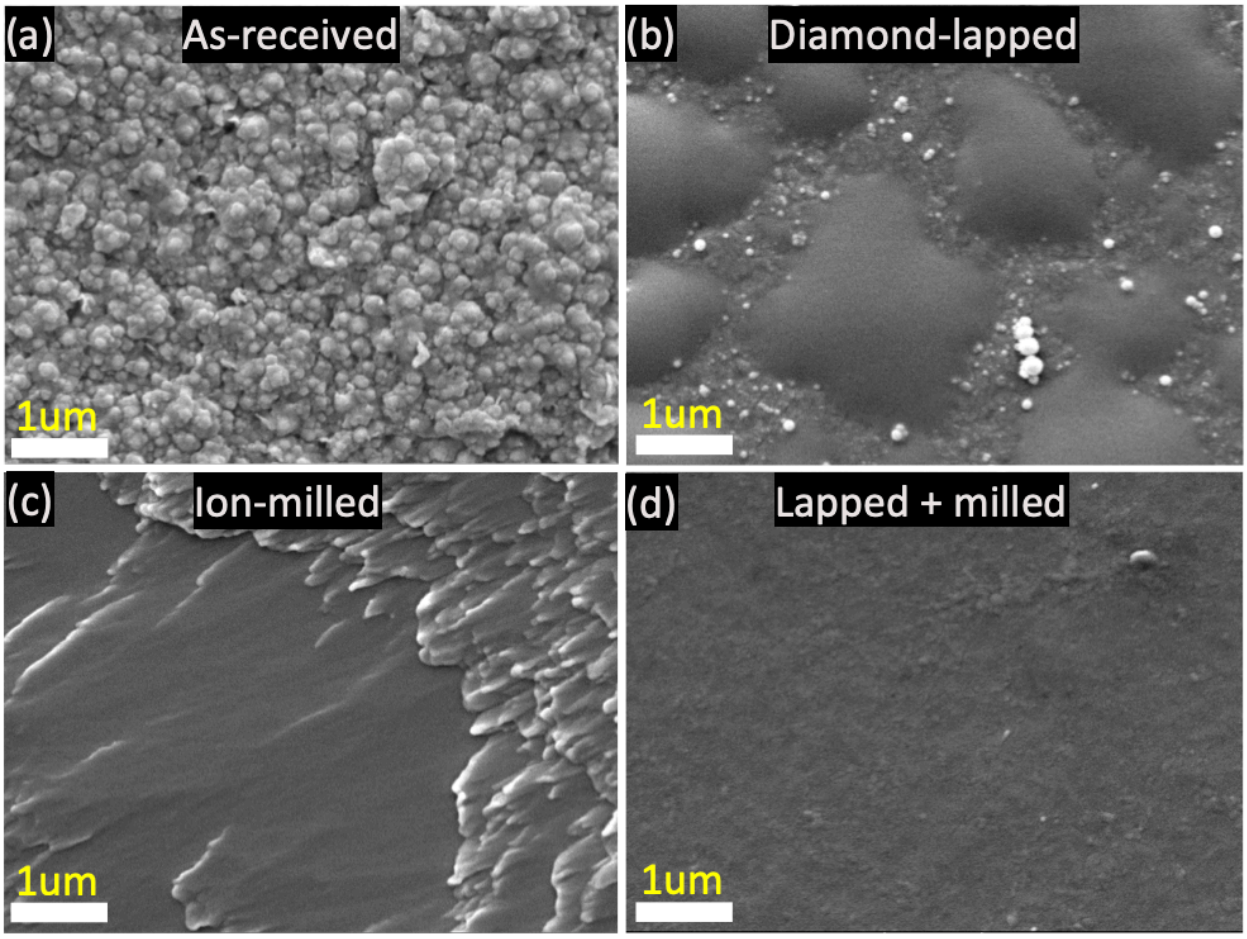

Figure 10.4.1. Scanning electron microscopy images of (a) as-received, (b) diamond-lapped, (c) ion-milled, and (d) diamond-lapped + ion-milled surfaces of PBN.

I then changed my polishing process to employ a semi-automatic precision polishing system (Multiprep Polishing System from Allied High Tech Products, Inc.) to prepare deposition-ready PBN surfaces. Table 10.4.1 The order of the steps and the values of the equipment parameters typically used in this method to successfully polish PBN substrates are presented in Table 1. The approximate thickness of the PBN removed in most of the steps is also noted.

Table 10.4.1. Pyrolytic boron nitride polishing procedure

Polishing media/Lubricant	Platen rotation and direction	Sample rotation (RPM)	Target thickness removal/Duration
6 μm DLF/water	150 RPM, CW	8 RPM, CCW	~ 200 μm
3 μm DLF/water	150 RPM, CW	8 RPM, CCW	~ 100 μm
1 μm DLF/RedLube	150 RPM, CW	8 RPM, CCW	~ 100 μm
Final P Cloth/ 0.04 μm Colloidal Silica	150 RPM, CW	8 RPM, CCW	30 seconds

DLF: diamond lapping film
CW: clockwise
CCW: counter-clockwise
RPM: revolutions per minute

A 600 g load was applied to the sample during each polishing step. Between each polishing step, the sample surface and platen were cleaned with micro-organic soap to prevent debris from the previous step from contaminating the sample or subsequent polishing media, thereby reducing the density and total quantity of scratches caused by polishing. If contamination-induced scratches developed on the sample surface at any step, the sample was polished for a few minutes using the diamond lapping film with the grit size of the previous step to remove the scratches. The final values of thickness of the PBN substrates were typically 200 – 300 μm. The employed polishing procedure produced surface finishes with < 3 nm RMS roughness over a 2.5 μm × 2.5 μm area. Figure 10.4.2 shows a collection of atomic microscopy

(AFM) (NT-MDT NTegra) images taken of several different PBN samples that were polished using the semi-automatic precision procedure described above. The RMS roughness (R_q) is indicated in each image in the Figure.

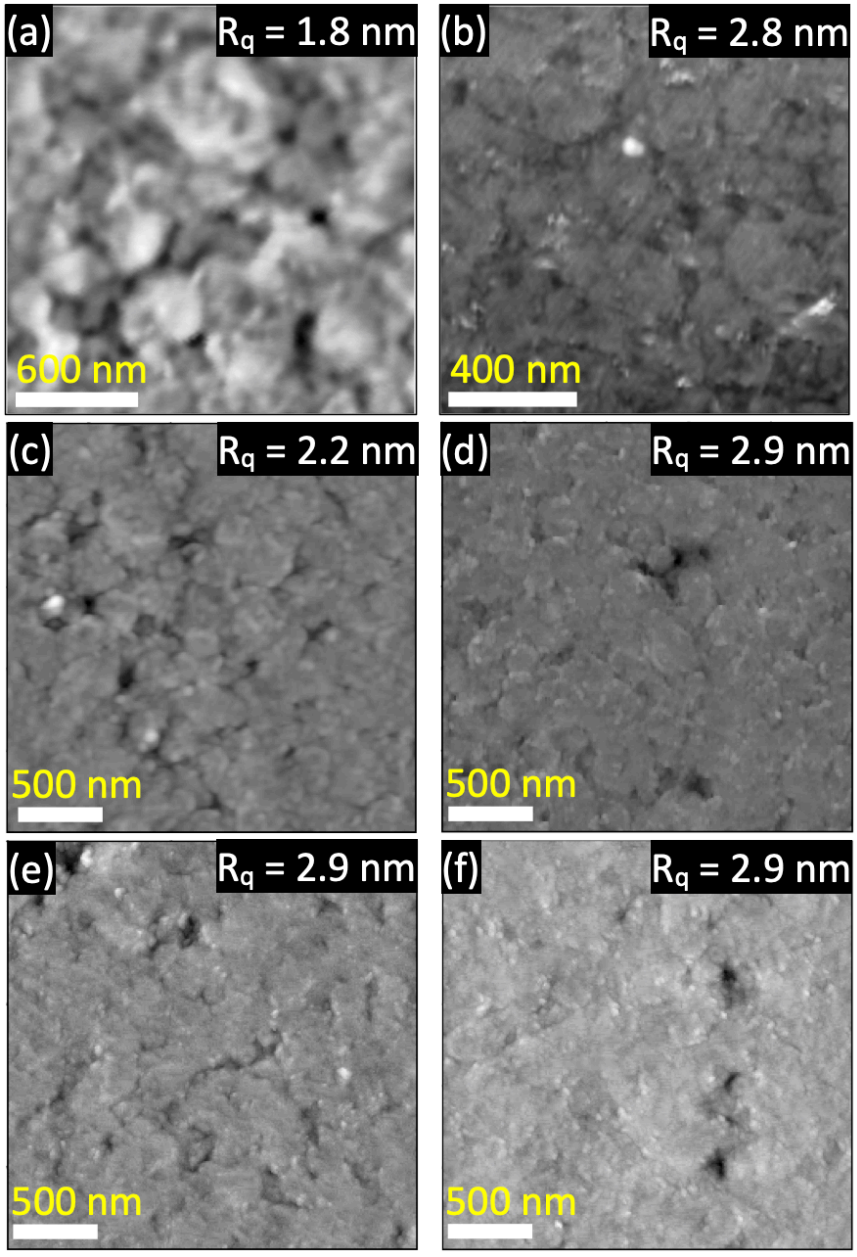

Figure 10.4.2. AFM images of several different polished samples of PBN that were prepared using the semi-automatic precision polishing procedure detailed in the text. Table 1 provides the steps and polishing settings that were typically used to achieve the surface finish indicated by the RMS roughness values, R_q, in each image.

Subjecting the as-polished PBN substrates to a three-hour anneal in a 2 slm H_2 atmosphere at ~ 1060 °C and a total chamber pressure of 10 Torr resulted in a further reduction of surface roughness to 1.2 nm over a 2.5 μm × 2.5 μm area. Figure 10.4.3 shows the AFM images of the as-received PBN surface (a), the as-polished surface (b), and the polished surface annealed in H_2 for 3 hours (c).

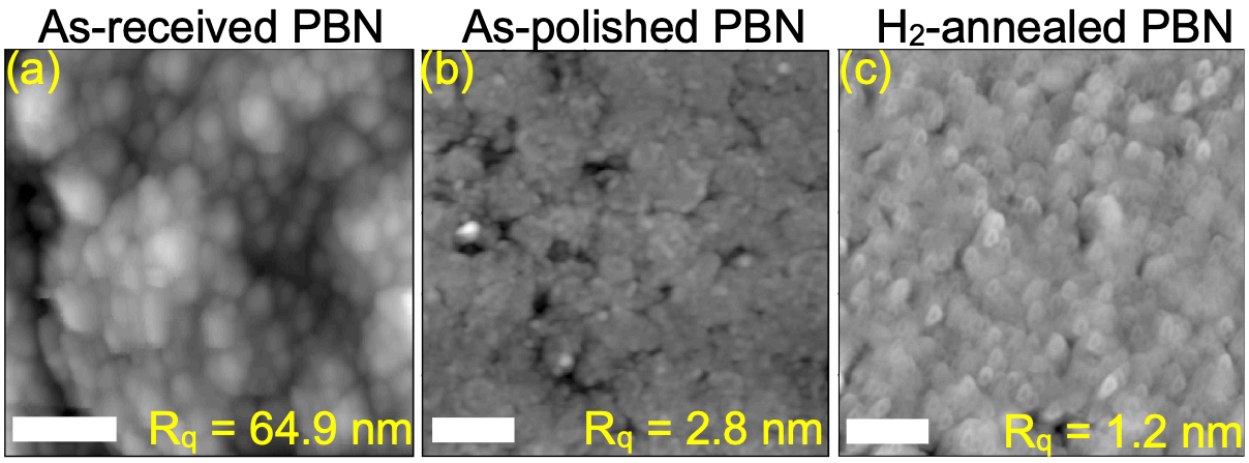

Figure 10.4.3. AFM images acquired over 2.5 μm × 2.5 μm areas of the (a) as-received, (b) as-polished using the semi-automatic precision system and (c) polished and H_2-annealed surfaces of PBN. The values of the RMS roughness are given by Rq. The scale bars are 500 nm.

10.5. Appendix E: Etching polished surfaces of pyrolytic boron nitride

Figure 10.4.3 from Appendix D revealed that a 3 hour anneal of pyrolytic boron nitride (PBN) in H_2 (2 slm) at ~ 1060 ^oC and 10 Torr chamber pressure would etch the surface. It also had the concomitant effect of reducing the RMS roughness. It was therefore of interest to determine what conditions might lead to the observation of an exposed grain structure of semi-automatic precision polished PBN. Another polished PBN sample was thus exposed to a 4 hour anneal in the same H_2 environment. The atomic force microscopy (AFM) images of the surface microstructures of the as-polished and the polished and annealed PBN are presented in Figures 10.5.1 (a) and (b), respectively. Figures 10.5.1 (c) and (d) show the respective surfaces of an as-deposited boron nitride (BN) thin film on polished PBN and the same surface after a 4 hour anneal in H_2.

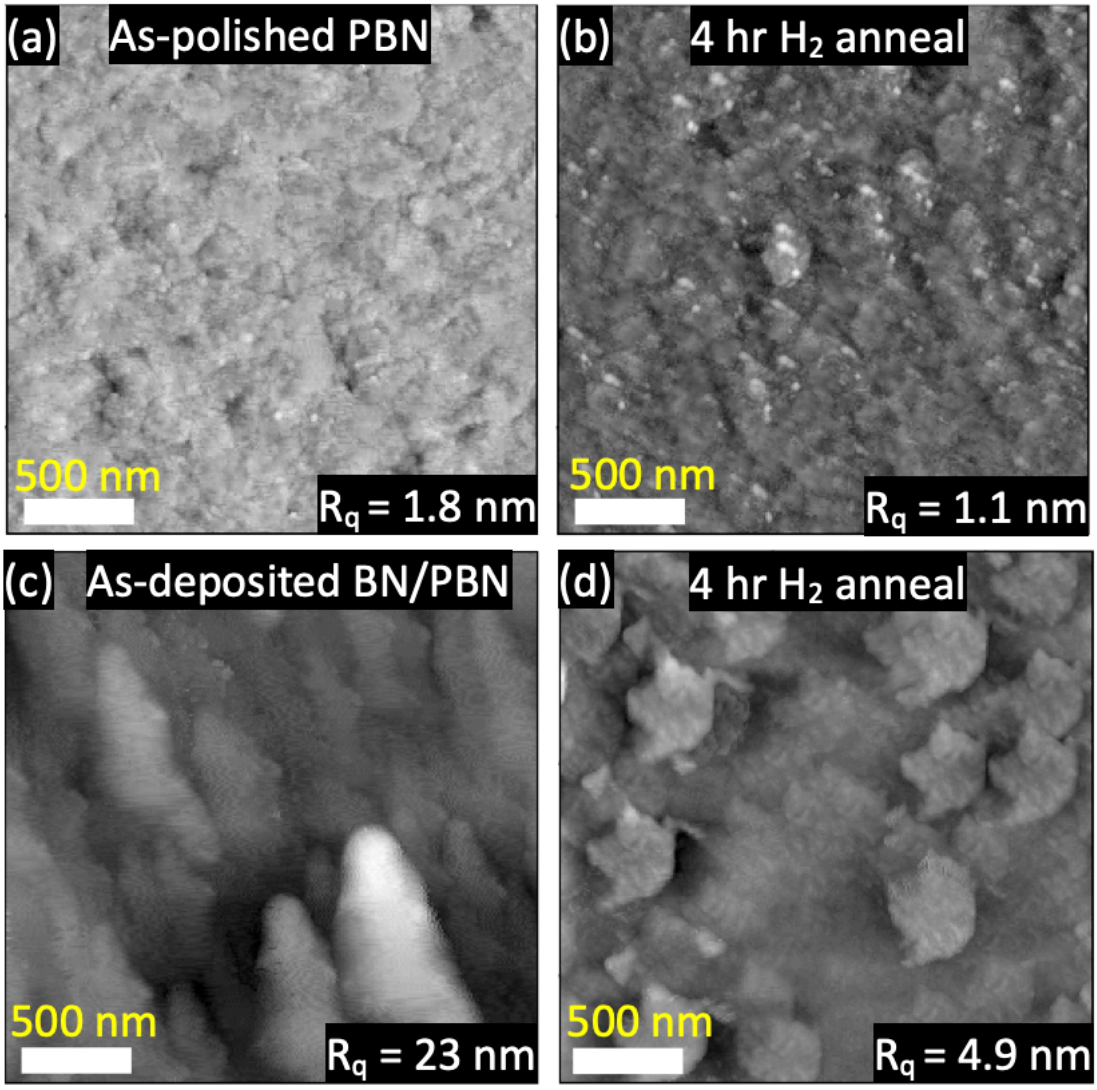

Figure 10.5.1. AFM images of (a) the as-polished PBN and (c) an as-deposited BN thin film on PBN surfaces. Micrographs (b) and (d) are AFM images of the (a) and (c) surfaces, respectively, after a 4 hour H_2 anneal at 1060 °C. Values of the RMS roughness are given by R_q in each image.

Etching of the PBN surface was also attempted with HF/DI-H_2O room-temperature (RT) solutions. Two PBN samples were first simultaneously polished. The resulting surface finishes were rather poor (RMS roughness of 3 – 7 nm) as observed in the AFM images in Figures 10.5.2 (a) and (b). The sample shown in Fig. 10.5.2 (a) was placed in a 10% HF:DI-H_2O solution and sonicated for 10 minutes at RT. The resulting surface is displayed in Fig. 10.5.2 (c). The sample

shown in Fig. 10.5.2 (b) was similarly sonicated in a 10% HF:DI-H_2O solution, but for 45 minutes. Both treatments resulted in marked reductions in surface roughness, with the 45 minute treatment resulting in an image that revealed the polycrystalline microstructure of the material.

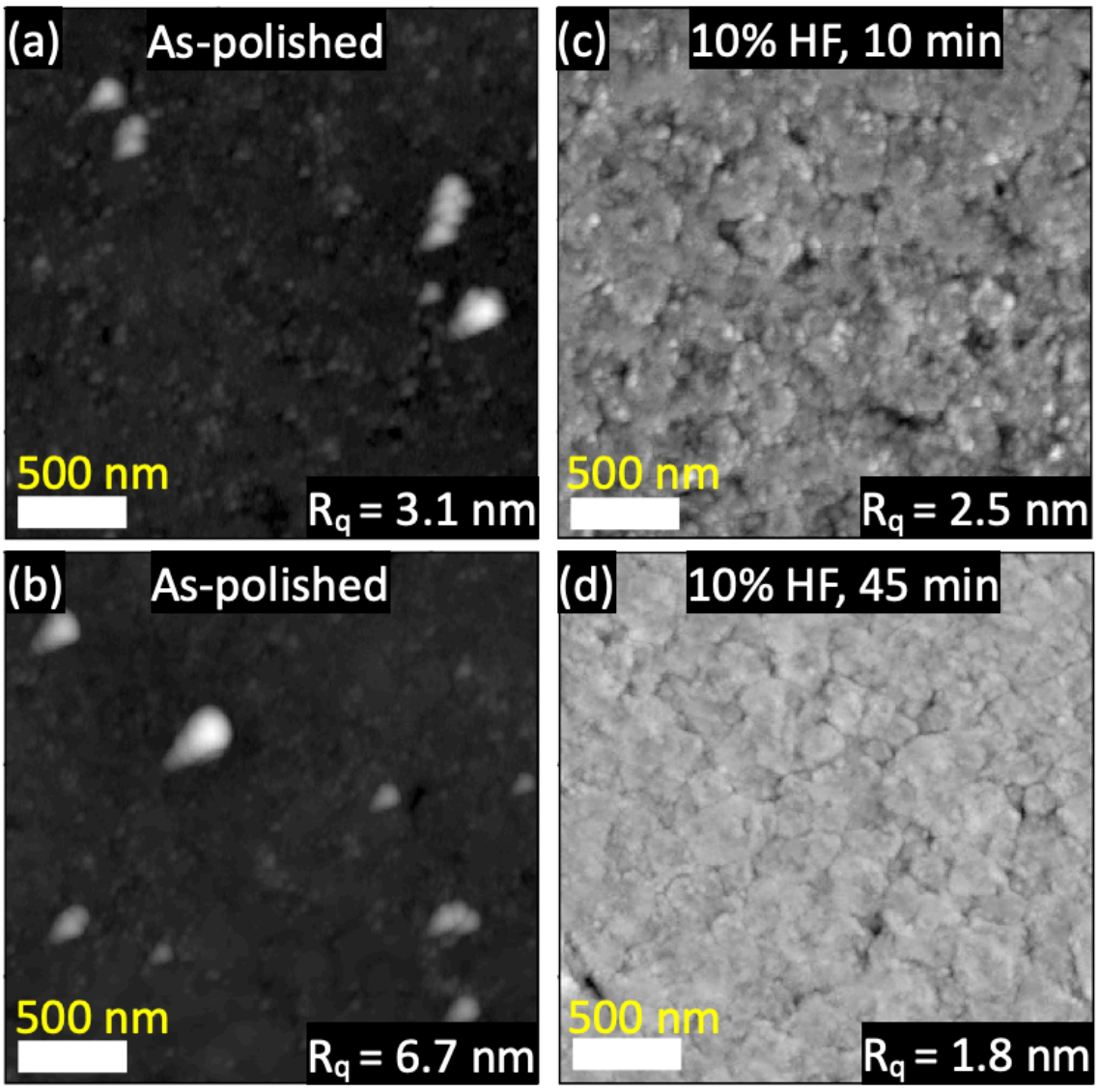

Figure 10.5.2. (a) and (b)AFM images of as-polished PBN surfaces prepared at the same time. Sample (a) was subjected to a 10 minute RT sonication in 10% HF, and the resulting surface microstructure is shown in the AFM image in (c). Sample (b) was subjected to a 45 minute sonication in 10% HF, and the resulting surface microstructure is shown in the AFM image in (d). The RMS roughness values are given by R_q.

10.6. Appendix F: Inability to grow sp^2-boron nitride on polished pyrolytic boron nitride via flow-modulated epitaxy at the prescribed growth conditions

Similar to the experiments concerning the flow-modulated epitaxial (FME) growth of sp^2-boron nitride (BN) on (0001) 4H-SiC (see Paper 3 in Section 6), FME depositions were attempted on polished pyrolytic boron nitride (PBN) substrates. On 4H-SiC, the following growth conditions were employed: substrate temperature of ~1030 ^oC, chamber pressure of 10 Torr, B_2H_6 flow rate of 2 sccm, NH_3 flow rate of 0.80 slm, H_2 flow rate of 2 slm, and a FME cycle of 1 s B_2H_6 – 2 s H_2 – 4 s NH_3 – 2 s H_2 for 1800 cycles (equivalent to 4.5 hours of continuous growth). On 4H-SiC, use of these parameters resulted in the partial ordering in the [0001] direction of sp^2-BN layers for roughly 4 nm before transitioning into random nanocrystalline growth. On polished PBN, these same growth conditions were applied except the PBN substrate temperature was measured to be roughly 1060 ^oC. Thin films of sp^2-BN were also continuously grown on PBN via chemical vapor deposition (CVD) at the same temperature, pressure, and gas flow rate for 4.5 hours.

Figure 10.6.1 shows the atomic force microscopy (AFM) images of (a) as-polished PBN, (b) continuously grown CVD-BN on PBN, (c) PBN subjected to the FME process, as well low-magnification cross-sectional transmission electron microscopy (TEM) images of (d) a CVD-BN film on PBN and (e) the results of an attempted FME-BN growth on PBN. Examination of Figure 10.6.1(b) reveals that deposition was achieved for the continuous CVD process on PBN, as the surface exhibits rough, protruding features that are non-existent on the as-polished PBN surface in Fig. 10.6.1(a). Figure 10.6.1(c), on the other hand, exhibits a surface whose features are essentially the same as those of the as-polished surface, which suggests that the employed FME process may not induce BN film growth on PBN. The TEM image in Fig. 10.6.1(d)

confirms that deposition occurred during the continuous CVD process of the growth of BN on PBN, as there are visible differences between the microstructure of the deposited BN film and that of the PBN substrate. Conversely, the cross-sectional TEM image in Fig. 10.6.1(e) confirms the results noted above and shown in Fig. 10.6.1(c), namely, that there is no indication of any material transition between the PBN and a BN film as a result of using the FME process. The employed growth conditions for the film were markedly different than those used in the high temperature CVD process used to produce the bulk PBN material (PBN is typically deposited at temperatures above 1600 ^{o}C). Thus, it is not likely that the apparent absence of a transition from the PBN substrate to a BN film is due to a total reproduction of the PBN surface throughout the volume of a film. It is more likely that the employed FME process does not allow nucleation of BN on PBN. It could be that B layers that are deposited during the first step of the FME process do not adequately stick to the PBN surface for a sufficient period to be converted to BN during the subsequent introduction of NH_3. Longer initial pulses of B_2H_6 were not attempted, because, such conditions led to non-stoichiometric BN films with excess B in their growth on (0001) 4H-SiC.

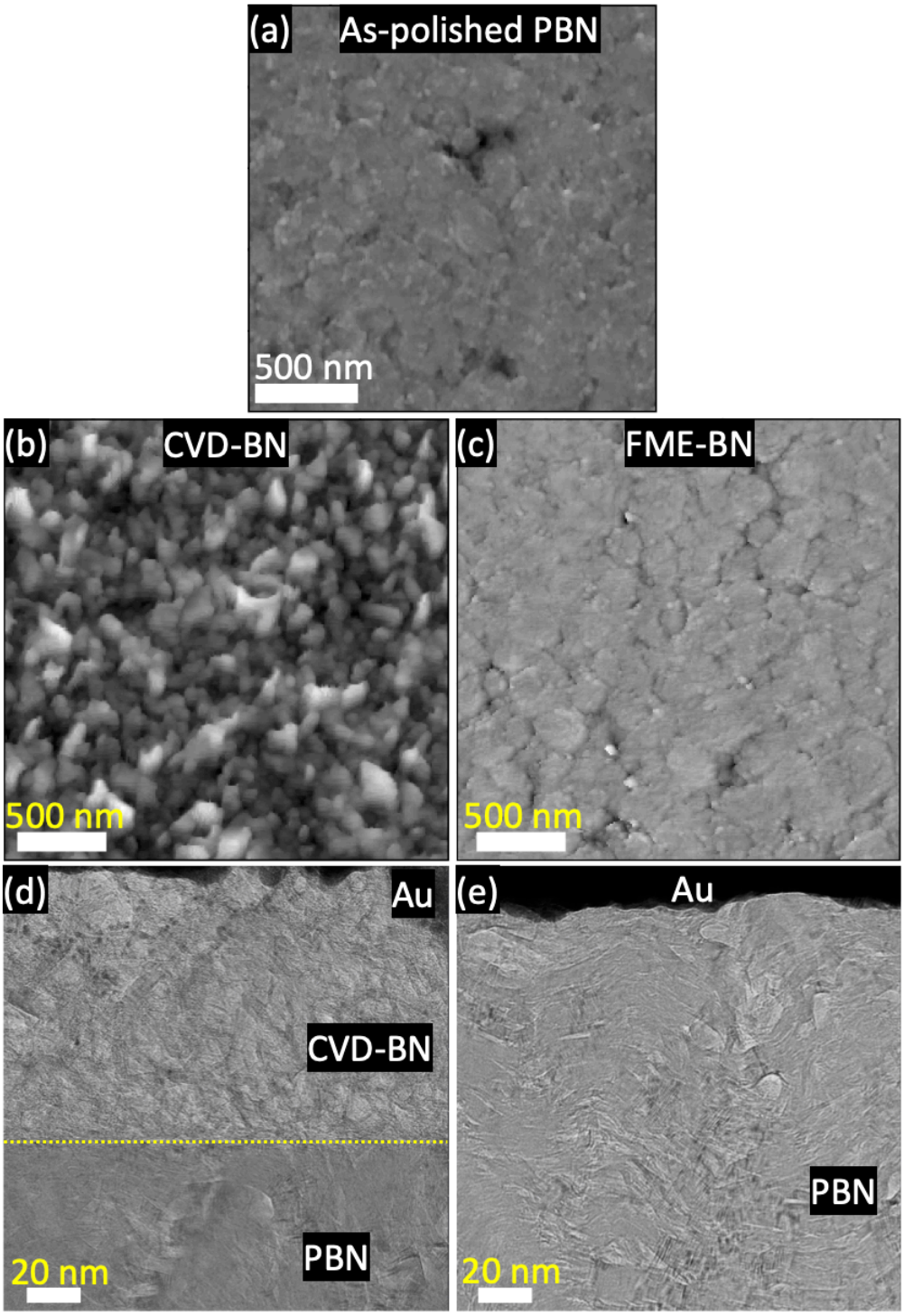

Figure 10.6.1. AFM images of (a) as-polished PBN, (b) continuously grown CVD-BN on PBN, (c) PBN subject to the FME process, as well low-magnification cross-sectional transmission electron microscopy (TEM) images of the (d) CVD-BN on PBN and the attempted (e) FME-BN growth on PBN.

10.7. Appendix G: Chemical vapor deposition of boron nitride thin films using the single-source precursor borazine

Results from secondary ion mass spectrometry (SIMS) detailed in Appendix 3 revealed that the use of triethyl-boron ($B(C_2H_5)_3$) for the deposition of boron nitride (BN) thin films resulted in the incorporation of substantial atomic percentages of C into these films. To mitigate this incorporation (or molecules containing C) from a precursor gas, borazine ($B_3N_3H_6$) was subsequently installed in the Davis Group chemical vapor deposition (CVD) gas cabinet. Initially, the strategy for BN growth using borazine was to deposit this compound at a relatively low growth temperature (650 ^oC) on a variety of substrates ((0001) AlN/Al_2O_3, Ni/ Al_2O_3, (0001) 4H-SiC, and polished pyrolytic boron nitride (PBN)) and then anneal at ~ 1000 ^oC to dehydrogenate the deposited $B_xN_yH_z$ product and improve crystallinity in an attempt to achieve sp^2-BN. The specific growth parameters are detailed in Table 10.7.1.

Table 10.7.1. Growth parameters of the depositions using borazine for CVD of BN.

	Sample 1	Sample 2	Sample 3	Sample 4	Sample 5	Sample 6
Substrate	25 nm (0001) AlN/sapphire	25 nm (0001) AlN/sapphire	100 nm Ni/ sapphire	(0001) 4H-SiC	5 nm RMS PBN	c-plane sapphire
Chamber pressure	20 Torr	20 Torr	20 Torr	20 Torr	20 Torr	20 Torr
Growth Temperature	650 °C	650 °C	650 °C	650 °C	650 °C	650 °C
Diluent gases	1 slm H_2 during growth; 1 slm N_2 during anneal	1 slm N_2 during growth; 1 slm N_2 during anneal	1 slm N_2 during growth; 1 slm N_2 during anneal	1 slm N_2 during growth; 1 slm N_2 during anneal	1 slm N_2 during growth; 1 slm N_2 during anneal	1 slm N_2 during growth; 1 slm N_2 during anneal
Borazine flow rate	2.2 sccm (H_2 carrier 20 sccm)	2.2 sccm (H_2 carrier 20 sccm)	2.2 sccm (H_2 carrier 20 sccm)	2.2 sccm (H_2 carrier 20 sccm)	2.2 sccm (H_2 carrier 20 sccm)	2.2 sccm (H_2 carrier 20 sccm)
Bubbler Pressure	300 Torr	300 Torr	300 Torr	300 Torr	300 Torr	300 Torr
Bubbler Temp.	-15 °C	-15 °C	-15 °C	-15 °C	-15 °C	-15 °C
Deposition time	30 min	30 min	30 min	30 min	30 min	30 min
Post-growth annealing	Ramp up 1000 °C within 1 hour, hold for 1 hr	Ramp up 1000 °C within 1 hour, hold for 1 hr	Ramp up 1000 °C within 1 hour, hold for 1 hr	Ramp up 1000 °C within 1 hour, hold for 1 hr	Ramp up 1000 °C within 1 hour, hold for 1 hr	Ramp up 1000 °C within 1 hour, hold for 1 hr

Sputter-depth x-ray photoelectron spectroscopy (XPS) measurements were conducted at the Swagelok Center for Surface Analysis of Materials at Case Western Reserve University with the assistance of Dr. Kevin Abassi. From these measurements, it was concluded that regardless of the substrate choice, the films (1) grew to only a thickness of ~ 300 nm and (2) were non-stoichiometric, containing an N deficit in the ratio of ~ 0.4 – 06:1 compared to B throughout the entire thickness of the film. Figures 10.7.1(a) and (b) show these observations in the sputter-

depth profiles for the BN/SiC and BN/PBN samples, respectively. Figure 10.7.1(c) shows the N:B atomic ratio of the films grown on SiC, PBN, and AlN/sapphire as a function of sputtering time.

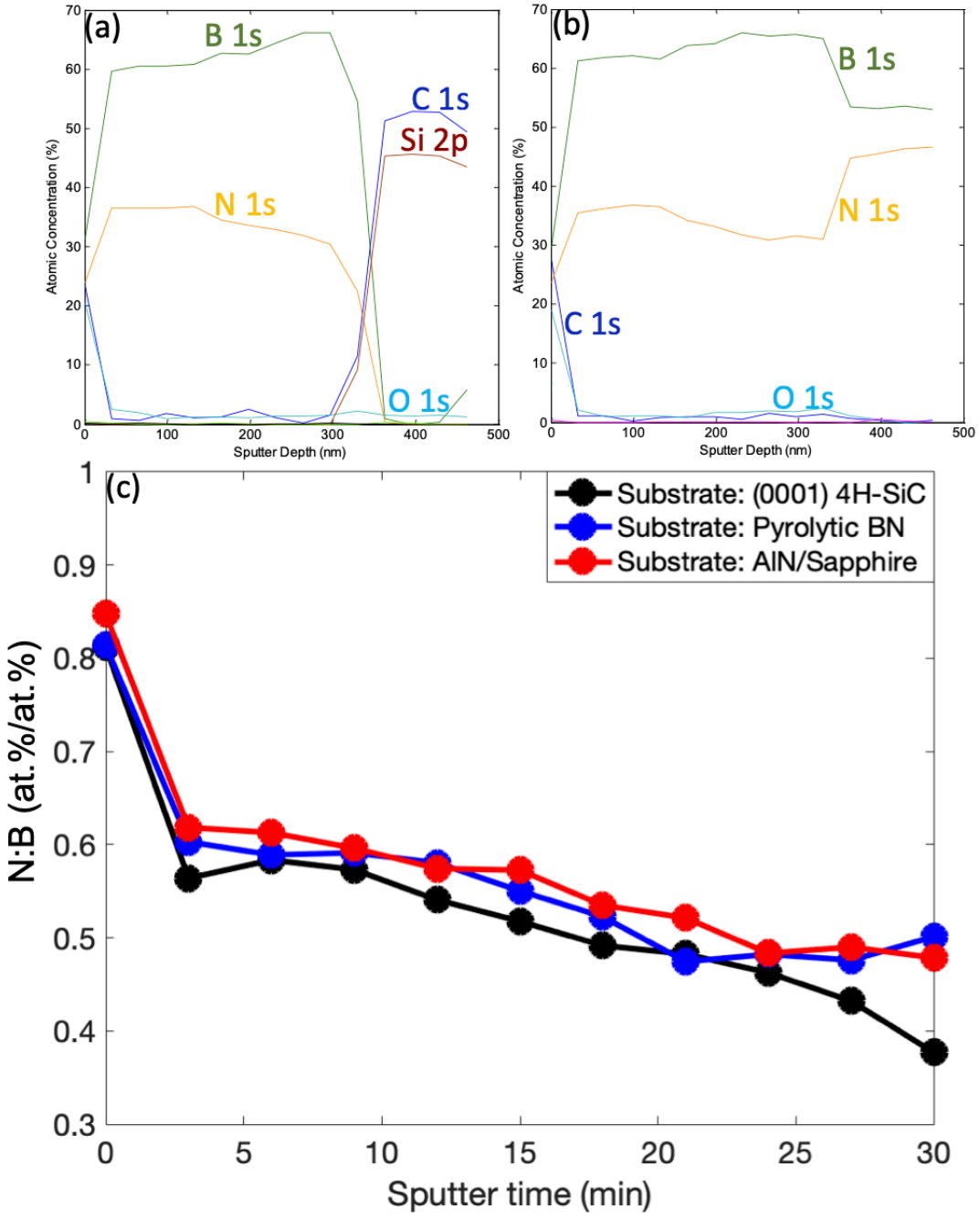

Figure 10.7.1. Sputter-depth XPS profiles of BN films grown on (a) 4H-SiC and (b) PBN. (c) N:B atomic ratio as a function of sputter time for BN films grown on 4H-SiC, PBN, and AlN/sapphire.

After these initial experiments, several depositions using were performed to try to address the stoichiometry issue. The new strategy employed was to increase the growth temperature to 1050 ^{o}C for one growth series, and in a second growth series introduce NH_3 into the chamber during growth to increase the V/III ratio. Unfortunately, it was discovered from sputter-depth XPS profiles that these new batch of samples contained up to 40 at.% oxygen throughout the films' thicknesses, which was indication of a severe leak or contamination of the borazine source. After several months of troubleshooting, it was determined that the borazine source had become contaminated. After removal of the borazine bottle, analysis of subsequent AlN thin film samples (grown using legacy recipes developed by the Lab Group) with sputter-depth XPS profiling indicated that any process gas lines were leak tight and that the remaining process gas bottles were not contaminated. Continued depositions of BN thin films did not commence until a new B-source precursor was obtained; diborane (B_2H_6) was chosen because of (1) its lack of inherent C and (2) its ease of handling. Unlike borazine and TEB, diborane at room temperature is gaseous and will not spontaneously condense. Thus, a bubbler attachment and an accompanying pressure controller are unnecessary for diborane, and its flow rate can be controlled with only a mass flow controller.

10.8. Appendix H: Modifying experimentally determined thermodynamic functions of the boron nitride polymorphic system to be used to calculate phase diagrams in CALPHAD software

Dr. Bryan Webler was instrumental in modifying the experimentally determined thermodynamic functions of the boron nitride (BN) polymorphic system [1] so that they could be used to calculate chemical vapor deposition (CVD) phase diagrams. Solozhenko [1] provided the heat capacity ($C_p(T)$) of hexagonal (h), rhombohedral (r), cubic (c), and wurtzite (w) -BN in the form:

$$C_p(T) = \delta_0 \left(\frac{T^2}{T^2+\delta_1 T+\delta_2}\right)^2 \quad \text{Eq. 10.8.1}$$

The coefficients δ_0, δ_1, and δ_2 for each phase is listed in Table 10.8.1. Solozhenko and Gavrichev [2] also listed the thermodynamic properties (C_p^o, S^o, and ΔH_f^o) of the BN polymorphs at standard conditions, and they are listed in Table 10.8.2.

Table 10.8.1. Coefficients δ_0, δ_1, and δ_2 for h-BN, r-BN, c-BN, and w-BN as referenced from Solozhenko [1].

Polymorph	δ_0	δ_1	δ_2
h-BN	53.63023	68.87958	36927.91
r-BN	55.1086	96.3183	27992.881
c-BN	46.83548	-11.6608	66261.937
w-BN	47.81094	3.45185	61875.367

Table 10.8.2. C_p^o, S^o, and ΔH_f^o for h-BN, r-BN, c-BN, and w-BN as referenced from Solozhenko and Gavrichev [1,2].

Polymorph	C_p^o [J/mol K]	S^o [J/mol K]	ΔH_f^o [J/mol]
h-BN	19.85	14.8	-2.50×10^5
r-BN	20.63	15.83	-2.48×10^5
c-BN	15.95	6.71	-2.67×10^5
w-BN	16.45	7.34	-2.63×10^5

To use this thermodynamic information in CALPHAD (Calculation of Phase Diagrams) software packages such as Thermocalc and FactSage, the $C_p(T)$ functions were first fitted, using Excel Solver to minimize the squared error, to the power form:

$$C_P(T) = a + bT + cT^{-2} + dT^2 \qquad \text{Eq. 10.8.2}$$

The coefficients of Eq. 10.8.2 for each BN polymorph are listed in Table 10.8.3. Figure 10.8.1 shows the $C_p(T)$ calculated from Solozhenko [1] and the power form fit of each polymorph in Fig. 10.8.1(a)-(d) and the error, calculated as the square of the difference between $C_p(T)$ (from Solozhenko's data) and $C_p(T)$ (from the power form fit).

Table 10.8.3. Coefficients of Eq. 10.8.2 for each BN polymorph.

Polymorph	a [J/mol K]	b [J/mol K^2]	c [J K/mol]	d [J/mol K^3]
h-BN	35.14122024	0.01223	-1771066.113	-2.39×10^{-6}
r-BN	33.92860771	0.013172	-1613094.923	-2.50×10^{-6}
c-BN	36.02684626	0.009503	-2133838.042	-2.06×10^{-6}
w-BN	35.42913871	0.010158	-2066079.925	-2.15×10^{-6}

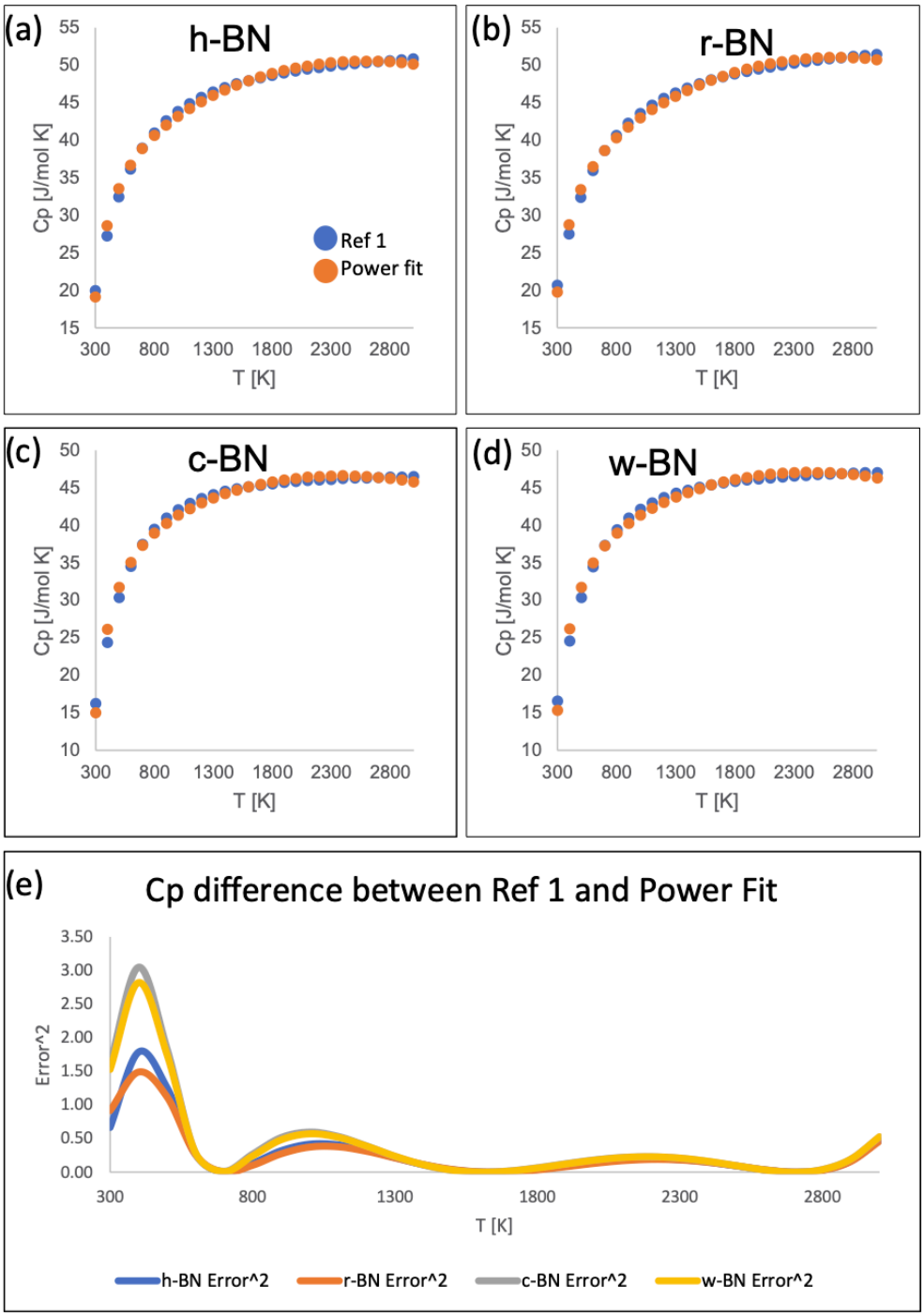

Figure 10.8.1. $C_p(T)$ of each BN polymorph: (a) h-BN, (b) r-BN, (c) c-BN, and (d) w-BN. The blue dots in these plots represent the data from Solozhenko [1] while the orange dot curves represent the $C_p(T)$ data calculated from the power form fit (see Eq. 10.8.2 and Table 10.8.3). (e) The error in the power form fit curves for each polymorph was calculated as the square of the difference between $C_p(T)$ determined from Solozhenko's data [1] and that determined by the power form fit calculations.

Next, all of the thermodynamic information provided thus far was used to generate $\Delta G(T)$ = (G(T) -G(298)) curves for each BN phase in the functional form of

$$G^{BN}(T) - G^{BN}(298) = a_0 + \frac{a_1}{T} + a_2 T + a_3 T^2 + a_4 T^3 + a_5 T \ln T \qquad \text{Eq. 10.8.3}$$

by using the integral

$$\int_{298}^{T} dG = G^{BN}(T) - G^{BN}(298) = -\int_{298}^{T} \left[S^{BN}(298) + \int_{298}^{T} \frac{C_P}{T} dT \right] dT \qquad \text{Eq. 10.8.4}$$

Because we are dealing with more than one BN phase, it is important that $\Delta G(T)$ for each phase is specified with the same reference state. Keeping $G^{BN}(298)$ as the reference state is meaningless because the value would be different for each of the four BN polymorphs. The standard state Gibbs free energy $G^{BN}(298)$ term can be rewritten as

$$G^{BN}(298) = H^{BN}(298) - 298 * S^{BN}(298) \qquad \text{Eq. 10.8.5}$$

where $H^{BN}(298)$ is standard state enthalpy. The standard heat of formation can be rewritten as

$$\Delta H_f^{BN}(298) = H^{BN}(298) - H_B(298) - H_N(298) \qquad \text{Eq. 10.8.6}$$

Rearranging Eq. 10.8.6 to solve for $H^{BN}(298)$ yields

$$H^{BN}(298) = -(\Delta H_f^{BN}(298) + H_B(298) + H_N(298)) \qquad \text{Eq. 10.8.7}$$

Substituting Eq. 10.8.7 into Eq. 10.8.5, and substituting that result for $G^{BN}(298)$ in Eq. 10.8.3, we are left with

$$G^{BN}(T) - H_B(298) - H_N(298) = a_0 + \frac{a_1}{T} + a_2 T + a_3 T^2 + a_4 T^3 + a_5 T \ln T + \Delta H_f^{BN}(298) + 298 * S^{BN}(298) \qquad \text{Eq. 10.8.8}$$

In this way, we have expressed the Gibbs free energy of each BN phase relative to their standard element reference (SER), defined as the enthalpy (H) of the most stable form of the constituting element(s) at 298.15 K and atmospheric pressure [3]. The three terms on the left side of Eq. 10.8.8 can be collectively and simply be written as G(T) – HSER. The sum of the

terms $\Delta H_f^{BN}(298) + 298 * S^{BN}(298)$ on the right side of Eq.8, evaluate to a number in units of J/mol (see Table 2) and thus can be combined into the a_0 term. Thus, Eq. 8 can be rewritten simply as

$$G^{BN}(T) - HSER = a_0 + \frac{a_1}{T} + a_2 T + a_3 T^2 + a_4 T^3 + a_5 T \ln T \qquad \text{Eq. 10.8.9}$$

The coefficients for Eq. 10.8.9 for each BN phase are listed in Table 10.8.4.

Table 10.8.4. Coefficients of the *HSER*-corrected Gibbs free energy expression (Eq. 10.8.9) of each BN polymorph.

Polytype	a_0 [J/mol]	a_1 [J K/mol]	a_2 [J/mol K]	a_3 [J/mol K^2]	a_4 [J/mol K^3]	a_5 [J/mol K]
h-BN	-2.669×10^5	8.855×10^5	2.341×10^2	-6.115×10^{-3}	3.980×10^{-7}	-35.141
r-BN	-2.641×10^5	8.065×10^5	2.243×10^2	-6.586×10^{-3}	4.170×10^{-7}	-33.929
c-BN	-2.853×10^5	1.070×10^6	2.494×10^2	-4.752×10^{-3}	3.430×10^{-7}	-36.027
w-BN	-2.809×10^5	1.03×10^6	2.445×10^2	-5.079×10^{-3}	3.580×10^{-7}	-35.429

Solozhenko [1] plotted the temperature dependencies of Gibbs free energy for transformations between the BN polymorphs, and this plot is shown from its original publication in Figure 10.8.2 (a). Fig. 10.8.2(b) shows the same plot where the calculation used $G^{BN}(298)$ as the reference state, while Fig. 10.8.2(c) shows the plot where the calculation used $HSER$ as the reference state. It appears that Solozhenko's plot more closely agrees with that in Fig. 10.8.2(b), indicating that Solozhenko's calculations used $G^{BN}(298)$ as the reference state. The differences in the Gibbs free energies between the calculations utilizing $G^{BN}(298)$ and $HSER$ as the reference states for the c-BN ➔ h-BN, w-BN ➔ h-BN, c-BN ➔ w-BN, and h-BN ➔ r-BN transformations were determined in the present research to be 589.2, 76.9, 412.3, and -806.8 J/mol, respectively.

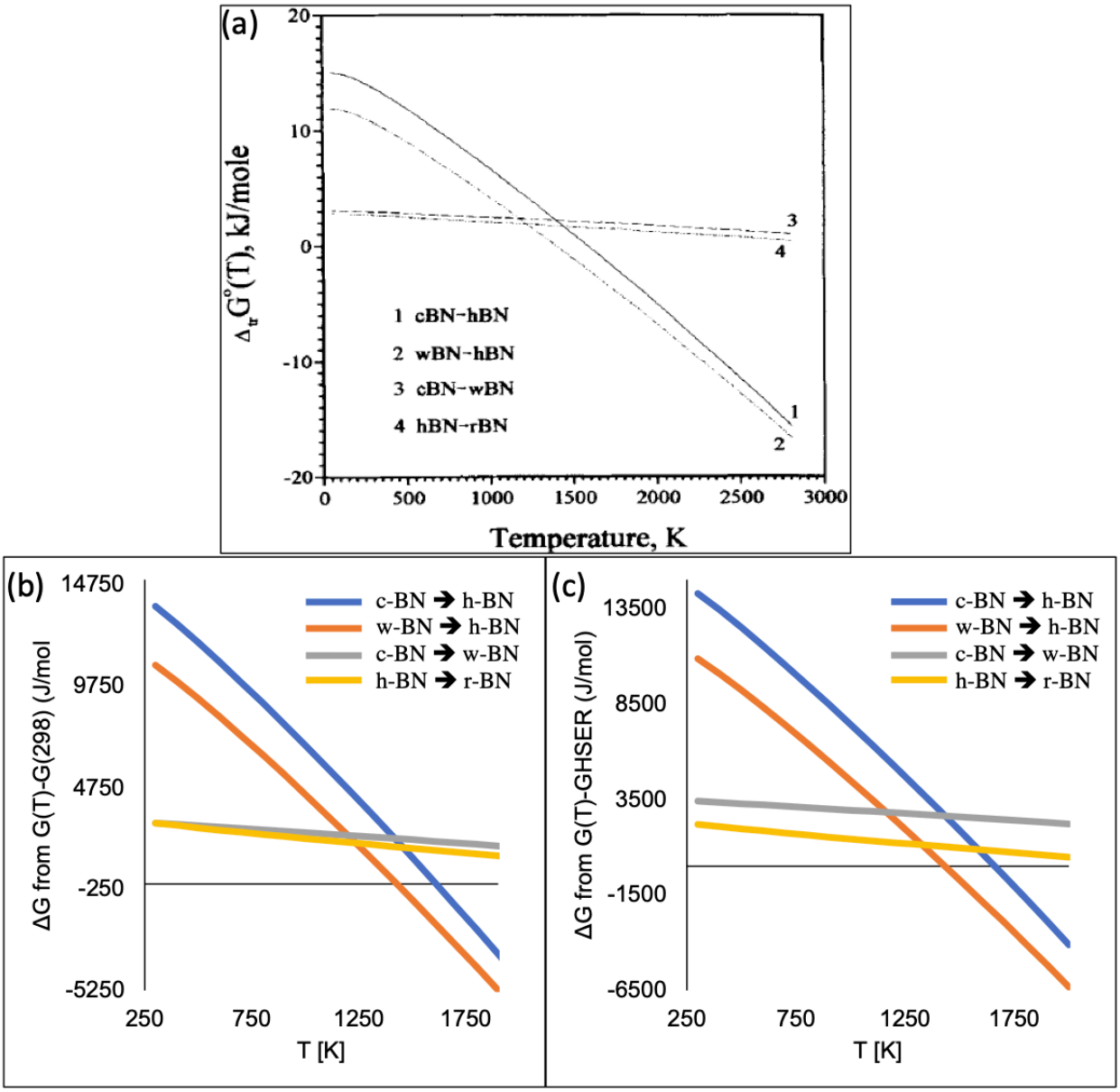

Figure 10.8.2. Gibbs free energy of transformations between the BN polymorphs as shown in (a) Solozhenko's publication [1], (b) as calculated using *G(298)* as the reference state, and (c) as calculated using *HSER* as the reference state.

The Gibbs free energy curves of each BN polymorph used in Thermocalc to calculate CVD phase diagrams were corrected using the $HSER$ reference state (Table 10.8.4). The constructed database containing the thermodynamic information for the BN polymorphs that was imported into Thermocalc is presented in Appendix I (Section 10.9).

To create the BN database for FactSage, the coefficients of $C_p(T)$ (Table 10.8.3) in conjunction with S^o and ΔH_f^o values for each polymorph (Table 2) were imported into the software which was then used to automatically calculate G(T) curves with respect to $HSER$. The coefficients to the Gibbs free energy equations (Eq. 10.8.9) of each BN polymorph as calculated by FactSage are presented in Figure 10.8.3. The average differences between G(T) as calculated from the values in Table 10.8.4 and that by FactSage are -96.2, 391.2, 173.3, and -183.7 J/mol for h-BN, r-BN, c-BN, and w-BN, respectively.

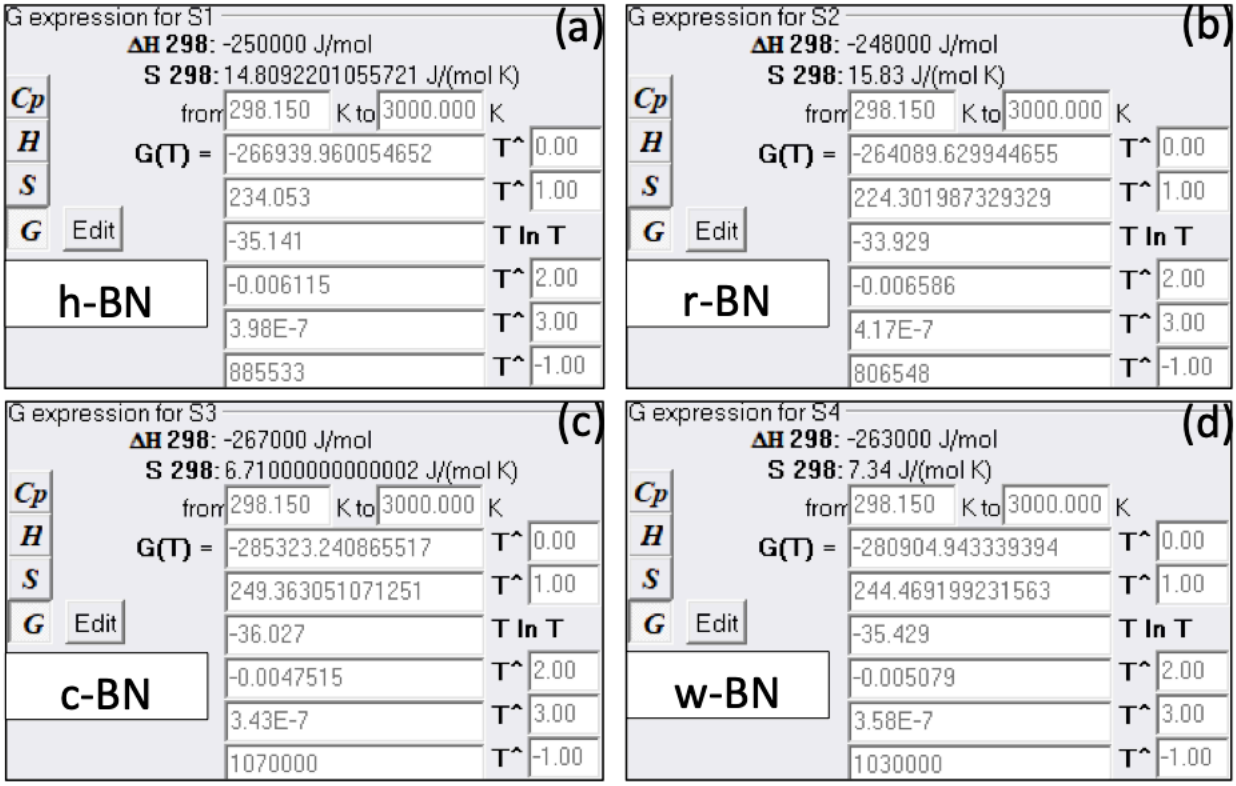

Figure 10.8.3. Gibbs free energy of functions (with respect to *HSER*) of the BN polymorphs calculated within FactSage: (a) h-BN, (b) r-BN, (c) c-BN, and (d) w-BN.

Appendix H References

[1] V. L. Solozhenko, High Press. Res. **13**, 199 (1995). Boron nitride phase diagram. State of the art. DOI:10.1080/08957959508200884.

[2] V. L. Solozhenko and K. S. Gavrichev, in *Wide Band Gap Electron. Mater.*, edited by M. Prelas, P. Gielisse, G. Popovici, B. Spitsyn, and T. Stacy, 1st ed. (Kluwer Academic Publishers, Minsk, Belarus, 1995), pp. 377–392. Thermodynamic properties of boron nitride. DOI:10.1007/978-94-011-0173-8.

[3] A. T. Dinsdale, Calphad **15**, 317 (1991). SGTE Data for Elements. DOI:10.1016/0364-5916(91)90030-N.

10.9. Appendix I: Edited SSUB3 database used in Thermocalc calculations of B-N-C-H equilibria

The SSUB3 database, used by the Scientific Group Thermodata Europe (SGTE) contains thermochemical information for pure condensed and gaseous substances [1]. When initially working with Thermocalc, it was of interest to create phase diagrams built from the TEB (triethylboron, $B(C_2H_5)_3$) – NH_3 – H_2 system to predict the presence of specific, condensed boron nitride (BN) polymorphs and gas phase equilibria depending on initial conditions (pressure, temperature, and composition). For this task, the SSUB3 database was edited by Dr. Bryan Webler to contain only the thermodynamic information of the pure elements B, N, C and H, their myriad gaseous and condensed compounds, and the BN polymorphs. The edited database is pasted below in its raw .txt/.tdb (**t**hermodynamic **d**ata**b**ase) form. The added information for the BN phases is highlighted throughout the text.

SSUBplusBN.TDB:

```
$ Database file written 2018-12-17
$ From database: SSUB3
 ELEMENT /-   ELECTRON_GAS              0.0000E+00  0.0000E+00  0.0000E+00!
 ELEMENT VA   VACUUM                    0.0000E+00  0.0000E+00  0.0000E+00!
 ELEMENT B    BETA_RHOMBO_B             1.0811E+01  1.2220E+03  5.9000E+00!
 ELEMENT C    GRAPHITE                  1.2011E+01  1.0540E+03  5.7400E+00!
 ELEMENT H    1/2_MOLE_H2(GAS)          1.0079E+00  4.2340E+03  6.5285E+01!
 ELEMENT N    1/2_MOLE_N2(GAS)          1.4007E+01  4.3350E+03  9.5751E+01!

 SPECIES B10H14                 B10H14!
 SPECIES B1C1                   B1C1!
 SPECIES B1C2                   B1C2!
 SPECIES B1H1                   B1H1!
 SPECIES B1H2                   B1H2!
 SPECIES B1H3                   B1H3!
 SPECIES B1H6N1                 B1H6N1!
 SPECIES B1N1                   B1N1!
 SPECIES B2                    B2!
 SPECIES B2C1                   B2C1!
 SPECIES B2H6                   B2H6!
 SPECIES B3H6N3                 B3H6N3!
 SPECIES B4C1                   B4C1!
 SPECIES B5H9                   B5H9!
 SPECIES C1H1                   C1H1!
 SPECIES C1H1N1_HCN                 C1H1N1!
 SPECIES C1H1N1_HNC                 C1H1N1!
 SPECIES C1H2                   C1H2!
 SPECIES C1H3                   C1H3!
 SPECIES C1H4                   C1H4!
```

```
SPECIES C1N1                C1N1!
SPECIES C1N2_CNN              C1N2!
SPECIES C1N2_NCN              C1N2!
SPECIES C2                  C2!
SPECIES C2H1                C2H1!
SPECIES C2H1N1                C2H1N1!
SPECIES C2H2                C2H2!
SPECIES C2H3                C2H3!
SPECIES C2H4                C2H4!
SPECIES C2H5                C2H5!
SPECIES C2H6                C2H6!
SPECIES C2N1_CCN              C2N1!
SPECIES C2N1_CNC              C2N1!
SPECIES C2N2                C2N2!
SPECIES C3                  C3!
SPECIES C3H1                C3H1!
SPECIES C3H1N1                C3H1N1!
SPECIES C3H4_1                C3H4!
SPECIES C3H4_2                C3H4!
SPECIES C3H6                C3H6!
SPECIES C3H6_2                C3H6!
SPECIES C3H8                C3H8!
SPECIES C3N1                C3N1!
SPECIES C4                  C4!
SPECIES C4H1                C4H1!
SPECIES C4H10_1               C4H10!
SPECIES C4H10_2               C4H10!
SPECIES C4H2                C4H2!
SPECIES C4H4                C4H4!
SPECIES C4H4_1_3              C4H4!
SPECIES C4H6_1                C4H6!
SPECIES C4H6_2                C4H6!
SPECIES C4H6_3                C4H6!
SPECIES C4H6_4                C4H6!
SPECIES C4H6_5                C4H6!
SPECIES C4H8                C4H8!
SPECIES C4H8_1                C4H8!
SPECIES C4H8_2                C4H8!
SPECIES C4H8_3                C4H8!
SPECIES C4H8_4                C4H8!
SPECIES C4H8_5                C4H8!
SPECIES C4N1                C4N1!
SPECIES C4N2                C4N2!
SPECIES C5                  C5!
SPECIES C5H1N1                C5H1N1!
SPECIES C5N1                C5N1!
SPECIES C60                 C60!
SPECIES C6H15B                B1C6H15!
SPECIES C6H6                C6H6!
SPECIES C6N1                C6N1!
SPECIES C6N2                C6N2!
SPECIES C9N1                C9N1!
SPECIES H1N1                H1N1!
SPECIES H1N3                H1N3!
SPECIES H2                  H2!
SPECIES H2N1                H2N1!
SPECIES H2N2_1_1N2H2            H2N2!
SPECIES H2N2_CIS              H2N2!
SPECIES H2N2_TRANS              H2N2!
SPECIES H3N1                H3N1!
SPECIES H4N2                H4N2!
SPECIES N2                  N2!
SPECIES N3                  N3!

FUNCTION F1391T    298.15 +558741.081-13.340364*T-20.91611*T*LN(T)
   +7.20885E-05*T**2-5.63569667E-09*T**3+4306.9065*T**(-1); 4800 Y
    +593321.479-80.4363033*T-13.38924*T*LN(T)-5.13201E-04*T**2
   -2.51243833E-09*T**3-26985320*T**(-1); 10000 N !
FUNCTION F1368T    298.15 +35719.8665-742.595159*T+102.9528*T*LN(T)
   -.5464555*T**2+9.07147E-05*T**3-225559.45*T**(-1); 400 Y
```

```
    -12892.3573+184.63672*T-46.224*T*LN(T)-.35411075*T**2
   +4.85348833E-05*T**3+2637970*T**(-1); 600 Y
    -77448.7425+1113.01602*T-188.3528*T*LN(T)-.2174362*T**2
   +2.44556167E-05*T**3+8061880*T**(-1); 1000 Y
    -227784.156+2678.32782*T-415.2963*T*LN(T)-.0639556*T**2
   +4.844075E-06*T**3+26886595*T**(-1); 1600 Y
    -366769.22+3646.5291*T-546.7735*T*LN(T)-.00815951*T**2
   +3.64899833E-07*T**3+54699500*T**(-1); 3000 Y
    -425805.521+3899.74941*T-578.7392*T*LN(T)-3.9619135E-04*T**2
   +9.12941833E-09*T**3+75395700*T**(-1); 6000 N !
FUNCTION F1462T    298.15 +819014.012-31.9756267*T-25.80349*T*LN(T)
   -.009170965*T**2+1.30752E-06*T**3+16360.605*T**(-1); 800 Y
    +817135.086+6.44812575*T-31.91701*T*LN(T)-.002164057*T**2
   -4.75160167E-08*T**3+50350.1*T**(-1); 2600 Y
    +800482.495+27.7009544*T-33.62021*T*LN(T)-.0037317085*T**2
   +1.23175517E-07*T**3+9965575*T**(-1); 5500 Y
    +715628.055+253.084626*T-60.22322*T*LN(T)-2.1112525E-05*T**2
   +2.628245E-08*T**3+60956750*T**(-1); 6000 N !
FUNCTION F1468T    298.15 +778206.128+23.8462342*T-37.62667*T*LN(T)
   -.015152905*T**2+1.86568667E-06*T**3-1881.1325*T**(-1); 1000 Y
    +762702.698+181.146396*T-60.35236*T*LN(T)-7.19561E-05*T**2
   -4.60731E-08*T**3+2015704*T**(-1); 4200 Y
    +786228.057+74.0287453*T-46.85278*T*LN(T)-.003154117*T**2
   +7.750975E-08*T**3-4041597*T**(-1); 6000 N !
FUNCTION F1663T    298.15 +438634.121+.487669024*T-25.51574*T*LN(T)
   -.003599787*T**2-8.3802E-08*T**3-65902.75*T**(-1); 800 Y
    +431905.323+60.6127222*T-33.91464*T*LN(T)+2.7803635E-04*T**2
   -2.635735E-07*T**3+857056.5*T**(-1); 1900 Y
    +506133.014-316.410008*T+14.73958*T*LN(T)-.01347488*T**2
   +4.34139E-07*T**3-19911350*T**(-1); 3500 Y
    +300895.2+283.015176*T-56.71971*T*LN(T)-.002922938*T**2
   +1.63579533E-07*T**3+87173100*T**(-1); 5800 Y
    -200719.32+1479.84894*T-195.9874*T*LN(T)+.01428863*T**2
   -2.35617833E-07*T**3+4.2671285E+08*T**(-1); 6000 N !
FUNCTION F1712T    298.15 +309752.904-9.09841304*T-26.63895*T*LN(T)
   -.011276995*T**2+9.34868E-09*T**3-61010.7*T**(-1); 700 Y
    +310119.645-34.4051787*T-22.26708*T*LN(T)-.01837512*T**2
   +1.71489167E-06*T**3+73910.35*T**(-1); 1400 Y
    +274585.874+243.984452*T-60.78432*T*LN(T)+3.617634E-04*T**2
   -9.644785E-09*T**3+6282680*T**(-1); 6000 N !
FUNCTION F1727T    298.15 +83198.6171-86.8456232*T-12.87203*T*LN(T)
   -.030065115*T**2+2.44170667E-06*T**3-235475.25*T**(-1); 800 Y
    +71889.2846+23.4582694*T-28.59129*T*LN(T)-.02110519*T**2
   +1.620855E-06*T**3+1215614.5*T**(-1); 1600 Y
    +19486.0299+378.655738*T-76.65203*T*LN(T)-.0011497315*T**2
   +3.81149667E-08*T**3+12116605*T**(-1); 4700 Y
    +5379.33085+427.301126*T-82.59504*T*LN(T)-5.582035E-05*T**2
   +1.10261683E-09*T**3+18352525*T**(-1); 6000 N !
FUNCTION F1771T    298.15 -122101.128-178.158362*T-1.603648*T*LN(T)
   -.0959838*T**2+1.16213833E-05*T**3-192800.45*T**(-1); 700 Y
    -149406.731+173.985418*T-54.57203*T*LN(T)-.0500562*T**2
   +4.09134167E-06*T**3+2455527.5*T**(-1); 1400 Y
    -240430.18+853.289141*T-147.8587*T*LN(T)-.00696291*T**2
   +3.01020167E-07*T**3+19314100*T**(-1); 3300 Y
    -293700.795+1076.97071*T-176.0018*T*LN(T)-3.237487E-04*T**2
   +7.34525333E-09*T**3+38439680*T**(-1); 6000 N !
FUNCTION F1821T    298.15 +557185.979-59.4876631*T-22.13135*T*LN(T)
   -.010520405*T**2+1.22989117E-06*T**3-78479.5*T**(-1); 1000 Y
    +547615.854+37.6857652*T-36.17827*T*LN(T)-.001138335*T**2
   +2.72286667E-08*T**3+1171495.5*T**(-1); 6000 N !
FUNCTION F1913T    298.15 +829926.969-93.2007055*T-13.63395*T*LN(T)
   -.033960835*T**2+7.30767333E-06*T**3-67153.4*T**(-1); 600 Y
    +815354.412+137.9026*T-49.68482*T*LN(T)+.00543292*T**2
   -7.11178167E-07*T**3+1030739.5*T**(-1); 1400 Y
    +823475.255+55.7356682*T-37.91694*T*LN(T)-.001645613*T**2
   +5.37223333E-08*T**3+105366.3*T**(-1); 6000 N !
FUNCTION F1929T    298.15 +766451.975+37.2707382*T-37.72971*T*LN(T)
   -.01712391*T**2+2.36950833E-06*T**3+20469.57*T**(-1); 900 Y
    +751376.887+200.9671*T-61.66618*T*LN(T)+1.9616045E-04*T**2
   -4.39825833E-08*T**3+1839663*T**(-1); 4800 Y
```

```
     +796481.729+45.4256517*T-42.68606*T*LN(T)-.0032453955*T**2
    +6.99416333E-08*T**3-17589540*T**(-1); 6000 N !
FUNCTION F1975T    298.15 +27306.2833-167.644062*T-.4655732*T*LN(T)
    -.10923545*T**2+1.39321867E-05*T**3+27295.47*T**(-1); 700 Y
     -7011.34498+272.53397*T-66.60291*T*LN(T)-.05235645*T**2
    +4.69880333E-06*T**3+3372631*T**(-1); 1300 Y
     -93616.4339+961.476296*T-162.173*T*LN(T)-.0048996925*T**2
    +2.19709167E-07*T**3+18247720*T**(-1); 3300 Y
     -128807.411+1114.66695*T-181.541*T*LN(T)-1.6398765E-04*T**2
    +3.77104333E-09*T**3+30339030*T**(-1); 6000 N !
FUNCTION F2118T    298.15 -526508.32-212.752878*T+6.610176*T*LN(T)
    -.21447395*T**2+3.71497333E-05*T**3+201761.5*T**(-1); 600 Y
     -567995.406+474.355376*T-101.6302*T*LN(T)-.0874596*T**2
    +8.92426333E-06*T**3+3224148.5*T**(-1); 1000 Y
     -625374.714+1050.45273*T-184.6554*T*LN(T)-.033519905*T**2
    +2.28082333E-06*T**3+10727610*T**(-1); 1800 Y
     -719373.844+1641.11909*T-263.6142*T*LN(T)-.0036392015*T**2
    +1.33447983E-07*T**3+32003415*T**(-1); 3800 Y
     -757272.453+1779.31815*T-280.656*T*LN(T)-2.173316E-04*T**2
    +4.47453667E-09*T**3+47958680*T**(-1); 6000 N !
FUNCTION F2177T    298.15 +65999.845-413.027897*T+41.17228*T*LN(T)
    -.24759865*T**2+2.96437833E-05*T**3-140561.05*T**(-1); 400 Y
     +53683.4409-209.593493*T+9.731524*T*LN(T)-.2208148*T**2
    +2.96042333E-05*T**3+663530*T**(-1); 600 Y
     +17879.0907+303.38793*T-68.75986*T*LN(T)-.1455308*T**2
    +1.6339635E-05*T**3+3687966*T**(-1); 1000 Y
     -82240.0906+1345.58602*T-219.852*T*LN(T)-.04339896*T**2
    +3.29830333E-06*T**3+16226075*T**(-1); 1600 Y
     -179332.156+2018.89074*T-311.2277*T*LN(T)-.00476976*T**2
    +2.04984667E-07*T**3+35779060*T**(-1); 3200 Y
     -216236.376+2172.59907*T-330.546*T*LN(T)-2.458644E-04*T**2
    +5.696865E-09*T**3+49138780*T**(-1); 6000 N !
FUNCTION F3895T    298.15 +710430.933-17.7062919*T-20.97529*T*LN(T)
    +1.998237E-04*T**2-3.34617167E-08*T**3+1680.6515*T**(-1); 3400 Y
     +698015.711+2.57175186*T-23.05071*T*LN(T)-6.04604E-05*T**2
    +6.74291667E-10*T**3+8558245*T**(-1); 10000 Y
     +736197.571-32.7975309*T-19.44529*T*LN(T)-1.5396035E-04*T**2
    -6.15402167E-11*T**3-56188350*T**(-1); 20000 N !
FUNCTION F4246T    298.15 +589091.036+6.37586112*T-28.31773*T*LN(T)
    +2.3216165E-04*T**2-7.36439667E-07*T**3-27186.245*T**(-1); 900 Y
     +591708.657-35.2925324*T-21.90158*T*LN(T)-.00592793*T**2
    +2.9876E-07*T**3-172733.6*T**(-1); 2800 Y
     +579194.621+42.13831*T-32.13932*T*LN(T)-.002507963*T**2
    +9.59279833E-08*T**3+2285342*T**(-1); 6400 Y
     +409696.643+452.714152*T-79.92745*T*LN(T)+.003347292*T**2
    -3.63044167E-08*T**3+1.115888E+08*T**(-1); 12000 Y
     +800166.03-30.0457765*T-28.18561*T*LN(T)+2.7641345E-04*T**2
    -1.923675E-09*T**3-4.4613505E+08*T**(-1); 20000 N !
FUNCTION F4265T    298.15 +120351.138+24.6526787*T-32.57666*T*LN(T)
    -.01162231*T**2+8.85030667E-07*T**3+141605.9*T**(-1); 1600 Y
     +91152.7411+219.071127*T-58.83538*T*LN(T)-7.90401E-04*T**2
    +1.96663667E-08*T**3+6401660*T**(-1); 5600 Y
     +35091.6923+353.984562*T-74.57322*T*LN(T)+.001214588*T**2
    -2.90453667E-08*T**3+44751805*T**(-1); 10000 N !
FUNCTION F4270T    298.15 +181847.846+51.3883732*T-37.44319*T*LN(T)
    -.00828483*T**2+5.45153E-07*T**3+90771.3*T**(-1); 1400 Y
     +161354.028+186.411098*T-55.58462*T*LN(T)-.0012597365*T**2
    +4.39184667E-08*T**3+4370728.5*T**(-1); 4500 Y
     +147259.267+237.011668*T-61.803*T*LN(T)-5.768925E-05*T**2
    +1.17421133E-09*T**3+10363305*T**(-1); 6000 N !
FUNCTION F4298T    298.15 +381898.015-5.8112289*T-27.63198*T*LN(T)
    -.007897355*T**2-3.87669333E-08*T**3-62547*T**(-1); 900 Y
     +378165.881+8.88081456*T-29.13698*T*LN(T)-.00988883*T**2
    +6.15529E-07*T**3+710779*T**(-1); 2200 Y
     +340850.246+220.65528*T-57.01662*T*LN(T)-4.862414E-04*T**2
    +1.48344217E-08*T**3+10277000*T**(-1); 6000 N !
FUNCTION F4331T    298.15 +137013.412-8.99457393*T-25.84363*T*LN(T)
    -.021245325*T**2+1.58670483E-06*T**3-33266.495*T**(-1); 1600 Y
     +84303.6035+343.362209*T-73.42088*T*LN(T)-.0017754415*T**2
    +6.12003E-08*T**3+11112475*T**(-1); 4400 Y
```

```
    +64161.9832+414.726089*T-82.17617*T*LN(T)-1.024296E-04*T**2
   +2.10901667E-09*T**3+19781775*T**(-1); 6000 N !
FUNCTION F4354T    298.15 -77295.563-147.095197*T-2.234656*T*LN(T)
   -.048463265*T**2+4.33754333E-06*T**3-305431.45*T**(-1); 1000 Y
    -110499.85+168.104152*T-47.22933*T*LN(T)-.021108925*T**2
   +1.1779525E-06*T**3+4316954*T**(-1); 2000 Y
    -181918.388+576.950971*T-101.1311*T*LN(T)-.002684469*T**2
   -2.361885E-08*T**3+22404635*T**(-1); 6000 N !
FUNCTION F4447T    298.15 +433394.876-43.6694537*T-23.31166*T*LN(T)
   -.00681527*T**2+6.12133333E-07*T**3-94160.55*T**(-1); 1000 Y
    +426972.042+22.5552259*T-32.86587*T*LN(T)-6.942125E-04*T**2
   -9.76663333E-08*T**3+690880.5*T**(-1); 2800 Y
    +404088.032+53.935739*T-35.62476*T*LN(T)-.0022908465*T**2
   +7.38622833E-08*T**3+14932100*T**(-1); 5500 Y
    +385913.889+165.613174*T-49.66302*T*LN(T)+5.46946E-04*T**2
   -1.726725E-08*T**3+5261955*T**(-1); 9800 Y
    +483141.867-42.8350229*T-26.03462*T*LN(T)-.0016491445*T**2
   +1.81745833E-08*T**3-43086590*T**(-1); 19000 Y
    +11383.8285+389.145496*T-70.6705*T*LN(T)+2.0369425E-04*T**2
   +3.91913E-09*T**3+8.78364E+08*T**(-1); 20000 N !
FUNCTION F4474T    298.15 +620891.31+24.210392*T-37.08092*T*LN(T)
   -.01239698*T**2+9.982715E-07*T**3+72736.6*T**(-1); 1500 Y
    +585408.45+265.15468*T-69.64695*T*LN(T)+9.002435E-04*T**2
   -2.169545E-08*T**3+7323580*T**(-1); 6000 N !
FUNCTION F4477T    298.15 +491013.214-54.0941794*T-22.68211*T*LN(T)
   -.037322295*T**2+6.18339333E-06*T**3-34410.6*T**(-1); 700 Y
    +468712.208+233.167234*T-65.88173*T*LN(T)+8.042115E-05*T**2
   +5.994055E-08*T**3+2131359.5*T**(-1); 1900 Y
    +473689.136+217.47595*T-64.09586*T*LN(T)+2.517867E-04*T**2
   -6.87131833E-09*T**3+343771.95*T**(-1); 6000 N !
FUNCTION F4656T    298.15 +803005.137+419.915369*T-97.48141*T*LN(T)
   +.08202995*T**2-1.97357E-05*T**3+690749.5*T**(-1); 500 Y
    +826732.964-2.78397075*T-30.08349*T*LN(T)-.002621389*T**2
   +8.30959667E-08*T**3-868501*T**(-1); 4300 Y
    +850321.493-26.7776267*T-27.96957*T*LN(T)-.0019408995*T**2
   +3.222655E-08*T**3-22380050*T**(-1); 12000 Y
    +409662.376+520.53814*T-86.66656*T*LN(T)+.0015642485*T**2
   -7.28093667E-09*T**3+6.04612E+08*T**(-1); 20000 N !
FUNCTION F4935T    298.15 +555907.867+57.0634842*T-39.08261*T*LN(T)
   -.00569665*T**2-4.27085667E-07*T**3+135750.65*T**(-1); 1000 Y
    +560368.69-14.5499453*T-28.12154*T*LN(T)-.015627865*T**2
   +1.1143725E-06*T**3-38275.195*T**(-1); 2100 Y
    +500130.672+354.303072*T-77.12859*T*LN(T)+.001864081*T**2
   -4.41159667E-08*T**3+13617155*T**(-1); 6400 Y
    +548031.854+234.921123*T-63.15948*T*LN(T)+6.031155E-05*T**2
   -8.38662167E-10*T**3-17395655*T**(-1); 10000 N !
FUNCTION F4941T    298.15 +592373.866+105.022577*T-49.5495*T*LN(T)
   -.019252425*T**2+2.12674833E-06*T**3+252275.1*T**(-1); 1000 Y
    +573050.216+288.206974*T-75.74176*T*LN(T)-.0029359265*T**2
   +1.41014317E-07*T**3+2990485.5*T**(-1); 3200 Y
    +554709.269+373.323837*T-86.60353*T*LN(T)-8.324045E-05*T**2
   +1.91413E-09*T**3+8876435*T**(-1); 6000 N !
FUNCTION F4946T    298.15 +210657.364+102.660059*T-43.33318*T*LN(T)
   -.015969725*T**2+1.09745783E-06*T**3+366936*T**(-1); 1700 Y
    +162805.829+400.859267*T-83.17592*T*LN(T)-8.50672E-04*T**2
   -8.40052167E-09*T**3+11371695*T**(-1); 4700 Y
    +284779.332+156.173741*T-55.55581*T*LN(T)-.003209261*T**2
   +1.402618E-08*T**3-81696300*T**(-1); 9200 Y
    +643212.249-464.67941*T+13.72962*T*LN(T)-.009112535*T**2
   +1.07541683E-07*T**3-4.2679415E+08*T**(-1); 10000 N !
FUNCTION F4958T    298.15 +253597.563-148.811942*T-7.989506*T*LN(T)
   -.0560301*T**2+7.22032833E-06*T**3-86107.5*T**(-1); 700 Y
    +237578.897+66.4331994*T-40.61565*T*LN(T)-.026213335*T**2
   +2.05575833E-06*T**3+1400582*T**(-1); 1500 Y
    +180976.129+465.400317*T-94.92649*T*LN(T)-.0026392345*T**2
   +1.00493533E-07*T**3+12635730*T**(-1); 3900 Y
    +155481.051+562.46419*T-106.9625*T*LN(T)-1.2237275E-04*T**2
   +2.58523833E-09*T**3+22815630*T**(-1); 6000 N !
FUNCTION F4964T    298.15 +47209.5269-186.336653*T+1.510335*T*LN(T)
   -.0796424*T**2+1.11523633E-05*T**3-126378.45*T**(-1); 600 Y
```

```
     +30955.0457+58.8547956*T-36.41994*T*LN(T)-.040167385*T**2
    +3.41469333E-06*T**3+1183016*T**(-1); 1300 Y
     -31590.202+549.033592*T-104.2592*T*LN(T)-.007018595*T**2
    +3.29534167E-07*T**3+12115675*T**(-1); 3000 Y
     -77650.6893+755.842185*T-130.5377*T*LN(T)-3.066123E-04*T**2
    +7.24598833E-09*T**3+27459580*T**(-1); 6000 N !
FUNCTION F5014T    298.15 +103695.78-248.192017*T+6.535456*T*LN(T)
    -.0876786*T**2+1.08003583E-05*T**3-293497.1*T**(-1); 700 Y
     +80275.9858+60.5182301*T-40.0912*T*LN(T)-.046084495*T**2
    +3.772465E-06*T**3+1925892*T**(-1); 1400 Y
     -4338.1575+691.320485*T-126.6998*T*LN(T)-.00614309*T**2
    +2.665555E-07*T**3+17610670*T**(-1); 3300 Y
     -50997.0146+888.071661*T-151.4679*T*LN(T)-2.7785525E-04*T**2
    +6.34659667E-09*T**3+34266230*T**(-1); 6000 N !
FUNCTION F5026T    298.15 -90150.09-192.644467*T+2.384174*T*LN(T)
    -.0962022*T**2+1.15030917E-05*T**3-161159.75*T**(-1); 700 Y
     -114140.24+121.641652*T-45.03662*T*LN(T)-.05415545*T**2
    +4.43007333E-06*T**3+2130084*T**(-1); 1400 Y
     -212082.164+853.908038*T-145.619*T*LN(T)-.007637925*T**2
    +3.37957333E-07*T**3+20220470*T**(-1); 3200 Y
     -268113.331+1093.5554*T-175.8524*T*LN(T)-3.4791075E-04*T**2
    +8.02933833E-09*T**3+39919465*T**(-1); 6000 N !
FUNCTION F5062T    298.15 +792153.988+14.7311886*T-36.28539*T*LN(T)
    -.018125745*T**2+2.50772167E-06*T**3+52950.15*T**(-1); 900 Y
     +778705.39+169.814399*T-59.16569*T*LN(T)-6.96421E-04*T**2
    +1.31973417E-09*T**3+1546836*T**(-1); 5300 Y
     +791060.551+128.184545*T-54.09811*T*LN(T)-.001596146*T**2
    +3.02705333E-08*T**3-4150787*T**(-1); 6000 N !
FUNCTION F5067T    298.15 +672447.252+14.0337*T-35.19268*T*LN(T)
    -.020993075*T**2+3.203695E-06*T**3+42892.37*T**(-1); 800 Y
     +658020.921+186.12618*T-60.76239*T*LN(T)-4.012427E-04*T**2
    +1.79268833E-08*T**3+1597736*T**(-1); 4000 Y
     +655191.86+199.068856*T-62.40644*T*LN(T)+6.739555E-06*T**2
    -1.69353833E-10*T**3+2526253*T**(-1); 6000 N !
FUNCTION F5072T    298.15 +290548.421+121.602*T-52.47563*T*LN(T)
    -.01735357*T**2+1.64181417E-06*T**3+216215.45*T**(-1); 1300 Y
     +261478.785+354.552639*T-84.87749*T*LN(T)-7.94942E-04*T**2
    +4.774245E-09*T**3+5246010*T**(-1); 6000 N !
FUNCTION F5113T    298.15 +829826.554-14.7696351*T-32.21563*T*LN(T)
    -.014548565*T**2+1.77806833E-06*T**3-100277.6*T**(-1); 1000 Y
     +809388.444+179.25291*T-59.93982*T*LN(T)+.0025413955*T**2
    -2.54139667E-07*T**3+2769455*T**(-1); 2800 Y
     +959399.017-367.175865*T+7.286391*T*LN(T)-.010483215*T**2
    +2.00694833E-07*T**3-58720050*T**(-1); 5100 Y
     +645204.419+237.848566*T-60.73106*T*LN(T)-.0047721765*T**2
    +1.3846755E-07*T**3+1.945987E+08*T**(-1); 8000 Y
     -79243.2062+1580.27099*T-211.8741*T*LN(T)+.009202285*T**2
    -1.030498E-07*T**3+8.44019E+08*T**(-1); 10000 N !
FUNCTION F5130T    298.15 +611989.348+96.3308561*T-48.29552*T*LN(T)
    -.020416105*T**2+2.40121167E-06*T**3+286785.6*T**(-1); 900 Y
     +603734.835+194.753441*T-62.91113*T*LN(T)-.008746555*T**2
    +6.34741E-07*T**3+1176564*T**(-1); 1600 Y
     +428832.638+1236.10822*T-200.7133*T*LN(T)+.03914231*T**2
    -2.50175333E-06*T**3+42232610*T**(-1); 2100 Y
     +581080.642+349.628056*T-83.7538*T*LN(T)-6.025005E-04*T**2
    +2.010855E-08*T**3+5274980*T**(-1); 4000 N !
FUNCTION F5136T    298.15 +356487.153+185.17418*T-62.59063*T*LN(T)
    -.02202228*T**2+2.01058E-06*T**3+447283.2*T**(-1); 1300 Y
     +338282.743+349.57551*T-85.86694*T*LN(T)-.008694175*T**2
    +5.73491667E-07*T**3+3148123*T**(-1); 1600 Y
     -10396.965+2437.01372*T-362.3165*T*LN(T)+.08781705*T**2
    -5.735055E-06*T**3+84547750*T**(-1); 2000 Y
     +314302.001+510.439848*T-107.3719*T*LN(T)-8.47611E-04*T**2
    +2.89172E-08*T**3+7302895*T**(-1); 4000 N !
FUNCTION F5142T    298.15 +181410.617-122.851573*T-10.20607*T*LN(T)
    -.09533745*T**2+1.50758583E-05*T**3; 600 Y
     +166868.714+123.51993*T-49.16033*T*LN(T)-.048685235*T**2
    +4.554395E-06*T**3+1025661.5*T**(-1); 1350 N !
FUNCTION F5145T    298.15 +173490.978-86.0624782*T-17.22925*T*LN(T)
    -.0839689*T**2+1.23994933E-05*T**3; 600 Y
```

```
    +164149.935+76.784887*T-43.11068*T*LN(T)-.05198975*T**2
   +4.980055E-06*T**3+635844.5*T**(-1); 1350 N !
FUNCTION F5148T    298.15 +9960.10176-169.389262*T-5.296785*T*LN(T)
   -.11043535*T**2+1.3915705E-05*T**3-29916.7*T**(-1); 700 Y
    -20079.5568+230.805154*T-65.85768*T*LN(T)-.05571235*T**2
   +4.55149E-06*T**3+2783191*T**(-1); 1400 Y
    -123982.893+1002.03018*T-171.6758*T*LN(T)-.00713415*T**2
   +3.037055E-07*T**3+22144770*T**(-1); 3400 Y
    -176512.668+1224.25918*T-199.6496*T*LN(T)-5.34708E-04*T**2
   +1.37195383E-08*T**3+40697190*T**(-1); 4000 N !
FUNCTION F5157T    298.15 +14789.4507-271.642378*T+11.34939*T*LN(T)
   -.13386645*T**2+2.00341833E-05*T**3-272154.55*T**(-1); 600 Y
    -5877.08746+63.1182105*T-41.1683*T*LN(T)-.07381185*T**2
   +7.01085E-06*T**3+1272695.5*T**(-1); 1350 N !
FUNCTION F5161T    298.15 -109364.396-321.907815*T+21.52618*T*LN(T)
   -.1721779*T**2+2.66239E-05*T**3-291993*T**(-1); 600 Y
    -136284.127+126.13378*T-49.09882*T*LN(T)-.08908635*T**2
   +8.15831167E-06*T**3+1652173.5*T**(-1); 1000 Y
    -139266.757+270.053278*T-72.22463*T*LN(T)-.0649997*T**2
   +4.53440333E-06*T**3; 1473.10 Y
    +257891.373-1948.43811*T+217.2249*T*LN(T)-.15124325*T**2
   +8.672805E-06*T**3-96828650*T**(-1); 2200 Y
    +99792.4667-390.62824*T+2.18137*T*LN(T)-.0596624*T**2
   +2.314065E-06*T**3-1.0470605E+08*T**(-1); 2800 Y
    +4552037.53-17003.1518*T+2055.691*T*LN(T)-.47848015*T**2
   +1.82760667E-05*T**3-1.903921E+09*T**(-1); 3400 Y
    -224887.496+1106.77062*T-188.6147*T*LN(T)-.01046*T**2; 4000 N !
FUNCTION F5175T    298.15 +590110.187+118.990688*T-53.75038*T*LN(T)
   -.014523885*T**2+9.63548667E-07*T**3+242117.9*T**(-1); 1600 Y
    -107989.978+4371.50824*T-618.5786*T*LN(T)+.1872713*T**2
   -1.25304267E-05*T**3+1.6058455E+08*T**(-1); 1900 Y
    +527634.18+485.866585*T-102.0276*T*LN(T)+.0012918695*T**2
   -1.24413333E-08*T**3+14435335*T**(-1); 4000 N !
FUNCTION F5190T    298.15 +1015583.43+114.927796*T-53.39543*T*LN(T)
   -.01399763*T**2+8.26027167E-07*T**3+181008.25*T**(-1); 2500 Y
    +937071.116+522.054721*T-106.1735*T*LN(T)+.0016641645*T**2
   -4.03015E-08*T**3+21906740*T**(-1); 7000 Y
    +974994.003+406.652032*T-92.4518*T*LN(T)-2.6888155E-04*T**2
   +7.07303167E-09*T**3+7587140*T**(-1); 10000 N !
FUNCTION F5205T    298.15 +751541.722+252.532282*T-73.01*T*LN(T)
   -.0216856*T**2+2.96625833E-06*T**3+733430*T**(-1); 800 Y
    +739011.333+395.36198*T-94.137*T*LN(T)-.00478225*T**2+2.37405E-07*T**3
   +2194465*T**(-1); 3200 Y
    +712634.362+524.463672*T-110.728*T*LN(T)-2.049E-04*T**2+5.39E-09*T**3
   +10118465*T**(-1); 4000 N !
FUNCTION F5195T    298.15 -137766.886-262.245087*T+8.962001*T*LN(T)
   -.1969312*T**2+2.74147E-05*T**3-206440*T**(-1); 600 Y
    -178579.034+346.123228*T-84.951*T*LN(T)-.10048435*T**2
   +8.73554E-06*T**3+3128305*T**(-1); 1300 Y
    -258789.548+1055.24805*T-184.924*T*LN(T)-.04513245*T**2
   +2.99413E-06*T**3+15193975*T**(-1); 1500 N !
FUNCTION F5200T    298.15 -146155.003-277.516061*T+14.289*T*LN(T)
   -.2069239*T**2+2.98628333E-05*T**3-154585*T**(-1); 600 Y
    -195079.37+449.056779*T-97.801*T*LN(T)-.09222675*T**2
   +7.70571667E-06*T**3+3862255*T**(-1); 1500 N !
FUNCTION F5210T    298.15 +420839.085+277.118737*T-75.491*T*LN(T)
   -.02448245*T**2+1.97030333E-06*T**3+682970*T**(-1); 1600 Y
    +367789.415+651.154953*T-126.464*T*LN(T)-.00206835*T**2
   +7.59616667E-08*T**3+11366585*T**(-1); 4000 N !
FUNCTION F5218T    298.15 +288051.702-62.1217039*T-23.51726*T*LN(T)
   -.10484665*T**2+1.70475E-05*T**3+166261.7*T**(-1); 600 Y
    +271269.255+222.99465*T-68.63141*T*LN(T)-.05050485*T**2
   +4.70099667E-06*T**3+1349256.5*T**(-1); 1350 N !
FUNCTION F5213T    298.15 +370172.153-109.109385*T-11.397*T*LN(T)
   -.1111325*T**2+1.61656983E-05*T**3+358940*T**(-1); 700 Y
    +325301.98+486.389913*T-101.491*T*LN(T)-.0296325*T**2
   +2.12065333E-06*T**3+4595505*T**(-1); 1900 Y
    +243710.536+1013.16655*T-172.226*T*LN(T)-.00194705*T**2
   +6.80733333E-08*T**3+22628525*T**(-1); 4000 N !
FUNCTION F5222T    298.15 +148974.923-154.988667*T-9.679935*T*LN(T)
```

```
   -.13252255*T**2+1.875805E-05*T**3-64604.3*T**(-1); 700 Y
    +143586.528-18.9490501*T-32.19739*T*LN(T)-.0996706*T**2
   +1.0683635E-05*T**3; 1350 N !
FUNCTION F5225T    298.15 +121653.925-773.246123*T+98.0989*T*LN(T)
   -.3288666*T**2+8.00427167E-05*T**3-1078152*T**(-1); 500 Y
    +69670.1413+288.910378*T-76.01784*T*LN(T)-.06784355*T**2
   +6.41405167E-06*T**3+1865350.5*T**(-1); 1350 N !
FUNCTION F5229T    298.15 +171954.749-626.535566*T+70.21254*T*LN(T)
   -.27331145*T**2+6.370085E-05*T**3-1007086.5*T**(-1); 500 Y
    +134813.21+143.300138*T-56.40032*T*LN(T)-.0793759*T**2
   +7.720665E-06*T**3+1073901*T**(-1); 1350 N !
FUNCTION F5232T    298.15 +137810.196-224.576236*T+2.364458*T*LN(T)
   -.14050145*T**2+2.03154833E-05*T**3-328490*T**(-1); 600 Y
    +121325.209+49.3857422*T-40.8135*T*LN(T)-.0897223*T**2
   +9.02328333E-06*T**3+865653*T**(-1); 1350 N !
FUNCTION F5235T    298.15 +151050.533-349.7586*T+27.653*T*LN(T)
   -.17688495*T**2+2.748815E-05*T**3-55550*T**(-1); 600 Y
    +103768.902+358.874068*T-81.845*T*LN(T)-.0637295*T**2
   +5.44480167E-06*T**3+3783270*T**(-1); 1400 Y
    -17659.4864+1268.26244*T-206.872*T*LN(T)-.0052678*T**2
   +2.01658333E-07*T**3+26324075*T**(-1); 4000 N !
FUNCTION F5240T    298.15 +7830.75067-135.953552*T-5.378*T*LN(T)
   -.1516055*T**2+1.77087667E-05*T**3+697635*T**(-1); 1000 N !
FUNCTION F5242T    298.15 +12533.4694-811.558153*T+99.93819*T*LN(T)
   -.3308519*T**2+7.42945833E-05*T**3-1242512*T**(-1); 500 Y
    -34223.5657+125.568769*T-53.29244*T*LN(T)-.1034473*T**2
   +1.02151667E-05*T**3+1500742*T**(-1); 1350 N !
FUNCTION F5246T    298.15 -9954.98882-420.389759*T+33.53622*T*LN(T)
   -.19866405*T**2+3.05487167E-05*T**3-458273.5*T**(-1); 600 Y
    -41465.8704+91.7966661*T-46.86917*T*LN(T)-.10633385*T**2
   +1.0445635E-05*T**3+1888323*T**(-1); 1350 N !
FUNCTION F5250T    298.15 -19845.8404-271.195989*T+10.01855*T*LN(T)
   -.17302075*T**2+2.49936167E-05*T**3-356884.75*T**(-1); 600 Y
    -46739.5847+154.950922*T-56.55596*T*LN(T)-.09892585*T**2
   +9.35312333E-06*T**3+1703068*T**(-1); 1350 N !
FUNCTION F5254T    298.15 +25802.6842-440.237142*T+43.351*T*LN(T)
   -.2105867*T**2+3.14729833E-05*T**3-227945*T**(-1); 600 Y
    -29324.4938+373.689954*T-82.076*T*LN(T)-.08318905*T**2
   +7.05010833E-06*T**3+4327090*T**(-1); 1500 N !
FUNCTION F5257T    298.15 -6.10167508-885.983713*T+114.5039*T*LN(T)
   -.3592508*T**2+8.41611667E-05*T**3-1525313*T**(-1); 500 Y
    -47563.4441+107.259988*T-49.09213*T*LN(T)-.1065104*T**2
   +1.0644305E-05*T**3+1115990*T**(-1); 1350 N !
FUNCTION F5260T    298.15 +766190.11+175.281824*T-66.11008*T*LN(T)
   -.02485482*T**2+2.71599333E-06*T**3+303174.9*T**(-1); 1100 Y
    +747394.017+365.107005*T-93.49276*T*LN(T)-.00697279*T**2
   +5.12352333E-07*T**3+2748645*T**(-1); 1600 Y
    +641403.271+987.677312*T-175.6647*T*LN(T)+.020971405*T**2
   -1.28130683E-06*T**3+27835945*T**(-1); 2300 Y
    +729737.729+490.304718*T-110.3911*T*LN(T)-2.998301E-04*T**2
   +9.56094833E-09*T**3+5620205*T**(-1); 4000 N !
FUNCTION F5266T    298.15 +505178.266+249.554301*T-77.19564*T*LN(T)
   -.032306965*T**2+3.55103E-06*T**3+384942.65*T**(-1); 1000 Y
    +477127.139+527.180379*T-117.116*T*LN(T)-.006743855*T**2
   +4.38569E-07*T**3+4119420*T**(-1); 2100 Y
    +452542.745+670.426473*T-136.0499*T*LN(T)-1.581368E-04*T**2
   +4.07757333E-09*T**3+10228920*T**(-1); 6000 N !
FUNCTION F5280T    298.15 +1028316.51+169.994576*T-62.97185*T*LN(T)
   -.0317015*T**2+4.09694E-06*T**3+186275.3*T**(-1); 900 Y
    +999750.247+470.150388*T-106.5965*T*LN(T)-.0014783715*T**2
   +7.07236167E-08*T**3+3747842.5*T**(-1); 3500 Y
    +990603.918+513.736611*T-112.1708*T*LN(T)-6.611165E-06*T**2
   +1.10554567E-10*T**3+6565820*T**(-1); 10000 N !
FUNCTION F5291T    298.15 +565832.392+339.066064*T-92.08698*T*LN(T)
   -.032563725*T**2+3.09118167E-06*T**3+593472*T**(-1); 1300 Y
    +538888.167+588.621481*T-127.5575*T*LN(T)-.011726025*T**2
   +7.94542833E-07*T**3+4465412*T**(-1); 1600 Y
    +78339.6712+3348.96742*T-493.1949*T*LN(T)+.11612845*T**2
   -7.57889333E-06*T**3+1.1185815E+08*T**(-1); 2000 Y
    +507650.922+802.448311*T-156.2272*T*LN(T)-.001025462*T**2
```

```
   +3.49275E-08*T**3+9687785*T**(-1); 4000 N !
FUNCTION F5297T    298.15 +805264.415+172.325118*T-67.07879*T*LN(T)
   -.046217805*T**2+5.59493833E-06*T**3+137768.7*T**(-1); 1100 Y
    +757692.075+650.330567*T-135.9344*T*LN(T)-.0018180185*T**2
   +2.17601E-07*T**3+6320010*T**(-1); 1600 Y
    +753984.872+690.986539*T-141.6552*T*LN(T)+.0010635605*T**2
   -4.53243667E-08*T**3+6141515*T**(-1); 4000 N !
FUNCTION F5304T    298.15 +2466802.51+88.4522193*T+10.293*T*LN(T)
   -1.15472*T**2+1.77008333E-04*T**3+4621630*T**(-1); 800 Y
    +1709986.12+9262.28939*T-1356.31*T*LN(T)-.0366229*T**2
   +1.98371667E-06*T**3+84578000*T**(-1); 3300 N !
FUNCTION F5325T    298.15 +71643.2857-315.496947*T+25.001*T*LN(T)
   -.2161207*T**2+3.431025E-05*T**3+151720*T**(-1); 600 Y
    +13101.0393+567.138312*T-111.518*T*LN(T)-.07424425*T**2
   +6.56452833E-06*T**3+4867785*T**(-1); 1300 Y
    -109518.172+1531.0277*T-245.03*T*LN(T)-.00845165*T**2
   +3.60173333E-07*T**3+26305545*T**(-1); 3500 Y
    -158376.968+1751.98658*T-273.057*T*LN(T)-.0015082*T**2
   +4.57316667E-08*T**3+41807370*T**(-1); 4000 N !
FUNCTION F5343T    298.15 +975471.743+331.335526*T-96.19741*T*LN(T)
   -.03440444*T**2+3.61062167E-06*T**3+444252.4*T**(-1); 1200 Y
    +946374.618+614.371665*T-136.7612*T*LN(T)-.009127355*T**2
   +6.49230333E-07*T**3+4395259.5*T**(-1); 1600 Y
    +792130.776+1515.52918*T-255.5837*T*LN(T)+.03091199*T**2
   -1.889E-06*T**3+41063565*T**(-1); 2300 Y
    +922631.664+781.147178*T-159.2122*T*LN(T)-4.802916E-04*T**2
   +1.55775667E-08*T**3+8213105*T**(-1); 4000 N !
FUNCTION F5349T    298.15 +710605.869+415.263895*T-108.8752*T*LN(T)
   -.03960015*T**2+4.03372833E-06*T**3+540637.5*T**(-1); 1200 Y
    +676554.273+739.657698*T-155.2022*T*LN(T)-.011433625*T**2
   +8.11543167E-07*T**3+5270510*T**(-1); 1600 Y
    +436938.374+2148.75871*T-341.2276*T*LN(T)+.05188615*T**2
   -3.23635667E-06*T**3+62001300*T**(-1); 2200 Y
    +647125.674+947.008843*T-183.1233*T*LN(T)-6.645755E-04*T**2
   +2.20063E-08*T**3+9956720*T**(-1); 4000 N !
FUNCTION F5357T    298.15 +1229982.77+561.176741*T-140.7773*T*LN(T)
   -.047192335*T**2+4.511485E-06*T**3+609497.5*T**(-1); 1300 Y
    +1186647.33+955.88265*T-196.7217*T*LN(T)-.014963935*T**2
   +1.02521983E-06*T**3+6950290*T**(-1); 1600 Y
    +759569.233+3481.45539*T-530.4628*T*LN(T)+.09945365*T**2
   -6.31484167E-06*T**3+1.0764755E+08*T**(-1); 2100 Y
    +1142482.62+1252.9145*T-236.4529*T*LN(T)-4.184909E-04*T**2
   +2.05288333E-08*T**3+14633295*T**(-1); 4000 N !
FUNCTION F10447T   298.15 +211801.621+24.4989816*T-20.78611*T*LN(T); 6000 N
   !
FUNCTION F10577T   298.15 +349844.617+14.1020529*T-29.25363*T*LN(T)
   +.0011332935*T**2-7.194045E-07*T**3-10581.05*T**(-1); 900 Y
    +349690.802-2.66410316*T-26.34868*T*LN(T)-.0031129585*T**2
   +1.26865583E-07*T**3+242619.5*T**(-1); 2600 Y
    +377351.663-86.5823367*T-16.43317*T*LN(T)-.00415333*T**2
   +1.06912267E-07*T**3-12256680*T**(-1); 6000 Y
    +112360.659+457.057239*T-78.44235*T*LN(T)+.0022764175*T**2
   -1.76759833E-08*T**3+1.9949745E+08*T**(-1); 16500 Y
    +468990.776+107.412651*T-41.98719*T*LN(T)+6.128755E-04*T**2
   -3.41992333E-09*T**3-4.600016E+08*T**(-1); 20000 N !
FUNCTION F10606T   298.15 +281443.328-10.138183*T-31.62033*T*LN(T)
   -.028592885*T**2+3.50043833E-06*T**3+115220.1*T**(-1); 800 Y
    +266295.06+164.476888*T-57.40154*T*LN(T)-.00872063*T**2
   +5.58152333E-07*T**3+1806677*T**(-1); 2100 Y
    +235799.423+343.09084*T-81.03807*T*LN(T)-4.0989945E-04*T**2
   +2.43429667E-09*T**3+9383725*T**(-1); 6000 N !
FUNCTION F10854T   298.15 -9522.97393+78.5273873*T-31.35707*T*LN(T)
   +.0027589925*T**2-7.46390667E-07*T**3+56582.3*T**(-1); 1000 Y
    +180.10884-15.6128262*T-17.84857*T*LN(T)-.00584168*T**2
   +3.14618667E-07*T**3-1280036*T**(-1); 2100 Y
    -18840.1661+92.3120249*T-32.05082*T*LN(T)-.0010728235*T**2
   +1.14281783E-08*T**3+3561002.5*T**(-1); 6000 N !
FUNCTION F10909T   298.15 +181695.921-8.95646872*T-27.17438*T*LN(T)
   -.008276815*T**2+5.01971833E-08*T**3-79167.1*T**(-1); 900 Y
    +176890.989+19.7206608*T-30.77769*T*LN(T)-.00851653*T**2
```

```
   +4.38273833E-07*T**3+790952.5*T**(-1); 2200 Y
    +158568.703+130.442515*T-45.49406*T*LN(T)-.003192605*T**2
   +7.58613833E-08*T**3+5186700*T**(-1); 6000 N !
FUNCTION F10920T   298.15 +278543.593-132.335237*T-11.29365*T*LN(T)
   -.039609675*T**2+5.06716167E-06*T**3-179074.6*T**(-1); 700 Y
    +265272.042+40.9184154*T-37.41842*T*LN(T)-.01654095*T**2
   +1.20156783E-06*T**3+1093557*T**(-1); 1700 Y
    +220908.567+328.357673*T-76.05898*T*LN(T)-.001203253*T**2
   +3.22393E-08*T**3+10877605*T**(-1); 6000 N !
FUNCTION F10925T   298.15 +243108.449-131.699573*T-10.04616*T*LN(T)
   -.03855888*T**2+4.44032833E-06*T**3-210340.75*T**(-1); 800 Y
    +226001.683+65.9056141*T-39.21192*T*LN(T)-.016235705*T**2
   +1.19297867E-06*T**3+1683940.5*T**(-1); 1700 Y
    +182200.978+358.524587*T-78.69521*T*LN(T)-2.383138E-04*T**2
   -3.47482167E-08*T**3+10904680*T**(-1); 5300 Y
    +254116.983+143.611044*T-52.95996*T*LN(T)-.004252278*T**2
   +8.06085667E-08*T**3-25992570*T**(-1); 6000 N !
FUNCTION F10931T   298.15 +207653.255-142.056556*T-8.430374*T*LN(T)
   -.03979746*T**2+4.65783333E-06*T**3-238312.05*T**(-1); 800 Y
    +189877.189+65.1453683*T-39.06339*T*LN(T)-.016076395*T**2
   +1.16499367E-06*T**3+1711475*T**(-1); 1700 Y
    +157001.347+305.000993*T-71.81432*T*LN(T)-.001752856*T**2
   +2.04542E-09*T**3+7803560*T**(-1); 4500 Y
    +182365.175+192.871054*T-57.77639*T*LN(T)-.004769903*T**2
   +1.14961967E-07*T**3+1707626.5*T**(-1); 6000 N !
FUNCTION F11101T   298.15 -53688.8734-38.3667414*T-21.21774*T*LN(T)
   -.022871695*T**2+1.80809167E-06*T**3-76698.65*T**(-1); 1100 Y
    -74633.9373+137.490887*T-45.82843*T*LN(T)-.00981344*T**2
   +4.74353E-07*T**3+3291161*T**(-1); 2600 Y
    -123038.477+373.34644*T-76.17662*T*LN(T)-.001227198*T**2
   +1.40479833E-08*T**3+18061240*T**(-1); 6000 N !
FUNCTION F11153T   298.15 +86927.7704-135.248393*T-9.500891*T*LN(T)
   -.07254055*T**2+1.0957435E-05*T**3-66788*T**(-1); 600 Y
    +69326.6133+135.209763*T-51.478*T*LN(T)-.027945695*T**2
   +2.05087E-06*T**3+1319633*T**(-1); 1600 Y
    +769.96061+590.510669*T-112.8954*T*LN(T)-.0029814015*T**2
   +1.05599267E-07*T**3+15929030*T**(-1); 4200 Y
    -32055.3396+708.209184*T-127.3663*T*LN(T)-1.5857495E-04*T**2
   +3.25521E-09*T**3+29951250*T**(-1); 6000 N !
FUNCTION F12782T   298.15 +466446.153-13.3752579*T-20.89393*T*LN(T)
   +8.45521E-05*T**2-1.0018685E-08*T**3+2788.7865*T**(-1); 2950 Y
    +481259.036-52.5441357*T-16.37613*T*LN(T)-2.283738E-04*T**2
   -2.78997167E-08*T**3-7559105*T**(-1); 6000 N !
FUNCTION F12981T   298.15 -8000.12538-8.81620423*T-27.22332*T*LN(T)
   -.0012599175*T**2-5.39381E-07*T**3-38326.695*T**(-1); 800 Y
    -10569.6461+2.77534096*T-28.42384*T*LN(T)-.003189275*T**2
   +2.06638E-07*T**3+416969.05*T**(-1); 2200 Y
    -22468.6303+71.8176265*T-37.55014*T*LN(T)-6.158995E-06*T**2
   -4.22547E-09*T**3+3427512*T**(-1); 6000 N !
FUNCTION F13027T   298.15 +426260.222-44.8788475*T-24.40177*T*LN(T)
   -.02510581*T**2+3.41313667E-06*T**3+61652.95*T**(-1); 800 Y
    +409926.892+144.323861*T-52.34995*T*LN(T)-.0035522355*T**2
   +2.39819667E-07*T**3+1869491.5*T**(-1); 2200 Y
    +398090.062+216.588606*T-61.96494*T*LN(T)-5.55378E-05*T**2
   +1.47712917E-09*T**3+4654831*T**(-1); 6000 N !
FUNCTION F1389T    298.15 -2942.1444+107.494933*T-16.05029*T*LN(T)
   -.00500612*T**2-5.65217667E-11*T**3+314807.1*T**(-1); 2000 N !
FUNCTION F1362T    298.15 -61177.6009+166.059138*T-30.141*T*LN(T)
   -.1571225*T**2-1.76465E-04*T**3; 371.90 Y
    -608640.235+11472.7845*T-1869.155*T*LN(T)+2.2871375*T**2
   -6.47436833E-04*T**3+28477665*T**(-1); 500 Y
    -12912.2316-643.403029*T+106.897*T*LN(T)-.533644*T**2+8.7825E-05*T**3
   -3792815*T**(-1); 700 Y
    -94849.4382+914.517947*T-141.209*T*LN(T)-.23796555*T**2
   +2.61500667E-05*T**3-60*T**(-1); 1500 N !
FUNCTION F1816T    298.15 -261040.369+126.459602*T-18.7341*T*LN(T)
   -.019441475*T**2+2.07715E-06*T**3+422878.4*T**(-1); 1200 Y
    -284729.181+357.047504*T-51.63636*T*LN(T)+3.9540955E-07*T**2
   -1.98643167E-11*T**3+3437095*T**(-1); 3240 Y
    -332388.511+496.275015*T-67*T*LN(T)-2.701375E-14*T**2+9.95781E-19*T**3
```

```
    -1.313297E-04*T**(-1); 3500 N !
 FUNCTION F2133T    298.15 -109777.52+709.89764*T-105.9207*T*LN(T)
    -2.54235E-04*T**2-1.78226667E-06*T**3+2397154.5*T**(-1); 2700 N !
 FUNCTION F2173T    298.15 +21463.7566+71.2933713*T-19.58124*T*LN(T)
    -.23432215*T**2+3.590155E-05*T**3-504553.5*T**(-1); 900 Y
     -108017.637+1772.25947*T-275.5065*T*LN(T)-.01530038*T**2
    +1.429879E-06*T**3+11328915*T**(-1); 1500 N !
 FUNCTION F1349T    298.15 -7735.28368+107.111863*T-15.6641*T*LN(T)
    -.006864515*T**2+6.188775E-07*T**3+370843*T**(-1); 1100 Y
     -16649.4743+184.801744*T-26.6047*T*LN(T)-7.9809E-04*T**2
    -2.55601667E-08*T**3+1748269.5*T**(-1); 2348 Y
     -21357.9884+222.327208*T-31.4*T*LN(T); 6000 N !
 FUNCTION F5302T    298.15 +2232387.45+1624.15871*T-217.988*T*LN(T)
    -.88971*T**2+1.13199333E-04*T**3+7681900*T**(-1); 1000 N !
 FUNCTION F5323T    298.15 +8456.49693+740.043096*T-136.106*T*LN(T); 353 N !
 FUNCTION F3871T    298.15 -17368.4408+170.730317*T-24.3*T*LN(T)
    -4.723E-04*T**2+2562600*T**(-1)-2.643E+08*T**(-2)+1.2E+10*T**(-3);
    4765.30 Y
     -17368.4408+170.730317*T-24.3*T*LN(T)-4.723E-04*T**2+2562600*T**(-1)
    -2.643E+08*T**(-2)+1.2E+10*T**(-3); 6000 N !
 FUNCTION F3893T    298.15 -16359.4285+175.609805*T-24.31*T*LN(T)
    -4.723E-04*T**2+2698000*T**(-1)-2.61E+08*T**(-2)+1.11E+10*T**(-3); 6000
    N !
 FUNCTION F11151T   298.15 +27918.2693+338.319206*T-64.265*T*LN(T)
    -.0531085*T**2+1.45030667E-06*T**3-163535*T**(-1); 800 N !
 FUNCTION TRIETB 298.15 -.17*T**2-401.89*T-147567; 3000 N !

FUNCTION GBNHEX 298.15
 -2.55E+05
 -12526.7
 +885533*T**(-1)
 +234.053*T
 -0.00612*T**2
 +3.98E-07*T**3
 -35.141*T*LN(T); 3000 N !
FUNCTION GBNRHO 298.15
 -2.52E+05
 -11369.4
 +806548*T**(-1)
 +224.292*T
 -0.00659*T**2
 +4.17E-07*T**3
 -33.929*T*LN(T); 3000 N !
FUNCTION GBNCUB 298.15
 -2.69E+05
 -16300.8
 +1.07E+06*T**(-1)
 +249.321*T
 -0.00475*T**2
 +3.43E-07*T**3
 -36.027*T*LN(T); 3000 N !
FUNCTION GBNWUR 298.15
 -2.65E+05
 -15735.7
 +1.03E+06*T**(-1)
 +244.496*T
 -0.00508*T**2
 +3.58E-07*T**3
 -35.429*T*LN(T); 3000 N !
FUNCTION UN_ASS 298.15 +0; 300 N !

 TYPE_DEFINITION % SEQ *!
 DEFINE_SYSTEM_DEFAULT ELEMENT 2 !
 DEFAULT_COMMAND DEF_SYS_ELEMENT VA /- !

 PHASE GAS:G %  1  1.0  !
   CONSTITUENT GAS:G :B,B10H14,B1C1,B1C2,B1H1,B1H2,B1H3,B1H6N1,B1N1,B2,B2C1,
   B2H6,B3H6N3,B5H9,C,C1H1,C1H1N1_HCN,C1H1N1_HNC,C1H2,C1H3,C1H4,C1N1,
   C1N2_CNN,C1N2_NCN,C2,C2H1,C2H1N1,C2H2,C2H3,C2H4,C2H5,C2H6,C2N1_CCN,
   C2N1_CNC,C2N2,C3,C3H1,C3H1N1,C3H4_1,C3H4_2,C3H6,C3H6_2,C3H8,C3N1,C4,C4H1,
```

```
C4H10_1,C4H10_2,C4H2,C4H4,C4H4_1_3,C4H6_1,C4H6_2,C4H6_3,C4H6_4,C4H6_5,
C4H8,C4H8_1,C4H8_2,C4H8_3,C4H8_4,C4H8_5,C4N1,C4N2,C5,C5H1N1,C5N1,C60,
C6H15B,C6H6,C6N1,C6N2,C9N1,H,H1N1,H1N3,H2,H2N1,H2N2_1_1N2H2,H2N2_CIS,
H2N2_TRANS,H3N1,H4N2,N,N2,N3 :  !

 PARAMETER G(GAS,B;0)                298.15 +F1391T#+R#*T*LN(1E-05*P);
6000 N !
 PARAMETER G(GAS,B10H14;0)            298.15 +F1368T#+R#*T*LN(1E-05*P);
6000 N !
 PARAMETER G(GAS,B1C1;0)              298.15 +F1462T#+R#*T*LN(1E-05*P);
6000 N !
 PARAMETER G(GAS,B1C2;0)              298.15 +F1468T#+R#*T*LN(1E-05*P);
6000 N !
 PARAMETER G(GAS,B1H1;0)              298.15 +F1663T#+R#*T*LN(1E-05*P);
6000 N  !
 PARAMETER G(GAS,B1H2;0)              298.15 +F1712T#+R#*T*LN(1E-05*P);
6000 N  !
 PARAMETER G(GAS,B1H3;0)              298.15 +F1727T#+R#*T*LN(1E-05*P);
6000 N  !
 PARAMETER G(GAS,B1H6N1;0)            298.15 +F1771T#+R#*T*LN(1E-05*P);
6000 N  !
 PARAMETER G(GAS,B1N1;0)              298.15 +F1821T#+R#*T*LN(1E-05*P);
6000 N !
 PARAMETER G(GAS,B2;0)               298.15 +F1913T#+R#*T*LN(1E-05*P);
6000 N !
 PARAMETER G(GAS,B2C1;0)              298.15 +F1929T#+R#*T*LN(1E-05*P);
6000 N !
 PARAMETER G(GAS,B2H6;0)              298.15 +F1975T#+R#*T*LN(1E-05*P);
6000 N !
 PARAMETER G(GAS,B3H6N3;0)            298.15 +F2118T#+R#*T*LN(1E-05*P);
6000 N !
 PARAMETER G(GAS,B5H9;0)              298.15 +F2177T#+R#*T*LN(1E-05*P);
6000 N !
 PARAMETER G(GAS,C;0)                298.15 +F3895T#+R#*T*LN(1E-05*P);
6000 N !
 PARAMETER G(GAS,C1H1;0)              298.15 +F4246T#+R#*T*LN(1E-05*P);
6000 N REF2556 !
 PARAMETER G(GAS,C1H1N1_HCN;0)        298.15 +F4265T#+R#*T*LN(1E-05*P);
6000 N !
 PARAMETER G(GAS,C1H1N1_HNC;0)        298.15 +F4270T#+R#*T*LN(1E-05*P);
6000 N !
 PARAMETER G(GAS,C1H2;0)              298.15 +F4298T#+R#*T*LN(1E-05*P);
6000 N !
 PARAMETER G(GAS,C1H3;0)              298.15 +F4331T#+R#*T*LN(1E-05*P);
6000 N !
 PARAMETER G(GAS,C1H4;0)              298.15 +F4354T#+R#*T*LN(1E-05*P);
6000 N !
 PARAMETER G(GAS,C1N1;0)              298.15 +F4447T#+R#*T*LN(1E-05*P);
6000 N REF2634 !
 PARAMETER G(GAS,C1N2_CNN;0)          298.15 +F4474T#+R#*T*LN(1E-05*P);
6000 N REF2643 !
 PARAMETER G(GAS,C1N2_NCN;0)          298.15 +F4477T#+R#*T*LN(1E-05*P);
6000 N REF2644 !
 PARAMETER G(GAS,C2;0)               298.15 +F4656T#+R#*T*LN(1E-05*P);
6000 N REF2743 !
 PARAMETER G(GAS,C2H1;0)              298.15 +F4935T#+R#*T*LN(1E-05*P);
6000 N REF2820 !
 PARAMETER G(GAS,C2H1N1;0)            298.15 +F4941T#+R#*T*LN(1E-05*P);
6000 N REF2822 !
 PARAMETER G(GAS,C2H2;0)              298.15 +F4946T#+R#*T*LN(1E-05*P);
6000 N REF2823 !
 PARAMETER G(GAS,C2H3;0)              298.15 +F4958T#+R#*T*LN(1E-05*P);
6000 N REF2826 !
 PARAMETER G(GAS,C2H4;0)              298.15 +F4964T#+R#*T*LN(1E-05*P);
6000 N REF2827 !
 PARAMETER G(GAS,C2H5;0)              298.15 +F5014T#+R#*T*LN(1E-05*P);
6000 N REF2838 !
 PARAMETER G(GAS,C2H6;0)              298.15 +F5026T#+R#*T*LN(1E-05*P);
6000 N REF2840 !
 PARAMETER G(GAS,C2N1_CCN;0)          298.15 +F5062T#+R#*T*LN(1E-05*P);
```

```
6000 N REF2867 !
 PARAMETER G(GAS,C2N1_CNC;0)          298.15 +F5067T#+R#*T*LN(1E-05*P);
6000 N REF2868 !
 PARAMETER G(GAS,C2N2;0)             298.15 +F5072T#+R#*T*LN(1E-05*P);
6000 N REF2869 !
 PARAMETER G(GAS,C3;0)               298.15 +F5113T#+R#*T*LN(1E-05*P);
6000 N REF2892 !
 PARAMETER G(GAS,C3H1;0)             298.15 +F5130T#+R#*T*LN(1E-05*P);
6000 N REF2903 !
 PARAMETER G(GAS,C3H1N1;0)           298.15 +F5136T#+R#*T*LN(1E-05*P);
6000 N REF2904 !
 PARAMETER G(GAS,C3H4_1;0)           298.15 +F5142T#+R#*T*LN(1E-05*P);
6000 N REF2905 !
 PARAMETER G(GAS,C3H4_2;0)           298.15 +F5145T#+R#*T*LN(1E-05*P);
6000 N REF2908 !
 PARAMETER G(GAS,C3H6;0)             298.15 +F5148T#+R#*T*LN(1E-05*P);
6000 N REF2911 !
 PARAMETER G(GAS,C3H6_2;0)           298.15 +F5157T#+R#*T*LN(1E-05*P);
6000 N REF2916 !
 PARAMETER G(GAS,C3H8;0)             298.15 +F5161T#+R#*T*LN(1E-05*P);
6000 N REF2919 !
 PARAMETER G(GAS,C3N1;0)             298.15 +F5175T#+R#*T*LN(1E-05*P);
6000 N REF2927 !
 PARAMETER G(GAS,C4;0)               298.15 +F5190T#+R#*T*LN(1E-05*P);
6000 N REF2932 !
 PARAMETER G(GAS,C4H1;0)             298.15 +F5205T#+R#*T*LN(1E-05*P);
6000 N REF2938 !
 PARAMETER G(GAS,C4H10_1;0)          298.15 +F5195T#+R#*T*LN(1E-05*P);
6000 N REF2933 !
 PARAMETER G(GAS,C4H10_2;0)          298.15 +F5200T#+R#*T*LN(1E-05*P);
6000 N REF2935 !
 PARAMETER G(GAS,C4H2;0)             298.15 +F5210T#+R#*T*LN(1E-05*P);
6000 N REF2940 !
 PARAMETER G(GAS,C4H4;0)             298.15 +F5218T#+R#*T*LN(1E-05*P);
6000 N REF2944 !
 PARAMETER G(GAS,C4H4_1_3;0)         298.15 +F5213T#+R#*T*LN(1E-05*P);
6000 N REF2942 !
 PARAMETER G(GAS,C4H6_1;0)           298.15 +F5222T#+R#*T*LN(1E-05*P);
6000 N REF2947 !
 PARAMETER G(GAS,C4H6_2;0)           298.15 +F5225T#+R#*T*LN(1E-05*P);
6000 N REF2950 !
 PARAMETER G(GAS,C4H6_3;0)           298.15 +F5229T#+R#*T*LN(1E-05*P);
6000 N REF2953 !
 PARAMETER G(GAS,C4H6_4;0)           298.15 +F5232T#+R#*T*LN(1E-05*P);
6000 N REF2956 !
 PARAMETER G(GAS,C4H6_5;0)           298.15 +F5235T#+R#*T*LN(1E-05*P);
6000 N REF2959 !
 PARAMETER G(GAS,C4H8;0)             298.15 +F5240T#+R#*T*LN(1E-05*P);
6000 N REF2961 !
 PARAMETER G(GAS,C4H8_1;0)           298.15 +F5242T#+R#*T*LN(1E-05*P);
6000 N REF2963 !
 PARAMETER G(GAS,C4H8_2;0)           298.15 +F5246T#+R#*T*LN(1E-05*P);
6000 N !
 PARAMETER G(GAS,C4H8_3;0)           298.15 +F5250T#+R#*T*LN(1E-05*P);
6000 N !
 PARAMETER G(GAS,C4H8_4;0)           298.15 +F5254T#+R#*T*LN(1E-05*P);
6000 N !
 PARAMETER G(GAS,C4H8_5;0)           298.15 +F5257T#+R#*T*LN(1E-05*P);
6000 N !
 PARAMETER G(GAS,C4N1;0)             298.15 +F5260T#+R#*T*LN(1E-05*P);
6000 N !
 PARAMETER G(GAS,C4N2;0)             298.15 +F5266T#+R#*T*LN(1E-05*P);
6000 N !
 PARAMETER G(GAS,C5;0)               298.15 +F5280T#+R#*T*LN(1E-05*P);
6000 N !
 PARAMETER G(GAS,C5H1N1;0)           298.15 +F5291T#+R#*T*LN(1E-05*P);
6000 N !
 PARAMETER G(GAS,C5N1;0)             298.15 +F5297T#+R#*T*LN(1E-05*P);
6000 N !
 PARAMETER G(GAS,C60;0)              298.15 +F5304T#+R#*T*LN(1E-05*P);
```

```
 6000 N !
  PARAMETER G(GAS,C6H15B;0)             298.15 +TRIETB#+R#*T*LN(1E-05*P);
 6000 N !
  PARAMETER G(GAS,C6H6;0)               298.15 +F5325T#+R#*T*LN(1E-05*P);
 6000 N !
  PARAMETER G(GAS,C6N1;0)               298.15 +F5343T#+R#*T*LN(1E-05*P);
 6000 N !
  PARAMETER G(GAS,C6N2;0)               298.15 +F5349T#+R#*T*LN(1E-05*P);
 6000 N  !
  PARAMETER G(GAS,C9N1;0)               298.15 +F5357T#+R#*T*LN(1E-05*P);
 6000 N !
  PARAMETER G(GAS,H;0)                 298.15 +F10447T#+R#*T*LN(1E-05*P);
 6000 N !
  PARAMETER G(GAS,H1N1;0)               298.15 +F10577T#+R#*T*LN(1E-05*P);
 6000 N !
  PARAMETER G(GAS,H1N3;0)               298.15 +F10606T#+R#*T*LN(1E-05*P);
 6000 N  !
  PARAMETER G(GAS,H2;0)                298.15 +F10854T#+R#*T*LN(1E-05*P);
 6000 N !
  PARAMETER G(GAS,H2N1;0)               298.15 +F10909T#+R#*T*LN(1E-05*P);
 6000 N !
  PARAMETER G(GAS,H2N2_1_1N2H2;0)       298.15 +F10920T#+R#*T*LN(1E-05*P);
 6000 N  !
  PARAMETER G(GAS,H2N2_CIS;0)           298.15 +F10925T#+R#*T*LN(1E-05*P);
 6000 N  !
  PARAMETER G(GAS,H2N2_TRANS;0)         298.15 +F10931T#+R#*T*LN(1E-05*P);
 6000 N  !
  PARAMETER G(GAS,H3N1;0)               298.15 +F11101T#+R#*T*LN(1E-05*P);
 6000 N !
  PARAMETER G(GAS,H4N2;0)               298.15 +F11153T#+R#*T*LN(1E-05*P);
 6000 N !
  PARAMETER G(GAS,N;0)                 298.15 +F12782T#+R#*T*LN(1E-05*P);
 6000 N !
  PARAMETER G(GAS,N2;0)                298.15 +F12981T#+R#*T*LN(1E-05*P);
 6000 N !
  PARAMETER G(GAS,N3;0)                298.15 +F13027T#+R#*T*LN(1E-05*P);
 6000 N !

PHASE AMORPHOUS  %  1  1.0  !
   CONSTITUENT AMORPHOUS  :B :  !

   PARAMETER G(AMORPHOUS,B;0)           298.15 +F1389T#; 6000 N !

 PHASE B10H14_L  %  1  1.0  !
   CONSTITUENT B10H14_L  :B10H14 :  !

   PARAMETER G(B10H14_L,B10H14;0)       298.15 +F1362T#+21966-59.0642646*T;
   6000 N !

 PHASE B10H14_S  %  1  1.0  !
   CONSTITUENT B10H14_S  :B10H14 :  !

   PARAMETER G(B10H14_S,B10H14;0)       298.15 +F1362T#; 6000 N !

 PHASE B1N1_L  %  1  1.0  !
   CONSTITUENT B1N1_L  :B1N1 :  !

 PARAMETER G(B1N1_L,B1N1;0)           298.15 +F1816T#+81000-25*T; 6000 N !

 PHASE B1N1_HEX  %  1  1.0  !
   CONSTITUENT B1N1_HEX  :B1N1 :  !
   PARAMETER G(B1N1_HEX,B1N1;0) 298.15 GBNHEX#; 3000 N !

 PHASE B1N1_CUB  %  1  1.0  !
   CONSTITUENT B1N1_CUB  :B1N1 :  !
   PARAMETER G(B1N1_CUB,B1N1;0) 298.15 GBNCUB#; 3000 N !

 PHASE B1N1_RHO  %  1  1.0  !
   CONSTITUENT B1N1_RHO  :B1N1 :  !
   PARAMETER G(B1N1_RHO,B1N1;0) 298.15 GBNRHO#; 3000 N !
```

```
PHASE B1N1_WUR  %  1  1.0  !
  CONSTITUENT B1N1_WUR  :B1N1 :  !
  PARAMETER G(B1N1_WUR,B1N1;0) 298.15 GBNWUR#; 3000 N !

PHASE B4C1_S  %  1  1.0  !
  CONSTITUENT B4C1_S  :B4C1 :  !

  PARAMETER G(B4C1_S,B4C1;0)            298.15 +F2133T#; 6000 N !

PHASE B5H9_L  %  1  1.0  !
  CONSTITUENT B5H9_L  :B5H9 :  !

  PARAMETER G(B5H9_L,B5H9;0)            298.15 +F2173T#; 6000 N !

PHASE B_L  %  1  1.0  !
  CONSTITUENT B_L  :B :  !

 PARAMETER G(B_L,B;0)                 298.15 +F1349T#+50200-21.3798978*T;
  6000 N !

PHASE B_S  %  1  1.0  !
  CONSTITUENT B_S  :B :  !

  PARAMETER G(B_S,B;0)                 298.15 +F1349T#; 6000 N !

PHASE C60_S  %  1  1.0  !
  CONSTITUENT C60_S  :C60 :  !

  PARAMETER G(C60_S,C60;0)             298.15 +F5302T#; 6000 N !

PHASE C6H6_L  %  1  1.0  !
  CONSTITUENT C6H6_L  :C6H6 :  !

  PARAMETER G(C6H6_L,C6H6;0)            298.15 +F5323T#; 6000 N !

PHASE C_L  %  1  1.0  !
  CONSTITUENT C_L  :C :  !
  PARAMETER G(C_L,C;0)                 298.15 +F3871T#+117369
 -24.6299289*T; 6000 N !

PHASE C_S  %  1  1.0  !
  CONSTITUENT C_S  :C :  !
  PARAMETER G(C_S,C;0)                 298.15 +F3871T#; 6000 N !

PHASE DIAMOND  %  1  1.0  !
  CONSTITUENT DIAMOND  :C :  !
  PARAMETER G(DIAMOND,C;0)             298.15 +F3893T#; 6000 N !

PHASE H4N2_L  %  1  1.0  !
  CONSTITUENT H4N2_L  :H4N2 :  !
  PARAMETER G(H4N2_L,H4N2;0)            298.15 +F11151T#; 6000 N !
```

Appendix I References

[1] A. T. Dinsdale, Calphad **15**, 317 (1991). SGTE Data for Elements. DOI:10.1016/0364-5916(91)90030-N.

10.10. Appendix J: $B_2H_6 – NH_3 – H_2$ chemical vapor deposition phase diagrams generated by FactSage

Using FactSage, chemical vapor deposition (CVD) phase diagrams of the B_2H_6-NH_3-H_2 precursor system were calculated to identify phase fields of specific boron nitride (BN) as a function of thermodynamic conditions (initial composition, temperature, and pressure). The initial composition is defined by $[B_2H_6]/([B_2H_6] + [NH_3])$ (mol/mol) which was allowed to vary between 0 and 1. A restraining condition was applied using $[H_2]/([B_2H_6] + [NH_3])$ (mol/mol) which was set to either 0 or 10 or 100. The temperature range was 400 – 1600 °C, and the pressure was set to either 0.01 or 1 or 100 Torr. The custom polymorphic BN database for FactSage described in Appendix H (Section 10.8) was used so that all four BN polymorphs could be considered for the calculations. Although the following diagrams show that c-BN has been calculated in this research to be the stable BN polymorph, the reasons why the cubic and wurtzitic BN phases should not be considered for equilibrium calculations such as this are detailed in the published paper by me and my co-authors Professors B. Webler, C. Pistorius, and R. Davis [1]. The following Figures show sets of CVD phase diagrams calculated from the B_2H_6-NH_3-H_2 at total pressures of 0.01 Torr (Fig. 10.10.1), 1 Torr (Fig. 10.10.2) and 100 Torr (Fig. 10.10.3). At each pressure, phase diagrams were calculated with $[H_2]/([B_2H_6] + [NH_3])$ set to either 0, 10, or 100.

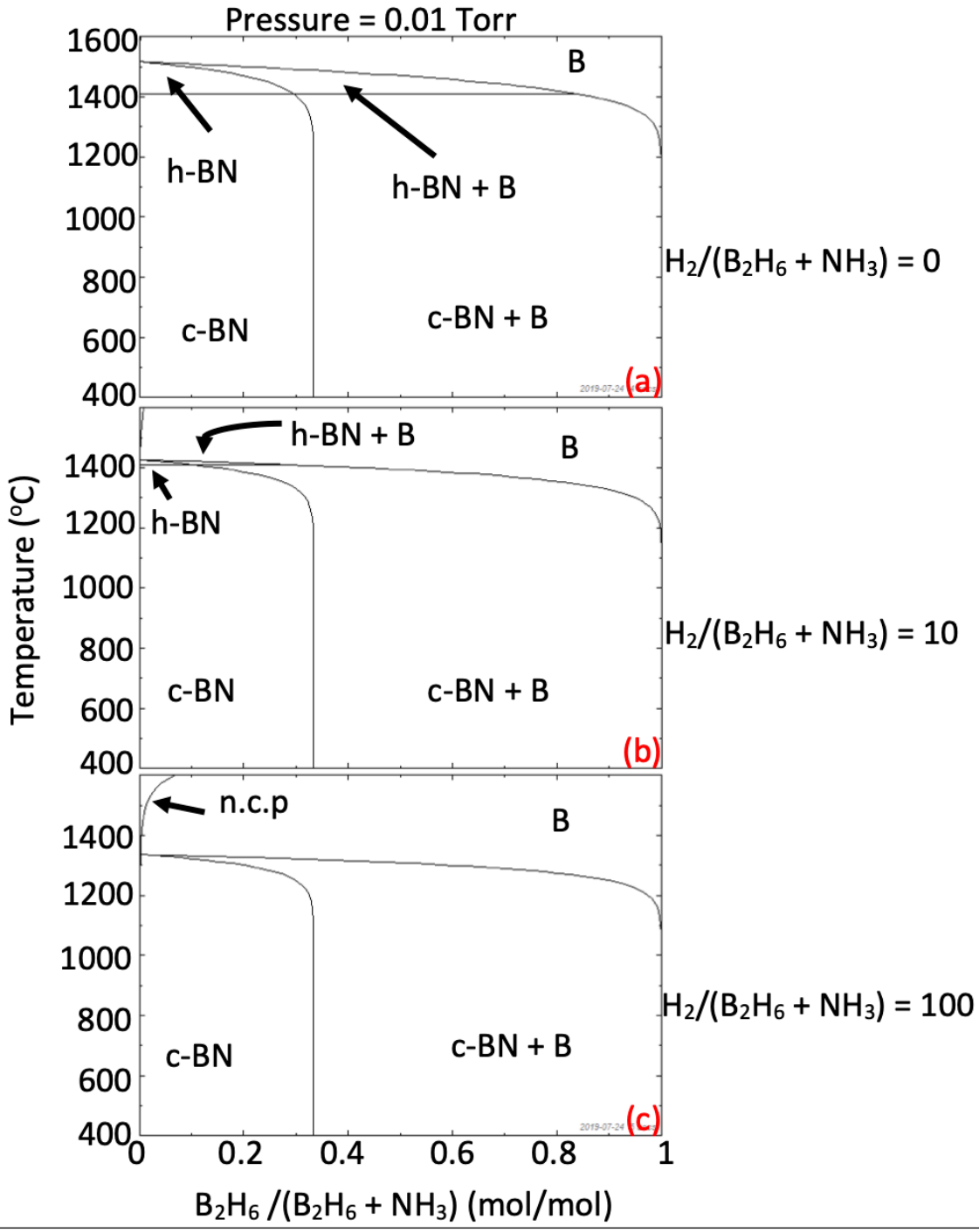

Figure 10.10.1. CVD phase diagrams of the B_2H_6-NH_3-H_2 system calculated at 0.01 Torr. The $[H_2]/([B_2H_6] + [NH_3])$ ratio is set to either (a) 0, (b), 10, or (c) 100.

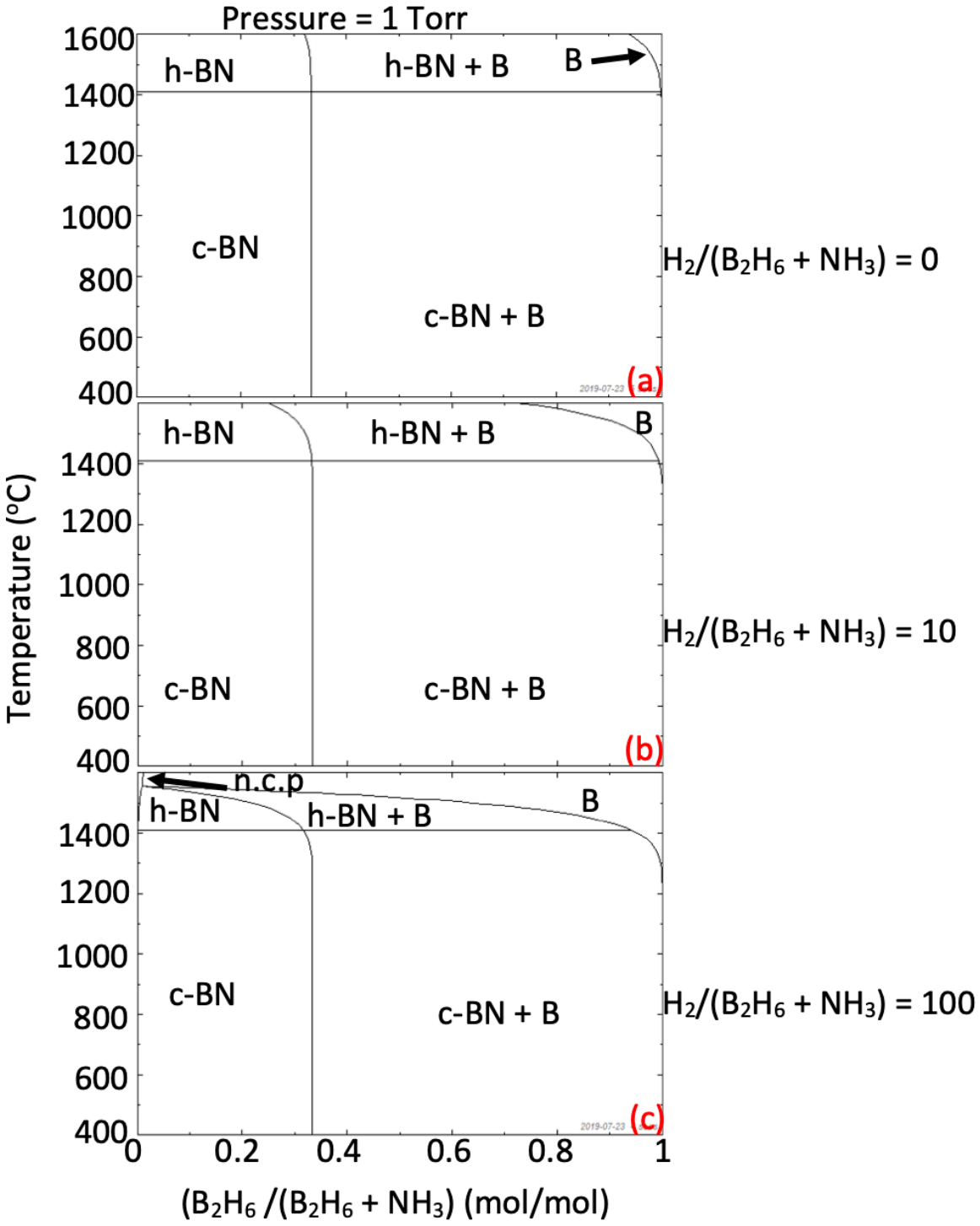

Figure 10.10.2. CVD phase diagrams of the B_2H_6-NH_3-H_2 system calculated at 1 Torr. The $[H_2]/([B_2H_6] + [NH_3])$ ratio is set to either (a) 0, (b), 10, or (c) 100.

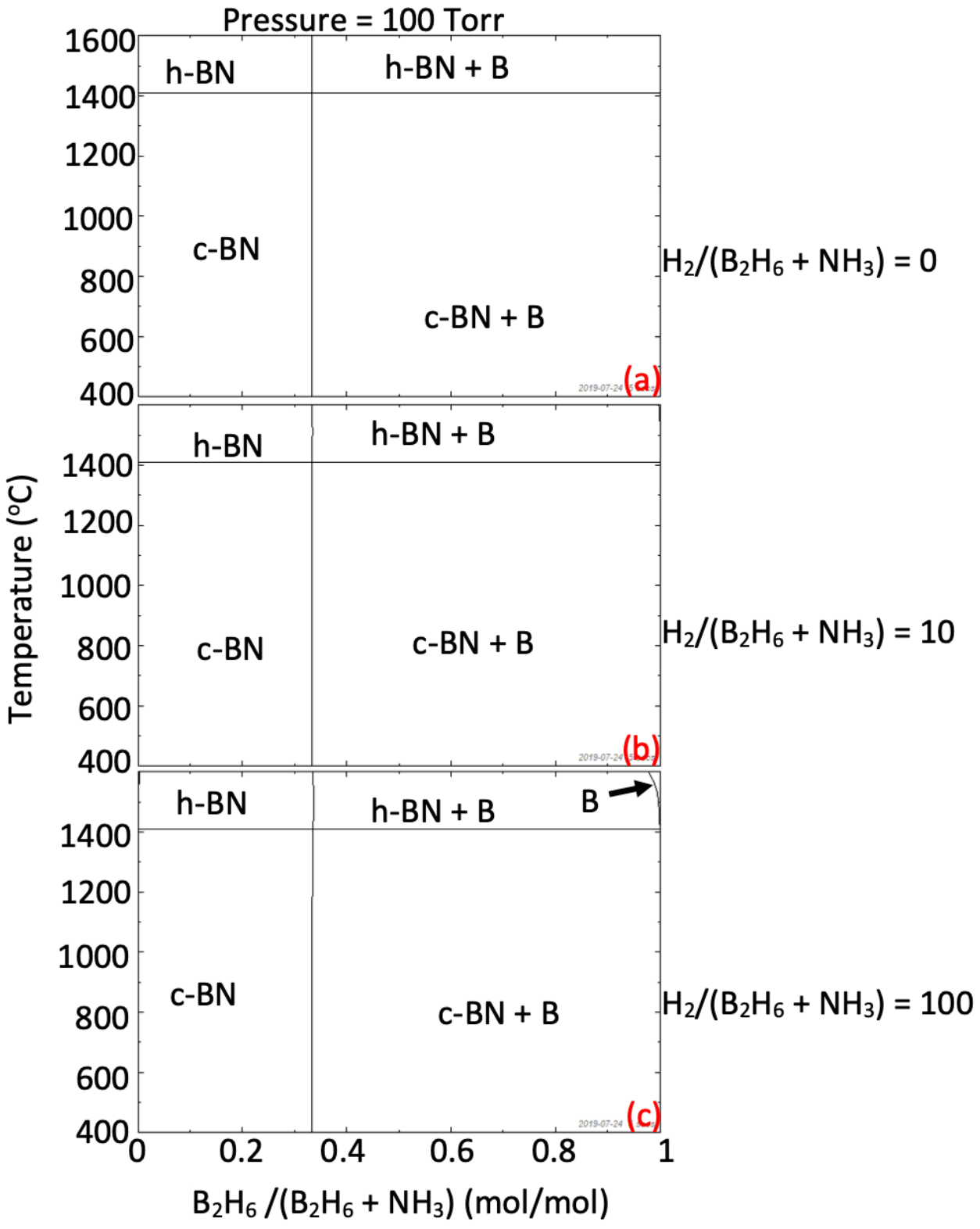

Figure 10.10.3. CVD phase diagrams of the B_2H_6-NH_3-H_2 system calculated at 100 Torr. The $[H_2]/([B_2H_6] + [NH_3])$ ratio is set to either (a) 0, (b), 10, or (c) 100.

Appendix J References

[1] P. M. Jean-Remy, B. A. Webler, P. C. Pistorius, and R. F. Davis, J. Cryst. Growth **572**, 1 (2021). Thermodynamic Calculations for the Chemical Vapor Deposition of Hexagonal Boron Nitride Using Triethylboron, Ammonia, and Hydrogen. DOI:10.1016/j.jcrysgro.2021.126283.